Light Scattering by Non-Spherical Particles

Diffusion de la lumière par das particules non-sphériques: simulation numérique et applications techniques

Zur Erlangung des akademischen Grades Doktor-Ingenieur (Dr.-Ing.)
genehmigte Dissertation von Patrick Günter Stegmann, M.Sc. aus Erlenbach am Main
Tag der Einreichung: 2015-12-16, Tag der Prüfung: 2015-10-20
Darmstadt 2016 — D 17

1. Gutachten: Prof. Dr.-Ing. Cameron Tropea
2. Gutachten: Prof. Gérard Gréhan

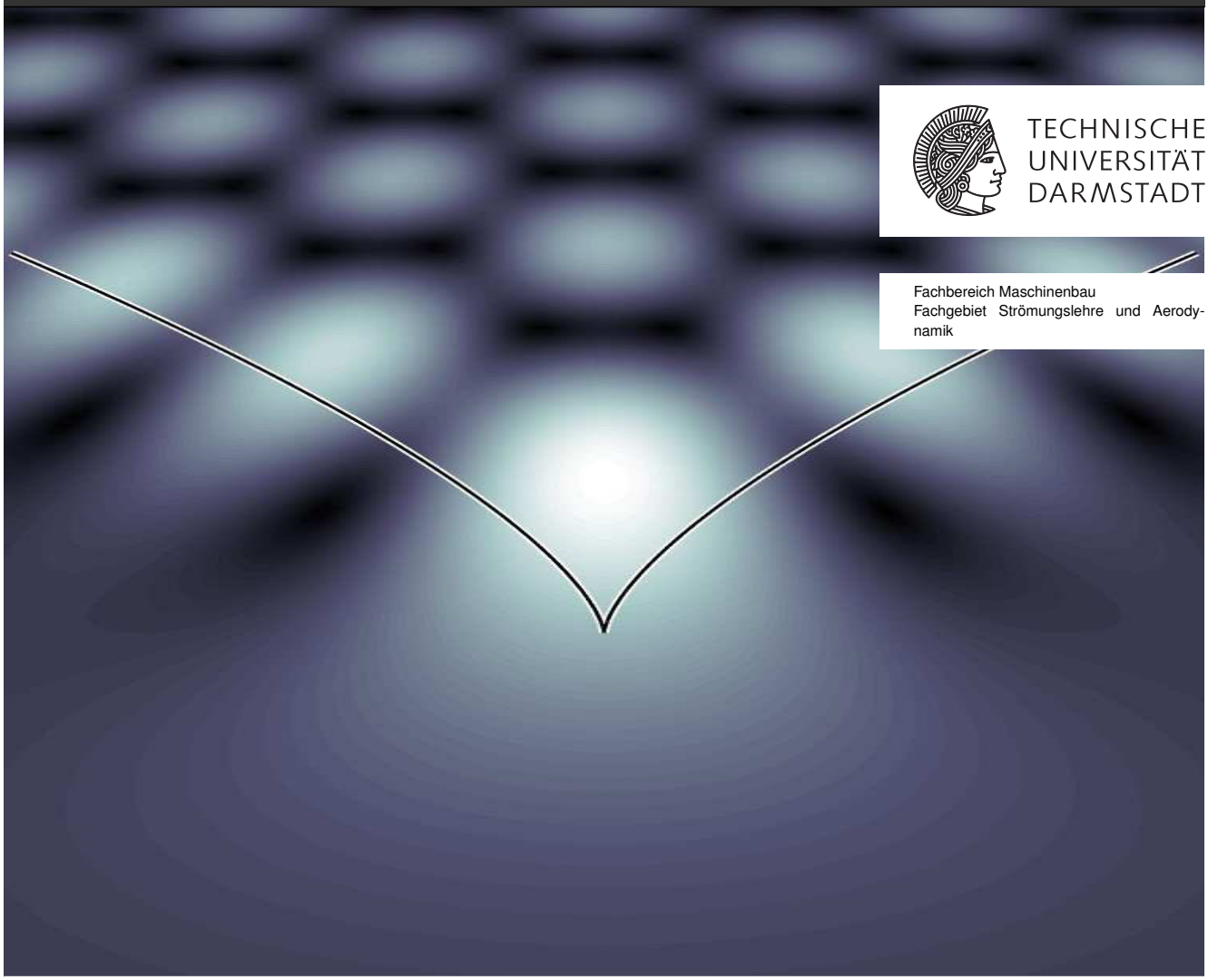

TECHNISCHE UNIVERSITÄT DARMSTADT

Fachbereich Maschinenbau
Fachgebiet Strömungslehre und Aerodynamik

In Collaboration with:
Complexe de Recherche Interprofessionel en Aérothermochimie, Rouen

Light Scattering by Non-Spherical Particles
Diffusion de la lumière par das particules non-sphériques: simulation numérique et applications techniques

Genehmigte Dissertation von Patrick Günter Stegmann, M.Sc. aus Erlenbach am Main

1. Gutachten: Prof. Dr.-Ing. Cameron Tropea
2. Gutachten: Prof. Gérard Gréhan

Tag der Einreichung: 2015-12-16
Tag der Prüfung: 2015-10-20

Darmstadt 2016 — D 17

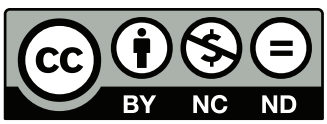

Erklärung zur Dissertation

Hiermit versichere ich, die vorliegende Dissertation ohne Hilfe Dritter nur mit den angegebenen Quellen und Hilfsmitteln angefertigt zu haben. Alle Stellen, die aus Quellen entnommen wurden, sind als solche kenntlich gemacht. Diese Arbeit hat in gleicher oder ähnlicher Form noch keiner Prüfungsbehörde vorgelegen.

Darmstadt, den 2015-10-20

(Patrick Günter Stegmann, M. Sc.)

Für meine Familie.

Abstract

Non-spherical particles are ubiquitous in nature as well as process engineering applications. Especially the reliable detection of ice crystals in flight by commercial airliners has received a considerable amount of attention from physicists and engineers alike during the recent years. While the problem of the scattering of a plane electromagnetic wave by a homogeneous and isotropic spherical particle such as a raindrop can be considered completely solved, the same is not true for non-spherical particles. Here is still an intense focus of research and development. This includes, but is not limited to the theoretical, numerical, and experimental side of the problem, due to a manifold number of difficulties. This work describes several different numerical and semi-analytic methods, which may be applied to the solution of the scattering problem. These methods have been developed in order to cover the entire range of the characteristic Mie size parameter. Most importantly, a direct application of the methods is the calibration and interpretation of the measurement results of the PHIPS probe, which was used to conduct a HALO campaign for the characterisation of atmospheric ice crystals. Specifically, the calculation methods of the finite integration of Maxwell's equations, as well as the transition operator method, which is widely used in the fields of classical as well as quantum mechanical scattering theory. Unique among existing codes, the geometrical optics derivative methods are applicable to any geometry and to any sort of continuous or discontinuous refractive index distribution. Furthermore, the predictive methods have been applied to a number of representative example geometries, and the influence of wave polarisation and particle orientation has been investigated through statistical sampling. Additionally, a computational class has been implemented in order to consider the influence of shaped beam incidence on the scattered light intensity distribution. Such a shaped beam plays a central role in measurement devices based on the Time-Shift principle, where the particle illumination is provided by a laser beam with a Gaussian profile. The limits of applicability of the different computational approaches are also indicated in the thesis. Furthermore, several modern measurement approaches have been evaluated with regards to their applicability to non-spherical particles. This includes the aforementioned Time-Shift principle, and Interferometric Imaging. The analysis of the different measurement techniques is documented in the experimental section of the thesis. Tentative measurements of the phase functions of ice crystals in a laboratory environment have also been conducted and the specific requirements for handling and conducting optical experiments with ice crystals are also explained in the document. As a common problem of all the measurement principle, the limited dynamic range of the optical detectors used in practice could be identified. A final important aspect addressed in the thesis is the production and storage of ice crystals with optical properties as natural as possible. For this purpose, a compact cloud chamber was developed, that provided the necessary properties, both in terms of quantity, as well as quality of the ice crystals produced by the device. Construction and operational details of the cloud chamber are reported in the last chapter of the thesis.

Kurzfassung

Nicht-sphärische Teilchen sind in der Natur sowie in verfahrenstechnischen Anwendungen sehr häufig anzutreffen. Insbesondere die Detektion von Eiskristallen während des Fluges durch Verkehrsflugzeuge ist ein Problem, dass in den vergangenen Jahren vermehrt Aufmerksamkeit erhalten hat. Während das Problem der Streuung einer ebenen elektromagnetischen Welle durch ein homogenes und isotropes sphärisches Teilchen, wie z.B. einen Regentropfen als vollständig gelöst anzusehen ist, ist dies bei nicht-sphärischen Partikeln nicht der Fall. Hier existiert nach wie vor ein Fokus der Forschung und Entwicklung sowohl auf theoretischer, numerischer, als auch experimenteller Seite, aufgrund einer Vielzahl an unterschiedlichen Schwierigkeiten. Diese Arbeit beschreibt verschiedene numerische und semianalytische Verfahren, die auf das Streuproblem angewandt werden können und dabei die gesamte Reichweite des maßgeblichen Mie-Größenparameters abdecken. Diese Methoden werden auf die Kalibration und Interpretation der Messergebnisse des PHIPS-Messinstruments angewandt, welches in einer HALO Kampagne zur Charakterisierung von atmosphärischen Eiskristallen erprobt wurde. Die Berechnungsmethoden im Einzelnen beinhalten zwei Derivate der geometrischen Optik, anwendbar auf beliebige Partikel-Geometrien mit homogenem, als auch inhomogenem Brechungsindex, das numerisch exakte Verfahren der Finiten Integration der Maxwell-Gleichungen, sowie die in der Lichtstreuung und Quantenmechanik häufig verwendete Transitionsoperator-Methode. Diese Berechnungsmethoden werden auf eine Reihe von Beispiel-Geometrien angewandt und der Einfluss von Polarisation und gemittelter Partikel-Orientierung werden untersucht. Zusätzlich wurde ein Verfahren implementiert, dass das Strahlprofil eines Laserstrahls auf die gestreute Lichtintensität berücksichtigt, welches beispielsweise in der Anwendung bei Time-Shift Messungen eine zentrale Rolle spielt. Die Grenzen der Anwendbarkeit der verschiedenen Berechnungsmethoden werden in der Arbeit erläutert. Des Weiteren werden mehrere moderne Messverfahren auf ihre Anwendbarkeit im Hinblick auf nicht-sphärische Teilchen hin überprüft. Dies beinhaltet unter anderem das Time-Shift Messverfahren, sowie interferometrische bildgebende Verfahren. Die Analyse der Anwendbarkeit der verschiedenen Messmethoden ist im experimentellen Abschnitt der Arbeit dokumentiert. Messungen der Streulicht-Phasenfunktionen von natürlichen Eiskristallen wurden ebenfalls durchgeführt und die spezifischen Vorbereitungen für die Untersuchungen von Eiskristallen in einem optischen Experiment werden in dieser Arbeit ebenfalls erläutert. Als gemeinsame Problematik konnte bei vielen Verfahren der limitierte Dynamikbereich der verwendeten Detektoren identifiziert werden. Ein abschließender wichtiger Aspekt in dieser Arbeit ist die Produktion und Aufbewahrung von Eiskristallen mit möglichst natürlichen optischen Eigenschaften in einer Laborumgebung. Hierfür wurde eine kompakte Wolkenkammer entwickelt, die die geforderten Eigenschaften an Produktionsmenge und Qualität von Eiskristallen erfüllt. Auslegung, Konstruktion und Betrieb des Apparates werden im letzten Kapitel der Dissertation detailliert wiedergegeben.

Contents

Nomenclature

Remark: All numerical values have either been cited from [Str07] or [BSM00]. Symbols that don't carry a physical unit are denoted by [-].
Dimensionless Numbers

- beam aspect ratio:
  $s = \frac{2 \cdot w_0}{l} = \frac{1}{k \cdot w_0} = \frac{1}{b_0} = \frac{\text{beam waist diametre}}{\text{diffraction length}}$
- Courant-Friedrichs-Lewy number:
  $CFL = \frac{v \cdot \Delta t}{\Delta x} = \frac{\text{causal speed} \times \text{time step size}}{\text{grid spacing}}$
- Mie size parameter:
  $x_M = \frac{2\pi \cdot r}{\lambda} = \frac{\text{particle circumference}}{\text{wavelength of the incident beam}}$
- Fresnel number:
  $F = \frac{r^2}{L \cdot \lambda} = \frac{\text{aperture/particle size}^2}{\text{distance of screen from aperture} \times wavelength}$
- Reynolds number:
  $Re = \frac{u_{max} \cdot L}{\nu} = \frac{\text{inertial stresses}}{\text{viscous stresses}}$

Roman Alphabet Symbols

symbol	dimension	unit	usage
L	L	$[m]$	lengthscale
P		[-]	probability / degree of linear polarisation
$h = 2\pi\hbar = 6.62606957(29) \times 10^{-34}$	ML^2T^-1	$[J \cdot s]$	Planck's constant
i			imaginary unit $\sqrt{-1}$
$e = 1.60217653(14) \cdot 10^{-19}$	Q	[Coulomb]	elementary charge
$e = 2.718281828\ldots$			Euler's number
m	M	[kg]	mass
$c = \frac{1}{\sqrt{\mu_0 \cdot \varepsilon_0}} = 2.99790 \times 10^8$	$\frac{L}{T}$	$\left[\frac{m}{s}\right]$	speed of light in vacuum
K			arbitrary constant
t			arbitrary small constant $t \to 0$
A			tensor
A			generic amplitude of a wave function
x	L	$[-, m]$	generic or canonical position vector
E	$MLT^{-2}Q^{-1}$	$\left[\frac{V}{m}\right]$	electric field intensity
H	$L^{-1}T^{-1}Q$	$\left[\frac{A}{m \cdot s}\right]$	magnetic field intensity
I	ML^2T^{-3}	$\left[\frac{W}{m^2}\right]$	Intensity/total irradiance, Identity matrix
B	$MT^{-1}Q^{-1}$	$\left[\frac{We}{m^2}\right]$	magnetic flux density
D	$L^{-2}Q$	$\left[\frac{Q}{m^2}\right]$	dielectric displacement
P	$L^{-2}Q$	$\left[\frac{Q}{m^2}\right]$	Polarisation

Q	ML^2T^{-3}	$\left[\frac{W}{m^2}\right]$	orthogonal matrix / parallel minus perpendicular linear polarised irradiance
d	L	[m]	interfocal distance
S	ML^2S^{-1}	$[J \cdot s]$	action, surface facet slope
L	ML^2T^{-1}	$[J]$	Lagrange function
H	ML^2T^{-1}	$[J]$	Hamilton function
$\mathscr{L}$	$ML^{-1}T^{-2}$	$\left[\frac{J}{s \cdot m^3}\right]$	Lagrangian density
$\mathscr{H}$	$ML^{-1}T^{-2}$	$\left[\frac{J}{s \cdot m^3}\right]$	Hamiltonian density
P_1, P_2	L	[m]	geometrical points
M		[-]	Müller matrix
M_{11}		[-]	Phase function
T		[-]	Transition matrix
S	ML^2T^{-3}	$\left[\frac{W}{m^2}\right]$	Scattering matrix / Poynting vector
$f(x_i)$			arbitrary function of x_i, flux of conserved quantity $u(x,t)$
P_n^m		[-]	Associated Legendre Function
H_n^m		[-]	Hermite-polynomials
L_n^m		[-]	Laguerre-polynomials
$g_{\mu\nu}$	$\frac{L^2}{dim(x^\mu) \times dim(x^\nu)}$	$\left[\frac{m^2}{unit(x^\mu) \times unit(x^\nu)}\right]$	covariant metric tensor
dA			electromagnetic potential 1-form / U(1) principle bundle connection
A_μ			covariant electromagnetic field potential tensor
dF			electromagnetic field 2-form / U(1) principle bundle curvature
$F_{\mu\nu}$			covariant electromagnetic field tensor
$G^{\mu\nu}$			contravariant dual field tensor
U	ML^2T^{-3}	$\left[-, \frac{W}{m^2}\right]$	concrete representation of a unitary group / Linear polarised irradiance under $\pi/4$
g			external forcing function
k	L^{-1}	$\left[\frac{1}{m}\right]$	wave vector
k	L^{-1}	$\left[\frac{1}{m}\right]$	wavenumber
p	MLT^{-1}	$\left[kg \cdot \frac{m}{s}\right]$	canonical momentum for a particle
u	$ML^{-1}T^{-1}$	$\left[\frac{J}{m^3}\right]$	electromagnetic energy density
$u(x,t)$			function representing a conserved quantity
$W(x,p)$		[-]	Wigner pseudo probability distribution
l,m,n		[-]	direction cosines
r		[-]	ray normal vector
b		[-]	ray binormal vector
V	ML^2T^{-3}	$\left[-, \frac{W}{m^2}\right]$	circularly polarised irradiance

n		[-]	integer number / index of refraction
p	$ML^{-1}T^{-2}$	[Pa]	thermodynamic pressure
T	K	[K]	thermodynamic temperature
G	ML^2T^{-2}	[J]	Gibb's free energy
$k_B = 1.38064852(79) \cdot 10^{-23}$	$ML^2T^{-2}K^{-1}$	$[J/K]$	Boltzmann constant
D_6			dihedral group

Greek Alphabet Symbols

symbol	dimension	unit	usage
α		[-]	offset in the complex plane
τ	T	$[s]$	timescale, affine parameter
ρ	$\frac{Q}{L^3}$	$\left[\frac{Coulomb\ kg}{m^3}\right]$	charge density
ε_{ijk}			Levi-Cività pseudo-tensor
δ_{ij}			Kronecker-delta
$\pi = 3.141592654\ldots$			Ludolf's number
Γ			generic generator of a one-parameter transformation
$\varepsilon_0 = 8.854 \cdot 10^{-12}$		$\left[\frac{Farad}{m}\right]$	dielectric constant
$\mu_0 = 4\pi \cdot 10^{-7}$		$\left[\frac{Henry}{m}\right]$	magnetic permeability
χ		[radians]	susceptibility / elevation angle of the Poincaré sphere
Φ			scalar potential
ω	T^{-1}	$\left[\frac{1}{s}\right]$	eigenfrequency / angular frequency
ν	T^{-1}	$\left[\frac{1}{s}\right]$	frequency
Ω		$[radians^2]$	solid angle
λ	L	$[m]$	wavelength, eigenvalue
$\Psi_n^{(m)}$			Spherical Bessel Function
Ψ, ψ		[radians]	generic scalar wave equation solution / eikonal / and azimuth angle of the Poincaré sphere
$\Gamma^{\mu}_{\alpha\beta}$	$\frac{dim\left(x^{\mu}\right)}{dim(x^{\alpha}) \times dim\left(x^{\beta}\right)}$		affine connection on a manifold
$d\chi$			gauge potential 1-form
θ		[radians]	polar / azimuth angle
ϕ		[radians]	elevation angle
κ	$M^{-1}L^{-3}T^3C^2$	$\frac{1}{\Omega m}$	electric conductivity / curvature of a parametric graph
κ_ν			frequency specific absorption coefficient
η			relative index of refraction
$\eta_{\mu\nu}$	$\frac{L^2}{dim(x^{\mu}) \times dim(x^{\nu})}$	$\left[\frac{m^2}{unit(x^{\mu}) \times unit(x^{\nu})}\right]$	contravariant Minkowski metric tensor
σ		[%]	standard deviation of Gaussian pdf / relative humidity

μ	$ML^2T^{-2}mol^{-1}$	$\left[\frac{J}{mol}\right]$	molar chemical potential

Sub- and Superscripts

symbol	usage
∞	refering to conditions in the far field
0	initial condition
-1	inverse mathematical operator, matrix or function
a	average
e	electric / electron-related / extra ordinary
m	magnetic
o	ordinary
M	Mie-
i	vector index in 3-space
j	vector index in 3-space
k	vector index in 3-space
α	vector index in 4-space
μ	vector index in 4-space
ν	vector index in 4-space, specific frequency
TE	transversal-electric
TM	transversal-magnetic
$\|\|$	parallel to a reference plane
$\perp$	perpendicular to a reference plane
CMOS	CMOS-related
$\hat{x}$	mathematical operator, normalized spatial vector
$\tilde{x}$	quantity defined on the dual grid
I	incident
T	transmitted
R	reflected
coherent	coherent
total	total
scatt	scattered
lens	lens property
gp	glare point
molec	molecular property
vap	vapour property
evap	evaporation property
cond	condensation property
crystal	crystal related
tet	tetrahedron

Mathematical Operators and functions

symbol	alternative	usage
$\nabla\mathbf{r}$	$\frac{\partial r_i}{\partial x_k}$	Gradient operator
$\nabla\cdot\mathbf{r}$	$\frac{\partial r_i}{\partial x_i}$, div $\mathbf{r}$	Divergence operator
$\nabla\times\mathbf{r}$	$\varepsilon_{ijk}\frac{\partial r_i}{\partial x_k}$, rot $\mathbf{r}$	Curl operator
$\Delta\mathbf{r}$	$\frac{\partial}{\partial x_i}\frac{\partial x_i}{\partial x_k}$, ∇^2	Laplace operator
$\Box\cdot\mathbf{r}$	$\Delta\mathbf{r}+\frac{1}{c^2}\cdot\frac{\partial\mathbf{r}}{\partial t}$	d'Alembert operator
$\mathbf{a}\cdot\mathbf{b}$	$a_k\cdot b_k$, $\langle a\,\vert\,b\rangle$	scalar (inner) product
$\mathbf{a}\times\mathbf{b}$	$\varepsilon_{ijk}\cdot a_i\cdot b_j$	vector product
$\Re e$		real part of an imaginary number

$\Im m$		imaginary part of an imaginary number
$\dot{x}$	$\frac{\partial x}{\partial t}$	first derivative with respect to time
$\ddot{x}$	$\frac{\partial^2 x}{\partial t^2}$	second derivative with respect to time
e^x	exp(x)	exponential function
$x!$		factorial function for elements $x \in \mathbb{N}$
$\Gamma(x)$		generalisation of the factorial function for elements $x \in \mathbb{C}$
ln x	$log_e(x)$	natural (base e) logarithm, Neperian logarithm
$log_{10}\, x$	log(x)	base 10 logarithm
$arctan\, x$	atan(x)	Arcus tangens
$x\ (mod\ y)$		x modulo y
$\mathscr{F}$		Fourier transform
d		exterior differentiation
$\star$		Hodge star
$\wedge$		exterior (wedge) product
Dx	$\frac{Dx}{Dt} = x_{,t}$	covariant / total derivative of x
$\bullet$		abstract operation of a mathematical group
$\langle \cdot \vert$		bra vector
$\vert \cdot \rangle$		ket vector
U^*		conjugate transpose of matrix or operator U
δS		variation of the action S
$\hat{D}(\alpha)$		displacement operator in the complex plane
$\Vert \cdot \Vert_2$		Euclidean norm
$[\cdot, \cdot]$		commutator bracket

Acronyms

Acronym	usage
ADDA	Amsterdam DDA code
AIDA	Aerosol Interaction and Dynamics in the Atmosphere
CCD	Charge coupled device
CFD	Computational Fluid Dynamics
CMOS	Complementary metal-oxide-semiconductor
CST	Computer Simlutation Technologies
DESY	Deutsches Elektronen-Synchrotron
DDA	Discrete Dipole Approximation
EOM	Equation of Motion
FDTD	Finite Difference Time Domain Method
FIT	Finite Integration Technique
FLMT	Fourier-Lorenz-Mie Theory
GLMT	Generalized Lorenz-Mie Theory
GO	Geometrical Optics
GSI	Gesellschaft für Schwerionenforschung
GSL	GNU Scientific Library
HALO	High Altitude and LOng Range
HAIC	High Altitude Ice Crystals
HeNe	Helium-Neon
IDE	integrated developement environment
IGO	Integral Geometrical Optics
IPI	Interferometric Particle Imaging
KIT	Karlsruhe Institute of Technology
LASER	Light Amplification by Stimulated Emission of Radiation
LMT	Lorenz-Mie Theory
MDR	Morphology Dependent Resonance
MGE	Maxwell's Grid Equations
MICC	Manchester Ice Cloud Chamber
ODE	ordinary differential equation

OOP	object-oriented programming
PC	Personal Computer
PDE	partial differential equation
PHIPS	Particle Habit Imaging and Polar Scattering
PISO	Pressure implicit with splitting of operator
PML	Perfectly Matched Layer
PRNG	Pseudo Random Number Generator
pw	plane wave (incidence)
QFT	Quantum Field Theory
RNG	Random Number Generator
RNG k-ε	Renormalisation Group k-ε model
RP	Rapid Prototyping
RTE	Radiation Transport / Radiative Transfer Equation
SID	Small Ice Detector
SIMPLE	Semi-Implicit Method for Pressure Linked Equations
TE	transversal electric
TEMF	Theorie Elektromagnetischer Felder
TM	transversal magnetic
T-Matrix	Transition matrix
UK	United Kingdom

List of Figures

All images shown in this document have been created by the author himself. Exceptions are explicitly identified as such.

List of Tables

List of Algorithms

1 Introduction

> How full of the creative genius is the air in which these are generated! I should hardly admire them more if real stars fell and lodged on my coat.
>
> —*Henry David Thoreau* on snowflakes.

A QUITE graphic introduction to the general programe of this manuscript may be given by looking at the impressive display of a naturally occuring halo shown in the photograph 1.1 taken by Joshua Thomas and published by the US National Weather Service Amarillo. This rare phenomenon in atmospherical optics is conceptionally similar to the more common rainbow, with the exception that the observer needs to look directly at the source of illumination, which normally is the sun or the moon, while the rainbow can only be observed when looking at a rain cloud in opposition to the sun. In scattering theory the obvious statement is formalised that the halo is a forward scattering feature while the common rainbow is a backscattering feature.
The halo captured in image 1.1 is caused by ice crystals dissolved in the terrestrial atmosphere. This graphic example serves to emphasize how a highly ordered, spatially coherent (in a geometrical sense) structure can emerge from the complete randomness of orientation, size and even shape of the ice crystals floating in the upper strata of the atmospheric currents. It is important to emphasize that this is true randomness in the strict definition and not deterministic chaos as found in nonlinear dynamics [Hag78].

Figure 1.1: Naturally occuring halo display in the boreal region of the northern hemisphere, courtesy of the US National Weather Survice of Amarillo, Texas. The 22 and 46 degree halos as well as sundogs, upper tangent arc, and parhelic circle are well visible. The image is used for research purposes under the conditions of fair use.

Details as to how such a halo is formed exactly may be found for instance in the book [WY12] by Yang et al. . The importance of such phenomena arising from chance lies in their potential for technical exploitation. The challenge in characterising non-spherical particles lies in identifying such optical features that are common to a particular class of particles. While the techniques described in this thesis are also applicable to the general class of non-spherical particles, the primary focus of the presentation will be given to ice crystals, due to their extraordinary impact on the safety of commercial aircraft [LAH98], their contribution to the terrestrial radiation budget [WY12] and the challenge in modelling all their unsusual properties, such as the possibly uniaxial refractive index and the self-similar shape [MT92].

1.1 The danger of ice crystals to aircraft engines

It is clear that given a specific traffic or weather situation, a commercial or other aircraft cannot always avoid a flight path intersecting a thundercloud. At operating altitudes of 9 kilometres or higher, so-called cumulonimbus clouds consist mainly of an upper part shaped like an anvil and which is thus fittingly termed by the latin translation *incus* in the scientific literature [LAH98]. In these upper regions of thunderclouds temperatures between 253 and 203 Kelvin prevail und conditions such as heavy precipitation or turbulence are rarely encountered. Nevertheless certain starting conditions can favour the presence of high mass fractions of ice in the incus. High humidity in the cloud base combined with strong updraught are an example of such conditions. As a consequence, unexpected airframe icing may be encountered in these altitudes. Since the end of the 20^{th} century several cases of such ice deposition and even engine thrust loss have been observed [LAH98, MSC06]. Such thrust loss events have occured with increasing frequency in tropical thunderclouds. Mason et al. suggest in [MSC06] that the guide vane assembly of the low pressure compressor is an especially critical area for ice crystal accretion, as depicted in figure 1.2 which also shows several other areas subject to adverse icing effects. Specifically the guide vane assembly of the low pressure compressor is usually has no anti icing system and does not rotate. Growth of layers of foreign material such as ice on the guide vane blades may easily upset both the sensitive thermodynamic and flow field conditions present in the generally highly stressed compressor. A deeper analysis of the sensitivity of turbine compressors may be found for instance in the seminal book [Brä15] of Bräunling.

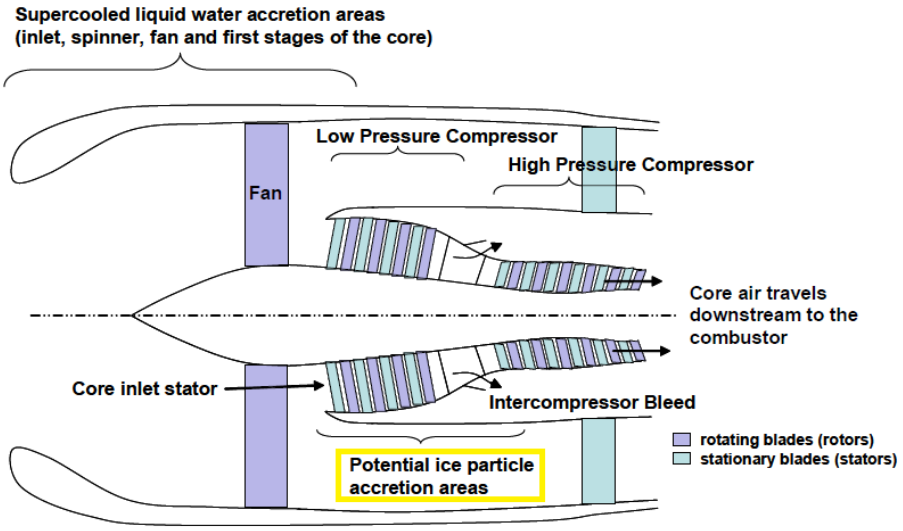

Figure 1.2: Sketch of possible accretion areas in a turbofan engine adapted from Mason [MSC06]. As shown, the main accretion area for ice is the warm low- to intermediate pressure compressor. The image is used for research purposes under the conditions of fair use.

Currently no measurement devices exist for the reliable indication of icing conditions, whether they are linked to supercooled liquid droplets or solid ice crystals. This also poses a problem in the field of atmospheric physics, as ice crystals are a common naturally occuring aerosol, which has a drastic influence on the climate of the earth. Without reliable experimental detection and characterization, no information on real ice crystals can be gained. Thus, the aim of this thesis is to provide another step towards being able to acquire full *in situ* knowledge about all the properties of ice crystals present under real atmospheric conditions.

1.2 Current progress in the optical characterisation of nonspherical particles

Given the famous original solution by Gustav Mie [Mie08] for the problem of the scattering of a time-harmonic electromagnetic plane wave by a dielectric sphere, modern advancements in computer technology and reformulations of the original solution such as the one given in the book of van de Hulst [Hul01] have allowed the possibility to calculate the exact scattered fields for a sphere potentially arbitrary in size, so long as the energy density of the field and the mass of the sphere remain small enough not to necessitate the inclusion of gravity. A testimony for the present ubiquitousness of Mie codes is the availability of Mie applications even for early smartphone models, such as the code published by Wriedt [Wri08].

In contrast, the scattering of light by non trivial shapes has entailed numerous difficulties. First exact solutions in the early 1970s were limited to still highly symmetric spheroidal particles, such as [AY75] published by Asano and Yamamoto. Nevertheless the foundations were layed in terms numerical or semi-analytical solution methods which could later be applied to more complicated problems as soon as more computational ressources were available due to the development of the calculation power of computers following Moore's law [Moo98]. Fully numerical methods include the the popular Finite Difference Time Domain (FDTD) method introduced in its present form by Yee [Yee66] in 1966 and the related Finite Integration Technique (FIT) developed by Prof. em. T. Weiland [Wei77] in 1977. Both of these methods had only limited applicability to scattering and other free space problems before the advent of Berenger's Perfectly Matched Layer technique published in [Ber94] for the representation of open (fully absorbing) boundaries. Both methods are computationally very expensive due to the required volume discretization of the scattering particle and are thus limited to particles with a maximum dimension of less than ten micrometres on a workstation using OpenMP.
Two computational methods that are very specific to the field of scattering theory are the so-called Discrete Dipole Approximation (DDA) first proposed by Purcell and Pennypacker [PP73] in 1973 in an astronomical context and Peter Waterman's nullfield T-Matrix method [Wat71] from 1971. Both methods can also be combined in order to calculate the T-matrix through use of the DDA formalism such as for instance in [TVP15]. Each of the two methods has distinct advantages when it comes to treating scattering problems, which is the reason for their wide popularity in the scattering community [YH07, MTM10]. While the T-matrix itself is conceptually identical to the transition operator $\hat{T}$ in quantum mechanical scattering (see e.g. ref. [IZ06]) and the inception of the T-matrix method by Waterman is not a feat as revolutionary as one is lead to believe, the method nevertheless excels in the exploitation of symmetries, both of the underlying field equations [Wat71] and of the scattering particle itself [Kah05]. The DDA in turn complements the T-matrix method by being readily applicable to any conceivable particle shape except spheres, including surface roughness. The current DDA reference implementation ADDA [Yur14, YH11] by Hoekstra and Yurkin was designed to be run on massively parallel architectures [Hoe94] from the start and the code is advertised to be easy to use. As such, the DDA method is widely popular in projects such as [Wor04], that require robust and quick light scattering calculations which do not entail a steep learning curve.
While the above methods are exact in the numerical sense, in practice they are most often limited to particle sizes below 10 micrometres. Larger particles are treated using derivations of the classic geometrical optics (GO) technique as discussed in the book of Born and Wolf [BW99] or Kravtsov [KO90]. Current reference implementations include the openly available code [Mac15] written by Prof. Macke during his Ph.D. thesis [Mac94, MMR96] from the TROPOS institute and the integral geometrical optics (IGO) method proposed by Dr. Ping Yang [YL97, YL96] which uses geometrical optics only to calculate the electromagnetic fields in the vicinity of the scattering particle and includes a farfield propagator mechanism in order to calculate the Müller matrix $\boldsymbol{M}$. Novel techniques with currently unclear impact include the *beam tracing with diffraction on facets* approach by Hesse et al. [HU03] and the volume integral *invariant imbedding T-matrix method* by Dr. Ping Yang [BY14].

1908	Gustav Mie explains the scattering of a plane electromagnetic wave by a spherical particle as a solution of Maxwell's equations
1966	Yee introduces the staggered grid formulation of the FDTD
1971	Waterman formulates the first account of the T-matrix method
1973	Purcell and Pennypacker invent the DDA
1975	Asano and Yamamoto solve the problem of scattering by a spheroidal particle
1977	Weiland introduces the Finite Integration Technique
1994	Hoekstra lays the foundations for the A-DDA code
	Berenger invents the PML boundary condition
	Macke publishes his ray tracing code
1996	Yang formulates the IGO algorithm

Table 1.1: Timetable of important events in the optical characterization of nonspherical particles with a focus on ice crystals.

Reliable experimental investigations into the optical properties of ice crystals have only been possible very recently, including for instance the measurements undertaken by Smith et al. [SCB$^+$15] or the Particle Habit Imaging and Polar Scattering probe developed by Schnaiter [ASA$^+$11] for ice crystal sizes large enough to allow imaging and forward diffraction measurements [KHG$^+$08, UKH$^+$14] using the Small Ice Detector (SID) in the converse case.

1.3 Scope of this work

Overview

This thesis will start with a comprehensive review of the equations used to calculate the behaviour of light. In the second part, several solution methods for these equations are discussed together with their range of applicability as well as the respective advantages and disadvantages. The third part will comprise the experiments conducted during the thesis at SLA which were mainly aimed at determining sizes of non-spherical particles. As a conclusion, several engineering applications related to the optical characterisation of non-spherical particles will be portrayed, including the PHIPS measurement device and an ice generator for laboratory scale ice particle production. The primary problem addressed in this thesis is the prediction of the influence of a Gaussian beam profile on the light scattered by large non-spherical particles, as it is of great importance for optical experiments and so far an unanswered question. Furthermore, for the first time a computational approach has been developed to take inhomogeneities in a particle into account during geometrical optics calculations. Also the Finite Integration Technique was investigated with respect to its applicability towards scattering problems.

Continuity of previous projects at SLA

While certainly a highly unusual topic for an engineering faculty, the subject of this thesis was a direct outgrowth of the two preceding theses furnished by Schäfer [Sch13] and Yu [Yu13]. While Schäfer had developed a reliable and compact time-shift probe, Yu had made first steps towards the application of rainbow refractometry to oblate spheroidal droplets. Due to the involvement of the Institute for Fluid Mechanics and Aerodynamics in the High Altitude Ice Crystals (HAIC) project of the European Union, naturally the question arose whether the existing expertise in the field of spray characterisation could be extended to ice particles. Especially applying the time-shift technique to ice crystals was initially seen as worthwhile, although from the perspective of light scattering theory it was immediately obvious that an unmodified time-shift probe would not deliver sufficiently precise measurement results. The reason for this was the interpretation of the measurement signals based on simple ray tracing considerations and Debye series solutions [Hul01], which of course were both necessarily relying on a perfectly spherical scatterer. Consequently, novel techniques had to be sought which would allow to solve the scattering problem also for non-spherical particles in conjuction with inhomogeneous incident fields such as the highly focused laser beam used in a time-shift probe. As the present author had already written the ray tracing code used by Yu [Yu13] to interpret the rainbow caustic measurements in his thesis, creating an appropriate geometrical optics solver for treating large non-spherical particles had become the starting point of this new project and the details of the code are given in chapter two. Using geometrical optics in scattering calculations is often seen as an advantage, as it is viewed as inherently less difficult to understand and to use when compared to exact methods. This misconception is rooted in the intuitive concept of geometrical optics but in truth the situation is quite the reverse when it comes to applying both approaches in their complete generality.

Large Mie parameter models

Geometrical optics in one of its incarnations is simply one of the few viable alternatives for calculating wave fields if the Mie parameter x_M exceeds a certain threshold. In order to include a shaped beam in the present model, the connection between the given field solution and the geometrical optics solver is made via the reduced spatial frequencies of the field. Another possible method for large x_M values is the so-called glare point model also applied here. This model represents a scattering particle by a set of so-called glare points and excels especially at treating large, highly irregular particles. While it is computationally less demanding than a geometrical optics model, it is nevertheless a drastically simplified representation of the real particle and provides only limited information about a concrete particle geometry and composition.

Small Mie parameter models

For lower values of x_M, exact solvers may be used. Three possible methods have been evaluated in this category. A mature numerical solver using a finite volume approach to calculate electromagnetic fields was provided by the institute for the theory of electromagnetic fields of the TU Darmstadt. This is a numerically exact solver for particles roughly smaller than

10 μm. It's two major disadvantages are the large computation time of about 5 hours for a 5 μm particle and the fact that it can only calculate one particle orientation at a time, which is a particular downside for non-spherical particles. A much faster alternative providing orientation-averaged scattered fields is the T-matrix code TSym. It was developed specifically for particles with a symmetric geometry. If such symmetries are not present and the particle is instead highly irregular, a DDA code can be applied and a simplified one-dimensional version has been implemented during this thesis as a proof-of-concept.

Experiments and Engineering

Primarily motivated by the validation of the geometrical optics code of the preceding chapter, the experimental section begins with the description of the experiment aimed at the measurement of phase functions of levitated ice crystals. The second part consists of an investigation of the time-shift technique when applied to irregular snow flakes. The third and last technique investigated in this thesis is Interferometric Particle Imaging (IPI). While the preceding two experiments work best for the characterisation of regular particles, IPI is applicable to any concievable particle, irrespective of its morphology. The penultimate chapter is dedicated to important engineering aspects connected to the experiments. First of all, the design iterations of devices for the provision of snow crystals will be explained. Second and last, it is demonstrated how the simulation codes may be applied to the interpretation of atmospheric probe measurement data.

2 Electromagnetic Radiation: Theory

Dixitque Deus: "“Fiat lux.”". Et facta est lux. Et vidit Deus lucem quod esset bona et divisit Deus lucem ac tenebras.

—Vulgata, Liber Genesis, 1, 3f. [Unk65]

THE evolution of light in spacetime and the scattering of light by a macroscopic particle are governed by Maxwell's equations, as is well known. This is nowadays the introductory statement of all current seminal reference books on optics, such as for instance Born & Wolf [BW99] or Hecht [Hec02]. Technically speaking, light is a wave-like excitation of the electromagnetic tensor field which is also responsible for electrostatic and magnetostatic phenomena. Under the two conditions that both ratio of the reduced Planck's constant and a typical problem length scale L tends to zero $\frac{\hbar}{L}$ and the metric of the spacetime under consideration is flat $g_{\mu\nu} \approx \eta_{\mu\nu}$, the scattering of light by any macroscopic particle is a problem that can at least in princple be solved exactly by assuming the model of the classical Maxwell equations to be an exact description of the natural phenomenon of light.
The current chapter will derive the basic equations used to model the propagation of light starting from differential geometric principles. After an explanation of Maxwell's equations, several novel concepts in the quantization of the electromagnetic field will be explained and their connection to classical geometrical optics will be made clear. Thus this chapter follows the path from the most abstract description of light to the most concrete specialised application cases.

2.1 Rigorous Geometrical Definition

2.1.1 Electromagnetism in terms of Exterior Differential Forms

In most cases, a rigorous definition of the electromagnetic field can only be found in introductory texts on gauge field theory such as the book [CBDMDB96]. In general, the electromagnetic field $\mathbf{F} = \frac{1}{2}F_{ij}dx^i \wedge dx^j$ is an (exterior) differential 2-form that according to the authors Choquet-Bruhat et al. [CBDMDB96], Deschamps [Des81] and Flanders [Fla89] must fulfill two distinct sets of equations written in Gaussian CGS units:

$$d\mathbf{F} = 0 \tag{2.1}$$

$$d \star \mathbf{F} = -\mathbf{J} \tag{2.2}$$

which are called homogeneous and inhomogeneous, respectively. Therein $\mathbf{J}$ is the charge-current 3-form, which is conserved automatically due to the properties of the exterior differentiation operator (2.4) leading to $d\mathbf{J} = 0$. Differential forms are a natural tool in differential geometry introduced by the French mathematician Élie Cartan [Car06] and several proponents exist for a shift in notation in electrodynamics away from Gibb's vector calculus to the much more compact notation in terms of forms. These proponents include Deschamps [Des81] and other authors [WSA97] claim pedagogical advantages of the forms approach. While the increased level of abstraction of forms over conventional vectors has advantages such as making all mathematical statements independent of a concrete coordinate system and making certain mathematical lemmas quite obvious to proove (see for instance [Des81]), it is this increase in abstraction that makes forms less readily applicable to an actual calculation problem, as through the abstraction concrete pyhsical meaning is lost. A detailled description of differential forms is not present in this section and will instead be left to the literature, such as the book by Flanders [Fla89]. In the following, only a few definitions essential for the understanding on the part of the reader are given. For a graphic introduction to forms, the reader is referred to the book of Arnol'd [Arn84].

Definition 1 *The (exterior) differential p-form is a covariant rank p tensor which is antisymmetric in the exchange of its indices. A 0-form f is a smooth function on a manifold. Following the theorem of Cartan [Car06] that on a finite dimensional Banach space, each differential p-form ω is uniquely defined as:*

$$\boxed{\omega = \sum_{i_1<\cdots<i_p}^{1\le i\le k} c_{i_1\ldots i_p}(x)\,dx_{i_1}\wedge\cdots\wedge dx_{i_p}} \tag{2.3}$$

where the coefficients $c_{i_1\ldots i_p}(x)$ are n times differentiable functions for a given point $x\in\mathbb{R}$. A differential form is not identical to an integral measure [CBDMDB96].

Definition 2 *The exterior derivative d is a linear operator on a differentiable manifold acting on a differential p-form ω from the left and produces a form $d\omega$ of degree (p+1). On a manifold parameterized by the values $\boldsymbol{x}=(x,y,z)\in\mathrm{R}$ with local coordinates $\left(\frac{\partial}{\partial x},\frac{\partial}{\partial y},\frac{\partial}{\partial z}\right)$, explicit expressions for the exterior derivative can be given:*

$$d\omega = \left(\frac{\partial}{\partial x}dx+\frac{\partial}{\partial y}dy+\frac{\partial}{\partial z}dz\right)\wedge\omega \tag{2.4}$$

If the operator (2.4) acts on a p-form, the partial derivatives act on the coefficients of the form and the differentials dx, dy, dz, which are orthonormal one-forms on $\mathbb{R}^3$ are multiplied with the differentials of the form through the wedge product $\wedge$. The explicit expressions for the exterior differentiation of the first four forms is given in the following:

- *0-form:* $df(\boldsymbol{x}) = \frac{\partial f}{\partial x}dx+\frac{\partial f}{\partial y}dy+\frac{\partial f}{\partial z}dz\equiv\nabla f$
- *1-form:* $dA(\boldsymbol{x}) = \left(\frac{\partial A_z}{\partial y}-\frac{\partial A_y}{\partial y}\right)dy\wedge dz+\left(\frac{\partial A_x}{\partial z}-\frac{\partial A_z}{\partial x}\right)dz\wedge dx+\left(\frac{\partial A_y}{\partial x}-\frac{\partial A_x}{\partial y}\right)dx\wedge dy$
- *2-form:* $dF(\boldsymbol{x}) = \left(\frac{\partial F_x}{\partial x}+\frac{\partial F_y}{\partial y}+\frac{\partial F_z}{\partial z}\right)dx\wedge dy\wedge dz$
- *3-form:* $dJ(\boldsymbol{x}) = 0$

The exterior derivative is a unique operator (proof see Flanders [Fla89]) with the following additional properties:

- *Linearity:* $d(\omega+\eta) = d\omega+d\eta$
- *Multiplicative Distributivity:* $d(\omega\wedge\eta) = d\omega\wedge\eta+(-1)^{deg\omega}\omega\wedge d\eta$
- *Poincaré lemma:* $d(d\omega) = 0$

Definition 3 *The Hodge star operator or dual $\star$ also acts on differential p-forms ω from the left creating an (n-p) form $\star\omega$ where n is the dimensionality of the base manifold. The explicit expression is:*

$$(\star\beta)_{i_{p+1}\ldots i_n} = \frac{1}{p!}\tau_{i_1\ldots i_n}\beta^{i_1\ldots i_p} \tag{2.5}$$

with the volume element n-form τ of the manifold X^n:

$$\tau = \sqrt{|g|}\cdot dx^1\wedge\cdots\wedge dx^n \tag{2.6}$$

where g is the determinant of the metric tensor. In the Euclidean space $\mathbb{R}^3$, one thus finds:

$$\begin{aligned}\star dx &= dy\wedge dz\\ \star dy &= dz\wedge dx\\ \star dz &= dx\wedge dy\end{aligned} \tag{2.7}$$

Definition 4 *The exterior (wedge) product $\wedge$ of an exterior differential p-form ω and a q-form κ is a (p+q)-form with:*

$$\omega\wedge\kappa = \frac{1}{p!q!}\cdot\sum_P(sign(P))\cdot P[\omega\cdot\kappa] \tag{2.8}$$

where P is a permutation of $(1,2,\ldots,p+q)$.

2.1.2 The Gauge Potential as a Connection on the U(1) Principal Fibre Bundle

Following the definitions of exterior differential forms and their operators, the remainder of the subsection will see fundamental properties of Electromagnetism derived from purely geometrical and symmetry considerations. On Minkowski space $M = \mathbb{R}^4$, the form of the homogeneous Maxwell equations 2.1 allows the existence of an electromagnetic potential 1-form $F = dA$ through the application of Poincaré's lemma, the so-called *gauge potential* [CBDMDB96]:

$$dF = d(dA) = d\left(A_\mu dx^\mu\right) = 0 \tag{2.9}$$

The representation of equation 2.9 in coordinates x_μ leads to the familiar expression 2.28 for the electromagnetic field tensor. Application of Poincaré's lemma also leads to the vanishing of the gradient of any scalar function χ, which means that the homogeneous equation is gauge invariant:

$$dA' = d(A + d\chi) = dA \tag{2.10}$$

The invariance of the action of the electromagnetic field under this gauge transformation has as a consequence the conservation of electric charge and current (see for instance reference [Sch12] for a derivation). This is an application of the famous Noether's theorem [Noe18], where a symmetry of a field equation leads to a conserved quantity. Looking at the wavefunction or matter field ψ describing the behaviour of a single electron with charge e coupled to an electromagnetic field A_μ, the local and global (i.e. $\chi = const.$) gauge invariance of the Maxwell equations leads to a local (global) phase shift of the electron [Sch12]:

$$\psi' = e^{i(\chi(x,t)+2\pi n)}\psi \tag{2.11}$$

This phase factor is an element of the Lie group U(1) as explained in detail in subsection 2.1.3. The equation governing the evolution of the matter field ψ in space and time is in this argument the Schrödinger equation [Foc26b]. In order for the Schrödinger equation to stay invariant under the phaseshift 2.11, all partial derivatives need to be replaced by a covariant derivative, as detailled by Chouquet et al. [CBDMDB96] or Scheck [Sch12], for instance:

$$D = d - i \cdot n \cdot e\, A \tag{2.12}$$

which is also called the *gauge covariant derivative* in mathematics and minimal coupling in a field theoretical context of physics and the direct coupling of the electromagnetic potential 1-form with the charges is experimentally verified through the famous Aharonov-Bohm effect [AB59]. It can also be shown [CBDMDB96], that the 2π- periodicity of the phase factor 2.11 leads to the quantization of the electromagnetic charge e, as the electromagnetic potential couples to $n \in \mathbb{N}_0$ particles with charge e. An engineering example for a gauge covariant derivative would be the total derivative $\frac{D}{Dt}$ of the Navier Stokes equations, which arises from the postulation of invariance of Newton's equations under transformations of the Galilean group and the group of rotations SO(3). From the perspective of differential geometry [CBDMDB96], the electromagnetic potential 2.9 appearing in the covariant derivative 2.12 is a connection defined on a principal U(1) fibre bundle P(M,G). The base manifold M of P is Minkowski space $\mathbb{R}^4$ with a fibre F identical to the structure group $G = \mathrm{U}(1)$ attached at each point x_μ, which makes the fibre bundle a principal bundle and the structure group a Lie group. Figuratively speaking, a circle such as the one shown in figure 2.1 representing the transformation 2.11 can be found at every point in space. Finally, the relation between the field strength 2-form and the potential 1-form $F = dA$ is identical to the definition of a curvature on a principle bundle as given in reference [CBDMDB96]. In summary, the electromagnetic field can be viewed from a geometrical perspective as a physical entity that distorts the space in which a charged particle moves in a similar way as gravitation does for a massive object according to the theory of Einstein [Ein16].

2.1.3 Circle Group U(1)

A subsection is dedicated to the description of the so called circle group. It is necessary to describe this abstract mathematical concept at this point, as it is essential for the proper understanding of the numerical integration routines in the upcoming sections as well as the geometrical definition of the Lorentz force associated with the electromagnetic field itself. Following the definition of Bröcker [Brö04] the so-called circle group categorised as U(1) is an algebraic structure whose set of elements are all complex numbers $z \in \mathbb{C}$ with unit absolute value $|z| = 1$ as shown in figure 2.1.

The group operation $\bullet$ connecting three elements of the group $z_3 = z_1 \bullet z_2$ is the complex multiplication:

$$z_3 = z_1 \cdot z_2 \tag{2.13}$$

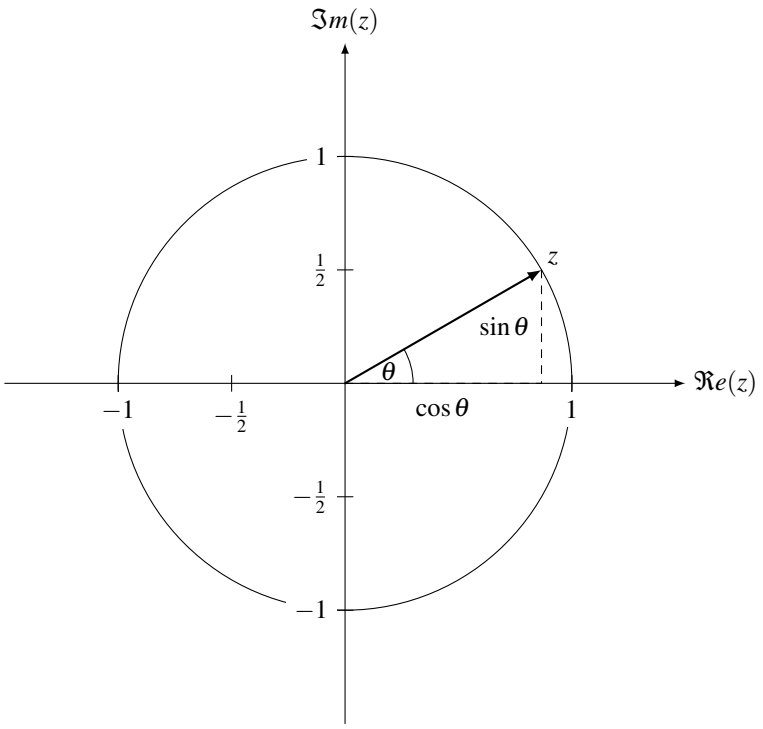

Figure 2.1: The unitary group $\mathrm{U}(1)$ in the complex plane.

which reduces to an addition of the corresponding real arguments $\theta \in [0, 2\pi) \to 1 \cdot e^{i\theta}$ in the polar representation of the complex numbers, where i is the imaginary unit number:

$$z_3 = e^{i\theta_3} = e^{i(\theta_1+\theta_2)} \tag{2.14}$$

The exponential representation is a 1×1 matrix which is itself isomorphic to the 2×2 matrices of two-dimensional rotations. Starting from the exponential it is trivial to show that the group operation is indeed unitary

$$UU^* = I \tag{2.15}$$

where U is the unitary group element, the asterisk * denotes the hermitian conjugate and I is the identity matrix, which is exactly 1 in the present case. Furthermore it is straightforward to show that the group is also abelian (commutative):

$$z_3 = z_1 \bullet z_2 = z_2 \bullet z_1 \tag{2.16}$$

As the real group parameter θ is continuous and the group operation $exp(i\theta)$ is differentiable to an arbitrary order, $\mathrm{U}(1)$ is a Lie group as defined in reference [Brö04]. Now, in order to justify the introduction of such an abstract entity, one needs to look further at the time evolution of a harmonic wave, which is of course the main topic of this thesis. It is well known, that the operator $\hat{U}$ for propagating a harmonic wave forward in time is given by the exponential:

$$\hat{U}(t) = exp(-i\omega\Delta t)\cdot \tag{2.17}$$

where ω is the frequency of the wave in Hertz and Δt is a time difference in seconds. An in-depth justification for choosing the $(-,+,+,+)$ metric can be found for instance in the classic text of Synge [Syn58]. At this point it is evident for the reader, that the operator $\hat{U}$ is just a 1×1 representation of $\mathrm{U}(1)$ with all the same properties and real group parameter Δt. Foremost among these is the unitarity of $\hat{U}$, which is trivial to confirm. This operator occurs in slightly different forms also in other contexts related to wave phenomena. The time evolution of a solution to the Schrödinger equation for instance according to Feynman [FLS65] or Le Bellac [LBCTL13] is given by:

$$\hat{U}(\Delta t) = exp\left(-\frac{i}{\hbar}\hat{H}\Delta t\right)\cdot \tag{2.18}$$

Or as a final example the operator of translations in a wave field, i.e. the change in phase of a coherent wave:

$$\hat{U}(t) = exp(i\,k\,\tau)\cdot \tag{2.19}$$

with the wavenumber k and the real number τ as a replacement of the time difference Δt as a parameter of the transformation. One can now see clearly that equation 2.11 also is a representation of an element of the group $\mathrm{U}(1)$. An exponential function like 2.17 or 2.11 arises as a solution of a first order ordinary differential equation of the following form:

$$\frac{d\hat{U}(t)}{dt} = -i \cdot \omega \, \hat{U}(t) \tag{2.20}$$

which in turn is associated with an infinitesimal displacement transformation dt along the parameter t, as explained by Hermann Weyl [Wey50] and obvious through a Taylor expansion of the operator 2.17 truncated at first order:

$$\hat{U}(t+dt) = (1 - \underbrace{i \cdot \omega}_{generator} \, dt)\hat{U} \tag{2.21}$$

According to the theorem of Stone [Neu32], the factor in the exponential besides the real parameter in equations such as 2.11, 2.17 or 2.18 needs to be a hermitian operator and is called an *infinitesimal generator*. In the case of the harmonic operator 2.17, the generator is simply the frequency ω, which is just a real number and thus a trivially hermitian 1×1 matrix and for the Schrödinger equation the generator of the time evolution is the Hamiltonian operator $\hat{H}$, which is of course hermitian in order to be measurable. A large number of other representations of transformations is also known to take a form such as 2.11 including spatial rotations of the SO(3) group [LBCTL13] and Lorentz boosts [Jac75]. Besides the connection to the gauge invariance explained in section 2.1, the further importance of the group $\mathrm{U}(1)$ for the content of this thesis stems from the fact that Maxwell's equations 2.33 can be brought into the form of equation 2.20, which is the basis of their numerical solution in the context of time-dependent methods such as FDTD and FIT explained in further detail in section 3.3. An important criterion to assess the physical credibility of numerical simulations is the violation of conservation laws. For the electromagnetic field, the energy density is given by equation 2.37 and the unitary time evolution 2.17 of an electromagnetic wave field conserves the magnitude of the electric and magnetic vectors therein, just as the time evolution operator 2.18 conserves the norm of the wavefunction and thus probability. This is not the case if 2.17 is replaced by a non-unitary discrete ODE solver like the commonly used leapfrog scheme. Thus the numerical calculation of electromagnetic fields using **FDTD or FIT schemes violates exact energy conservation**, which is a fact commonly not acknowledged in standard textbooks on these numerical methods, such as the one by Gedney [Ged11].

2.2 Classical Electrodynamics

A brief discussion of the regular approach to Maxwell's equations is given in this section. The equations listed here are the direct basis for all numerical simulations in the chapters to come. Consequently, this section is the most important one in terms of basic theory. It is well known that Maxwell's original formulation of his equations in the article on the dynamical theory of the electromagnetic field [Max65] was quite different from the formulation used today. A detailled account of the convoluted development leading to the present form of the equations may be found by the interested reader in the survey article [Bor67] written by Bork. Contrary to the increasing number of claims in recent popular pseudo-scientific literature [SM05], no parts of the original equations relevant to the description of existing physical phenomena have been intentionally or accidentally removed or mutilated. Instead, the original number of 20 equations has been compacted to 4 and the cumbersome quaternion notation has been exchanged with the descriptive vector calculus of Gibbs [GW29].

2.2.1 Lagrangian density of the Electromagnetic Field

As is customary in field theory, the electromagnetic field can also be derived from a variational principle in a way that is similar to Fermat's principle [Som64]. According to standard references such as Jackson [Jac75] or Peskin and Schroeder [PS05], the Lagrangian *density* $\mathscr{L}$ (not Lagrange function L), or Lagrangian for short, of the electromagnetic field on a manifold whose metric tensor is the Lorentz tensor $\eta_{\mu\nu}$is given by:

$$\mathscr{L} = \mathscr{L}_{\text{field}} + \mathscr{L}_{\text{int}} = -\frac{1}{16\pi} F_{\mu\nu} F^{\mu\nu} - \frac{1}{c} J_\mu A^\mu \tag{2.22}$$

where $\mathscr{L}_{\text{int}}$ is the Lagrangian of the interaction between field and current and $\mathscr{L}_{\text{field}}$ is the Lagrangian of the field alone. The interaction Lagrangian also contains the coupling expressed in the covariant derivative 2.12. The rank-2 tensor $F_{\mu\nu}$ is again the covariant antisymmetric electromagnetic field tensor 2.9 defined by taking the exterior derivative of the electromagnetic potential A_μ:

$$F_{\mu\nu} = \partial_\mu A_\nu - \partial_\nu A_\mu \tag{2.23}$$

The Greek indices such as μ and ν run from 1 to 4 and the Einstein summation convention holds. Similar to the discrete case prevalent in mechanical problems [Arn84], the continuous field distribution may also be derived from a variational principle. According to Jackson [Jac75] or Itzykson [IZ06] for instance, the variation δS of the action functional S calculated from the Lagrangian 2.22 needs to vanish for a physical field configuration, which amounts to finding a local extremum of 2.22 as explained for instance in the mathematical reference work [BSM00]:

$$\delta S = \delta \iiiint \mathscr{L} d^4x = 0 \tag{2.24}$$

The main advantage in using this Lagrangian approach is the ease of determining invariances such as Lorentz invariance. Given Noether's theorem [Noe18], it is again straightforward to find an expression of the conserved 4-current J^μ belonging to the corresponding symmetry based on the field Lagrangian, as taken here from Scheck [Sch12] and Itzykson et al. [IZ06].

$$J^\mu(x) = \frac{\partial \mathscr{L}}{\partial(\partial_\mu A_\mu)} \cdot \Gamma \cdot \theta \tag{2.25}$$

Where Γ is the generator of the corresponding representation of the one-parameter symmetry group and θ is the parameter, such as time, distance or rotation angle. Taking the total derivative of the Lagrangian 2.22 in the process of verifying relation 2.24 then leads to the so-called *Euler Lagrange equations* [Jac75]:

$$\partial^\nu \frac{\partial \mathscr{L}}{\partial(\partial^\nu A^\mu)} = \frac{\partial \mathscr{L}}{\partial A^\mu} \tag{2.26}$$

which leads to the familiar covariant expression for the inhomogeneous set of Maxwell's equations equivalent to a representation of of equation 2.2 in Minkowski coordinates:

$$\frac{1}{4\pi}\partial^\mu \partial^\nu F_{\mu\nu} = \frac{1}{c}\partial^\mu J_\mu \tag{2.27}$$

The homogeneous equation in turn follows from the definition of the field strength tensor 2.23. A detailled derivation is given for instance in the book [Jac75] by Jackson or [Syn58] by Synge.

$$\partial_\mu G^{\mu\nu} = \frac{1}{2}\partial_\mu \varepsilon^{\mu\nu\lambda\kappa} F_{\lambda\kappa} = 0 \tag{2.28}$$

Where $G^{\mu\nu}$ is the contravariant dual field strength tensor. Finally the contravariant electromagnetic field strength tensor $F^{\mu\nu}$ can be represented as a 4×4 matrix and each element can be related to the components of the measureable field vectors **E** and **B**, i.e. the electric field and magnetic induction.

$$F^{\mu\nu} = \begin{pmatrix} 0 & -E_x & -E_y & -E_z \\ E_x & 0 & -B_z & B_y \\ E_y & B_z & 0 & -B_x \\ E_z & -B_y & B_x & 0 \end{pmatrix} \tag{2.29}$$

And the covariant tensor is given by $F_{\mu\nu} = \eta_{\mu\gamma} F^{\gamma\delta} \eta_{\delta\nu}$.

2.2.2 Maxwell's equations

Given the tensor equations 2.27 and 2.28 as well as the breakdown 2.29 of the field strength tensor, one can formulate Maxwell's equations in microscopic form using Gibbs' vector calculus notation and bring them into the most commonly used form present in most of the basic literature on electromagnetism, such as Fließbach [Fli12b], Stratton [Str07] and Jackson [Jac75]:

$$\left.\begin{aligned} \nabla \cdot \mathbf{E} &= \underbrace{\frac{1}{\varepsilon_0} \cdot \rho_e}_{\text{electric source density}} && \text{Gauss' law} \\ \nabla \cdot \mathbf{B} &= \underbrace{\mu_0 \cdot \rho_m}_{\text{magnetic source density}} && \text{Gauss' law for magnetism} \\ -\nabla \times \mathbf{E} &= \underbrace{\frac{\partial \mathbf{B}}{\partial t}}_{\textit{induction}} + \mu_0 \cdot \mathbf{j}_m && \text{Faraday's law of induction} \\ \nabla \times \mathbf{B} &= \mu_0 \cdot \varepsilon_0 \cdot \frac{\partial \mathbf{E}}{\partial t} + \underbrace{\mu_0 \cdot \mathbf{j}_e}_{\text{electric current}} && \text{Ampère's Law} \end{aligned}\right\} \quad \text{Maxwell's equations} \tag{2.30}$$

where $\nabla\cdot$ is the symbol for the divergence of a vector field and $\nabla\times$ the symbol for its rotation and the equations have been written in rationalized MKSA units as defined for instance in the article [Nic51]. Further physical quantities in the set of equations 2.30 include the electric charge ρ_e, the electric current $\mathbf{j}_e$ and the disputed magnetic charge ρ_m and magnetic current $\mathbf{j}_m$. Physical constants entering the equations are the electric permittivity ε_0 and the magnetic susceptiblity μ_0 of the absolute vacuum defined by $\varepsilon_0 = \frac{1}{\mu_0 c^2}$ in reference [MTN08]. A detailled and rigorous account on how to connect the microscopic equations 2.30 to bulk media is given for instance by Gouesbet et al. [GG11], where any possible variation in material behaviour is considered. In this thesis, instead the usual phenomenological approach is adopted, based on the introduction of two new vectors **P** and **M** called electric and magnetic polarization. These two vectors take create the influence of bulk matter in the model. The effect of these two vectors is introduced into Maxwell's equations by creating two new effective fields:

$$\mathbf{D} = \varepsilon_0\mathbf{E} + \mathbf{P} \ : \text{dielectric displacement field} \tag{2.31}$$

$$\mathbf{H} = \frac{1}{\mu_0}\mathbf{B} + \mathbf{M} \ : \text{magnetic field} \tag{2.32}$$

which transforms Maxwell's equations into their macroscopic form in the presence of matter ([GG11]), again written in rationalized MKSA units:

$$\left.\begin{aligned} \nabla\cdot\mathbf{D} &= \rho_e \\ \nabla\cdot\mathbf{B} &= 0 \\ \nabla\times\mathbf{E} &= -\frac{\partial\mathbf{B}}{\partial t} \\ \nabla\times\mathbf{H} &= \underbrace{\frac{\partial\mathbf{D}}{\partial t}}_{\text{displacement current}} + \mathbf{j}_e \end{aligned}\right\} \quad \text{Maxwell's equations applicable to bulk media} \tag{2.33}$$

From these equations it is evident that the magnetic field **H** is not required to be solenoidal, i.e. it is possible that $\nabla\cdot\mathbf{H} \neq 0$ may occur. This makes it possible to simulate the behaviour of a magnetic monopole by proper arrangement of magnets, which has been done on various occasions in the past [LRP$^+$10].

It is well known that Maxwell's equations support wave-like solutions whose physical existence was first verified experimentally by Heinrich Hertz in his Ph.D. thesis [Her80]. These waves have henceforth provided the starting point for modern optics [Som64] [BW99] and where first promoted by Mie [Mie08] to a tool for solving light scattering problems only around 20 years after Hertz' discovery. Closure of equations 2.33 is achieved by prescribing a set of *constitutive equations*:

$$\begin{aligned} \mathbf{D} &= \varepsilon\mathbf{E} \\ \mathbf{H} &= \mu\mathbf{B} \end{aligned} \tag{2.34}$$

where ε is the electric permittivity tensor of the bulk medium and μ the magnetic susceptibility. As can be inferred from the shape of equations 2.34, permittivity and susceptiblity take the form of 3×3 matrices in actual calculations. For homogeneous isotropic media, these are diagonal matrices with only one constant scalar real or complex value along the diagonal. If the medium is inhomogeneous, this value depends on the position in space. Furthermore, if the medium is anisotropic, the entries along the diagonal are unequal. If there are two different possible values ε_o and ε_e, the medium is said to be *uniaxially* anisotropic [Som64] [BW99]. The tensor ε then may take the following form:

$$\varepsilon_{ij} = \begin{pmatrix} \varepsilon_o & 0 & 0 \\ 0 & \varepsilon_e & 0 \\ 0 & 0 & \varepsilon_e \end{pmatrix} \tag{2.35}$$

In optical scattering problems, the scatterer medium is often assumed to be homogeneous and isotropic and the susceptibility is assumed to be that of vacuum to a good approximation. Exceptions to this rule have only appeared in the recent decades. The treatment of inhomogeneous particles will also be covered in a seperate section in this thesis. Derived from the Maxwell equations is Poynting's theorem, which is given here in it's simple differential form, although authors such as Mishchenko [Mis10] recently started to argue that only its integral formulation can have physical validity.

$$\frac{\partial u}{\partial t} + \nabla\cdot\mathbf{S} = -\mathbf{j}_e\cdot\mathbf{E} \tag{2.36}$$

where energy density u of the electromagnetic field in the presence of matter is defined by Jackson [Jac75] as:

$$u = \frac{1}{8\pi}(\mathbf{E}\cdot\mathbf{D} + \mathbf{B}\cdot\mathbf{H}) \tag{2.37}$$

which is the sum of the energy densities for electric and magnetic field alone, and the *Poynting vector* **S** is given by:

$$\mathbf{S} = \frac{c}{4\pi}\mathbf{E}\times\mathbf{H} \tag{2.38}$$

Equation 2.36 is a typical continuity equation, illustrating the conservation of the energy density u of the field.

The quantization of the electromagnetic field is discussed here both for the sake of a complete description *and* as a preparation for subsections 2.3.1 and 2.4 concerning non-classical states of light and the so-called *reverse quantization* of geometrical optics, as well as to show connections of the descriptions of quantized fields to the experimental technique of Interferometric Particle Imaging (IPI) described in section 4.3. Starting from the classical microscopic Maxwell's equations, the electromagnetic field may be quantized in two distinct ways in order to arrive at a true quantum field theory (QFT). While the first is the rigorous canonical quantization explained by Dirac [Dir88], the second and more intuitive approach is the so-called path integral quantization developed by Feynman [Fey42] [FH65]. The following explanation will concentrate on the canonical quantization procedure, as it is the approach relevant to this thesis. The description is based on the derivations made in Dirac [Dir88] and Landau Lifshitz [LL80].
Given a field defined by a Lagrangian such as 2.22, the canonical quantization of the field follows the same scheme as in the case of regular quantum mechanics. The sole difference is that the field is continuous and thus there is no position operator $\hat{\mathbf{x}}$ of a particle to use. Naturally, the field potential $A_\mu(\mathbf{x})$ is now promoted to an operator.

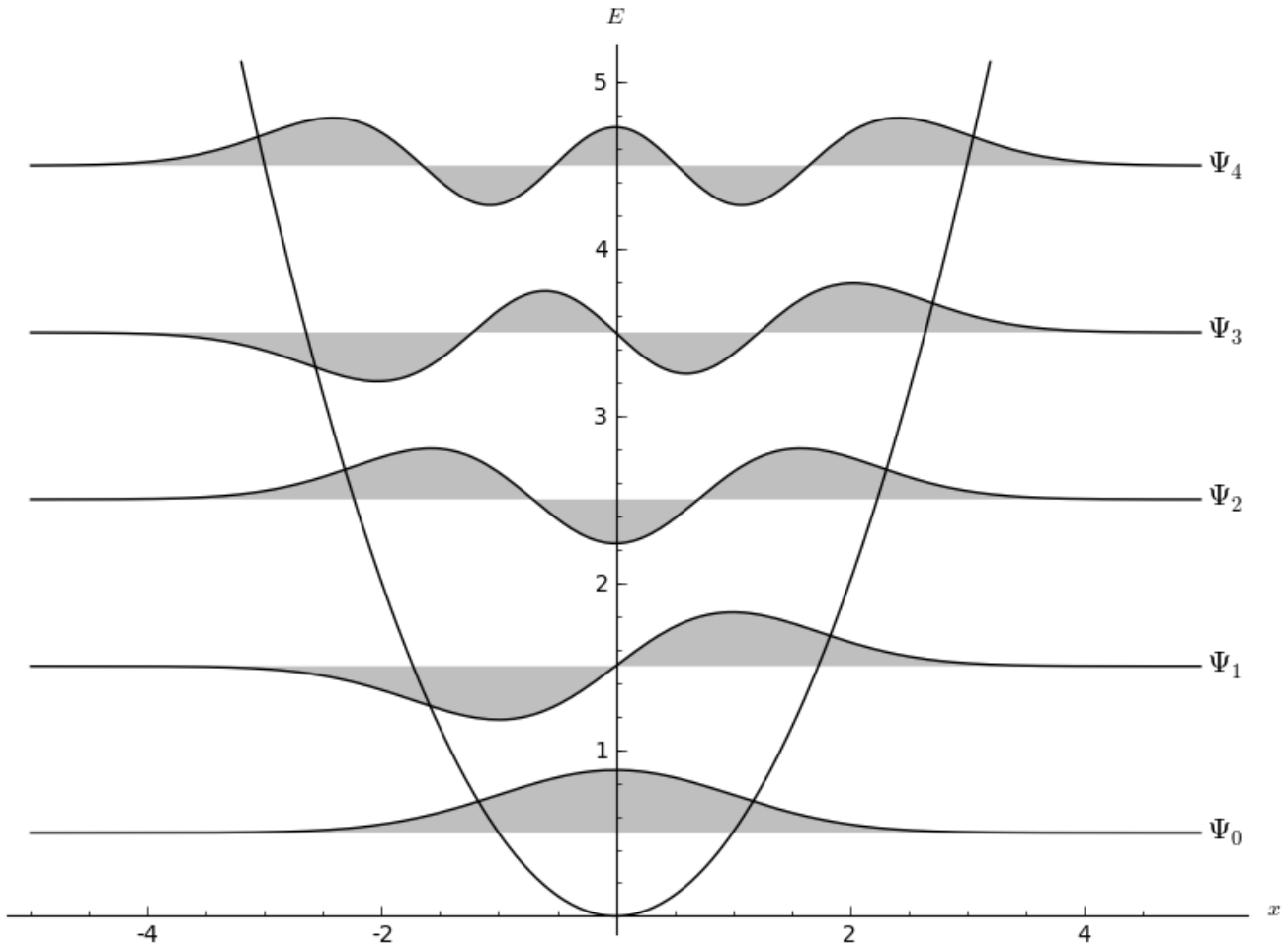

Figure 2.2: First five eigenfunctions $\Psi_0 \dots \Psi_4$ of the quantum harmonic oscillator Hamiltonian. The ground state Ψ_0 has a non-zero eigenvalue E_0 and is thus itself different from zero everywhere.

Given a fixed volume L^3 free of charges and currents and using the Coulomb gauge, the electromagnetic vector potential $\mathbf{A} = A_{1\dots3}$ may be expanded in terms of plane waves according to [LL80] and [FH65]:

$$\mathbf{A} = \sum_{\mathbf{k}} \left(\mathbf{a}_\mathbf{k} e^{i\mathbf{kr}} + \mathbf{a}_\mathbf{k}^* e^{-i\mathbf{kr}} \right), \quad \omega = |\mathbf{k}| = \omega \tag{2.39}$$

where the amplitude coefficients $\mathbf{a}_\mathbf{k}$ and $\mathbf{a}_\mathbf{k}^*$ are orthogonal to the wave vectors $\mathbf{k}$ and have a harmonic time dependence $e^{-i\omega t}$. Analogous to the situation in classical mechanics [Arn84], the field equations can then be brought in a Hamiltonian form by defining canonical field variables:

$$\mathbf{q}_\mathbf{k} = \frac{1}{\sqrt{4\pi}}(\mathbf{a}_\mathbf{k} + \mathbf{a}_\mathbf{k}^*) \tag{2.40}$$

$$\mathbf{p}_\mathbf{k} = \frac{-i\omega}{\sqrt{4\pi}}(\mathbf{a}_\mathbf{k} + \mathbf{a}_\mathbf{k}^*) = \dot{\mathbf{q}}_\mathbf{k} \tag{2.41}$$

whose commutation relation is:

$$[\mathbf{p}_\mathbf{k}, \mathbf{q}_\mathbf{k}] = -i \tag{2.42}$$

where $[\cdot,\cdot]$ is the commutator bracket as defined in [LL90]. These operators can now be used to define a Hamilton operator of the electromagnetic field:

$$H = \frac{1}{2}\sum_\mathbf{k} \left(\mathbf{q}_\mathbf{k}^2 + \omega^2 \mathbf{p}_\mathbf{k}^2\right) \tag{2.43}$$

which is identical in form to a simple one-dimensional quantum harmonic oscillator Hamilton operator of frequency ω as described in [LL90] and [LBCTL13]. Accordingly, the eigenvalues and energy levels of the Hamilton operator 2.43 are already known and the corresponding eigenfunctions are depicted in figure 2.2. Explicitly, the energy levels E are given by:

$$E = \sum_\mathbf{k} \left(N_\mathbf{k} + \frac{1}{2}\right)\omega \tag{2.44}$$

where $N_\mathbf{k} \in \mathrm{N}_0$ and $E = \frac{1}{2}\cdot\omega$ is the vacuum energy for $N_\mathbf{k} = 0$. One can then further define the so-called *ladder operators* from the canonical operators as:

$$c_\mathbf{k} = \frac{1}{\sqrt{2\omega}}(\omega q_\mathbf{k} + i p_\mathbf{k}) \tag{2.45}$$

$$c_\mathbf{k}^* = \frac{1}{\sqrt{2\omega}}(\omega q_\mathbf{k} - i p_\mathbf{k}) \tag{2.46}$$

with the commutation relation $[c_\mathbf{k}, c_\mathbf{k}^*] = 1$. The Hamiltonian operator in this case takes the form:

$$H = \omega\left(c_\mathbf{k}^* c_\mathbf{k} + \frac{1}{2}\right) \tag{2.47}$$

The corresponding operators 2.46 and 2.45 are called raising and lowering operator, respectively, together forming the number operator $\hat{n} = c_\mathbf{k}^* c_\mathbf{k}$, and provide the bridge to the content of the following section 2.3.1.

2.3.1 Non-Classical States of Light

The following subsection is concerned with several classes of non-classical states of the electromagnetic field constructable via its quantization. These states are listed here both in order to ensure both a complete representation of the modern understanding of light as well as to prepare the reader for the connection of these states to the Interferometric Particle Imaging (IPI) Technique described in the section on the experiments of this thesis. The description of the states largely follows the book [WFM08], which is standard reference in the field of quantum optics. Original publications, such as for instance from Glauber, will be cited where it is appropriate. The non-classical states of light will be visualized using the so-called Wigner pseudo probability distribution $W(\mathbf{x},\mathbf{p})$, or Wigner function for short, which was first defined by Eugene Wigner [Wig32] in an article from 1932. For a pure state with a density operator given by $\hat{\rho} = |\psi\rangle\langle\psi|$, where ψ is the wave function, the Wigner function is reduced to the following form [WFM08]:

$$W(x,p) = \int_{-\infty}^{\infty} \frac{e^{-\frac{i}{\hbar}p\zeta}}{2\pi\hbar}\psi\left(x+\frac{\zeta}{2}\right)\psi^*\left(x-\frac{\zeta}{2}\right)d\zeta \tag{2.48}$$

where $\hbar$ is the reduced Planck constant, ψ^* is the complex conjugate wave function and x and p are algebraic postion and momentum respectively in phase space. The square of the Wigner function 2.48 gives the probability of a quantum mechanical system having a specific position x and momentum p in phase space. In contrast, in classical situations, x and p would be completely defined. Thus classical particles would form infinitely thin line trajectories instead of a surface distribution. A classical harmonic oscillator would form a circle, for instance. A plane wave would form a line perpendicular to the momentum axis and a spherical wave the complementary wave perpendicular to the position axis. The most important non-classical states of light known as of 2015 are listed in the following.

- **Fock State:**
  A so-called Fock state or also number state is a quantum harmonic oscillator state as described in the preceding section. The definition of a quantum harmonic oscillator is given in all textbooks on quantum mechanics [LL90], while the connection to Electromagnetism is emphasized in books on QFT [LL80] and quantum optics [WFM08]. An arbitrary number state has as a basis $|n\rangle$ the eigenstates of the number operator $\hat{n}$ of the quantum harmonic oscillator. The electromagnetic vacuum, i.e. darkness, is the lowest eigenstate $|0\rangle$ defined by:

  $$c_{\mathbf{k}}|0\rangle = |0\rangle \tag{2.49}$$

  That is, there is no lower possible mode of the oscillator as $|0\rangle$. Applying the raising or lowering operator to a number state consequently leads the state into a higher or lower mode, which is mathematically expressed as:

  $$c_{\mathbf{k}}|n\rangle = \sqrt{n}\,|n-1\rangle \tag{2.50}$$

  $$c^*_{\mathbf{k}}|n\rangle = \sqrt{n+1}\,|n+1\rangle \tag{2.51}$$

  Going to a higher mode of the field is said to increase the number of photons present in the quantization volume L^3 in a QFT context. Figures 2.3 show states with exactly one, two, three and four states present respectively. The Wigner function $W_n(x,p)$ of a Fock state then is in terms of position x and momentum p:

  $$W_n(x,p) = \frac{(-1)^n}{\pi\hbar} e^{-2\frac{H}{\hbar\omega}} L_n\left(4\frac{H}{\hbar\omega}\right) \tag{2.52}$$

  where H is the Hamilton operator and L_n is the Laguerre polynomial of degree n as tabulated for instance in Abramowitz & Stegun [AS64]. A sample gallery of Wigner functions for the lowest 4 number states $|1\rangle$, $|2\rangle$, $|3\rangle$ and $|4\rangle$ is shown in figure 2.3.

- **Vacuum:**
  The actual electrodynamic vacuum is the lowest Fock state with a photon number of exactly zero as defined by equation 2.49. Thus there are no particles/photons present. It is important to note that despite no photons being present, the Wigner function of this state is not zero everywhere, as it would be the case for a classical oscillator, but a Gaussian function centered at the origin instead. Its illustration is shown in figure 2.4.

- **Coherent state:**
  A so-called coherent state is the quantum-optical representation of a classical state. In phase space it is represented as a vacuum state with a mean shifted away from the origin, such that the expectation value of position and momentum are non-zero. The coherent state was contrived in the article [Sch26] by Schrödinger as early as 1926 as a non-diffusing wavefunction representative of a classical particle in quantum mechanics. In fact, Schrödinger explicitly equates the coherent state with a classical point mass. Later Glauber [Gla63] applied the concept to the electromagnetic radiation field and further developed its theoretical basis. While Schrödinger gave an explicit expression for the wavefunction, Glauber defined the coherent state via a unitary displacement operator $\hat{D}(\alpha)$ depending on a complex number α and acting on the vacuum state $|0\rangle$:

  $$|\alpha\rangle = \hat{D}(\alpha)\,|0\rangle \tag{2.53}$$

  The representation of a coherent state while using number states $|n\rangle$ as a set of basis vectors is given by:

  $$|\alpha\rangle = e^{-\frac{|\alpha|^2}{2}} \sum_{n=0}^{\infty} \frac{\alpha^n}{\sqrt{n!}}\,|n\rangle \tag{2.54}$$

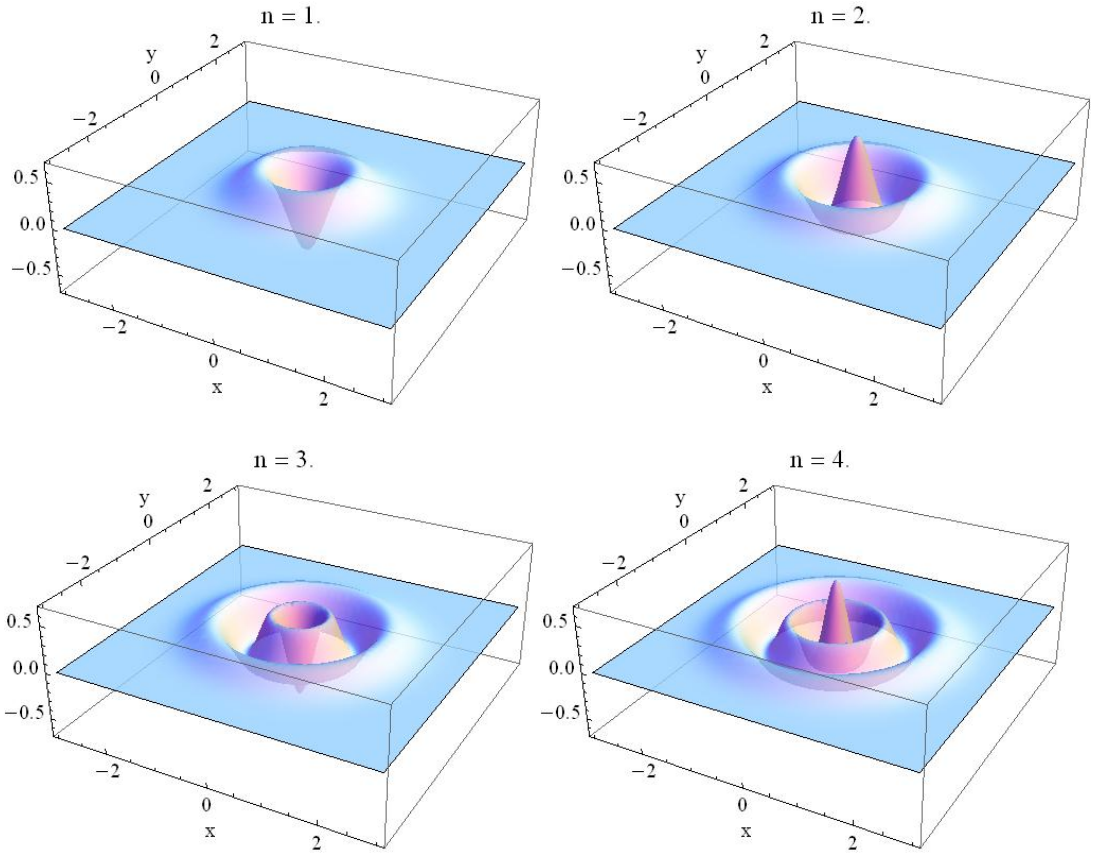

Figure 2.3: The Wigner functions for the first four Fock states

An the corresponding Wigner function for position x and momentum p can be written as:

$$W_{coherent}(x,p) = \frac{2}{\pi} e^{-\frac{1}{2}\left(x^2+p^2\right)} \tag{2.55}$$

which is depicted in figure 2.5 and takes the form of a Gaussian function with a mean shifted away from the origin, i.e. a vacuum state $|0\rangle$ shifted by the complex parameter α, as expected.

- **Cat state:** A cat state is the superposition of two coherent states with equal distance from the origin. The name is a reference to Erwin Schrödingers famous *Gedankenexperiment* [Sch35], where a (macroscopic) cat is both in the complementary states $|\text{alive}\rangle$ and $|\text{dead}\rangle$ before opening its box, as the electromagnetic field in a cat state is in a superposition of two different coherent states symmetrical around the origin. In the cat example, the state is evidently given by the normalized superposition:

$$|\text{cat}\rangle = \frac{|\text{alive}\rangle + |\text{dead}\rangle}{\| \, |\text{alive}\rangle + |\text{dead}\rangle \, \|} \tag{2.56}$$

With $\|\cdot\|$ being a suitable norm for the states. Making reference to the previous definition of a coherent state in terms of a complex displacement parameter α, a cat state $|\Psi\rangle$ is then defined as:

$$|\Psi\rangle = |\alpha\rangle + |-\alpha\rangle \tag{2.57}$$

The cat state is the most relevant one for this thesis due to the connection of its mathematical formalism to the Fourier optics used in the IPI measurement principle. The Wigner function of the cat state has been evaluated numerically, which is possible using the Mathematica suite [WR10] as well as the open source python module QuTiP [JNN13] and the result is shown in figure 2.6. The Wigner function shown in figure 2.6 not only displays the Gaussian peaks of the two (in this case squeezed) coherent states, but also an interference ridge in the middle between the two coherent states. The Wigner function in this area may take negative real values, indicating interference and thus non-classicality in the usual explanation [WFM08]. The Mathematica code for producing figure 2.6 is given in the listing below.

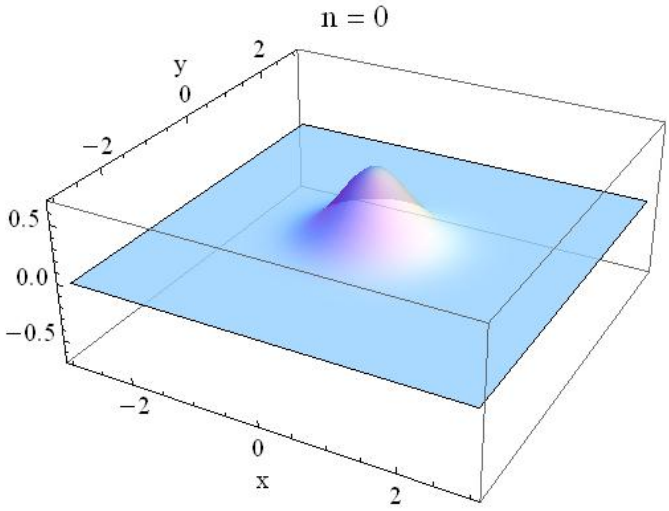

Figure 2.4: The Wigner function of the electromagnetic vacuum state. The figure shows a Gaussian function centered at the origin (0,0).

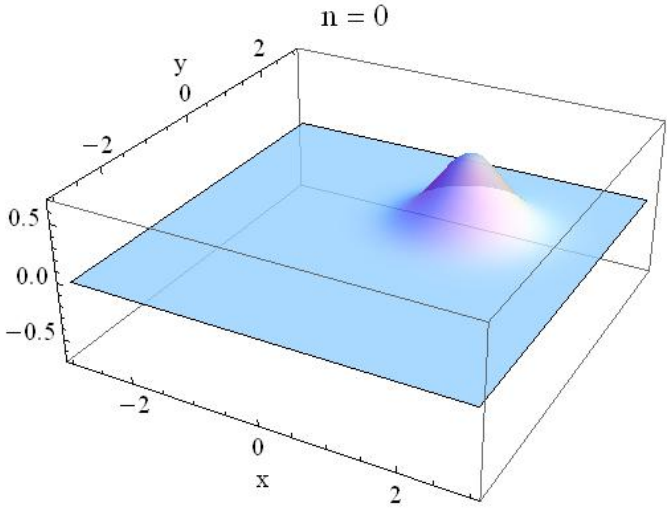

Figure 2.5: The Wigner function of a coherent (i.e. classical) state. Note the correspondance with figure 2.4.

```
1
2 (* slit-screen wave function modeled as a superposition of two Gaussian functions *)
3 Psi[x_] := Exp[-4 (x - 3)^2] + Exp[-4 (x + 3)^2]
4
5 (* Wigner function as Fourier transform of the coordinate wave function *)
6 Wig[x_, p_] := 2/(3 \[Pi]) Integrate[Psi[x + s/2] Exp[-I s p] Psi[x - s/2], {s, -Infinity,
      Infinity}]
7
8 Plot3D[Wig[x, p], {x, -4, 4}, {p, -6, 6}, PlotRange -> All]
```

While a cat state is often shown as a paradigm example of non-classical effects, it will be used in section 4.3 as an interpretation of the entirely classical Young's double slit experiment.

2.4 Reverse Quantization and Geometrical Optics

The connection between Maxwell's equations (2.33) and Geometrical Optics (GO) is given in section 3.1. Nevertheless it is also possible take the reverse step (thus the name), starting from GO and arriving at Maxwell's equations. Surprisingly enough, this is possible by applying the canonical quantization procedure as used for instance in section 3.1. This fact

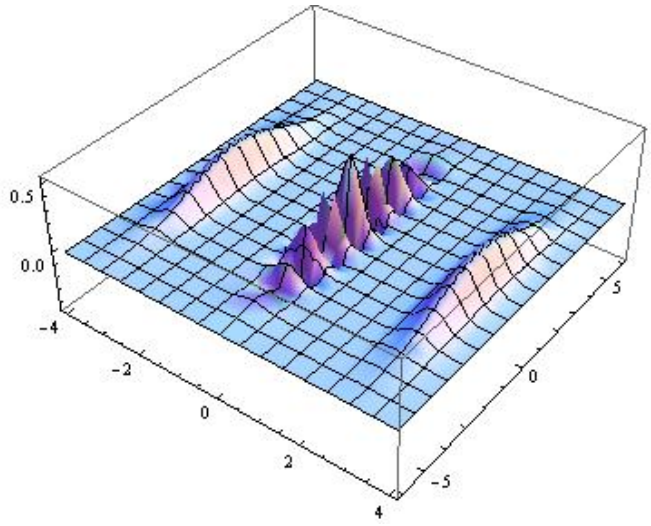

Figure 2.6: The Wigner function of a Schrödingers cat state consisting of two symmetrical coherent states and an interference ridge in between.

was first published by Gloge and Marcuse [GM69] in 1969 but has recieved little attention since then and the current section will give a short review of his findings in order to illuminate the connection between the qualitatively different descriptions of light at different scales. Similar to the variational formulation in equation (2.22) for the full Maxwell equations, a Lagrange function may also be defined for the intuitive concept of light rays in Geometrical Optics [BW99].

$$L = n(x,y,z)\sqrt{1+\left(\frac{\partial x}{\partial z}\right)^2+\left(\frac{\partial y}{\partial z}\right)^2} \tag{2.58}$$

where n is the inhomogeneous refractive index in the space with the coordinates (x,y,z). The variational principle (2.59) that leads to Geometrical Optics is the famous principle of Fermat [Hec02, BW99], minimizing the optical path length (2.58) between two points P_1 and P_2:

$$\delta S = \delta \int_{P_1}^{P_2} n(x,y,z)\sqrt{1+\left(\frac{\partial x}{\partial z}\right)^2+\left(\frac{\partial y}{\partial z}\right)^2}\,dz = 0 \tag{2.59}$$

The canonical momenta then are given by [GM69]:

$$p_x = \frac{\partial L}{\partial\left(\frac{\partial x}{\partial z}\right)} \tag{2.60}$$

$$p_y = \frac{\partial L}{\partial\left(\frac{\partial y}{\partial z}\right)} \tag{2.61}$$

which are called the optical momenta in this case and the corresponding Hamilton function as the Legendre transform of (2.58) can be derived as:

$$H = -\sqrt{n^2 - p_x^2 - p_y^2} \tag{2.62}$$

Following the argument of Gloge et al. [GM69], the canonical quantization again involves the promotion of the formerly algebraic momentum $\mathbf{p}$ and the Hamilton function H to the following operators acting on some wavefunction ψ from the left:

$$\hat{\mathbf{p}} = -i\frac{\lambda}{2\pi}\nabla \tag{2.63}$$

$$\hat{H} = i\frac{\lambda}{2\pi}\frac{\partial}{\partial z} \tag{2.64}$$

where i is the imaginary unit number, λ is some constant equivalent to Planck's reduced constant $\hbar$ in quantum mechanics and instead of the usual time dependance t, the operators depend on the spatial coordinate z. Taking the square of equation (2.62) and introducing the operators in the resulting equation leads to the final expression:

$$\Delta\psi + \underbrace{\left(\frac{2\pi n}{\lambda}\right)^2}_{k^2}\psi = 0 \tag{2.65}$$

Equation (2.65) is the Helmholtz equation for a wavenumber $k = \frac{2\pi n}{\lambda}$ describing a monochromatic wavefield ψ without polarization effects or one linear polarization component of a transversal wave field as illustrated in figure 3.3. As such, the equation presents the final step in the quantization of Geometrical Optics and the end of this chapter. While the quantization of wave optics leads to QFT and quantum optics, it is also possible to quantize Geometrical Optics and arrive at Wave Optics. Consequently there is a hierarchy of models with an increasing level of fidelity towards the full description of the electromagnetic field which can be traversed using quantization.

3 Simulation

> If we suppose that we know all the physical laws perfectly, of course we don't have to pay any attention to computers. It's interesting anyway to entertain oneself with the idea that we've got something to learn about physical laws; and if I take a relaxed view here [...] I'll admit that we don't understand everything.
>
> —R. P. Feynman in *Simulating Physics with Computers* [Fey82]

WHILE Maxwell's equations are in theory considerably easier to solve as for instance the Navier-Stokes equations [SA08, Pop00] due to their linearity, the practitioner in search for a solution of a scattering problem will be facing numerous difficulties. The main origins of these difficulties lie firstly in the enormous disparity of scales between the rapidly oscillating electromagnetic field and the objects scattering it, which is captured in the so-called Mie size parameter x_M. And secondly in the complex mathematics necessary in dealing with complex tensor quantities representing the electromagnetic field.

Given the comprehensive results of van de Hulst [Hul01] as well as Damaschke [Dam03] as well as Tropea et al. [ABDT03] which are in their generality not limited to spherical particles, the classical scattering of electromagnetic radiation may depend on the aforementioned Mie Size parameter as well as the refractive index η of the scatterer relative to the surrounding medium. This leads Van de Hulst to a two-dimensional classification diagram for the applicability of different methods for the prediction of scattered electromagnetic fields. As the refractive index of particles investigated in this thesis always has a value of around 1.3 to 1.35, the investigation of Tropea et al. in [ABDT03] is of larger significance to this thesis. Here, the intensity of a plane wave scattered by a spherical droplet over a droplet size parameter range has been investigated at one specific polar angle θ using exact Mie theory. The relation between scattered intensity and size shows three distinct regions. The first region attributed to Rayleigh scattering shows an exponential growth of the scattered intensity and is has no practical relevance for the particles considered in this thesis. The second region is the so-called *Interference region* and here the intensity displays large oscillations around an exponential mean with an exponent lower than in the Rayleigh region. This region is followed by the third and last so-called *optical region* where the oscillations of the intensity increase in frequency while simultaneously decreasing in relative amplitude, approaching again exponential growth in the limit of very large size parameters. At the time of the publication of van de Hulst's book [Hul01], the second region was seen as the most problematic, as it was only accessible via the mathematically complex Mie solution while large particles could be investigated using Geometrical Optics. With the advent of computers that were both powerful and easy to use, the situation began to reverse at the end of the last century. Both semi-analytical and fully numerical calculation methods applicable to the interference region can readily be implemented by undergraduate students and are otherwise available as opensource code or commercial software. In turn, it has become desirable to investigate the optical region using exact methods. Unfortunately the accumulation of numerical errors in semi-analytic methods and the enormous computational resources necessary for exact methods limit the application range of exact methods to below a certain threshold, beyond which they become non-credible or infeasible respectively.

Thus, given the current state of technology, the simulation of the light scattering by non-spherical particles needs to be discussed in two separate categories. According to Damaschke [Dam03] as well as Tropea et al. [ABDT03], a separation may be made at a size parameter of roughly $x_M \approx 100$. At an optical wavelength of $\lambda = 632.8$ typical for a HeNe laser, this leads to a particle radius of 10 μm. Below this physical Rubicon exact methods can and must be used, while crossing it necessitates the usage of approximate methods. In both categories, two methods will be discussed respectively that have been found to be readily applicable to the problems addressed in this thesis. This includes a Geometrical Optics derivative method and the Glare Point (GP) model developed by Brunel [BRJB15, BSC$^+$14] in the category of the approximate methods and the Finite Integration Technique (FIT) and the Transition Matrix (T-matrix) method as examples for exact methods. A special focus in this thesis has been placed on the treatment of shaped incident beams. Experimental devices such as the PHIPS device [ASA$^+$11] often employ lasers as sources of illumination, which are both coherent and have a Gaussian beam profile distinct from a plane wave. For spherical particles the beam shape influence has been discussed in-depth by Gouesbet and Gréhan [GG11] in the context of the Generalized Lorenz Mie Theory (GLMT). Nevertheless,

for non-spherical particles the influence of a shaped beam has up to now not recieved extensive attention, likely due to the fact that the plane wave case is already a difficult problem in its own right.

3.1 Geometrical Optics

Starting from Maxwell's equations as the rigorous description of classical light scattering processes, the geometrical optics model for the scattering of a Gaussian beam by a convex polyhedral object like an ice crystal is derived and all assumptions made in the process are explicitly mentioned.

3.1.1 Derivation from Maxwell's equations

Several possible avenues exist in order to derive the governing equations of geometrical optics from Maxwell's equations. All formulations have in common a specific *Ansatz*, in which the electromagnetic field tensor $\mathbf{F}^{\mu\nu}$ is expanded in terms of a certain smallness-parameter μ (as in Ref. [KO90]) and inverse powers of the wavenumber k (detailed in references [BW99], [Des72] and [KO90]) or correspondingly the wavelength $\lambda = \frac{2\pi}{k}$ (see ref. [LL75]). As can be seen from the example of the wavenumber and the wavelength, all these approaches share a certain equivalence. As such, the starting point for the present work is the detailed derivation given in the book of Kravtsov et. al. [KO90]. Given the Minkowski-metric $ds^2 = dx^2 + dy^2 + dz^2 - c^2dt^2$, Maxwell's equations in a region of vanishing 4-current are according to Synge [Syn58]:

$$G^{\mu\nu}_{,\ \nu} = 0 \tag{3.1a}$$
$$F^{*}_{\mu\nu,\ \nu} = 0 \tag{3.1b}$$

$$F^{*}_{\mu\nu} = \frac{1}{2} i \varepsilon_{\mu\nu\alpha\beta} F_{\alpha\beta} \tag{3.2}$$

Where a comma $,\nu$ indicates partial derivative with respect to the tensor component ν and Greek indices run from 1 to 4 with 4 being the imaginary time component. $\varepsilon_{\mu\nu\alpha\beta}$ is the Levi-Civita pseudo-tensor in spacetime and the relationship to the electric and magnetic field 3-vectors is given by:

$$E_r = i \cdot F_{r4} \tag{3.3a}$$
$$H_r = G^{*}_{r4} \tag{3.3b}$$

as well as the electric displacement $D_r = -i \cdot G_{r4}$ and the magnetic induction $B_r = -iF^{*}_{r4}$. The constitutive equations for a stationary non-magnetic material connect the 3-vectors and close the system of equations:

$$D_r = \varepsilon_{rs} \cdot E_s \tag{3.4a}$$
$$H_r = \mu_0 \cdot B_r \tag{3.4b}$$

where ε_{rs} is the dielectric permittivity tensor of the medium and μ_0 is the magnetic permittivity of the vacuum. If the time-dependance is $exp(-i\omega t)$, Maxwell's equations ((3.1)) reduce to (as is detailled in [KO90]):

$$\varepsilon_{ijk}\ G^{*}_{ik,j} + k_4\ G_{k4} = 0 \tag{3.5a}$$
$$\varepsilon_{ijk}\ (i\ F_{ik,j}) - k_4\ F^{*}_{k4} = 0 \tag{3.5b}$$

or equivalently:

$$\nabla \times \mathbf{H} + ik_4 \mathbf{D} = 0 \tag{3.6a}$$
$$\nabla \times \mathbf{E} - ik_4 \mathbf{B} = 0 \tag{3.6b}$$

where $k_4 = \omega/c$ and the tensor notation has been interchanged with the equivalent symbols in vector calculus for convenience. Subsequently, the electric permittivity is assumed to be a scalar field, thus excluding anisotropy. This set can be solved together with the constitutive equations using an ansatz proposed by Debye [KO90], which is essentially an expansion of the field vectors in terms of inverse powers of the wavenumber k_4:

$$\mathbf{X} = \sum_{m=0}^{\infty} \frac{\mathbf{X}_m}{(ik_4)^m} e^{ik_4 \psi} \tag{3.7}$$

where $\mathbf{X}$ may stand for $\mathbf{E}$ or $\mathbf{H}$. Inserting the expansion (3.7) into Maxwell's equations (3.1) and equating terms with equal powers of k_4 yields a system of equations. Truncating this system at k_4^0 yields:

$$\mathbf{p} \times \mathbf{H}_0 + \varepsilon \mathbf{E}_0 = 0 \tag{3.8a}$$

$$\mathbf{p} \times \mathbf{E}_0 - \mathbf{H}_0 = 0 \tag{3.8b}$$

which is complemented by the set of equations stemming from the truncation at k_4^1:

$$\mathbf{p} \times \mathbf{H}_1 + \varepsilon \mathbf{E}_1 = -\nabla \times \mathbf{H}_0 \tag{3.9a}$$

$$\mathbf{p} \times \mathbf{E}_1 + \varepsilon \mathbf{H}_1 = -\nabla \times \mathbf{E}_0 \tag{3.9b}$$

with the 3-momentum $\mathbf{p} = \nabla\psi$ being equal to the wave 3-vector $\mathbf{k}$. After a number of manipulations that are given in detail by Kravtsov [KO90] or to a simplified degree by Born and Wolf [BW99], shall not be repeated here. The zeroth order set of equations can only have a non-trivial solution if the phase of solution (3.7) satisfies the well-known *eikonal*-equation (or the permittivity ε is zero):

$$(\nabla\psi)^2 = \varepsilon \tag{3.10}$$

where the greek word *eikonal* can be translated as *image*. On the same grounds the set of first-order equations can be cast into the following two equations:

$$\hat{\mathbf{k}}\left(2\sqrt{\varepsilon}\nabla\Psi_n + \Psi_n\nabla\sqrt{\varepsilon}\right) + \Psi_n\sqrt{\varepsilon}\nabla\cdot\hat{\mathbf{k}} + 2\sqrt{\varepsilon}\kappa\Psi_b = 0 \tag{3.11}$$

$$\hat{\mathbf{k}}\left(2\sqrt{\varepsilon}\nabla\Psi_b + \Psi_b\nabla\sqrt{\varepsilon}\right) + \Psi_b\sqrt{\varepsilon}\nabla\cdot\hat{\mathbf{k}} - 2\sqrt{\varepsilon}\kappa\Psi_n = 0 \tag{3.12}$$

which are two coupled transport equations for the electric field vector amplitude $\mathbf{E} = \Psi_n \cdot \hat{\mathbf{n}} + \Psi_b \cdot \hat{\mathbf{b}}$. The field vector itself is transverse to the direction of the wave propagation which is given by the unit wave-vector $\hat{\mathbf{k}}$ and can be projected onto the principal normal axis $\Psi_n = \mathbf{E}\cdot\hat{\mathbf{n}}$ and the binormal axis $\Psi_b = \mathbf{E}\cdot\hat{\mathbf{b}}$ of $\hat{\mathbf{k}}$. Vectors with a hat, like $\hat{\mathbf{n}}$, are normalized to unit length $\|\hat{\mathbf{n}}\|_2 = 1$.

The variable κ is the scalar torsion of the curve to which $\mathbf{k}$ is tangential: $\kappa = \hat{\mathbf{v}}\cdot(\hat{\mathbf{k}}\cdot\nabla)\cdot\hat{\mathbf{b}}$. This set of transport equations (3.11) and (3.12) expresses in an hydrodynamic analogy the conservation of energy flux through a *ray tube* of cross-sectional area A[KO90]:

$$\nabla\cdot(\mathbf{k}\,A^2) = 0 \tag{3.13}$$

as well as the conservation of the polarization ellipse along a ray. The aforementioned concept of a *ray* will be further clarified in the following two sections. As a conclusion of this first section, the following assumptions have been made, in order to arrive at a simplified form of Maxwell's equations:

1. The problem is strictly monochromatic with time-dependence, and thus only one Fourier mode will be considered. This is not justified if a change in colour is relevant for the application, such as with methods based on inelastic scattering, flourescence scattering and problems involving fast moving velocity media ($v = \mathcal{O}(c)$).

2. The exact solution of the scattering problem takes the form of equation (3.7).

3. Terms of order k^{-2} and higher can be neglected in comparison to k^0 (i.e. eikonal) and k^{-1} (amplitude transport).

3.1.2 Algorithm Overview

This second section gives an overview of the workflow of the Geometrical Optics code which essentially relies on Ray Tracing to compute the scattered electromagnetic field. The following list enumerates all calculation steps in the same order as they are executed in the code.

1. Both laser beam and scattering particle as physical entities are initialized as computational objects, given their relevant properties, such as the frequency ω of the incident monochromatic light.

2. The user defines a *transition plane* between the two models of the laser beam as an electromagnetic field and as a bundle of straight rays. All geometric rays involved in the calculation will be emanating from this surface. In all calculations, this surface was chosen to be identical with the illuminated surface of the scattering particle.

3. On this surface, a starting point $\mathbf{x}_0$ is chosen, from which a light ray starts in the direction $\hat{\mathbf{k}}$. For reasons explained in section 5, this point will be chosen at random.

4. All other initial properties necessary for the definition of a Geometrical Optics light ray, such as initial electric field vector $\mathbf{E}_0$, inital phase φ_0, initial wave front curvature matrix Q and initial wave vector $\hat{\mathbf{k}}$ are calculated **from** the given electromagnetic field of the laser beam **at** the chosen starting point $\mathbf{x}_0$. The necessary formulae for this calculation are also explained in section 5.

5. An intersection check between the ray and the surfaces of the scattering particle is performed. The properties of the ray at the intersection point are calculated.

6. At the intersection point, a reflected and a refracted sub-ray or ray segment is created. The new direction, electric field and wavefront curvature matrix of the reflected and refracted ray are calculated using Descartes' law, the Fresnel equations for the electromagnetic amplitudes and a transfer equation for the curvature matrix. These new ray segments are connected to a *binary tree* together with the incident ray segment. The very first ray segment of a ray tree which depends on the properties of the shaped beam is called the *root* segment. This is illustrated in figure 3.1 below.

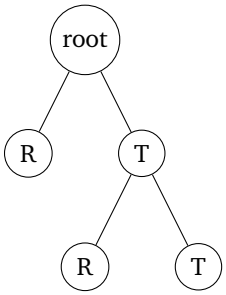

Figure 3.1: Binary ray tree with reflected (R) and transmitted (T) ray segments. Note the correspondence with figure 3.2.

7. If the reflected or refracted sub-ray does not interact with the scatterer again, its outgoing direction and electric field vector are stored in an array.

8. If the sub-ray does not leave the scatterer, a new intersection check with the scatterer surface is performed and the Ray Tracing procedure starts again at point 5. The process will be repeated recursively, until a given scattering order has been reached. The tracing of the ray segments is illustrated in figure 3.2.

9. When the Ray Tracing for a single ray-tree has been completed, the process starts again at point 3 for another ray-tree, until a large number ($\mathcal{O}(10^3)$) of ray-trees has been calculated.

10. After the Ray Tracing has been completed, the distribution of the scattered electric field over a spherical coordinate system enclosing the scatterer will be calculated. Given the direction of each outgoing ray, its corresponding electric field vector will be added to an angular bin in the spherical coordinate system. It is understood that this approach does not create a continuous distribution of the scattered electric field, but rather a histogram that approaches a continuous distribution for decreasing angular bin size.

Specifically, the algorithms for ray tracing a given particle are listed below. A distinction is made between convex and concave particles, which becomes immediately evident for anyone trying to write a ray tracer from scratch. The listing containing the algorithm for ray tracing convex particles is given in the list 1. It is understood that the limitation to convex particle shapes is a quite severe one, as once a ray has left the particle, it can never enter again. Despite this, the convex algorithm has two major advantadges over the concave version, justifying its appearence in this documentation. First, it is much easier to understand and can be readily implemented. Second, it does not require a steadily decreasing amplitude of the light rays through each interaction with the particle surface and can be applied even in cases where this physically justified circumstance is not given, such as computer graphics applications. When the specific intensity or

amplitude of the light rays does not decrease over the interaction count, this convex algorithm needs to be applied to a concave particle that is subdivided into convex ones, according to [AMHH08], further complicating the problem.

Algorithm 1: Ray tracing a convex particle.

```
Data: Particle Geometry, Number of Rotations, Number of Rays, Ray Starting Plane and Direction, Number of
      Internal Reflections
Result: Scattered Ray Segment Starting Position and Direction
Initialize Pseudo Random Number Generator (PRNG);
Initialize Particle Geometry;
Initialize Empty Ray Segment bin;
for Rotations : = 1 to Number of Rotations do
    Rotate Particle;
    for Rays : = 1 to Number of Rays do
        Draw Incident Ray Segment Starting Point from PRNG;
        if Ray Segment intersects particle then
            Calculate Reflected Ray Segment with Snell and Descartes;
            Add Reflected Ray Segment to Ray Segment bin;
            Calculate Refracted Ray Segment with Snell and Descartes;
            Refracted Ray Segment = Swap Ray;
            for order := 1 to Number of Internal Reflections do
                Intersection check Ray Segment → Particle Surface;
                Calculate Refracted and Reflected Ray Segments from Swap Ray;
                Swap Ray = Reflected Ray Segment;
                Add Refracted Ray Segment to Ray Segment bin;
            end
        else
            Ray misses particle → discard Ray;
        end
    end
    Perform Angular Binning for Polar Angle θ;
end
Calculate Orientation Average of Phase Function;
```

If not only results for a single orientation in space of the scattering particle are desired, the algorithm above can be repeated for a large number of random particle orientations. The proper results of each individual orientation will then be sampled to obtain a statistical result.
The listing for the case of a concave particle is the list number 2. As already mentioned, the algorithm requires the amplitude of a single ray to decrease steadily with each interaction of the particle surface, such that is highest amplitude is given in the incident ray segment, before any interaction with the particle. The concave algorithm is not as simple as algorithm 1 and in practical terms requires the usage of a programming language of suitable expressive power. The implementation effort is greatly simplified for instance through the ability of a suitable advanced and flexible container data structure such as the *std::vector<class T>* class in C++ [PLMS00], *boost::tuple<class T>* of the Boost library [boo14] or the inbuilt types of Python [pyt] created by Guido van Rossum [Ros95]. Several authors have written ray tracing codes for the treatment of scattering by non-spherical particles of concave topology, the most prominent one being the code of Professor Macke [MMR96]. Nevertheless, this is the very first time an algorithm for this task has been published in the literature. The algorithms both in listing 1 and 2 had to be redeveloped in their entirety by the author of the current thesis himself due to the complete lack of documentation of each previous code. Another consequence of the lack of documentation for the existing codes and their completely unstructured and outright byzantine coding style is that it is not at all clear whether the algorithm listed here is in any way related to the ones used in existing codes by Macke

[Mac15] or Yang [YL97], for instance. This is in stark contrast to the TSym code [Kah13] of Kahnert, who, despite the mathematical complexity of his combined Fortran 77 & GAP T-matrix code, managed to keep it readable.

Algorithm 2: Ray tracing a concave particle assuming a global decay of ray specific power during surface interactions.

```
Data: Particle Geometry, Ray Starting Plane, Direction and Amplitude, Number of Orientations, Truncation
      Amplitude
Result: Scattered Ray Starting Point, Direction and Complex Amplitude
Initialize Pseudo Random Number Generator (PRNG);
Initialize Particle Geometry;
Initialize Empty Ray Postprocessing bin;
for Rotation := 1 to Number of Orientations do
    for Rays : = 1 to Number of Rays do
        Rotate Particle;
        Draw Ray Segment Starting Point from PRNG;
        Initialize Ray container with incident Ray Segment;
        Incident Ray Segment.interaction count = 0;
        while container ≠ ∅ do
            temporary container = ∅;
            Determine current size of Ray container = container.end - container.start;
            for current wavefront := container.start to container.end do
                Intersection check Ray Segment → Particle surface;
                if Intersection = .False. & interaction count = 0 then
                    Miss → Remove Ray from container;
                else if Intersection = .True. then
                    Calculate Reflected and Refracted Ray Segments using Snell's law and the Fresnel equations;
                    if Refracted Ray.Amplitude < Truncation Amplitude then
                        add neither to container;
                    else
                        if Reflected Ray.Amplitude < Truncation Amplitude then
                            add Refracted Ray Segment only to temporary container;
                            adjust Ray → inside/outside particle;
                        else
                            add Refracted and Reflected Ray Segment to temporary container;
                            adjust Ray.inside/outside particle;
                        end
                    end
                else if Intersection = .False. & interaction count > 0 then
                    /* → Externally Reflected Ray segment or Refracted Ray segment leaving particle */;
                    add Ray Segment to Ray Postprocessing bin;
                end
            end
            Remove previous generating Ray Segment from container;
            Add temporary container to Ray container;
        end
    end
    Perform Angular Binning for Polar Angle θ;
end
Calculate Orientation Average of Phase Function;
```

A final alternative to ray tracing concave particles would be Monte Carlo ray tracing as discussed for instance in the article [FB09]. Therein the light ray is not split up into reflect and refracted ray segments, but instead can *either* reflect *or* refract according to a statistical rule such that the Fresnel equations are recovered in the ergodic limit. This draws upon an analogy to quantum mechanics with the electromagnetic wave being treated as a light corpuscle following a probabilistic behaviour that is ultimately dictated by a solution of a wave equation. The Geometrical Optics code also has several limitations depending its application case. It only allows monochromatic light and thus cannot consider, for

instance, a moving scatterer or a pulse of incident radiation. It also does not include diffraction, as the Mie parameter of the scattering problem is assumed to be very high.

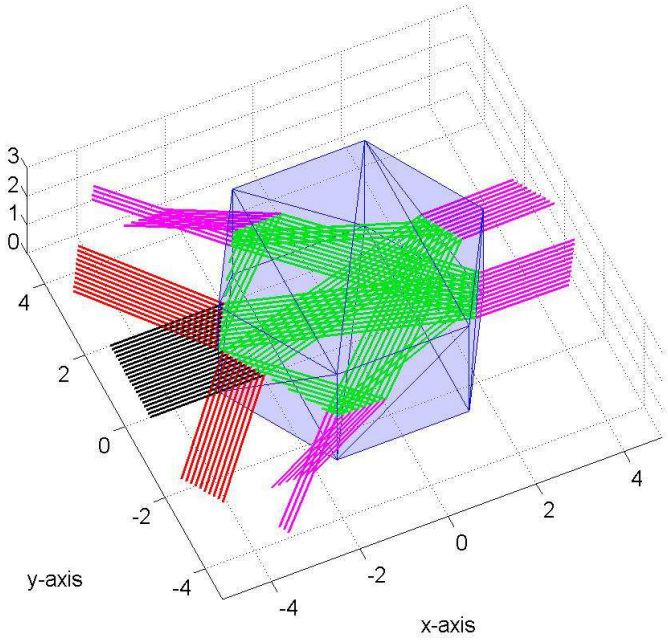

Figure 3.2: Illustration of the 3D ray-tracing process: root segments are shown in black, internal ray segments are green and external rays red or magenta.

3.1.3 Description of a Pencil of Radiation

The third section explains the ray model used in the ray tracing calculations. It will be explained how the relevant properties of a ray segment, such as direction $\hat{\mathbf{k}}$, electromagnetic field vector $\mathbf{E}$, phase φ and curvature matrix Q at an arbitrary point $\mathbf{x}(\tau)$ on the ray segment can be calculated from the corresponding properties at a previous starting point $\mathbf{x}_0$ of this segment. Geometrical Optics as such is an approximation for the propagation of oscillations of the electromagnetic field based on expanding Maxwell's equations in terms of a smallness parameter and truncating the resulting system of equations on 0^{th} or 1^{st} order. A rigorous derivation is given in the book [KO90] by Kravtsov. A primary assumption of the GO code presented here is that there are no continuous refractive index variations inside or outside the scattering particle. As a consequence, the light rays as characteristic curves of the eikonal equation [KO90][Des72] are piecewise straight lines:

$$\mathbf{x}(\tau) = \mathbf{x}_0 + \hat{\mathbf{k}} \cdot \tau \tag{3.14}$$

In equation (3.14), $\mathbf{x}_0$ is again the starting point of a straight ray segment, $\hat{\mathbf{k}}$ is the direction of propagation of the ray as well as the wave vector of the electromagnetic wave associated to the ray and τ is the parameter identifying the point $\mathbf{x}(\tau)$ which is element of the ray. As explained in references [KO90] and [Des72] and applied in reference [RORG11], the truncation of the expansion of Maxwell's equations at 1^{st} order allows a transversal electromagnetic field vector to be associated with each ray, which, in a homogeneous medium, can be reduced to the following form:

$$\mathbf{E}(\tau) = \mathbf{E}_0 \underbrace{\sqrt{\frac{detQ(\tau)}{detQ(0)}}}_{\sqrt{Divergence}} exp\left(-i(k\tau + \varphi_0)\right) \tag{3.15}$$

where the time-dependence $exp(i\omega t)$ for time t and frequency ω has been suppressed. The phase $\varphi = k\tau$ depends linearly on the distance τ along the ray segment starting from $\mathbf{x}_0$ and takes the wavenumber $k = \frac{2\pi}{\lambda}$, with λ being the wavelength,

as a proportionality constant. The matrix Q is the so-called wavefront curvature matrix and $\mathbf{E}_0$ is the electric field vector at the starting point $\mathbf{x}_0$ of the ray segment. This model of the electromagnetic field, combining the ray equation (3.14) and the field equation (3.15) is illustrated in the sketch 3.3. The sketch also shows the electric field vector $\mathbf{E}(\tau)$ as two scalar quantities E_r and E_b through its projection onto normal $\hat{\mathbf{r}}$ and binormal vector $\hat{\mathbf{b}}$ associated to the vector $\hat{\mathbf{k}}$.

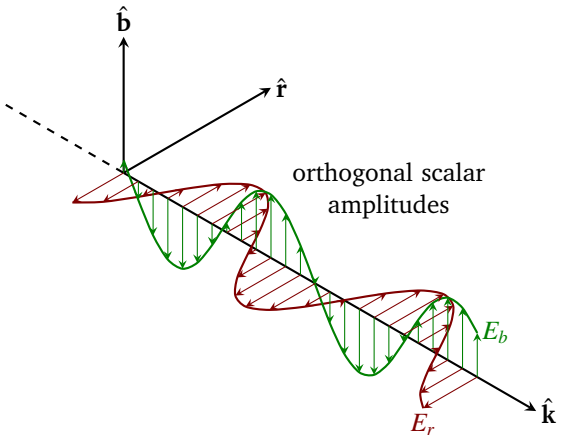

Figure 3.3: Decomposition of an elliptically polarized plane wave onto normal and binormal axis.

The divergence factor in equation (3.15) quantifies the influence of the change in cross-sectional area of the ray segment on the amplitude of the electric field vector. This is illustrated in figure 3.4 where the cross-section of the ray segment decreases as the initial wavefront converges to the focal lines 1 and 2. As the cross-section decreases, the amplitude of the electromagnetic oscillation increases correspondingly. This also leads to the possibility of caustics, which are curves and surfaces on which the intensity of the electromagnetic field becomes infinite according to geometrical optics. This is explained in greater detail by Berry [BU80] or again in the book by Kravtsov [KO90]. At the caustics, a phase-shift of $-\frac{\pi}{2}$ needs to be added to the phase [Hul01] for each focal line that is passed. At a focal point, this amounts to a phase-shift of $-\pi$, depending on the degeneracy of the eigenvalues of the Jacobian $D(\tau) = detQ(\tau)$ according to [KO90]. For practical calculations the $-\frac{\pi}{2}$ -phase shift is applied each time the Jacobian changes its sign.

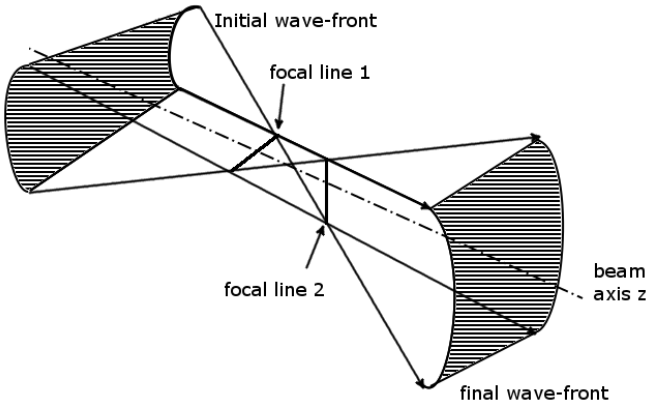

Figure 3.4: Astigmatic beam with two focal lines instead of one focal point

The vectors of the eigenbasis of Q are called the *principal axes* of the ray segment by Deschamps [Des72] and the eigenvalues of Q depending on τ then are:

$$Q(\tau) = \begin{pmatrix} \frac{1}{R_1+\tau} & 0 \\ 0 & \frac{1}{R_2+\tau} \end{pmatrix} \tag{3.16}$$

where R_1 and R_2 are the so-called principal wave front curvature radii as illustrated in figure 3.5 and they are interpreted physically as the distance between a wave front as a surface of constant phase and its two focal lines.

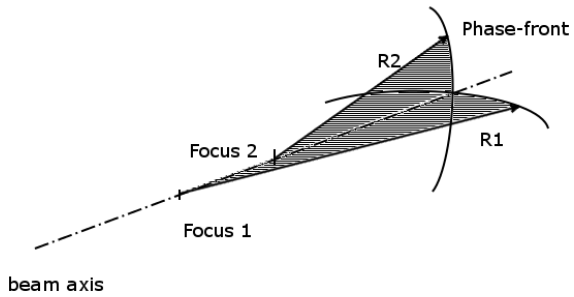

Figure 3.5: Principal wavefront curvature radii R_1 and R_2

If the matrix is not given anymore in the system of the principal axes, the diagonal elements will be non-vanishing. This is to be expected already after the first interaction of the ray with an interface. A general expression for the change of the curvature matrix along the ray has been given by Deschamps in [Des72]:

$$Q^{-1}(\tau) = Q^{-1}(0) + \tau \cdot \begin{pmatrix} 1 & 0 \\ 0 & 1 \end{pmatrix} \tag{3.17}$$

where the matrix inversion can be conveniently carried out by applying Cramer's rule to expression (3.17). This model for the calculation of the electric field $\mathbf{E}(\tau)$ at any given point $\mathbf{x}(\tau)$ along a ray segment is identical to the one proposed by Deschamps [Des72] and Kravtsov [KO90] and similar to the Vectorial Complex Ray Model (VCRM) implemented by Ren et al. in references [RORG11] and [JHR13]. It is also possible to execute conventional Geometric Optics calculations with the present code by equating the divergence factor with 1 and thus keeping the electric amplitude constant along a ray segment.

3.1.4 Description of the Scattering Particle

The three physical properties of a scatterer that influence the scattered electromagnetic field in Geometrical Optics are its refractive index n, its surface curvature matrix C and its geometrical shape. The following section is divided into two subsections. First, the two different methods used in the code to describe the shape of a scattering particle are explained. Second, the equations necessary to calculate the properties of reflected and refracted rays from the properties of an incident ray at an interface described by the particle surface are mentioned.

Description of particle shape

Due to its object-oriented nature, the code includes the possibility to to either represent a particle using an implicit surface equation or a subdivision of the surface into triangles for more complicated shapes. The surface curvature matrix and a ray surface intersection check are the only computational methods that need to be changed. The description of an ellipsoidal or spherical scatterer is possible through an implicit surface equation F:

$$F(x,y,z) = \frac{x^2}{a^2} + \frac{y^2}{b^2} + \frac{z^2}{c^2} - 1 = 0 \tag{3.18}$$

Where x, y, z are cartesian coordinates and a, b, c are the half-axes of the ellipsoid.

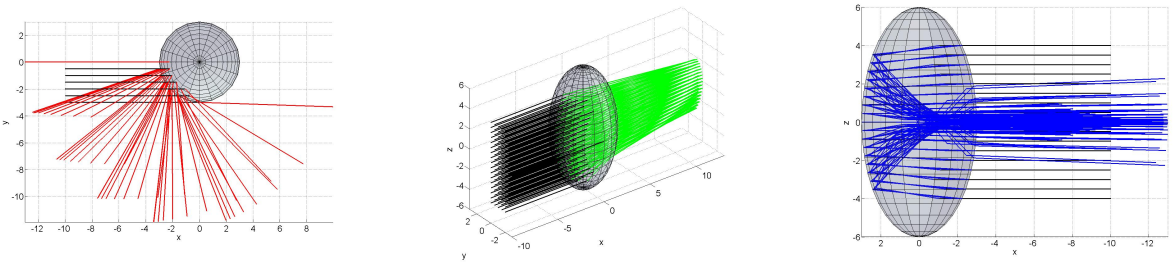

(a) Reflected Rays **(b)** Once refracted Rays **(c)** Twice refracted Rays

Figure 3.6: Various scattering orders in the ray tracing of a spheroid.

The intersection check of a ray as a straight line and this particle shape is straightforward. A slightly modified algorithm is given in the listing 3.

Algorithm 3: Intersection check between a ray and an implicitly defined sphere.

Data: $\mathbf{x}_0$, $\hat{\mathbf{k}}$, $\mathbf{c}$, r
Result: (REJECT/INTERSECT), τ, $\mathbf{p}$
$\mathbf{l} = \mathbf{c} - \hat{\mathbf{x}}_0$;
$s = \mathbf{l} \cdot \hat{\mathbf{k}}$;
$l^2 = \mathbf{l} \cdot \mathbf{l}$;
if $s < 0$ & $l^2 > r^2$ **then**
  return (REJECT,0,**0**);
end
$m^2 = l^2 - s^2$;
if $m^2 > r^2$ **then**
  return (REJECT,0,**0**);
end
$q = \sqrt{r^2 - m^2}$;
if $l^2 > r^2$ **then**
  $\tau = s - q$;
else
  $\tau = s + q$;
end
return (INTERSECT,τ, $\mathbf{x}_0 + \tau \cdot \hat{\mathbf{k}}$);

The normalized surface normal of such a particle is proportional to the gradient of the implicit surface equation:

$$\hat{\mathbf{n}} = \frac{\nabla F(\mathbf{x})}{\|\nabla F(\mathbf{x})\|_2} \tag{3.19}$$

Where $\|\cdot\|_2$ denotes the Euclidean norm for the vector $\mathbf{x}$ with the three components x,y and z. While the implicit surface description is mostly used for simple particle shapes, such as spheres, ellipsoids and cylinders, it is also possible to apply it to the description of non-trivial shapes by using for instance superellipsoids. This was demonstrated in the context of the T-Matrix formalism by Wriedt [Wri02] in 2002. A variety of superellipsoidal shapes is shown in figure 3.7. As can be seen, the parametric superellipsoid model covers a wide range of shapes, including astroids 3.7a and finite caped cylinders 3.7b. Wriedt uses the following formula for the implicit surface description of a superellipsoid.

$$\left(|x|^r + |y|^r\right)^{\frac{t}{r}} + |z|^t \leq 1 \tag{3.20}$$

where r and t are positive real parameters and (x,y,z) again coordinates in a threedimensional cartesian coordinate system.

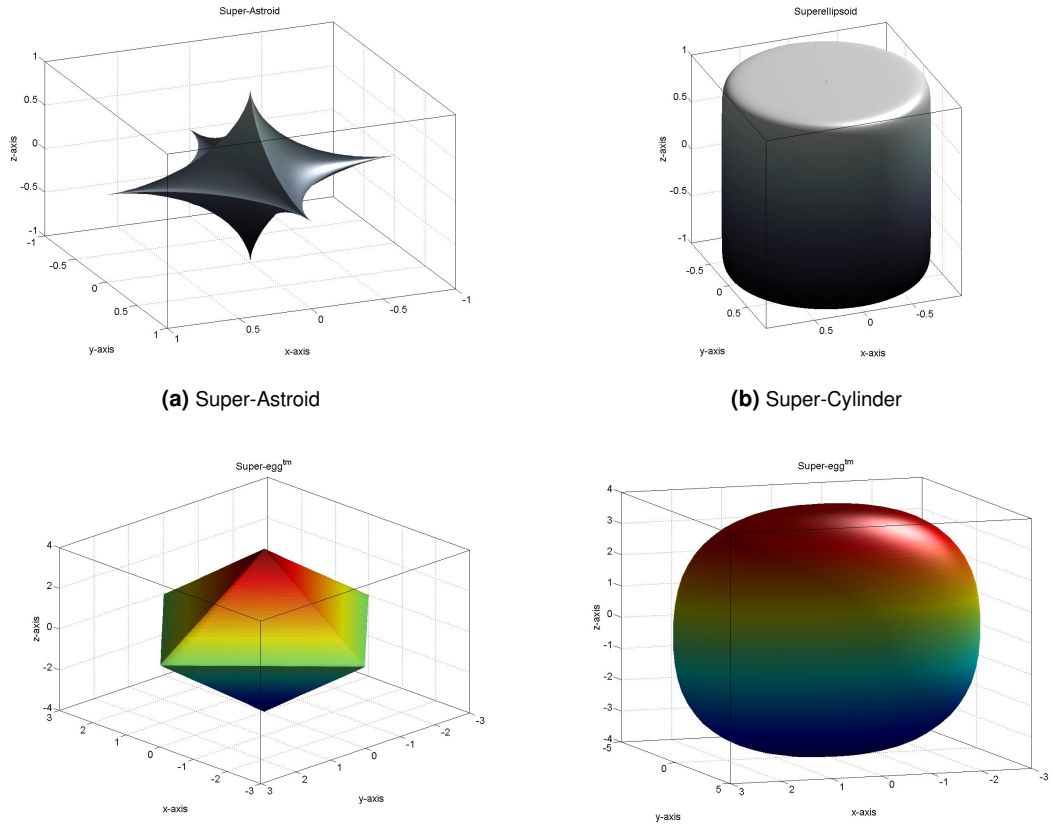

(a) Super-Astroid

(b) Super-Cylinder

(c) Double-Pyramid

(d) Super-Egg

Figure 3.7: A representative variety of superellipsoidal shapes.

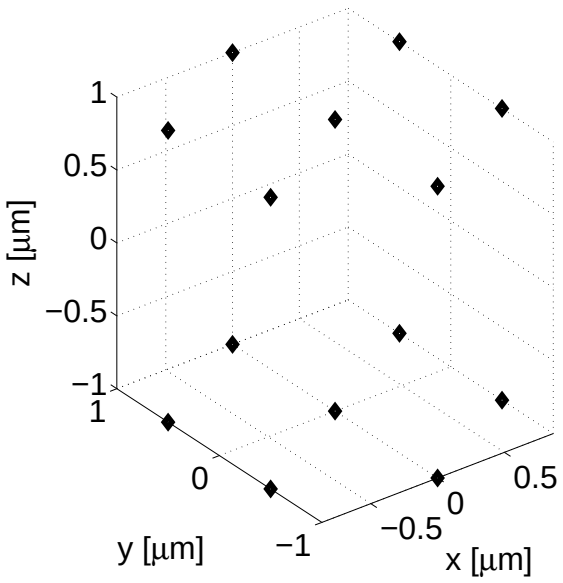

Figure 3.8: Edge and padding points indicated by diamond specks defining the shape of a hexagonal prism used to represent an ice crystal shape

In order to represent more complicated shapes and especially prismatic bodies like hexagonal prismatic ice crystals, the GO code can also handle surfaces represented by a mesh of triangles, i.e. triangulated surfaces. A hexagonal prism as a computational object thus would be represented as an ordered list of 24 triangles, which in turn have been created from an ordered list of edge points of the hexahedron as well as necessary padding points in between the edges as seen

in figure 3.8. A single triangle can be represented by its three edge points $\mathbf{x}_1$, $\mathbf{x}_2$ and $\mathbf{x}_3$ in Euclidean space. The normal vector $\mathbf{n} = \mathbf{a}_1 \times \mathbf{a}_2$ of this triangle can then be calculated as the cross-product of the two legs $\mathbf{a}_1$ and $\mathbf{a}_2$ of the triangle, which also form the basis of a local barycentric coordinate system attached to the triangle:

$$\mathbf{a}_1 = \mathbf{x}_2 - \mathbf{x}_1 \tag{3.21a}$$

$$\mathbf{a}_2 = \mathbf{x}_3 - \mathbf{x}_1 \tag{3.21b}$$

Per convention, the normal vector of each triangle points outward in the GO code. This explanation makes it clear, that the global topology of the surface of the prism depends on the ordering of the point triples $[\mathbf{x}_1, \mathbf{x}_2, \mathbf{x}_3]$ of each triangle. A wrong ordering will result in a normal vector pointing inward, or the particle surface mesh having holes. The resulting triangular surface mesh shown in figure 3.9 is a type of geometry that is very commonplace in computer graphics and a fast and efficient intersection check between a straight light ray and a triangle can be found in standard references for computer graphics, such as the book [AMHH08]. A brief overview of the algorithm is given in listing 4.

Algorithm 4: Intersection check between a ray and a triangle in 3D space.

Data: $\mathbf{x}_0$, $\hat{\mathbf{k}}$, $\mathbf{x}_1$,$\mathbf{x}_2$,$\mathbf{x}_2$
Result: (REJECT/INTERSECT), u,v,τ
$\mathbf{a}_1 = \mathbf{x}_2 - \mathbf{x}_1$;
$\mathbf{a}_2 = \mathbf{x}_3 - \mathbf{x}_1$;
$\mathbf{q} = \hat{\mathbf{k}} \times \mathbf{a}_2$;
$a = \mathbf{a}_1 \cdot \mathbf{q}$;
if $-\varepsilon < a < \varepsilon$ **then**
  return (REJECT, 0, 0, 0);
end
$f = \frac{1}{a}$;
$\mathbf{s} = \mathbf{x}_0 - \mathbf{x}_1$;
$u = f(\mathbf{s} \cdot \mathbf{q})$;
if $u < 0.0$ **then**
  return (REJECT, 0, 0, 0);
end
$\mathbf{r} = \mathbf{s} \times \mathbf{a}_1$;
$v = f \cdot (\hat{\mathbf{k}} \cdot \mathbf{r})$;
if $v < 0.0$.*or.* $u + v > 1.0$ **then**
  return (REJECT, 0, 0, 0);
end
$\tau = f \cdot (\mathbf{a}_2 \cdot \mathbf{r})$;
return (INTERSECT, u, v, τ);

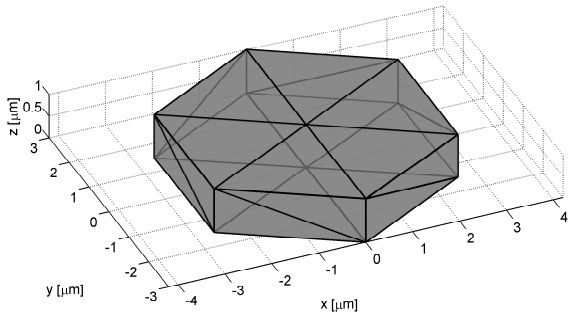

Figure 3.9: Surface triangulation of the hexagonal prism. Note the correspondance with figure 3.8.

In order to construct composite forms for ice crystals, a object-oriented Matlab code with an appropriate algebra has been written, that creates complex shapes by literally adding the simple hexagonal prismatic and bullet shapes to bullet rosettes and rivet-like shapes shown in figure 3.10.

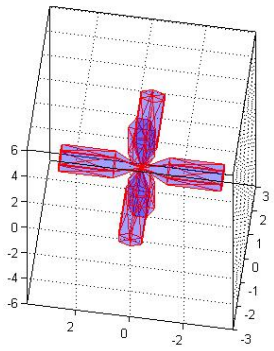

(a) Bullet Rosette

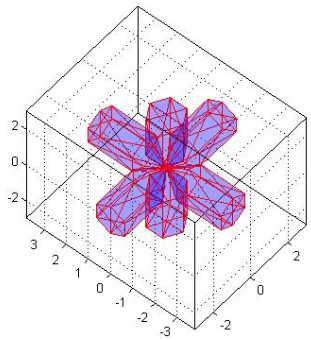

(b) Bullet Rosette

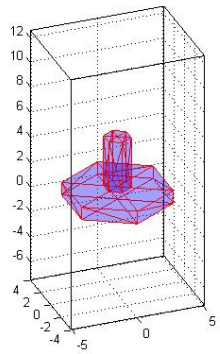

(c) Capped Column/Rivet

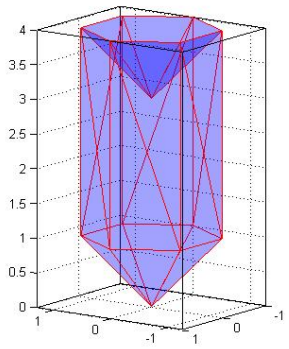

(d) Hollow Bullet

Figure 3.10: Composite shapes created by geometrically adding simple Bullet- and Prism particle objects in an OOP Matlab script.

In order to apply a geometrical transformation to the scattering particle for instance for the orientational averaging, it suffices to apply the representation of the transformation to all the points representing the surface triangulation of the particle. The transformations implemented in the present code are quaternion rotation about an arbitrary axis and translations using homogeneous coordinates. Both representations are used in computer graphics [AMHH08] due to their efficiency and reliability. For the quaternion rotation in the present case, the quaternion class of the boost library [boo15] has been used. The algorithm used in the code is shown in listing 5. Here an arbitrary point $\mathbf{x}$ is rotated by an angle ϕ around an arbitrary unit axis $\hat{\mathbf{u}}$ by applying the operation rules of the quaternion algebra.

Algorithm 5: Rotation of a point around an axis using quaternions.

Data: point coordinates $\mathbf{x}$, rotation axis $\hat{\mathbf{u}}$, rotation angle ϕ
Result: rotated point coordinates $\mathbf{x}'$
/* Create unit quaternion $\mathbf{q}$ from rotation angle ϕ and axis $\hat{\mathbf{u}}$ */;
$\mathbf{q} = \left(cos\frac{\phi}{2},\ u_x sin\frac{\phi}{2},\ u_y sin\frac{\phi}{2},\ u_z sin\frac{\phi}{2}\right)$;
/* Create unit quaternion $\mathbf{p}$ from point $\mathbf{x}$ to be rotated */;
$\mathbf{p} = \left(0,\ x_x,\ x_y,\ x_z\right)$;
/* conjugation of $\mathbf{p}$ by $\mathbf{q}$ */;
$\mathbf{p}' = \mathbf{q}\mathbf{p}\mathbf{q}^{-1}$;
$\mathbf{x}' = \left(p'_x,\ p'_y,\ p'_z\right)$;
return $\mathbf{x}$';

The given scheme of a transformation changing a vector based on another vector and a scalar parameter was already mentioned shortly in the section on the theory of electromagnetism 2.1.3. From a programmer's perspective, it is very advantages that a large number of different transformations such as rotations, translations, scaling and Lorentz boosts have

the same input and output in terms of data structures. This allows it to make use of several advanced features of object oriented programming languages, such as C++. In order to express the common structure of all the transformations, the concepts of Inheritance and Polymorphism as described for instance in the language references [Bre07, PFW12, BN94] may be used. The abstract concept of a mathematical transformation is represented as a likewise so-called *abstract class*, whose source code may be written in the following form:

```
#pragma once
#include<valarray>

class CTransformation {
protected:
        std::valarray<long double> initial_point;
public:
        void set_point(std::valarray<long double> a)
        {initial_point = a;};
        virtual std::valarray<long double> transform(std::valarray<long double>, long double) = 0;
};
```

The class is abstract, as there is no constructor method present in the class header file [BN94], making it impossible to create an object of this class. Another feature of importance in the source code is the virtual method *transform*, which is also purely virtual, as it is set equal to zero and has no concrete implementation in the CTransformation header. A specific and concrete transformation such as the previously discussed quaternion rotation can then be a child of the abstract parent class CTransformation. The C++ source code of the quaternion rotation class definition looks as follows:

```
#pragma once
#include<boost\math\quaternion.hpp>
#include "CTransformation.h"

class CRotationQuaternion: public CTransformation{
public:
        std::valarray<long double> transform( std::valarray<long double>, long double );
};
```

It is immediately obvious that the definition of the class CRotationQuaternion is much shorter than the definition of its abstract parent class CTransformation. This is due to the fact that the former *inherits* all public methods of the latter class through the *public* keyword. This is the principle of inheritence in object oriented programming [BN94]. Furthermore, the quaternion rotation class provides an actual implementation of the purely virtual *transform* method of its parent class. There can be multiple child classes of CTransformation, each having a different implementation of the transform method corresponding to a different geometrical transformation, but still bearing the same name. This is the principle of *Polymorphism*. For a given situation a conceptually identical method is specialized to appeal to the specific circumstances of the problem. The class definition used here also makes it possible to use *runtime polymorphism*, that is, to decide at runtime, which implementation of the transform method should be called, as explained in the following C++ code snippet taken from the main function of an example program:

```
        valarray<long double> justapoint(init1,3), theshift(init2,3);
        CTranslation translation;
        CRotation rotation;
        CTransformation * cctransf1 = &translation;
        CTransformation * cctransf2 = &rotation;
        cctransf1->set_point(justapoint);
        cctransf2->set_point(justapoint);
        cout << "Translation again: " << endl;
        for(size_t kk = 0; kk<justapoint.size();kk++){
                cout << cctransf1->transform(theshift,length)[kk] << endl;
        }
        cout << "Matrix rotation: " << endl;
        for(size_t kk = 0; kk<justapoint.size();kk++){
                cout << cctransf2->transform(theshift, M_PI/2.L)[kk] << endl;
        }
```

Going back to the description of the scattering particle itself, the representation of a surface by triangles also easily adapts to the representation of fractal shapes (a term coined by Benôit Mandelbrot [Man67] [Man82]) as substitutes for real

highly irregular ice crystals popularized by Macke in the publication [MT92], such as Koch fractals. An example of a three dimensional fractal with a tetrahedron as a generator is shown in figure 3.11. As the corresponding algorithm for creating this kind of fractal has as of now not yet been published, it had again to be redeveloped from scratch by the author of this thesis. The corresponding algorithm for creating 3D tetrahedral Koch fractals is given in listing 6 as pseudocode and the corresponding implementation as a Matlab script is given in the appendix of the thesis for the convenience of the reader.

Algorithm 6: Generation of Koch fractals of arbitrary order.

Data: highest order n_{max} of Koch fractal
Result: array of edge point coordinates **E** (geometry), array of edge point connectivity **C** (topology)
Initialize base Tetrahedron / Fractal Generator as a list of four triangles;
list of triangles = base triangles 1 to 4 ;
for *index1 := 1 to* n_{max} **do**
    swap list = $\emptyset$;
    for *index2 := 1 to length(list of triangles)* **do**
        Calculate three points on the edges connecting each triangle point from current triangle in list of triangles;
        Calculate fourth point along the centre normal of each triangle;
        Create Six new triangles from the list of new points;
        Add the Six new triangles to swap list;
    end
    clear list of triangles;
    list of triangles = swap list;
    clear swap list;
end
return **E** and **C** from final iteration of list of triangles;

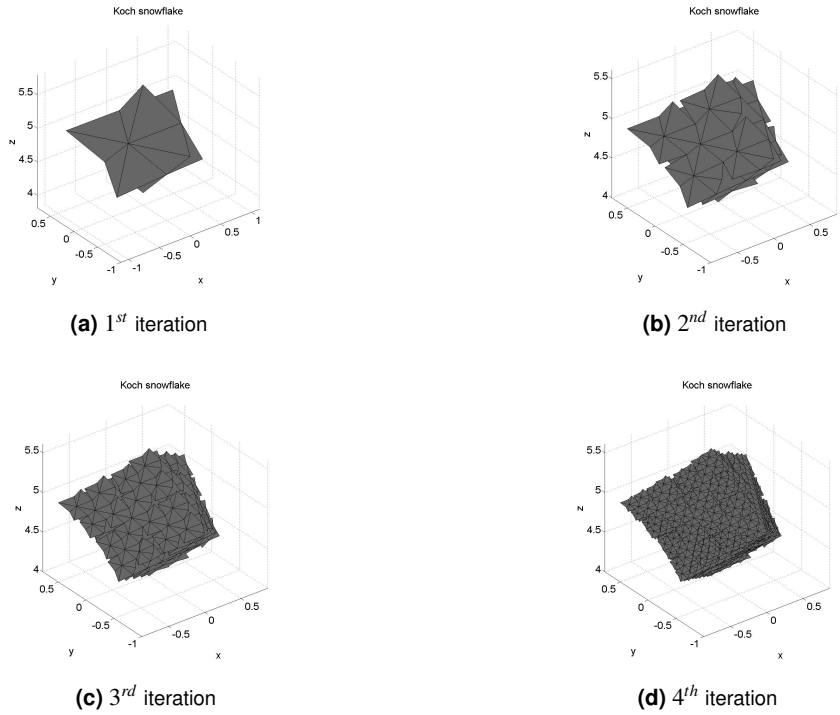

(a) 1^{st} iteration **(b)** 2^{nd} iteration

(c) 3^{rd} iteration **(d)** 4^{th} iteration

Figure 3.11: The first 4 iterations of a 3D Koch fractal with a trehadral basis shape.

Interface equations

Upon interaction with the particle surface defined in the previous subsection, a new reflected and refracted ray segment is created from the previous incident ray segment. The electric field **E**, the ray direction **k** and the curvature matrix Q of the new rays are calculated from the corresponding properties of the preceding ray segment. Beginning with the change

in ray direction, the code uses the familiar principle of the Snell's or Descartes' law in order to determine the reflected and refracted directions $\mathbf{k}_R$ and $\mathbf{k}_T$ as illustrated in figure 3.12.

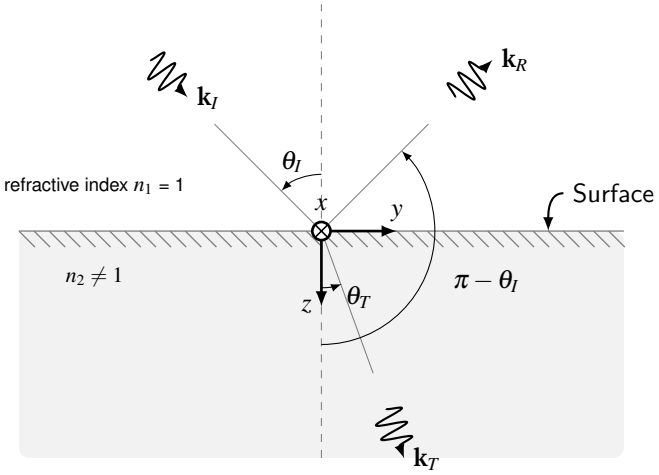

Figure 3.12: Sketch of the Snellius - Descartes law

In order to apply Descartes' law in the 3D ray-tracing code, the relation for reflection is reformulated as a Householder transformation:

$$\hat{\mathbf{k}}_R = \hat{\mathbf{k}}_I - 2(\hat{\mathbf{n}} \cdot \hat{\mathbf{k}}_I)\hat{\mathbf{n}} \tag{3.22}$$

where $\hat{\mathbf{k}}_R$ is the unit vector of the reflected ray segment, $\hat{\mathbf{k}}_I$ is the unit vector of the incident ray segment and $\hat{\mathbf{n}}$ is again the surface normal of the particle calculated through any matching of the two formulae of the previous subsection. The refracted direction is calculated through a rotation of the incident direction by applying the following transformation:

$$\hat{\mathbf{k}}_T = \eta \hat{\mathbf{k}}_I - (c - \eta d)\hat{\mathbf{n}} \tag{3.23}$$

Where $\hat{\mathbf{k}}_T$ is the unit direction of the refracted (i.e. transmitted) ray. The other quantities are given as: $d = -\mathbf{n} \cdot \mathbf{k}_I$, $c = \sqrt{1 - \eta^2(1 - d^2)}$ and the relative refractive index $\eta = \frac{n_1}{n_2}$. Both formulations are again relationships widely used for ray tracing in a computer graphics context such as the one in references [AMHH08] and [HH84].
The transformation of the electric field also relies on a conventional formulation using the Fresnel coefficients (see for instance references [BW99], [Som64] or [KO90]). In order to apply the formulae in the computational procedure, the electric field vector of the incident ray is projected onto a vector parallel (designated by $||$) and perpendicular (designated by $\perp$) to the plane of incidence defined through its normal vector $\hat{\mathbf{k}}_I \times \hat{\mathbf{n}}$, such that:

$$\mathbf{E}_I = \mathbf{E}_{||} + \mathbf{E}_{\perp} \tag{3.24}$$

Given the angle of incidence θ_I and of refraction θ_T calculated from Descartes' law, the Fresnel coefficients of the reflected field in two arbitrary media of real refractive indices n_1 and n_2 are:

$$R_{||} = \frac{n_1 cos\theta_T - n_2 cos\theta_I}{n_1 cos\theta_T + n_2 cos\theta_I} \tag{3.25a}$$

$$R_{\perp} = \frac{n_1 cos\theta_I - n_2 cos\theta_T}{n_1 cos\theta_T + n_2 cos\theta_T} \tag{3.25b}$$

while for the transmitted field they are:

$$T_{||} = \frac{2n_1 cos\theta_T}{n_1 cos\theta_T + n_2 cos\theta_I} \tag{3.26a}$$

$$T_{\perp} = \frac{2n_1 cos\theta_I}{n_1 cos\theta_I + n_2 cos\theta_T} \tag{3.26b}$$

Such that the final fields are:

$$\mathbf{E}_R = R_{||}\,\mathbf{E}_{||} + R_{\perp}\,\mathbf{E}_{\perp} \tag{3.27a}$$
$$\mathbf{E}_T = T_{||}\,\mathbf{E}_{||} + T_{\perp}\,\mathbf{E}_{\perp} \tag{3.27b}$$

As the light rays leave the scatterer and thus pass from a medium that is optically thick (ice) to a medium that is optically thin (air), total reflection may occur if the incidence of the ray onto the boundary is too shallow. A conditional in the code checks for the occurrence of this situation and in such an event no refracted ray is created and the resulting phase shift for the totally reflected ray is taken into account through the Fresnel coefficients taking complex values. As a new ray segment is created, its initial electric vector $\mathbf{E}_0$ from equation (3.15) is now equated with $\mathbf{E}_R$ or $\mathbf{E}_T$, depending on whether it is a reflected or refracted ray segment.
Finally, the condition that the incident, reflected and refracted wave must have the same phase at the particle surface not only leads to Descartes' law, but according to Deschamps [Des72] also to a transfer equation for the wavefront curvature matrix Q. The matrix equation reads:

$$k_T \Theta_T^T Q_T \Theta_T = k_I \Theta^T Q \Theta + hC \tag{3.28}$$

where C is the surface curvature matrix of the interface itself, k is again the wavenumber and $h = k_T cos\theta_T - k_I cos\theta_I$ is the variation of the wave vector after crossing the surface. The matrix Θ is the projection operator between the principal axes of the matrices Q and C and the superscript letter T denotes matrix transposition. Since the ice crystal surface is modeled as a set of triangular *plane* surfaces or facets, the curvature matrix is assumed to be equal to zero in the frame of all calculations documented in this paper:

$$C = \begin{pmatrix} 0 & 0 \\ 0 & 0 \end{pmatrix} \tag{3.29}$$

since for a perfectly plane surface, its principal curvature radii $R_i \to \infty$ clearly tend to infinity, and the projection operator Θ is the identity matrix **Id**. Of course, the situation is different for smooth objects like the spheroids investigated by Ren [RORG11], where the surface curvature matrix is a non-vanishing function of the particle coordinate system. After applying equation (3.28), the new (refracted) curvature matrix Q_T cannot be assumed to be diagonal and its eigenvalues and the new principal axes as its eigenvectors need to be determined anew. A formulation for a surface curvature matrix C for a smooth particle surface such as that of a sphere or spheroid is not within the scope of this work and calculations involving spheres have been performed excluding the curvature matrix transfer, resulting in an electric field amplitude which is constant along each ray segment.

3.1.5 Surface roughness model

It has been found that an important physical property of ice crystals influencing their light scattering properties is mesoscopic surface roughness. Experimental evidence and direct samples of mesoscopic surface roughness in natural atmospheric ice crystals can be found for instance in the article by Magee et al. [MMAC14]. In order to further extend the capabilities of the present GO code, a surface roughness model has been included. This task was greatly facilitated by the strict adherence to object oriented programming principles. For the implementation the model of Yang and Liou [YN98] was chosen. It is readily applicable to the entire range of particles included in the GO code and may easily be extended further towards more sophisticated models, as had been shown by Shcherbakov [Shc13]. The model of Yang and Liou introduces the simple notion that an essentially random surface roughness may influence an incident light ray through a random tilt of its normal vector $\hat{\mathbf{n}}$ only. In a local coordinate system tangent to the refractive surface at the intersection point between ray and surface, the slope of the surface facet can be proven to take the following form:

$$Z_{,x} = \frac{\partial Z}{\partial x} = \sqrt{m^{-2} - 1} \cdot cos\phi \tag{3.30}$$

$$Z_{,y} = \frac{\partial Z}{\partial y} = \sqrt{m^{-2} - 1} \cdot sin\phi \tag{3.31}$$

where $m = cos\theta$ and θ and ϕ are the tilt vectors of $\hat{\mathbf{n}}$ in a spherical coordinate system. The rotation of $\hat{\mathbf{n}}$ around the angles (θ, ϕ) may conveniently be realised via the quaternion rotation applied to the particle orientation sampling. The probability density function for the surface taking a slope value $(Z_{,x}, Z_{,y})$ is then a 2D Gaussian distribution:

$$P(Z_{,x}, Z_{,y}) = \frac{1}{\pi\sigma^2} \cdot exp\left(-\frac{Z_{,x}^2 + Z_{,y}^2}{\sigma^2}\right) \tag{3.32}$$

where σ is of course the standard deviation of the normal distribution. Yang and Liou give three distinctive physical ranges for σ:

1. slight roughness: $\sigma = 0 - 0.005$
2. moderate roughness: $\sigma = 0.005 - 0.05$
3. deep roughness: $\sigma = 0.05 - 0.2$

As will be shown in the later chapters, the categories have clear effects especially on the phase functions of ice crystals. Slight roughness has almost no influence on the phase function. Moderate roughness values lead to a disappearance of the 22° halo and the glory peak, while deep roughness leads to a disappearance of the 22° halo, leaving the phase function featureless save for the forward peak.

3.1.6 Description of a Shaped beam in the Geometrical Optics model

As a ray segment is determined by the equations (3.14), (3.15) and (3.17), it can be seen that in order to initialize the *root* element of a binary raytree consisting of reflected and refracted ray segments, four quantities are necessary:

1. Ray starting point $\mathbf{x}_0$
2. Initial electric field vector $\mathbf{E}_0$
3. Initial wave front curvature matrix $Q(0)$
4. Ray direction vector $\hat{\mathbf{k}}$

The enumeration above provides the roadmap for the four subsections that will explain how a shaped beam, such as a Gaussian beam will be included in the geometrical optics model. The thematic point of entry will literally be the starting point $\mathbf{x}_0$.

Determination of a starting point

The starting point of the root ray segment must lie on a chosen two-dimensional transition surface between the exact solution of the incident electromagnetic beam and the geometrical optics model. The positions of all the starting points $\mathbf{x}_0$ on this surface are a priori arbitrary, but experience has shown that the distribution of points should be random and uniform in cartesian coordinates. Furthermore, the points should lie inside an area that is identical to the area of the scattering particle projected into the transition plane, such as a circle for a spherical scatterer or an irregular polygon for a polyhedral scatterer of random orientation. This method has been pioneered in the Geometrical Optics code developed by Macke [Mac94]. The clipping of the starting points is especially important for scattering particles with an aspect ratio far from unity in order to avoid costly intersection checks for rays that are guaranteed *not* to hit the particle. A counter-example is shown in figure 3.13. Here the points lie in a circle and thus are favourable for the use with a spherical scatterer. The points are also randomly and uniformly distributed, but they are randomly distributed in *polar* coordinates and not in cartesian ones. This leads to a higher concentration of starting points and thus light rays at the centre.

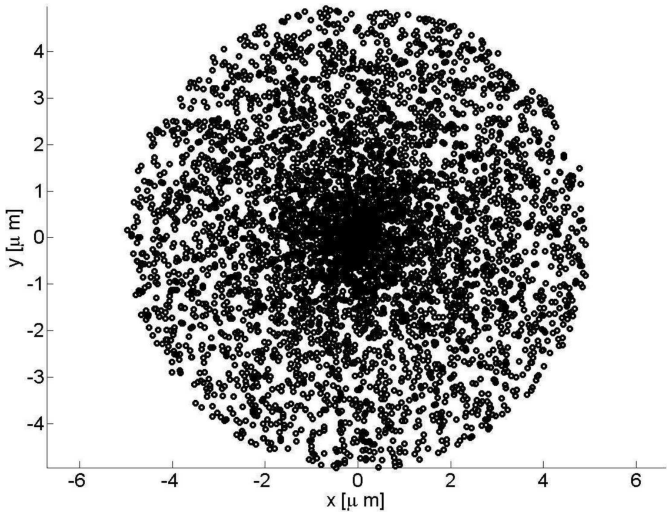

Figure 3.13: Randomized set of starting points as the illumination source. Note the non-uniform distribution of points clustering at the centre.

Calculations have shown, that any regularity that is present in the initial starting point distribution is also reflected in the distribution in of the scattered electromagnetic field. The concentration of points shown in figure 3.13 for instance leads to unphysical peaks in the forward and backward direction of the scattered intensity for a sphere as shown in figure 3.14 and an overall wrong intensity distribution.

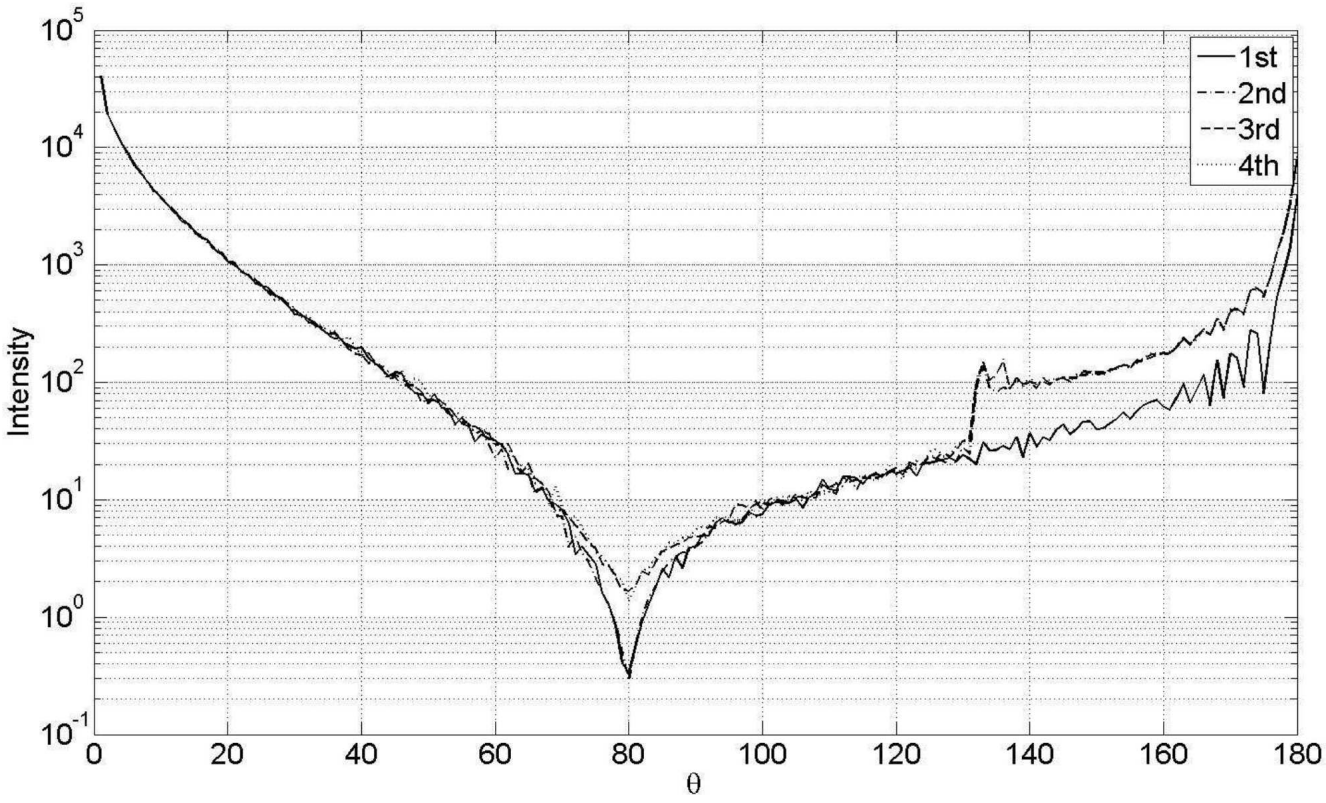

Figure 3.14: Overlay of the first four orders of the unphysical scattered intensity distribution of a plane wave ($\lambda = 308nm$) scattered by a sphere (radius 1mm, n= 1.32)

While the emphasis is on generating a uniform distribution of starting points, starting points distributed on a regular grid were also used, but the grid structure is also propagated through the ray-tracing procedure. The pseudo random number generator (PRNG) used in the code for the generation of a uniform random distribution of points is the default *mt19937* variation of the Mersenne-Twister algorithm [MN98] used in the GNU Scientific Library (GSL) [Gal] with a period of $2^{19937} - 1$.

This subsection will cover the calculation of the initial electric field vector $\mathbf{E}_0$ of the root segment of a raytree. As already stated in the second section an expression for the exact solution of the incident electromagnetic shaped beam is necessary to start with. In this work, a Gaussian beam in the TEM_{00} mode will be used as a representative shaped beam, since it is the case of the most practical interest. The Gaussian beam is attached to its own cartesian coordinate system with the basis $\hat{\mathbf{u}}_x$, $\hat{\mathbf{u}}_y$ and $\hat{\mathbf{u}}_z$ which is separate from the global cartesian coordinate system in which the ray tracing calculation takes place and to which it is related by a finite number of rotation and translation transformations. The beam propagates in the $\hat{\mathbf{u}}_z$ direction and is linearly polarized in the $\hat{\mathbf{u}}_x$ direction. The solution for such a beam was given by Davis in his publication [Dav79]. As this is a perturbation solution which is only exact in the limit of an infinite series, the solution is used which is truncated at 0^{th} order for the purpose of the geometrical optics calculations. Following the conventions of Gouesbet et al. in the book [GG11] we use the order $L-$ of approximation for the calculation of the electric field vector. Thus the model for the initial electric field vector is purely transversal, retaining only the scalar component E_x. As pointed out by Gouesbet et al. [GG11], this violates Gauss' law and this representation of a Gaussian beam is not a solution to Maxwell's equations. According to Davis [Dav79], this component E_x can be calculated through the scalar Helmholtz equation:

$$\Delta E_x + k^2 E_x = 0 \tag{3.33}$$

which, by assuming the beam to be nearly plane and of the form $E_x(x,y,z) = \psi(x,y,z) \cdot exp(-ikz)$, reduces to the paraxial wave equation, which is formally identical to the time-dependent Schrödinger equation [Dir88]:

$$\frac{\partial^2 \psi}{\partial x^2} + \frac{\partial^2 \psi}{\partial y^2} - 2ik\frac{\partial \psi}{\partial z} = 0 \tag{3.34a}$$

$$\left(\frac{-\hbar^2}{m}\Delta\right)|\psi(\mathbf{r},t)\rangle = 2i\hbar\frac{\partial}{\partial t}|\psi(\mathbf{r},t)\rangle \tag{3.34b}$$

which is formally identical to the time-dependent Schroedinger-equation [Dir88] of the wave function $|\psi(\mathbf{r},t)\rangle$ for the free (note the absence of the potential term $V(\mathbf{r})$) non-relativistic particle of mass m [LL90]. The wave function here is of course the projection $\langle \mathbf{r}|\phi\rangle$ of the state $|\phi(t)\rangle$ in the Schroedinger-picture onto position space [Dir88]. The beam-axis coordinate z of the Gaussian beam replaces the time evolution t of the free particle. This equation admits a solution for a free particle that was used by Davis and Kogelnik et al. [KL] to also describe a Gaussian beam, such that E_x now reads:

$$E_x(r,z) = \frac{w_0}{w(z)} exp\left[-i(kz-\Phi) - r^2\left(\frac{1}{w^2} + \frac{ik}{2R}\right)\right] \tag{3.35}$$

where $r = \sqrt{x^2+y^2}$, z are the beam radius and beam axis coordinate respectively in a cylindrical coordinate system r, ϕ, z that is aligned with the rotationally symmetric beam. The *beam-waist radius* is denoted as w_0 in equation (3.35). Further terms in this solution include the beam contour,

$$w^2(z) = w_0^2\left[1 + \left(\frac{\lambda z}{\pi w_0^2}\right)^2\right] \tag{3.36}$$

the Gouy-phase-shift,

$$\Phi = arctan\left(\frac{\lambda z}{\pi w_0^2}\right) \tag{3.37}$$

and the radius of curvature,

$$R(z) = z\left[1 + \left(\frac{\pi w_0^2}{\lambda z}\right)\right] \tag{3.38}$$

which will play a more prominent role in the next subsection. A plot of the field produced by equation (3.35) is shown in figure 3.15. It can be seen from this figure and from the expression for the beam contour that the beam expands by moving along the positive beam axis. In fact, the expansion gets stronger for smaller initial *localizations* $2 \cdot w_0$ of the beam. This is a classical analogue of Heisenberg's [Hei27] uncertainty relation $\Delta x \Delta p \geq \frac{\hbar}{2}$ in the frame of this approximation. The tighter the initial beam focus, the larger the spread of the associated wave vectors. The streamlines of the Poynting vector are also shown in figure 3.15 in order to visualize the flow of power in the Gaussian beam, having been calculated along the lines proposed by Berry [BM08].

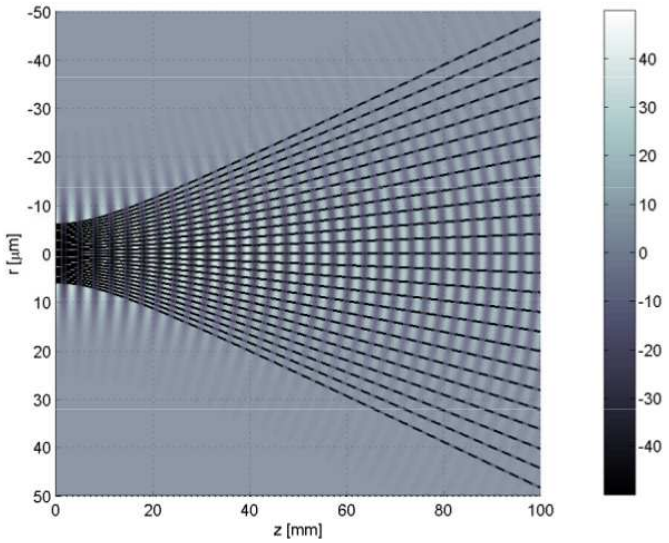

Figure 3.15: Wave function E_x of a paraxial Gaussian beam with streamlines of the Poynting vector superimposed

In order to determine the streamlines, Berry applied a methodology to the Gaussian beam he had developed in a previous publication [Ber09] with the aim of determining the so-called *optical current* of a scalar wavefield with the penultimate goal of understanding the distribution and transfer of energy through electromagnetic waves. In such a wavefield Berry [BM08] defines the Poynting vector as the expectation value of the local momentum operator defined in equation (2.61) applied to the scalar field. An explicit expression for the integral curves of the Poynting vector field or its streamlines in a hydrodynamic analogy can then be explicitly given in cylindrical coordinates ρ, ϕ, z:

$$\rho(z) = \rho_0 \sqrt{1+z^2} \tag{3.39}$$

$$\phi(z) = \phi_0 + \frac{l}{\rho_0^2} \cdot arctan(z) \tag{3.40}$$

Equations (3.39) and (3.40) then determine a family of hyperboloid curves shown in figure 3.15. Concluding this subsection, the initial electric field amplitude $\mathbf{E}_0$ at $\mathbf{x}_0$ can be calculated from equation (3.35) and written in the coordinate system of the beam as:

$$\mathbf{E}_0(\mathbf{x}_0) = E_x(\mathbf{x}_0) \cdot \hat{\mathbf{u}}_x \tag{3.41}$$

Calculation of initial wavefront curvature matrix

For both equations (3.15) and (3.17) an initial value for the wave front curvature matrix $Q(0)$ needs to be calculated from the wave solution (3.35). It can be derived rigorously from differential geometric arguments as in reference [JHR13]. For the purpose of the present investigation, the initial curvature matrix has been constructed directly from the curvature radius (3.38) of the field solution at the coordinate z_{eval} where the transition between ray and field solution takes place.

$$Q(\tau) = \begin{pmatrix} \frac{1}{R(z_{eval})+\tau} & 0 \\ 0 & \frac{1}{R(z_{eval})+\tau} \end{pmatrix} \tag{3.42}$$

The eigenbasis or principal axes of Q are simply defined to be the two basis vectors $\hat{\mathbf{u}}_x$ and $\hat{\mathbf{u}}_y$ perpendicular to the beam axis $\hat{\mathbf{u}}_z$.

Calculation of the initial wave vector

This last subsection explains the calculation of the wave vector $\mathbf{k}$, which in its normalized form $\hat{\mathbf{k}}$ is used in the ray equation (3.14). The full Fourier spectrum of a wave field is used for instance in the Fourier Lorenz Mie Theory (FLMT) [Dam03] to decompose a Gaussian beam. In the case of Geometrical Optics, the full spectrum of an incident beam can be limitied to the so-called *local spatial frequencies* as defined by Goodman [Goo05]. For this purpose, equation (3.35) can also be rewritten in the following form:

$$E_x(x,y,z) = A(x,y,z) \cdot exp\left(-iS(x,y,z)\right) \tag{3.43}$$

where the two real fields A and S are the amplitude and phase part of E_x respectively. Goodman now defines the local spatial frequencies as the gradient of the phase S:

$$S_{,x} = \frac{-kxz}{z^2+l^2} \tag{3.44a}$$

$$S_{,y} = \frac{-kyz}{z^2+l^2} \tag{3.44b}$$

$$S_{,z} = -k - k\frac{(x^2+y^2)(l^2-z^2)}{2(l^2+z^2)^2} + \frac{l}{l^2+z^2} \tag{3.44c}$$

for $l = \frac{\pi w_0^2}{\lambda}$ being the Rayleigh length, k the wave number and $S_{,x}$ denoting partial differentiation with respect to the coordinate x. These results are formally identical to the ones published by Jiang et al. in [JHR13]. The result published earlier by Ren and Xu in a related work [RORG11] deviates from both the present publication and publication [JHR13], as the denominator of the second summand of equation 9 for $\mathbf{F}_z$ should read: $w_0^2\ (z_R^2 + (z-d)^2)^2$ instead of the given expression. As the Gaussian beam is represented as a bundle of rays in the Geometrical Optics approximation of this code, the wave vectors of the ray bundle used in equation (3.14) are equated with the local spatial frequencies:

$$\mathbf{k}(x,y,z) = \nabla S(x,y,z) \tag{3.45}$$

3.1.7 Geometrical Optics Calculation Results

This subsection shows sample results of the Geometrical Optics derivative code developed for this thesis. The results consist of a validation section where the Ray tracing results are compared against exact GLMT results and a section where the results for the case of a hexagonal prism are shown. Both sections are preceded by an explanation of the relevant postprocessing quantities which are extracted from the simulations.

The Stokes Vector: Measurable Quantities in Optics

It is a well known fact first explicitly stated by Sommerfeld [Som64] that detectors that are usually employed in optical experiments such as CCD chips or photographic films are unable to follow the rapidliy oscillating electromagnetic field directly. It is said that such detectors are quadratic, i.e. they only detect the intensity of the underlying wave field. A widely used tool for the description of scattering experiments is the so-called Stokes vector formalism in conjuction with Müller matrices. This not only includes optical scattering [WY12], but in fact every other scattering experiment involving particles which carry spin, such as electrons [McM54, McM61]. The intensity and the polarization of a beam of light measured in an experiment are encoded in the *Stokes vector*, defined by:

$$\mathbf{I} = \begin{pmatrix} I \\ P \\ Q \\ V \end{pmatrix} = \begin{pmatrix} I \\ I\ p\ cos(2\psi)\ cos(2\chi) \\ I\ p\ sin(2\psi)\ cos(2\chi) \\ I\ p\ sin(2\chi) \end{pmatrix} \overset{\text{monochromatic}}{=} \begin{pmatrix} E_b^2 + E_r^2 \\ E_b^2 - E_r^2 \\ 2\ E_b\ E_r\ cos(\Delta\phi) \\ 2\ E_b\ E_r\ sin(\Delta\phi) \end{pmatrix} \tag{3.46}$$

The individual components of the vector are [McM61]:

- Intensity I of the beam.
- Degree of linear polarization P with respect to the orthogonal vectors $\hat{\mathbf{r}}$ and $\hat{\mathbf{b}}$.
- Degree of linear polarization Q with respect to axes that have been rotated by 45^o degrees.
- Degree of circular polarization Q.

The expression of the Stokes vector for a monochromatic beam also contains the phase difference $\Delta\phi$ between the two orthogonal scalar amplitudes E_b and E_r comprising a transversal spin-1 vector wave. A light beam is then characterized by its intensity and three parameters specifying its polarization state. These parameters may also be expressed in spherical coordinates. These coordinates are $I \cdot p$, $2\ \psi$ and $2\ \chi$. As a consequence, the Stokes vector may be visualized on the so-called Poincaré sphere [McM54] shown in figure 3.16, which is conceptually similar to the Bloch sphere [Blo46] for two orthogonal states $|0\rangle$ and $|1\rangle$ in quantum mechanics. The parameter p in the radial coordinate serves the normalization of the intensity:

$$p = \frac{\sqrt{P^2 + Q^2 + V^2}}{I} \tag{3.47}$$

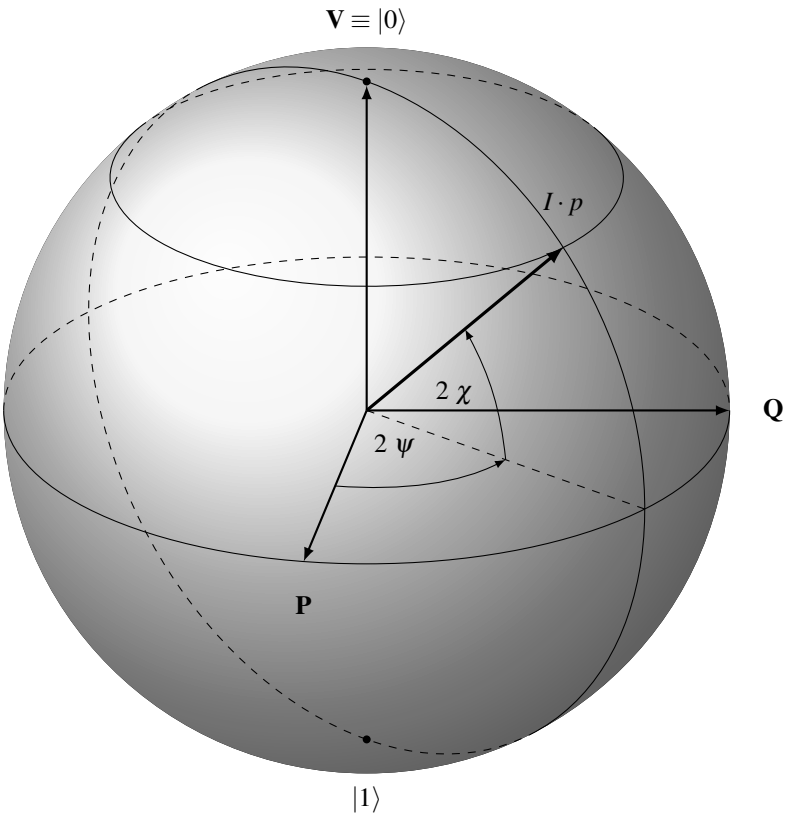

Figure 3.16: Illustration of the Poincaré sphere in 3D.

The use of the Stokes vector formalism in light scattering has been popularized again by Van de Hulst in his authoritative book [Hul01] where he had collected the accounts by different authors on how particle symmetries influence the Stokes vector of the light scattered by this particle. Combining the Stokes vector with the Müller matrix formalism leads to a linear relationship between the Stokes vector $\mathbf{I}$ of an incident plane wave and its scattered counterpart:

$$\mathbf{I}'(\theta) = M(\theta) \cdot \mathbf{I} \tag{3.48}$$

The scattered Stokes vector $\mathbf{I}'(\theta)$ now has a polar angular dependence through the Müller matrix $M(\theta)$ that encodes the scattering properties of the particle. The first element of the Müller matrix M_{11} is the so-called *Phase function*, which gives information on how much light is scattered in a certain polar direction. The Stokes formalism is also of central importance in the theory of Radiative transfer that is closely tied to the field of light scattering. Here, the Stokes vector is the quantity transported in the vectorial Radiative transfer equation (RTE), as explained in a mathematically rigorous fashion in the seminal work [Cha03] of Chandrasekhar. In order to calculate the phase function in the Geometrical Optics framework, a formulation is used in this thesis proposed by Macke in his Ph.D. thesis [Mac94]:

$$M_{11}(\theta_i) = \frac{I_{scatt}(\theta_i)}{\sum_{\theta_i} 2 \cdot I_{scatt}(\theta_i) \cdot \Delta\Omega(\theta_i)} \tag{3.49}$$

where θ_i is the discrete polar angle interval at which the light rays are collected and $\Delta\Omega(\theta_i)$ is the corresponding solid angle, i.e. the dimensionless area of a spherical surface at θ_i. For an explanation of the concept of solid angle see for instance the reference [AMHH08].

Extraction of physical observables

In order to calculate any experimentally observable quantities such as the one presented in subsection 3.1.7 in the derived Geometrical Optics code, it becomes necessary to collect each ray segment leaving the particle, such as the ones depicted in figure 3.2, into an angular bin (θ_i, ϕ_j) of a spherical coordinate system. The corresponding set of spherical coordinates (θ_i, ϕ_j) is calculated from the cartesian components of the wave vector $\hat{\mathbf{k}}$ of an outgoing ray segment. An illustration of the spherical coordinate grid surrounding the scattering particle is given in figure 3.17.

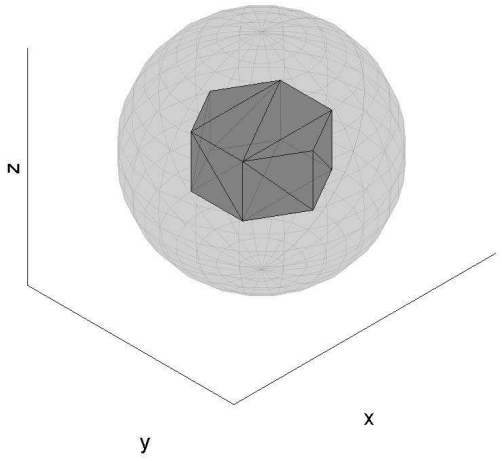

Figure 3.17: Spherical coordinate system around the scatterer for angular binning.

After the recording of the electric field of the ray at a specific coordinate, it is possible to treat the scattered rays as coherent by forcing the scattered field to be linear in the electric field amplitude [BW99].

$$\mathbf{E}_{total}(\theta_i, \phi_j) = \sum_{k=1}^{all\ rays} \mathbf{E}_k \tag{3.50a}$$

$$I_{total}(\theta_i, \phi_j) = \frac{c}{2} \left\| \mathbf{E}_{total}(\theta_i, \phi_j) \right\|^2 \tag{3.50b}$$

or by treating them as completely incoherent by calculating the individual intensities first:

$$I_k = \frac{c}{2} \left\| \mathbf{E}_k \right\|^2 \tag{3.51a}$$

$$I_{total}(\theta_i, \phi_j) = \sum_{k=1}^{all\ rays} I_k \tag{3.51b}$$

In the calculations performed in this study, the former option has been chosen, although the latter requires noticeably less computation time.

Spherical Particle Results

In this subsection, validation results for the Geometrical Optics code are presented. As validation results for a spherical particle shape are readily available, as explained in the introduction, this particular shape has been chosen as a test case. Figure 3.18 shows the logarithmic scattered intensity of a plane wave interacting with a perfectly spherical droplet. The two codes chosen for the comparison is the Geometrical Optics code developed as part of this thesis in the specialisation for a spherical scatterer and a Mie solver called MiePlot. MiePlot was developed by Philip Laven [Lav03] and is available online at [Lav15] as version 4.5. The parameters of the simulation are given in table 3.1.

particle radius R	wavelength λ	index of refraction n	Polarization	incident wave
400 μm	632.8 nm (red)	1.333	parallel	pw

Table 3.1: Calculation parameters for the comparison between Mie and Geometrical Optics results in figure 3.18.

All GLMT and Ray tracing calculations have been carried out on a regular desktop PC with specifications given in table 3.2.

CPU	RAM	GPU	hard disk space	Operating System
Intel Core i7 920, 4 core, 2.67 GHz	6 GB	NVidia GeForce 610	325 GB	Ubuntu Linux 12.04 LTS

Table 3.2: Specifications of the PC used to carry out RT and GLMT calculations.

It can be seen in figure 3.18 that the geometrical optics code performs well against the Mie code at least in the chosen case of a large particle. While the features such as the diffraction peak in the exact forward direction and the exact phase relationship cannot be reproduced by the geometrical optics code, the general agreement is good and essential features such as the first and second order rainbow together with Alexander's dark band [Dam03] are shown in an almost idential way by both Mie and Ray tracing code.

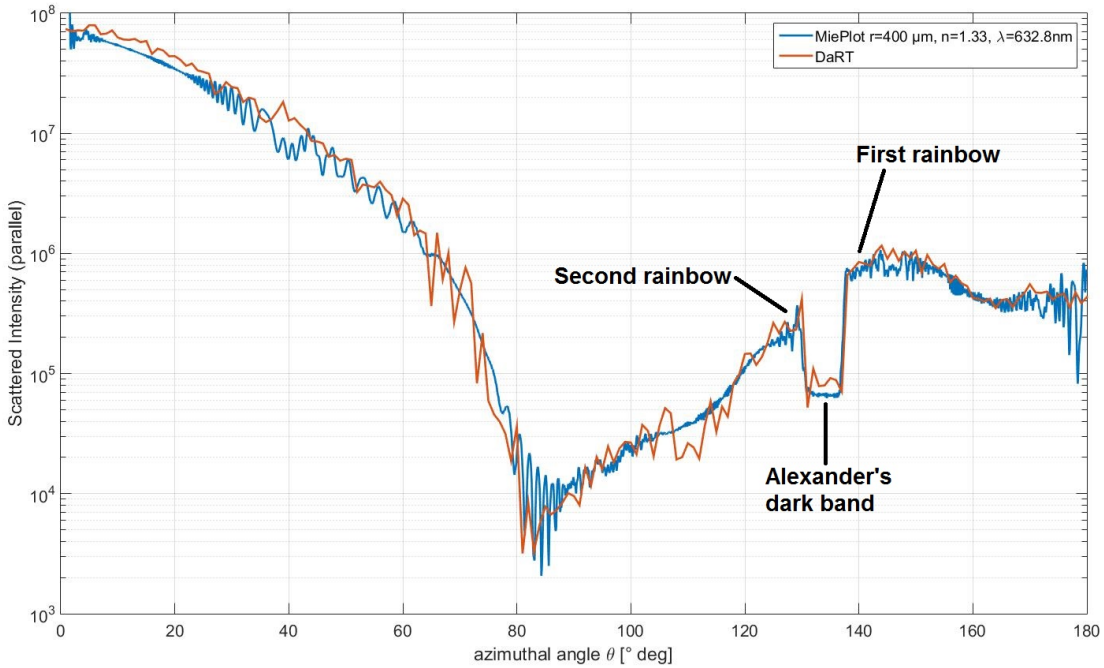

Figure 3.18: Comparison of the polar distribution of the scattered intensity between Mie and Geometrical Optics calculations.

The same Mie code is also capable of handling Gaussian beam incidence and the parameters are tabulated in 3.3, while the results can be seen in figure 3.19. Again, a large particle well in the optical regime has been chosen for comparison and the graph shows the scattered intensity over the polar angle θ. The results have been offset by a factor of 10^6 on the logarithmic scale for better visibility.

particle radius R	wavelength λ	index of refraction n	Polarization	incident wave
400 μm	632.8 nm (red)	1.333	parallel	Gaussian, $w_0 = 10\mu$m

Table 3.3: Calculation parameters for the comparison between GLMT and Geometrical Optics results in figure 3.19.

As one can see from the results in figure 3.19, again the agreement between the exact GLMT results and the Geometrical Optics code is good. The disappearance of the rainbow due to the Gaussian beam is captured well in both methods. Nevertheless, the exact interference is not seen in the GO results and a remnant feature of the rainbow can still be seen.

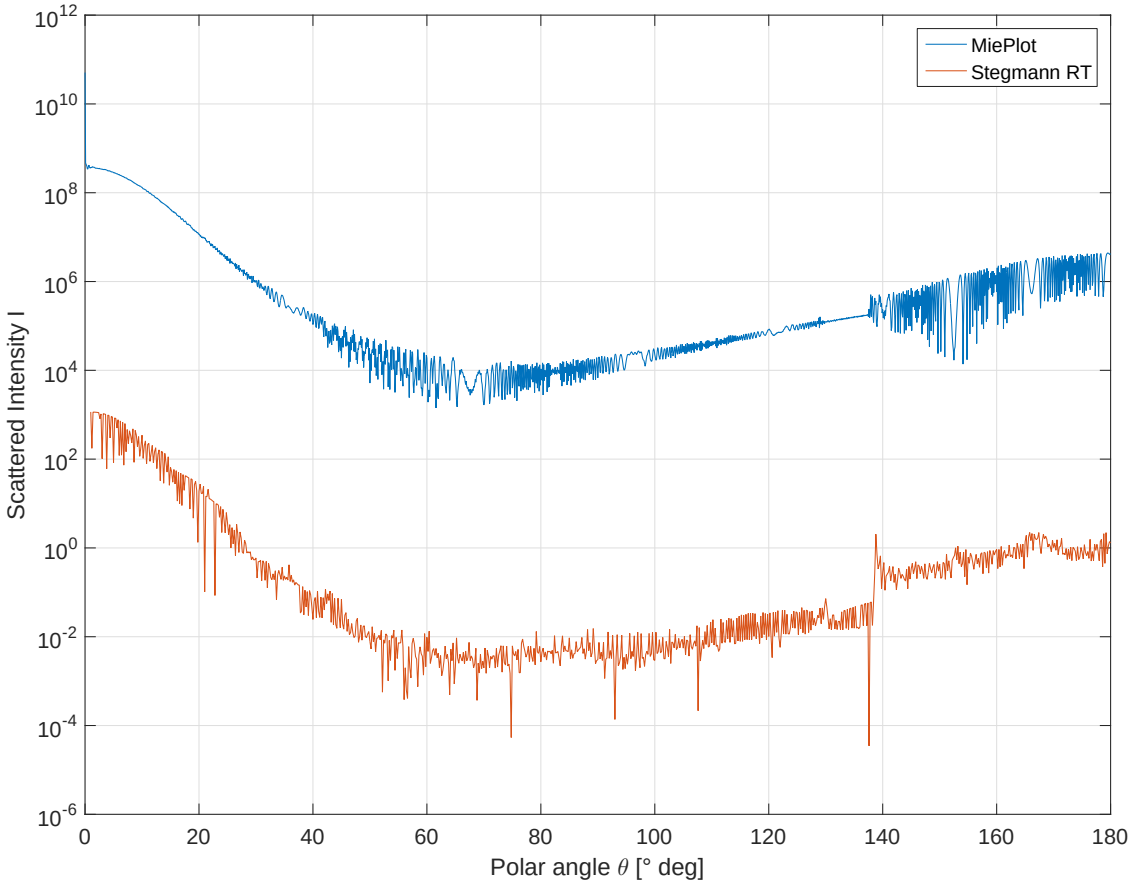

Figure 3.19: Comparison of the polar distribution of the scattered intensity between GLMT and Geometrical Optics calculations. Results have been shifted by a factor of 10^6 for better visibility.

After a satisfactory agreement of the GO results with exact calculations could be observed in the spherical case, the approach was deemed fit for application to the scattering by non-spherical particles.

Hexagonal Prism Results

The final application of the Geometrical Optics code is the case of a pristine hexagonal prism. This shape is a very common substitute for modeling properties of amtospheric ice crystals in a light scattering context, as it is used by Kahnert [Kah05], Macke [Mac94] and Yang [YL97, YN95], amongst others, due to the fact that water crystalises predominantly in a hexagonal prismatic shape [Pau35] under the conditions in the terrestrial atmosphere. A review article [KNL14] on

various possible particle shapes used to model the properties of non-spherical particles was published recently by Kahnert. It is important to note that while it has become possible to simulate the approximately real growth of ice crystals using phase field [BGN12] or level set [Cri14] CFD methods , no attempts have been made yet to use such shapes in light scattering calculations. In the current work, the hexagonal prism has been chosen as it is a very simple convex shape whose surface is representable through triangles. Despite its simplicity it nevertheless still produces the most prominent natural light scattering phenomena [WY12], indicating that a large fraction of atmospheric ice crystal must be hexagonal prismatic in shape.

particle radius R	wavelength λ	index of refraction n	Polarization	incident wave
100 μm	632.8 nm (red)	1.31	parallel	pw and $w_0 = 10\mu$m

Table 3.4: Calculation parameters for the comparison between Gaussian and plane wave incidence in figure 3.20.

It is worthwhile to compare the phasefunction results for a hexagonal prismatic ice crystal shown in figure 3.20 with the natural observed phenomena shown in the photograph 1.1 in the introduction of the thesis. As the reader can see in the photograph, the sun as a central bright spot is surrounded by a duo of rings of decreasing brightness called *halos*. The first one is called the 22° degree halo, as its relative distance to the sun is twenty-two degrees. Likewise, the second bright ring is called the 46° degree halo. Both these phenomena can be recovered in the phase function of figure 3.20 as intensity spikes at 22° and 46° degrees respectively. Furthermore, the fact that the sun is still visible as a bright central spot and not as diffuse as in rain clouds is explained by the strong peak in the exact forward direction. Lastly, the phasefunction shows a distinct glory peak in the exact backscattering direction (i.e. $\theta = 180°$ degrees) which is a 3^{rd} order refraction phenomenon. This means that the glory peak is created by light rays undergoing two internal reflections [WY12].

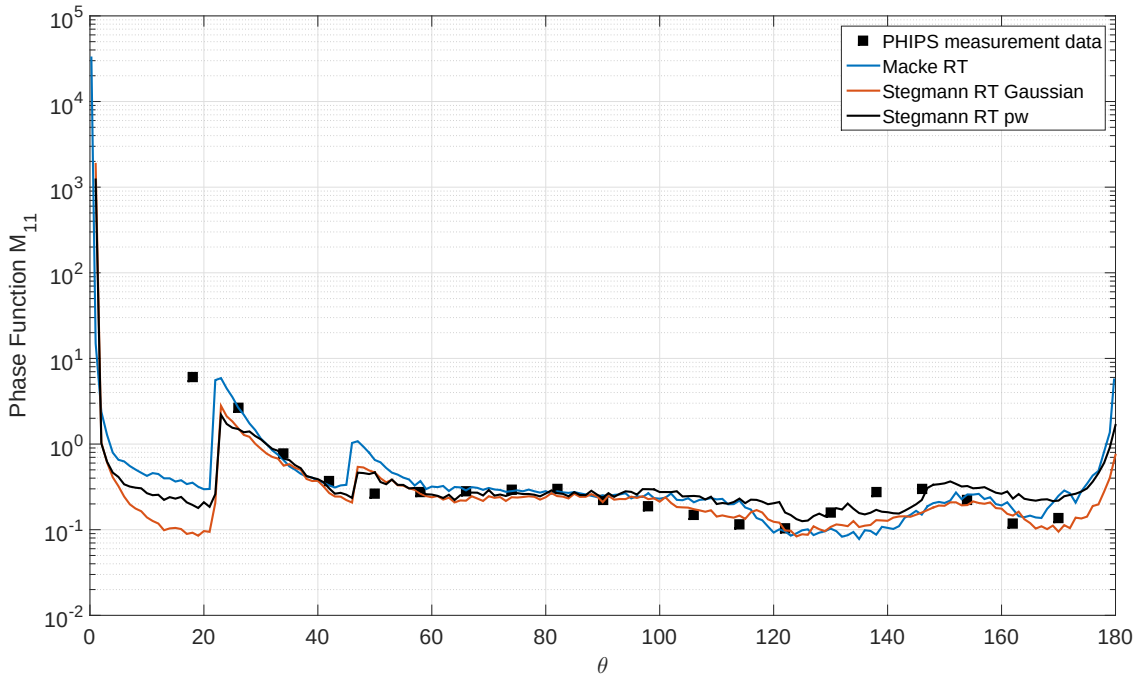

Figure 3.20: Polar phase function for a hexagonal prism with plane wave (pw) and Gaussian beam incidence

Figure 3.20 also shows a direct comparison of plane wave and Gaussian incidence cases. While the phase function remains largely unchanged when switching from pw to Gaussian beam incidence, a clear trend can be observed. The phase function for a Gaussian beam displays overall lower values in the general forward- and backscattering direction. An immediate physical explanation for this is furnished by the divergence of the focused Gaussian beam. As the focus of the Gaussian beam concides with the centre of gravity of the hexagonal prism for the pruposes of this simulation, the divergence of the wavevectors of the beam adds to the divergence of the scattered field. Figure 3.20 also shows a validation curve obtained from the ray tracing code of Macke [Mac94] and measured data for a single particle obtained by the PHIPS probe. All three results show a certain overall agreement and a complete discussion especially on the PHIPS results is given in chapter 5. In single particle detection and characterization experiments, it is of specific importance to decide upon a proper angular location of one or multiple optical detectors. The calculation result now suggest that using a laser-

beam does not create new scattering features in the forward region. Instead, the scattered intensity of existing features is enhanced. Thus, no change of position of an existing optical detector in the forward region is necessary. Meanwhile, the newly created hump at around 120° may be suggested as a trial detector position for enhanced detection of non-spherical particles in the backward direction. Also, the 120° hump differs significantly from the features of a comparable spherical particle in this specific angular region, namely the third order refraction rainbow, potentially indicating a criterion for the distinction of the two particle morphologies. At this point it finally needs to be stated explicitly that the Stokes vector formalism and the theory of radiative transfer have been developed at a time when there were no lasers and shaped beam light sources available. Thus it is questionable whether an interpretation of shaped beam scattering by a non-spherical particle really should be done via the phase function. In the results of figure 3.20, the Gaussian beam profile has been elevated to a geometric property of the scattering particle while **the incident wave is still pretended to be a plane wave**. While this is of less importance in the envisaged application case of the geometrical optics code in the validation of single scattering experiments, the fundamental origin of the concept of the phase function lies in the theory of radiative transfer [Cha03, WY12], and here the application of the phase functions shown in figure 3.20 should be given some second thought. The notion of the phase function is introduced in the stationary 3D scalar radiative transfer equation (RTE) (3.52), given here in cartesian coordinates (x,y,z) with direction cosines (l,m,n) and substance absorptivity κ_ν and mass density ρ,

$$-\frac{1}{\kappa_\nu \rho}\begin{pmatrix} l \\ m \\ n \end{pmatrix} \cdot \nabla I_\nu(x,y,z;l,m,n) = I_\nu(x,y,z;l,m,n) - \frac{1}{4\pi}\int_0^{\pi}\int_0^{2\pi} M_{11}(\theta,\phi;\theta',\phi') \cdot I_\nu(x,y,z;\theta',\phi') \cdot sin(\theta')\, d\theta' d\phi' \qquad (3.52)$$

in order to account for anisotropic scattering in a bulk scattering medium or tissue flooded by a radiation field $I_\nu(x,y,z;l,m,n)$ of frequency $\nu = \frac{\omega}{2\pi}$. The same holds true for the Müller matrix $M(\theta)$ in the vectorial case of a radiation field consisting of particles carrying spin, such as photons (spin 1) or neutrons $\left(spin \quad \frac{1}{2}\right)$ [RH73], which can be described by the full Stokes vector [Cha03]. From equation (3.52) it is evident that it does not make sense to use the Gaussian beam incidence phase function for radiative transfer calculations at locations (x,y,z) outside the *path* of the laser beam. A naïve potential remedy for this situation may be the usage of a spatially inhomogeneous phase function $M_{11}(x,y,z;\theta,\phi;\theta',\phi')$ in the RTE (3.52), such that the phase function for Gaussian beam incidence is only used at locations where the calculated radiation intensity is still a significant fraction of the unattenuated beam intensity calculated from equation (3.35), while a phase function for plane or spherical wave incidence is used everywhere else.
Figure 3.21 shows the influence of the surface roughness model on the phasefunction of a hexagonal prismatic ice crystal. For this result, a standard deviation of $\sigma = 0.005$ has been chosen, i.e. a value on the boundary between slight and moderate roughness. As already discussed, this leads to a disappearance of the 46° halo and the glory peak.

Tetrahedron results

Scattering calculations have also been performed for a tetrahedral particle. This particle shape was chosen as an example case to demonstrate the flexibility of the geometrical optics code. A common real world substance forming such crystal shapes would be magnetite. Another similar alternative shape not calculated here would be a NaCl cubic crystal. All calculation parameters have been chosen to be identical to the case of the hexagonal prism and the edge length of the tetrahedron is identical to the side length of the hexagonal prism.

Figure 3.22 shows the computed phase functions for both parallel and perpendicular polarisation of the incident plane wave. Both polarisations give the same result. The simulation shows a shallow forward peak and halo peaks at 19° and 35° degrees.

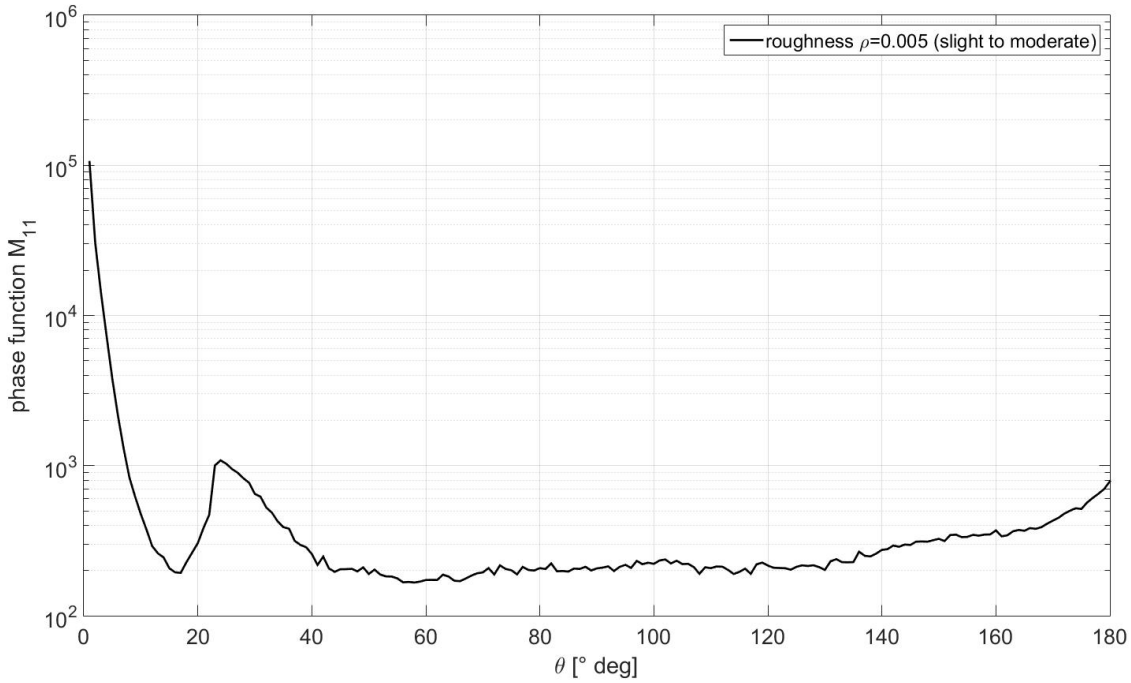

Figure 3.21: Polar phase function for a hexagonal prism with plane wave (pw) incidence and slight to moderate surface roughness ($\sigma = 0.005$). Note the absence of the 46° halo and the glory peak.

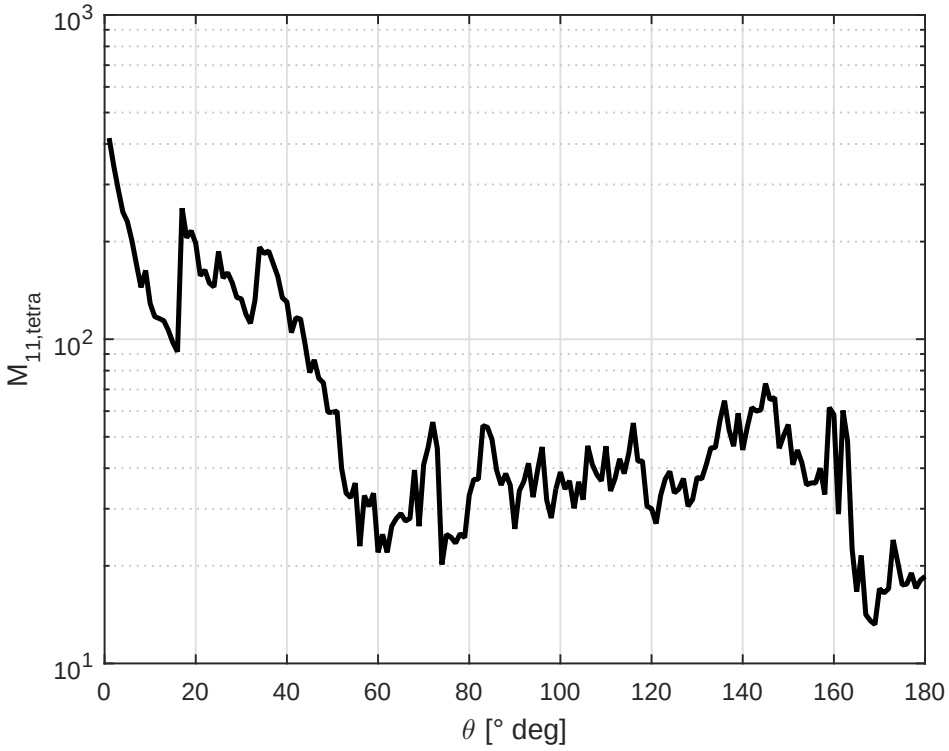

Figure 3.22: Polar phase function for a tetrahedron with plane wave (pw) incidence. Both incident polarisations give the same result.

For many real particles, the restriction of having a constant refractive index is indeed satisfied to a good approximation. Nevertheless there are also a number of cases where an inhomogeneous refractive index changes the optics of a particle. Of special interest for industrial applications are all the cases where the refractive index gradient is linked to a temperature gradient inside the particle, such as in combustion sprays [SH94] or freezing droplets. The methodology presented in this section is also applicable to metamaterials [Sha07, PSS06], which is a fairly recent discipline which nevertheless has received an enormous surge in interest due to the unusual optical phenomena realizable through metamaterials, such as cloaking devices [Leo06]. The exact relation to metamaterials will be discussed in section 6.1.

3.2.1 Hamiltonian Optics

As already discussed in section 2.4, light can be described in terms of a Hamilton function H by applying Fermat's principle of the shortest optical path. From a more rigorous point of view, this may also be seen as solving the nonlinear eikonal equation (3.10) through the application of the method of characteristics, where the light rays themselves are the characteristics. Using conventional Hamiltonian mechanics [Arn84] in the context of optics leads to the domain of Hamiltonian optics, of which a detailled outline may be found in the appendix of the book [BW99] by Born and Wolf. In practical terms there is no particular difference between the two different areas of application for the general Hamiltonian formalism. Just as in classical mechanics, the equations of motion (EOM) are written as:

$$\frac{dx_k}{dt} = \frac{\partial H}{\partial p_k} \tag{3.53}$$

$$\frac{dp_k}{dt} = -\frac{\partial H}{\partial x_k} \tag{3.54}$$

where x_k is the vector function determining the light ray trajector with the parameter t in complete analogy with the role of time in conventional mechanics. Finally p_k is the so-called *optical momentum*, distinguishable from the momentum of a point mass by its relation to the eikonal ψ:

$$\mathbf{p} = \nabla\psi \tag{3.55}$$

In a region of inhomogeneous refractive index, the Hamilton function can be brought in a form that is very favourable for numerical treatment:

$$H = \frac{1}{2}\left(\mathbf{p}^2 - n^2(\mathbf{x})\right) = 0 \tag{3.56}$$

Inserting the optical Hamilton function (3.56) into the EOMs gives the following final result:

$$\frac{d\mathbf{p}}{dt} = \frac{1}{2}\nabla n^2(\mathbf{x}) \tag{3.57}$$

$$\frac{d\mathbf{x}}{dt} = \mathbf{p} \tag{3.58}$$

Equations (3.57) and (3.58) form a set of coupled first order ordinary differential equations (ODEs), which can be solved analytically for a large number of specific refractive index distributions $n(\mathbf{x})$ of which a large selection can be found in the literature [Cor83, KO90, BW99]. An example of renewed interest in the scattering community is the *Lüneburg lens* refractive index distribution, which was named after its inventor Rudolf Karl Lüneburg [Lün64] and is similar in effect to the well known fish eye lens of Maxwell [Max54]. Lock has proposed that the future may see particles with a specifically tailored refractive index distribution in order to produce unconventional optical effects. The Lüneburg lens has the following refractive index distribution:

$$n(r) = \sqrt{2 - \left(\frac{r}{R}\right)^2} \tag{3.59}$$

where $r < R$ is the radial coordinate in a polar coordinate system and R is the radius of the entire lens. The refractive index given by this equation (3.59) is illustrated in figure 3.59 over the radial coordinate. This type of refractive index

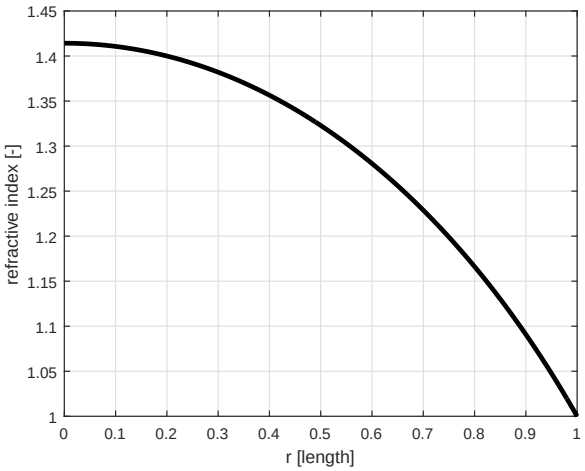

Figure 3.23: Lüneburg's refractive index distribution for a perfect lens.

distribution has recieved renewed attention in the light scattering community due to the work of Lock et al. in 2014. His combined Ray tracing [LLA14b] and FDTD study [LLA14a] revealed several unforeseen properties of such particles, including novel morphology dependent resonances (MDRs) which are distinct from the ones in the homogeneous case [Joh93] discussed by Johnson.
As already indicated, a completely general refractive index distribution and especially the combination between a continously and a discontinously varying refractive index necessitates the usage of numerical solution methods. As the set of equations (3.57) and (3.58) is a set of ODEs, it can be used by one of the standard ODE solver methods described for instance in [DR08] and in greater detail by Bulirsch and Stoer [SB05]. Besides powerful existing libraries for the numerical solution of ODEs, such as boost odeint [Ahn12b], the implementation of an ODE solver class and corresponding classes allows the usage of several advanced programming concepts in the programming language C++ and thus a short digression on the implementation aspects of such a solver shall follow here.

3.2.2 Efficient and Concise Implementation of an ODE solver in C++

An implementation of an ODE solver in C++ can be divided in two parts. First, the implementation of the solver class itself, and second, the implementation of the right hand side (RHS) function of an ODE. Generally, the solver should be able to deliver an output for differential equations of the following general form:

$$\frac{d\mathbf{x}(t)}{dt} = RHS(\mathbf{x}(t)), \quad \mathbf{x}(t_0) = \mathbf{x}_0 \tag{3.60}$$

where RHS is an arbitrary function of $\mathbf{x}(t)$, t the independent variable and $\mathbf{x}(t)$ an object of an arbitrary class for which a sufficient algebra has been defined a priori, such as `float`, `std::complex<float>`, and more exotic types such as `::boost::math::quaternion<float>`. The current implementation of the ODE solver library was written during a bachelor thesis [Deg14] by M. Degenhardt and the implemented numerical schemes are listed in table 3.5 according to their category.

Explicit	Implicit	Symplectic
explicit Euler's (1^{st} order consistency and convergence)	Implicit Euler's	Symplectic Euler's
classical Runge-Kutta (4^{th} order, RK4)		Verlet
Dormand-Prince ($4^{th}/5^{th}$ order RKDP5(4))		Leapfrog
Fehlberg ($7^{th}/8^{th}$ order)		

Table 3.5: ODE solver schemes implemented in the SLA ODE solver library as of August 2015.

A definition of the conventional Runge-Kutta methods can be found for instance in Bulirsch/Stoer [SB05] while an introduction to symplectic methods can be found in the articles [PF96, For06] by Forest et al. . Fourth and higher order symplectic integrators exist, such as the one published by Ruth in the manuscript [FR90], but are not yet part of the library as of August 2015. The Dormand-Prince method was published in the article [DP80] by the name-giving pair of

authors while the Fehlberg method was published in the technical report [Feh68], again by Fehlberg himself.
The unusual implementation of symplectic methods in the library shall also be explained here shortly. A symplectic numerical integrator preserves the symplecticity [Arn84] of the system of equations, i.e. it conserves the phase space volume $dx \wedge dp$ of the two canonical variables position x and momentum p. As this translates into longterm stability of the ODE solution, such solvers are of particular interest in the design of particle accelerators [For06], in celestial mechanics [GDC91, Ahn12a] and astrodynamics or molecular dynamics [GKZC04]. In order to reap the benefits of a symplectic integrator, the Hamilton function of a dynamical system nevertheless needs to be separable [PF96] for the most common types of symplectic integrators in the sense that there are no mixed terms of conjugate variables.

$$H(x,p) = V(x) + T(p) \tag{3.61}$$

It becomes obvious that $V(x)$ is a generalized potential energy and likewise $T(p)$ a generalized kinetic energy, in order for the Hamilton function to represent the sum total of the energy of the dynamical system. Incidently, the optical Hamilton function (3.56) has exactly this form with the refractive index distribution $n(\mathbf{x})$ playing the role of the potential and the symplectic integrators may consequently be applied to ray-optical problems.

Integration scheme inheritance

Both explicit Runge-Kutta schemes and symplectic integrators may be defined by specifying a set of coefficients, which is the well known *Butcher array* [SB05] in the Runge-Kutta case and the behaviour of all the numerical integrators is identical, inasmuch as they transform an input value x_n at timestep n into a new value x_{n+1} at $n+1$. Thus in a similar vein to the geometrical transformations of section 3.1.4, an abstract integrator base class can be formulated, from which the derived classes recieve a Butcher array, such that implementing a new ODE solver scheme only means creating a new specialisation of the Butcher array and not writing an entire new class or function. Unfortunately, the intrinsic sequential nature of the ODE integration makes it impossible to reduce the computation time of a single integration sequence through parallelization, as the computation of the value x_{n+1} requires the prior sequential execution of all integration steps up to the value x_n.

Right hand side function implementation

In the second paragraph on the subject, the efficient implementation of the RHS function will be discussed. A common approach for passing a certain computational function to another function, method or subroutine is to use a function pointer, which is a perfectly valid approach in languages such as C99 or Fortran 95 to 2008. A more advanced technique is nevertheless made possible due to the object-orientedness of C++. It becomes possible to define a mathematical function as a *Function Object* or *Functor* in C++, which is a class having an overloaded input operator `()`, as detailed in reference [BN94]. An example class implementing the right hand side function leading to a harmonic oscillator solution may look like this:

```
1   template <class T>
2   class harm_osc {
3           double m_gam;
4   public:
5           harm_osc( double gam ) : m_gam(gam) { }
6
7           void operator() (const std::vector<T> &x, std::vector<T> &dxdt, const T /* t */)
8           {
9                   dxdt[0] = x[1];
10                  dxdt[1] = -x[0] - m_gam*x[1];
11          }
12  };
```

While decreasing the readability of the source code, using functors nevertheless provides the programmer with two important advantages. First, the functor may be passed and treated as conveniently as any other object. In practice, this simplifies programming an ODE solver greatly, as the programmer is spared having to deal with pointers. Second, the compiler recieves a complete object with the functor, including information on the input and return data types, which allows the compiler to perform a better optimization of the code, increasing the execution speed of the final binary. This is in contrast to the function pointer, where the compiler only recieves a pointer forwarding the memory location of the function. A functor is a functional programming concept and due to the general increase of functional programming

concepts in all major programming languages, the current C++14 standard [Str] allows the usage of further functional concepts. For instance, it becomes possible to define a function as a lambda and then converting it to a functor via the `std::functional<class T>` library as exemplified below:

```
1       #include <functional>
2       #include <iostream>
3               ...
4               // store a lambda
5   std::function<void> harm_osc = [](  const state_type &x, state_type &dxdt, double t) {dxdt[0] =
        x[1]; dxdt[1] = -x[0] - gam*x[1]; };
6   harm_osc(q,p,t);
```

A final increase in performance and accuracy is possible by applying *Automatic Differentiation*, which is discussed in the book [BN94]. This is due to the fact that the EOM (3.57) contains not the refractive index distribution, but its gradient. In simple cases, this gradient may be calculated by hand, while for complex cases a finite difference approximation may be used. Nevertheless it is also possible for the computer to calculate the gradient exactly. As long as the refractive index distribution is made up of operators for which derivatives exist, such as `+`, `sin()` or `exp()`, the complete derivative can be calculated by applying the known rules of differentiation to create a parse tree of the derivate. This technique has been implemented in the `RallNo` class as part of the ODE solver work package of this thesis.

Ray Tracing Sample Solutions

This paragraph shows light ray curves for a sample case with a radial Gaussian refractive index distribution as follows:

$$n(x,y) = A \cdot exp\left(-\frac{(x^2+x^2)}{2 \cdot B}\right) \tag{3.62}$$

Where A and B are to real constants and x and y are the coordinates along the $\hat{\mathbf{x}}$ and $\hat{\mathbf{y}}$ axes. Numerical investigations have shown that qualitatively, two different outcomes can be distinguished. The first case is the one in which a light ray is simply deviated from its course, which would be a straight line in a completely homogeneous region of space. According to Hecht [Hec02], this provides a real world example for phenomena such as the well known *mirages*, and through a slightly different mathematical formulation also for gravitational lensing [Hec02, Fli12a, Ein36]. This case is illustrated in figure 3.24.

The second case is that in which, due to a specific choice of ray starting parameters or refractive index distribution, the light rays are trapped on a spatially bounded orbit. In this situation, the refractive index distribution effectively behaves like a black hole as described for instance by Landau & Lifshitz, forming an event horizon below which the light rays are trapped. This phenomenon also occurs for the aforementioned Lüneburg lens particle investigated by Lock et al. [LLA14b] but does not lead to an event horizon in the case of optical scattering. In reality, morphology dependent resonances (MDRs) will be observed in scattering experiments under such cirumstances. A wave-optical analysis [Joh93] then shows that the apparent violation of energy consevation is resolved through a process akin to quantum mechanical tunneling [LBCTL13], as the electromagnetic energy trapped inside the particle leaks through the potential barrier formed by the refractive index distribution of the particle. A particularly aesthetic trapped orbit exhibiting a floral pattern is shown as an example case, again for the Gaussian refractive index distribution in figure 3.25.

Finally it is also possible to determine the distortion of a structured background by the inhomogeneous refractive index distribution. A sample result is shown in figure 3.26. In this figure, a background plane shown in subfigure 3.26a structured by a division in a red and a green half was chosen as the starting plane, such that each pixel of the background was the starting point of a light ray. The light rays were then deviated by a Gaussian refractive index profile, identical to the situation shown in figure 3.24, but this time in 3D. The skew rays then were captured on an image plane parallel to the background plane after they had passed the Gaussian distribution. The resulting image is shown in subfigure 3.26b. Therein, a number of pixels remain black, as no light rays arive at the corresponding location anymore, but it can also be seen that the primary effect of the Gaussian distribution symmetric about the origin is an inversion of the background pattern which is similarly symmetric.

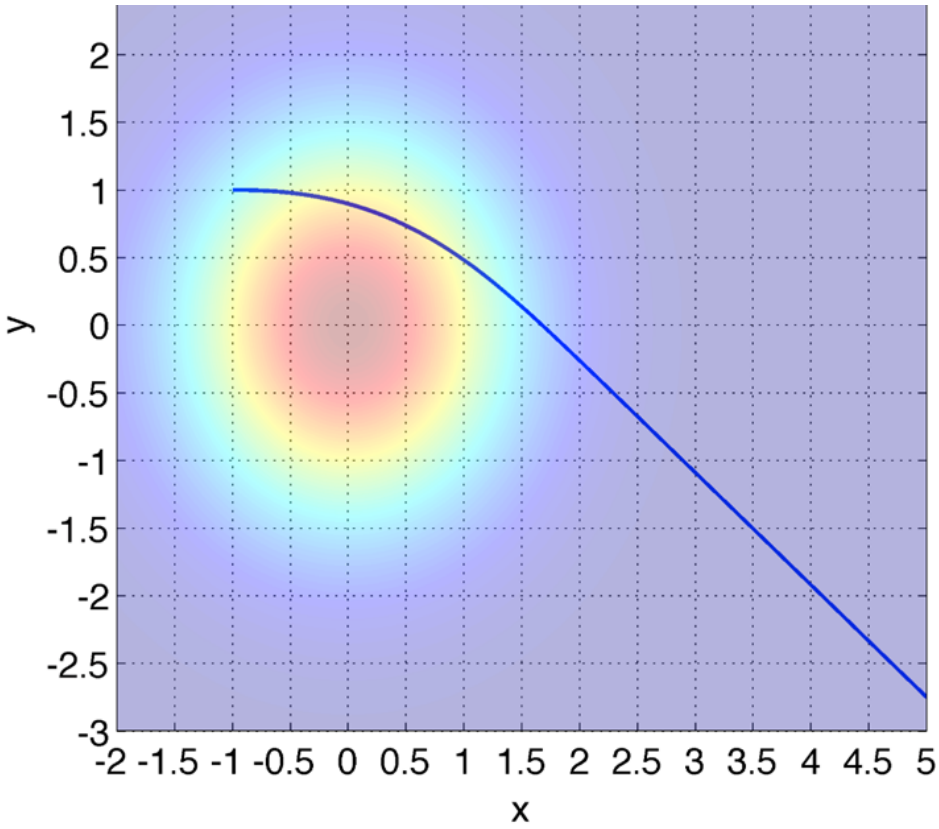

Figure 3.24: Ray curve in coordinate space deviated from its straight propagation by an inhomogeneous refractive index distribution.

3.2.3 Particles with discontinuities

In this paragraph, the treatment of particles with discontinuities in the refractive index will be discussed. An example for a particle with both an inhomogeneous and sharply bounded and thus discontinuous refractive index would be any particle having internal density or structure variations while still forming a sharp interface towards its surroundings. A concrete example would be a freezing droplet containing both liquid water and solid ice. The methodology of the previous section 3.2 may not be applied anymore under such circumstances, despite its convenience. This is due to the fact that at a discontinuous interface, the light ray is reflected and refracted at the same time and there is not one unique ray anymore. The greatest difficulty in treating discontinuities is to find them, that is, to find the ray parameter τ at which a light ray encounters the particle surface assumed to be discontinuous, in order to terminate the ray segment and create two new segments which become reflected and refracted, respectively. During the thesis of Degenhardt, two approaches have been considered in order to find the intersection point between ray and discontinuity as precisely as possible.

Step-back approach

The first approach, coined the step-back approach is very simple, as it does not need any extension of the previous ODE solver mechanism for the light rays. An intersection check for a straight ray segment must be given and the ray segments between each ODE solution step are assumed to be piece-wise straight. At each iteration of the ODE solver, the program must check whether the interface has already been passed by the ray while iterating. If this is true, the previous step of the curved ray is resumed and the iteration step is carried out again, but this time with a reduced step size. This process is repeated until a desired accuracy is reached, where the final intersection point is approximated by performing an intersection check between the particle surface and the piecewise straight ray segment between the last iteration point still inside the particle and the first iteration point directly outside the particle. A sample result is shown in figure 3.27. It can be seen that the intersection point between the curved light ray is indeed very well approximated.

While this method is easy to implement and has been shown to work reliably, it nevertheless has computational drawbacks. In order to approximate the intersection point for a given accuracy, the stepsize of the ODE integrator needs to

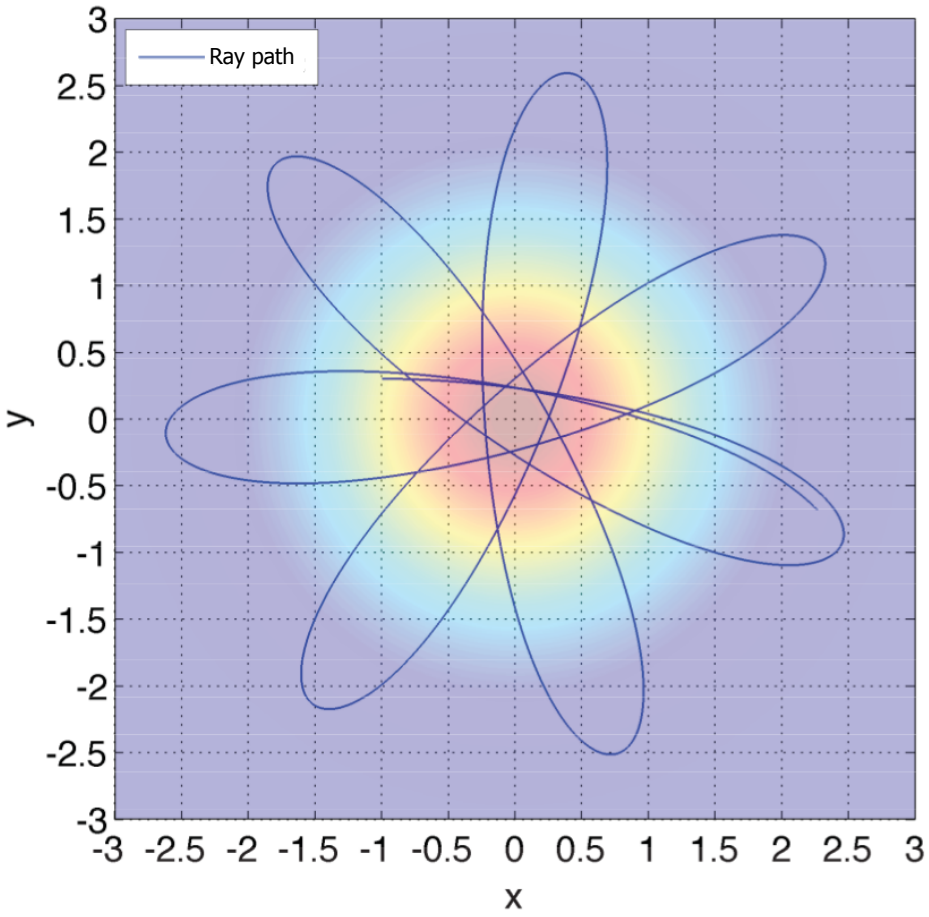

Figure 3.25: Trapped orbit of a light ray around the center of a radially symmetric inhomogeneity.

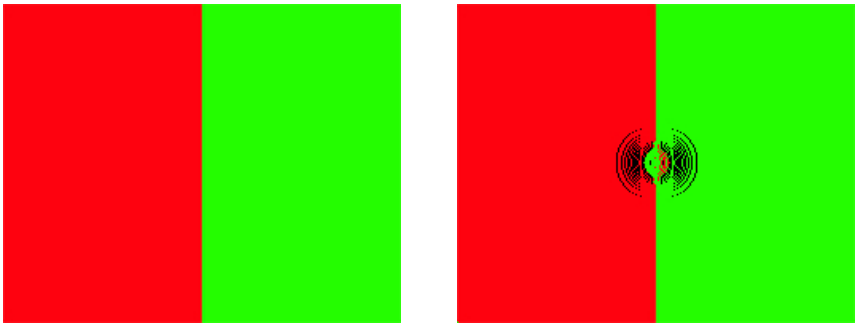

(a) Structured background **(b)** Distorted image in the image plane

Figure 3.26: Distortion of a structured background in red and green (left) by a Gaussian refractive index distribution (right).

be made ever smaller. As carrying out the ODE integration requires a certain number of operations, this may become computationally expensive if the desired accuracy is to small. While this is of no concern for a single ray alone, the calculation of the light scattering behaviour of a particle requires a very large number of individual rays. As a response to this, a second method has been developed and implemented.

Interpolation approach

While technically the first approach is a linear interpolation method too, the second algorithm was coined as such as the interpolation is carried out here in a more sophisticated manner. As the ODE solver not only provides the position $\mathbf{x}$ of a light ray, but also the first derivative of the curve in terms of the momentum $\mathbf{p}$ this additional information can be

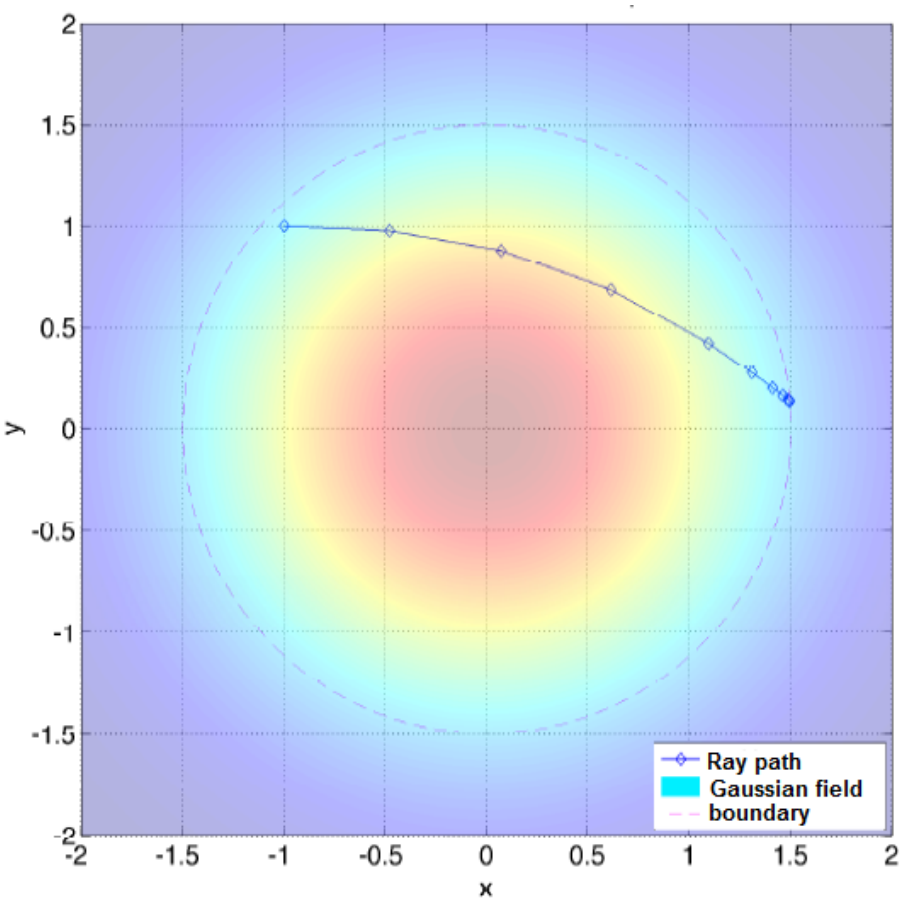

Figure 3.27: Intersection between a curved light ray and an arbitrary imposed particle boundary (dashed circle).

exploited to perform an interpolation with a cubic Hermite spline between the last point in the particle x_n and the first point outside x_{n+1}. In two dimensions this spline is defined as [DR08, PTVF95]:

$$x(s) = b_0 \cdot x_n + b_1 \cdot x_{n+1} + b_2 \cdot p_{x,n} + b_3 \cdot p_{x,n+1} \tag{3.63a}$$
$$y(s) = b_0 \cdot y_n + b_1 \cdot y_{n+1} + b_2 \cdot p_{y,n} + b_3 \cdot p_{y,n+1} \tag{3.63b}$$

where $s \in [0,1]$ is the curve parameter of the spline and the p's are the components of the momentum vector. The coefficients of the spline function or *blending functions* are given by:

$$b_0 = 2s^3 - 3s^2 + 1 \tag{3.64a}$$
$$b_1 = -2s^3 + 3s^2 \tag{3.64b}$$
$$b_2 = s^3 - 2s^2 + s \tag{3.64c}$$
$$b_3 = s^3 - s^2 \tag{3.64d}$$

In order to find the intersection point between a surface and a light ray one then needs to find the value of the parameter s somewhere between 0 and 1 for which the corresponding point $\mathbf{x}(s)$ fulfills both the Hermite spline function **and** the function defining the surface of the particle. For a circular scatterer for instance, one only needs to express the implicit surface function in terms of the spline parameter s by inserting equations (3.63):

$$F(s) = x^2(s) + y^2(s) - r^2 = 0 \tag{3.65}$$

which results in a nonlinear implicit equation for s. This situation is illustrated in figure 3.28. The method of choice for finding the desired parameter value is the Newton-Raphson method [Sto05, DR08] which iteratively approximates the parameter $s_{intersect}$ as follows:

$$s_{n+1} = s_n - \frac{F(s)}{\dot{F}(s)} \tag{3.66}$$

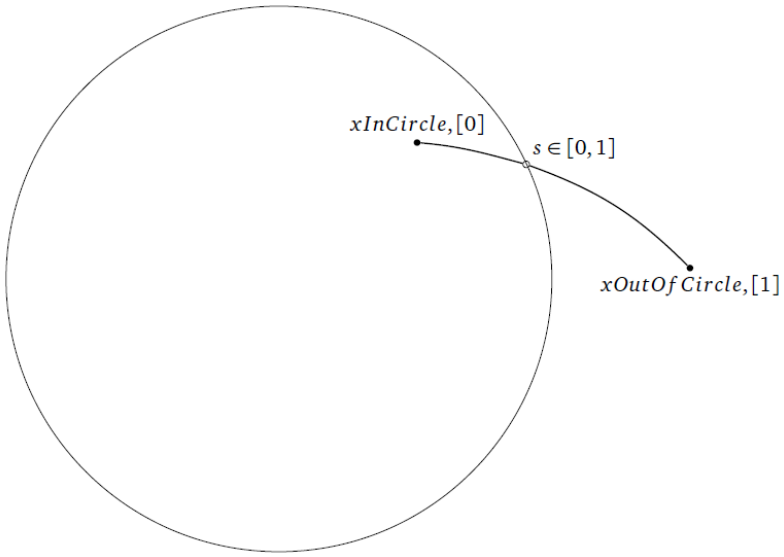

Figure 3.28: Explanatory sketch of the relation between the Hermite spline and the particle surface.

where $\dot{F}(s)$ is the derivative of $F(s)$ with respect to s. For the circular case the still needed derivative of equation (3.65) then is a matter of simple calculus:

$$\dot{F}(s) = 2x(s)\dot{x}(s) + 2y(s)\dot{y}(s) \tag{3.67}$$

where the first order spline derivatives are:

$$\dot{x}(s) = \dot{b}_0 \cdot x_n + \dot{b}_1 \cdot x_{n+1} + \dot{b}_2 \cdot p_{x,n} + \dot{b}_3 \cdot p_{x,n+1} \tag{3.68a}$$
$$\dot{y}(s) = \dot{b}_0 \cdot y_n + \dot{b}_1 \cdot y_{n+1} + \dot{b}_2 \cdot p_{y,n} + \dot{b}_3 \cdot p_{y,n+1} \tag{3.68b}$$

with the first order derivatives of the coefficients are:

$$\dot{b}_0 = 6s^2 - 6s \tag{3.69a}$$
$$\dot{b}_1 = -6s^2 + 6s \tag{3.69b}$$
$$\dot{b}_2 = 3s^2 - 4s + 1 \tag{3.69c}$$
$$\dot{b}_3 = 6s - 2s \tag{3.69d}$$

A sample result obtained using the interpolation approach is shown in figure 3.29 for the special case of a circular scatterer with a Gaussian refractive index profile inside. Again, the intersection point between the ray and the particle shell is found. As no additional refinement of the stepsize is needed in order to capture the intersection point with sufficient accuracy, this method is expected to work faster as the first one.

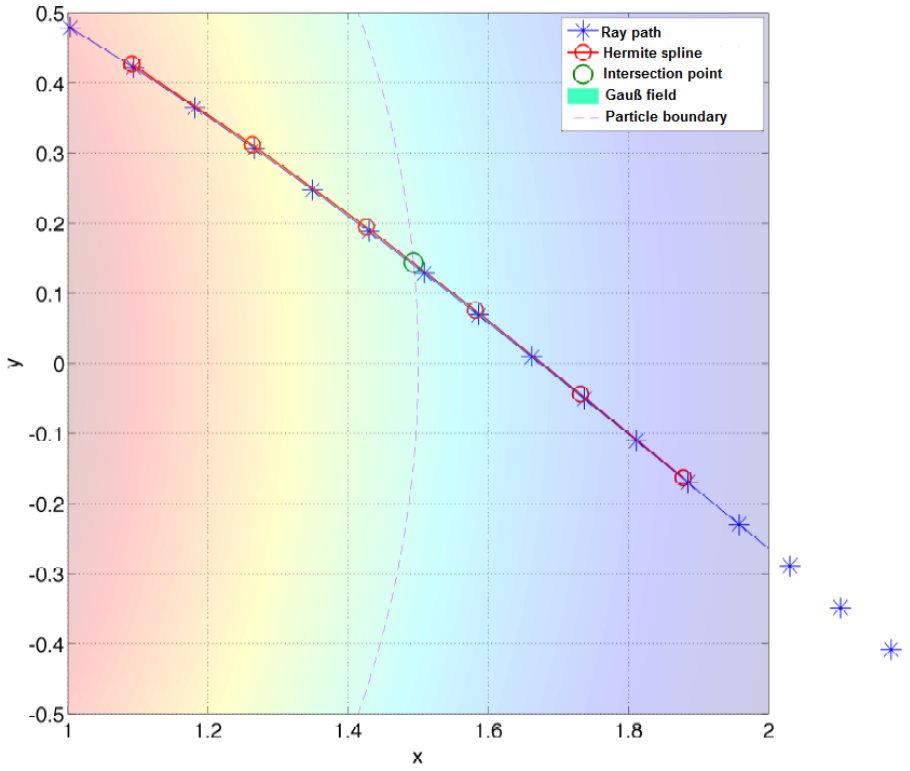

Figure 3.29: Hermite spline intersecting circular partice shell

3.3 FIT: Finite Integration Technique

The development of the finite integration technique (FIT) for the solution of Maxwell's equations started in 1977 with the first publication [Wei77] of Thomas Weiland. In this publication, a discrete integral formulation was applied to the time-harmonic form of Maxwell's equations. This approach is conceptually similar to the Finite Volume Method used in CFD, inasmuch as an integral formulation of a problem is solved in a discretised space. Nevertheless the FIT does not include a flux balance. Later, the approach was broadened to include time-dependent problems and several comprehensive explanations on the technique can be found in the articles [Wei96] and [Wei84b] by Weiland himself. The final method as it is used today is numerically equivalent to the more commonly used Finite-Difference-Time-Domain (FDTD) method originally proposed by Yee in 1966 [Yee66]. Initially, the finite integration technique was mainly used in the design of particle accelerator components, for instance at the *Deutsches Elektronen-Synchrotron* (DESY) [Wei84a] and later at the *Gesellschaft für Schwerionenforschung* (GSI) as part of the research at the *Theorie Elektromagnetischer Felder* (TEMF) institute. As the method serves to find approximate solutions for the full Maxwell equations, it is nonetheless not limited to any specific area of application and can be applied to a wide variety of tasks. Besides particle accelerator components, this includes the design of electronic circuits, electro- and magnetostatic problems, antenna systems, metamaterials [CST15] and also the interaction of electromagnetic fields with human tissue through the commercially developed HUGO model investigated at the TEMF institute in a series of Ph.D. theses [Bar07, Gao12, GBC+02].

3.3.1 Discretisation of Maxwell's Equations and Yee's dual grid

Starting from the integral formulation of Maxwell's equations as given for instance in the reference [Som64], a direct correspondance is given between the continuum and the FIT grid equations. As pointed out by Weiland in the article [Wei96], these equations are still exact on the grid. Often the discretized FIT equations are called Maxwell's grid equations (abbreviated as MGE).

continuum form	explanation	topological relations
$\iint\limits_A -\frac{\partial}{\partial t}\mathbf{B}\cdot d\mathbf{A} = \oint\limits_{\partial A}\mathbf{E}\cdot d\mathbf{r}$	Faraday's induction law	$\mathbf{C}\,\mathbf{e} = -\frac{\partial}{\partial t}\tilde{\mathbf{b}}$
$\iint\limits_{\partial V}\mathbf{B}\cdot d\mathbf{A} = 0$	Gauß' law for magnetism	$\mathbf{S}\,\tilde{\mathbf{b}} = 0$
$\iint\limits_A \left(\mathbf{J}+\frac{\partial}{\partial t}\mathbf{D}\right)\cdot d\tilde{\mathbf{A}} = \oint\limits_{\partial A}\mathbf{H}\cdot d\mathbf{r}$	Ampère's law	$\tilde{\mathbf{C}}\,\mathbf{h} = \frac{\partial}{\partial t}\tilde{\mathbf{d}}+\tilde{\mathbf{j}}$
$\iint\limits_{\partial \tilde{V}}\mathbf{D}\cdot d\tilde{\mathbf{A}} = \iiint\limits_{\tilde{V}}\rho d\tilde{V}$	Gauß' law	$\tilde{\mathbf{S}}\,\tilde{\mathbf{d}} = q$
continuum form	**explanation**	**constitutive relations**
$\mathbf{D} = \varepsilon\mathbf{E}$	electric constitutive relation	$\mathbf{d} = \mathbf{D}_\varepsilon\mathbf{e}$
$\mathbf{B} = \mu\mathbf{H}$	magnetic constitutive relation	$\mathbf{b} = \mathbf{D}_\mu\mathbf{h}$
$\mathbf{J}_L = \kappa\mathbf{E}$	conduction constitutive relation	$\mathbf{j}_L = D_\kappa\mathbf{e}$

Table 3.6: Maxwell's grid equations with the ternary matrices **C** and **S** being representations of the discrete curl $\nabla\times$ and divergence $\nabla\cdot$ operator respectively on the staggered grid shown in figure 3.31. The first four FIT MGEs are exact topological relations, while the constitutive relations account for the influence of the material geometry.

Spatial Discretisation

The MGE as defined in reference [Wei96] are defined on a grid doublet $\{G,\tilde{G}\}$ contained in the solution volume $\Omega\in\mathbb{R}^3$ which needs to be simply connected. The allocation of the magnetic flux density components is done on the so-called *dual* or *magnetic* grid $\tilde{G}$ shifted away in space from the primary or *electric* grid G on which the electric field components are calculated. The distance of the shift is exactly $\left[\frac{\Delta x}{2},\frac{\Delta y}{2},\frac{\Delta z}{2}\right]$, i.e. half the grid spacing in each of the three spatial dimensions for a Cartesian grid. All quantities calculated on the dual grid $\tilde{G}$ are henceforth marked by a tilde. The equations shown on the continuum side are of course equivalent to the differential formulation (2.33) in the continuous differntiable case. This grid in its two-dimensional form is shown in figure 3.30, while the three-dimensional form is shown in figure 3.31. Such a staggered grid arrangement was first proposed by Yee [Yee66] for the FDTD method and ensures second order accuracy in conjunction with the applied discretisation scheme by preserving the interdependent relationship between electric and magnetic field quantities [Ged11]. The numerical scheme would not be second order if the same discretisation would be applied to an unstaggered grid. While in principle there is no obstacle towards applying the FIT to an arbitrary grid [Wei84a, Wei84b], the most common implementation today is still the basic uniform rectangular and cubic lattice shown in figures 3.30 and 3.31. A single cubic cell of a FIT mesh must contain six faces and twelve edges for variable allocation in total, whether it is a cell of the primary or dual grid. Figure 3.30 illustrates how the finite integration technique (FIT) is succesfully applied to Maxwell's equations.

Following the explanation of Weiland in reference [Wei84b], the midpoint quadrature rule [DR08] is used to find an approximation of Faraday's equation for the electric and magnetic fields in a single cell of the lattice in figure 3.30.

$$\int\limits_{x_0}^{x_0+\Delta x} f(x)\,dx = \Delta x\cdot f\left(x+\frac{\Delta x}{2}\right)+\mathcal{O}\left(\Delta x^2\right) \tag{3.70}$$

where Δx is the grid spacing of the mesh as indicated in figure 3.30 and $f(x)$ is an arbitrary function of the independent spatial coordinate x. The right-hand side of Faraday's law as written in table 3.6 may then be approximated by the following expression.

$$\oint\limits_{\text{(cell face edges)}}\mathbf{E}\cdot d\mathbf{s} = E_1\cdot\Delta x+E_2\cdot\Delta x-E_3\cdot\Delta x-E_4\cdot\Delta x+\mathcal{O}\left(\Delta x^2\right) \tag{3.71}$$

While the surface integral on the right-hand side is likewise approximated.

$$\iint\limits_{\text{(cell face)}}\frac{\partial}{\partial t}\mathbf{B}\cdot d\mathbf{A} = \Delta x^2\cdot\dot{\mathbf{B}}+\mathcal{O}\left(\Delta x^4\right) \tag{3.72}$$

It is noteworthy to recognize that up to this point relations (3.71) and (3.72) are still exact on the domain $\{G,\tilde{G}\}$ shown in figures 3.30 or 3.31, as the application of the midpoint quadrature rule corresponds to the introduction of

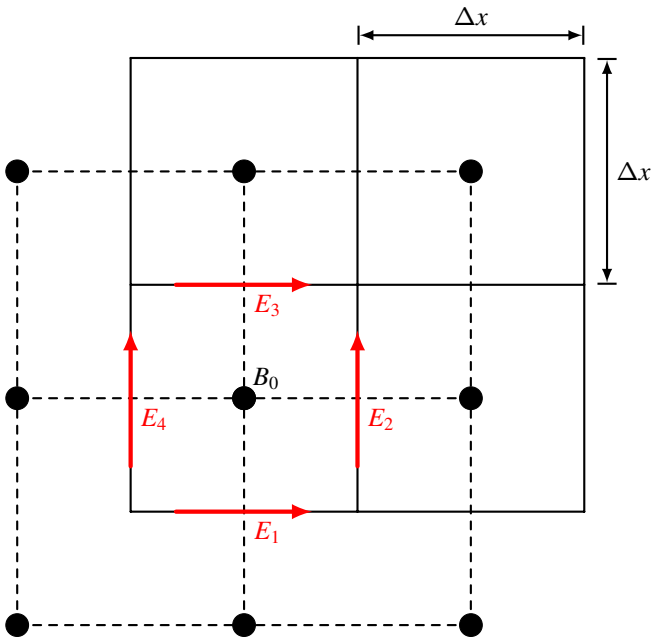

Figure 3.30: Sketch of Yee's dual grid in 2D with primary grid G in full and the dual grid $\tilde{G}$ as the dashed lines.

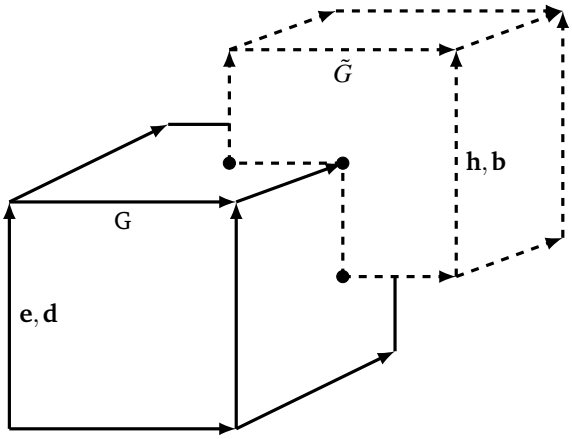

Figure 3.31: Structured dual grid cells for FDTD and FIT calculations first proposed by Yee.

a discrete numerical grid. The MGE found in table 3.6 are topological relations and thus are always exactly fulfilled. The approximation arises by specifing a discrete matrix representation of the div- and curl-operators in the MGE, all the while looking for a solution of the continuous Maxwell's equations. Thus also comes the moniker *Topological Maxwell's Equations*. Discretizing all other continuum Maxwell's equations then leads the set of matrix equations in the right column of table 3.6 for the unknown grid voltages and currents. Due to the integral approach, the actual variables used for book-keeping are the integrated fields, i.e. the voltage along a grid line L_i:

$$e_i = \int_{L_i} \mathbf{E} \cdot d\mathbf{s} \tag{3.73}$$

and the magnetic flux for the area A_i:

$$b_i = \iint_{A_i} \mathbf{B} \cdot d\mathbf{A} \tag{3.74}$$

both of which are collected in vectors $\mathbf{e}$ and $\mathbf{b}$, such that the semidiscrete form of Faraday's law finally reads:

$$c_{ik} e_k = -\frac{\partial b_i}{\partial t} \tag{3.75}$$

Along the same lines, the matrix relations in table 3.6 are derived for the remaining quantities magnetic voltage h_i, electric flux d_i and currents i_i.

Symplectic Time Discretisation

The (according to Gedney [Ged11]) widely preferred ODE integration method for solving the initial value problem posed by the time dependent Maxwell equations is the symplectic leapfrog scheme (i.e. replacing all time derivatives with central differences) already introduced in section 3.2 both for FDTD and FIT calculations. The time stepping for a time discretisation $f(t),\ t \in [t_0, t_N] \rightarrow f(t_n),\ t_n \in [t_0, t_N],\ n = 0, \ldots N$ at time step t_n then is conducted as follows:

$$\mathbf{b}_{n+1} = \mathbf{b}_n + \Delta t \mathbf{C}\mathbf{e}_{i+\frac{1}{2}} \tag{3.76a}$$

$$\mathbf{e}_{n+\frac{3}{2}} = \mathbf{e}_{n+\frac{1}{2}} + \Delta t \mathbf{D}_{\varepsilon}^{-1} \left(\tilde{\mathbf{C}} \mathbf{D}_{\mu}^{-1} \mathbf{b}_{n+1} - \mathbf{j}_{n+1} \right) \tag{3.76b}$$

Equation (3.76) again reflects the reciprocal interdependance of electric and magnetic fields on the discrete grid. Weiland recognizes in [Wei84b] that using the leapfrog method in conjunction with a FIT approach on a regular cartesian grid completes the equivalence with the classical Yee FDTD scheme published in [Yee66]. For further clarification, a simple 1D FDTD implementation in python may be found by the interested reader in the appendix of this thesis. While there is no canonical position or momentum in Maxwell's equations as such, the symplecticity is nevertheless preserved for the variables **E** and **B**, such that the phase space area $de \wedge db$ is conserved. In more mathematical terms, the phase space area is the so-called *symplectic structure* of an (even-dimensional) differential manifold as defined by Arnol'd [Arn84]. For the case of Hamiltonian mechanics, the differential structure would be the differential 2-form $dp \wedge dq$. The symplecticity of the time integration further ensures that, while the scheme is not unitary and the energy of the electromagnetic field consequently not conserved as explained in section 2.1.3, it is still bounded from above and below. Following Schuhmann [SW01], the semidiscrete MGE applied to a grid conserve a discrete analogon to the continuous electromagnetic energy (2.37) exactly.

$$W(t) = W_e(t) + W_m(t) = \frac{1}{2} \left(\mathbf{e}^T(t) \tilde{\mathbf{d}}(t) + \mathbf{h}^T(t) \tilde{\mathbf{b}} \right) \tag{3.77}$$

As the symplectic time integrator still does conserve the symplectic structure $de \wedge db$ of the problem, it is possible to define a modified electromagnetic energy, which is given in [GLS$^+$06].

$$W_{mod} = \frac{1}{2} \left(\tilde{\mathbf{e}}^T \tilde{\mathbf{e}} + \tilde{\mathbf{h}}^T \tilde{\mathbf{h}} \right) + \frac{\Delta t}{2} \cdot \tilde{\mathbf{h}}^T \tilde{\mathbf{C}}^T \tilde{\mathbf{e}} \tag{3.78}$$

This modified energy is conserved exactly by the symplectic integrator.

Stability

The leapfrog scheme is explicit and thus the FIT was shown by Weiland [Wei84b] to be stable only if the Courant-Friedrichs-Lewy number CFL fulfills the following condition in the one-dimensional case.

$$CFL = \frac{c\ \Delta t}{\Delta x} < 1 \tag{3.79}$$

If the CFL condition is fulfilled, the energy (3.78) of a FIT solution for a closed problem stays constant and the scheme is thus numerically stable. As for the continuum equations natural scales can be defined for which $CFL = 1$, the continuum dispersion relation is not satisfied by the FIT and FDTD method [Ged11], which is problematic in relativistic particle accelerator applications. According to Gjonaj et al. [LGW05], this can partly be remedied through the application of split-operator techniques. These techniques allow to construct modified numerical schemes with anisotropic numerical dispersion. In particular, it is possible to minimize or even eliminate numerical dispersion errors along a given propagation direction.

3.3.2 Time Domain Considerations

At first, the notion of reducing the computational cost of a finite difference problem by adding a dimension seems puzzling. In fact, there is no reduction of computational cost. As the original frequency domain problem is solved as a time domain calculation, the numerical representation as a boundary value problem is exchanged towards an initial value problem. Thus, instead of solving an extremely large and sparse system of equations in order to solver the 3D Helmholtz equation, a leap-frog computation needs to be performed for each physical grid point in order to solve the full 4D Maxwell's equations. Thus, the memory requirement for the large sparse matrix in the Finite Difference scheme

is traded for an increase in computational time in the Finite Difference Time Domain scheme, true to the principle that '*there ain't no such thing as a free lunch*'. A further, and for specific problems more important advantage of a time domain calculation is that it furnishes the solution for all frequencies. This is in contrast to the Helmholtz equation, where the response of the system for only one specific frequency is determined. For all time domain calulations, the standard Gaussian signal has been chosen as an excitation source to pass the calculation domain. The signal is shown in figure 3.32 and the definition of the signal as one possible excitation amongst many is given by Gedney [Ged11].

$$g(t) = e^{-\frac{(t-t_0)^2}{t_w}} \tag{3.80}$$

where t_0 is the start delay of the signal and t_w its corresponding half width. The frequency content of the pulse is also given by Gedney.

$$\mathscr{F}(g(t)) = G(f) = t_w\sqrt{\pi}e^{-(\pi f)^2 t_w^2}e^{-i2\pi f t_0} \tag{3.81}$$

The signal in equation (3.81) has its energy maximum at a frequency of 0 Hertz, which needs to be shifted to the frequency of interest, such that the energy peak corresponds to the wave length $\lambda = \frac{c}{f}$ of the incident light, since the time-harmonic field result is obtained from the time domain calculation via a Fourier transformation $\mathscr{F}$. In order

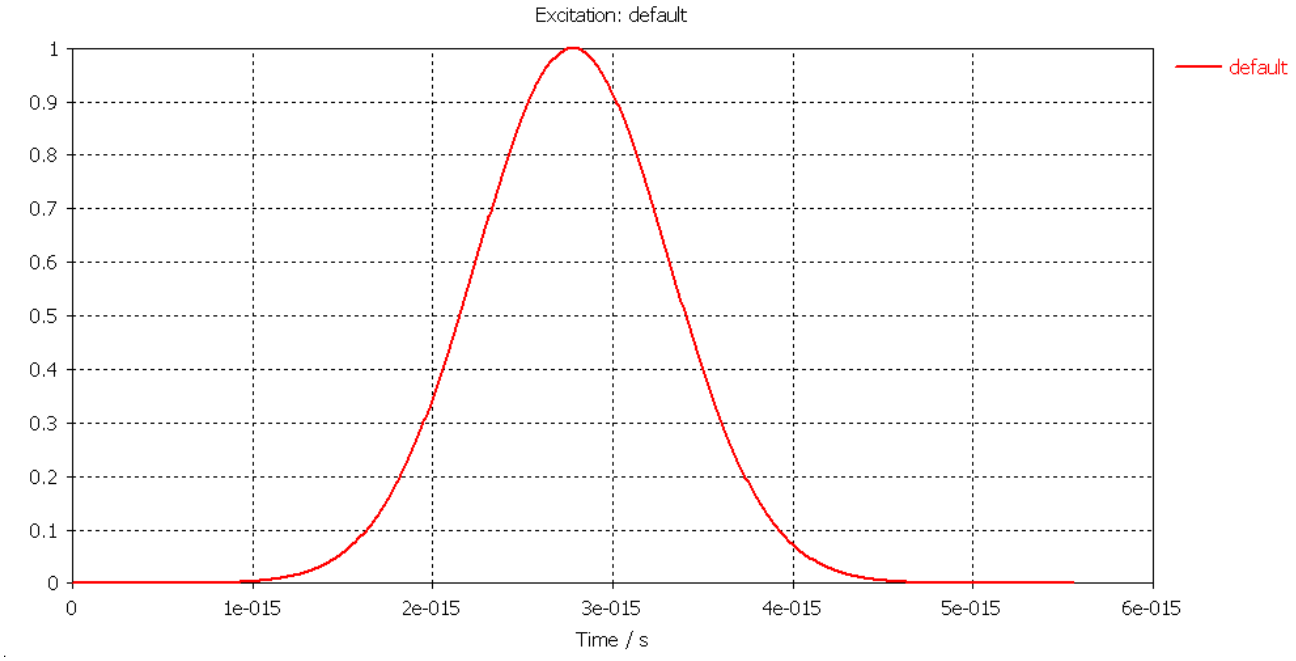

Figure 3.32: Gaussian frequency distribution as a time domain excitation signal of the FIT calculations.

to provide a truncation criterion for the discrete Fourier transform, the modified discrete energy (3.78) is monitored automatically, as shown in figure 3.33. As soon as the total energy contained in the calculation domain falls below a threshold of e.g. 30 dB of the incident peak energy, the simulation is judged completed. This criterion is called *asymptotic* convergence and provides a stopping criterion for the discrete Fourier transform acting on the time domain to obtain the frequency domain solutions. The pronounced staircase distribution of the energy over time in figure 3.33 is a common feature of all simulation runs and is due to the highly resonant nature of the scattering problem. The scatterer is a resonating structure which is excited by a pulse. Each sudden drop in energy corresponds to an internal reflection or scattering order of the pulse due to the particle.

3.3.3 Results obtained through the FIT

The following subsection shows several sample results obtained via the FIT method, including spherical and hexagonal scatterers. As a general scattering problem consists of a scattering object embedded in an infinite open domain, the volume discretisation of the FIT method needs to be truncated at a certain distance away from the scattering particle and terminated with the absorbing Perfectly Matched Layer (PML) boundary condition proposed by Berenger in his

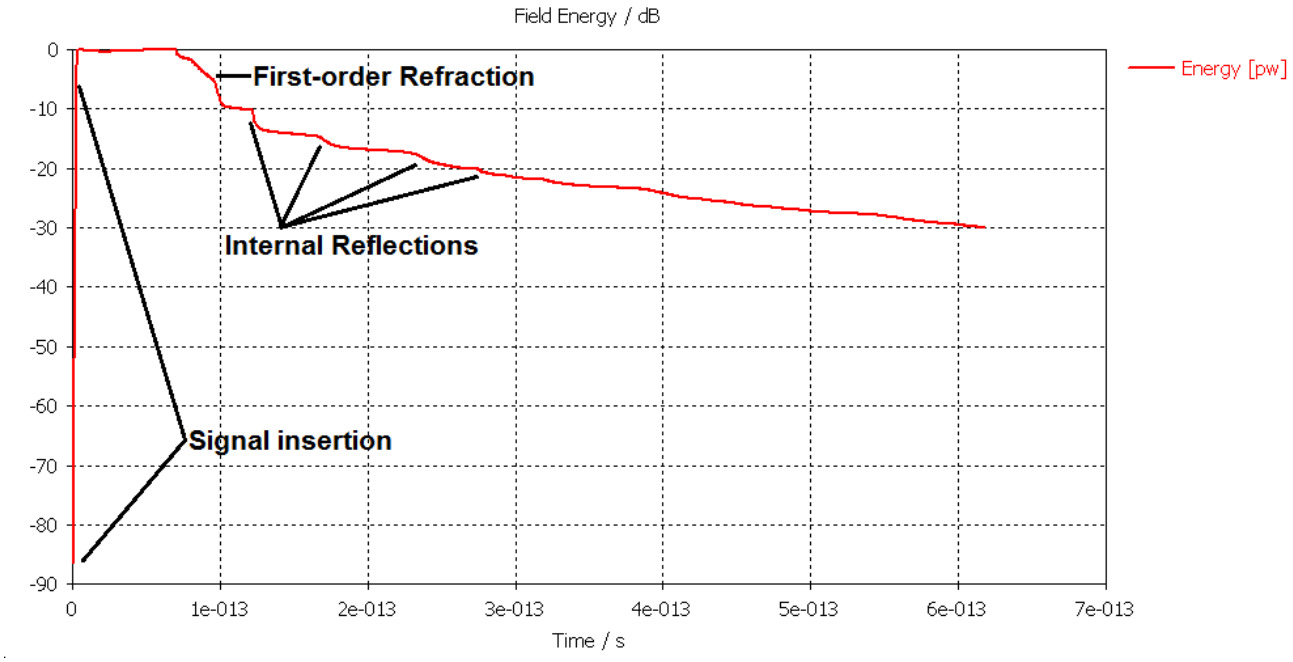

Figure 3.33: Modified electromagnetic energy contained in the computational domain as an FIT convergence criterion.

article [Ber94]. A simple Dirichlet boundary condition for the fields for instance would lead to a reflection of the waves impinging on the boundary. All calculations have been performed on a workstation with parameters summarized in table 3.7 using the commercial product CST Studio Suite 2015 [CST06], which is *the* FIT reference implementation. Due to the availability of computational hardware and theoretical expertise, the calculations have been performed at the TEMF institute of the TU Darmstadt in cooperation with Dr. Erion Gjonaj.

CPU	RAM	GPU	hard disk space	Operating System
Intel Xeon E5-2680 (Twelve core 2.5GHz)	512 GB	NVidia Quadro NVS310	6 TB	MS Windows 8

Table 3.7: Specifications of the Server used to carry out FIT simulations

Spherical Scatterers

The first two results 3.34 and 3.35 show the polar scattered power distribution in the far field for spherical scatterers. These cases have been computed primarily as verification cases in order to establish the connection to the Mie method. The refractive index in both cases was 1.33.

The calculations for the spherical scatterers have been performed on a grid with a stepsize of 8 nodes per wavelength of the incident light. The calculation time for each case was about 7 hours. The frequency of the two spherical test cases is $\omega = 2\pi \cdot f = 250THz$ for the 10 μm sphere in figure 3.34 and $\omega = 320THz$ for the 5 μm sphere in figure 3.35. The Mie result for the corresponding parameters are shown in figure 3.36.

As can be seen, the FIT calculations capture the forward scattering region well. Nevertheless the direct backscattering power is overestimated by the FIT calculation, as it shows a pronounced glory phenomenon, or underestimated by the Mie code of Laven [Lav03]. At this point, no clear decision can be made, which one of the *exact* methods is more accurate. Possible reasons for the discrepancy may be the low grid point count of 8 nodes per wavelength, which is recommended to exceed 10 for most applications [Ged11] or inaccuracies in the various numerical procedures for acquiring the harmonic far field quantities such as the FFT and the numerical integration during the far field propagation or alternatively the poor staircase approximation of the spherical surface by the cubic grid, which is a problem the FIT shares with the DDA. Inaccuracies on the part of the Mie code may include a too low truncation order for the basis of the function space representing the scattered field, as well as the finite angular width of the incident light source, disqualifying it as a true plane wave.

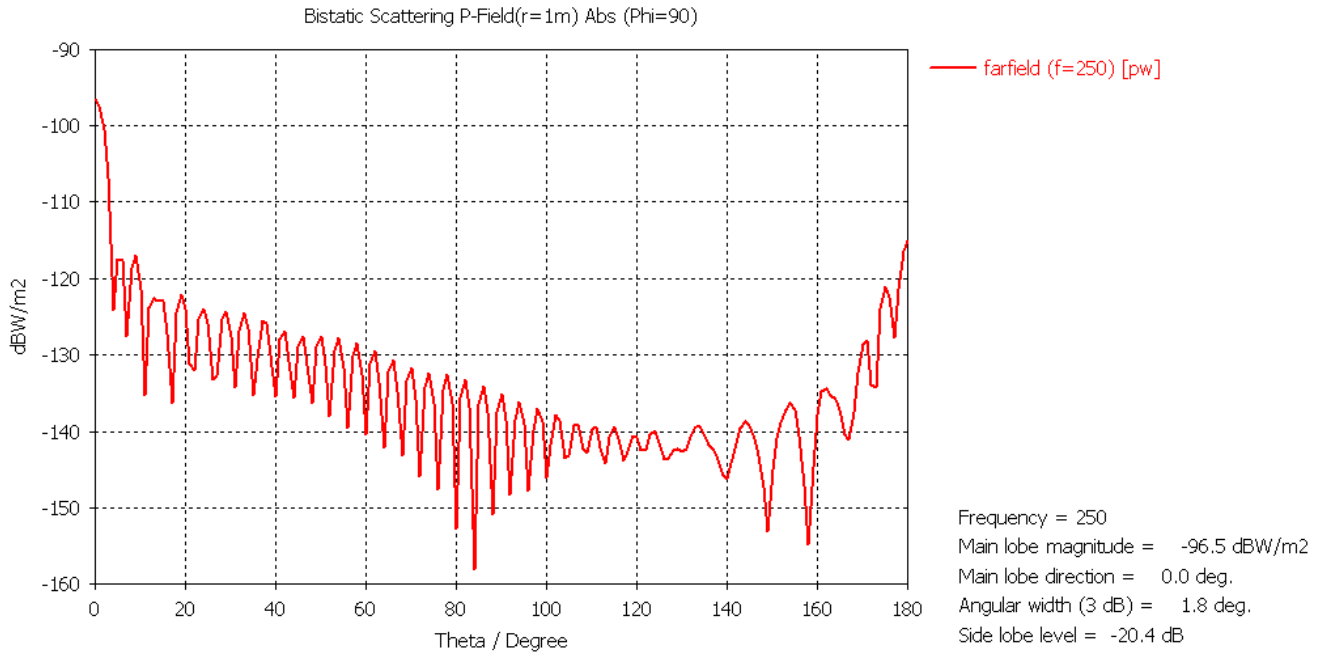

Figure 3.34: Polar scattered power distribution in the far field. Incident plane wave has perpendicular polarization and the particle size is 10 μm.

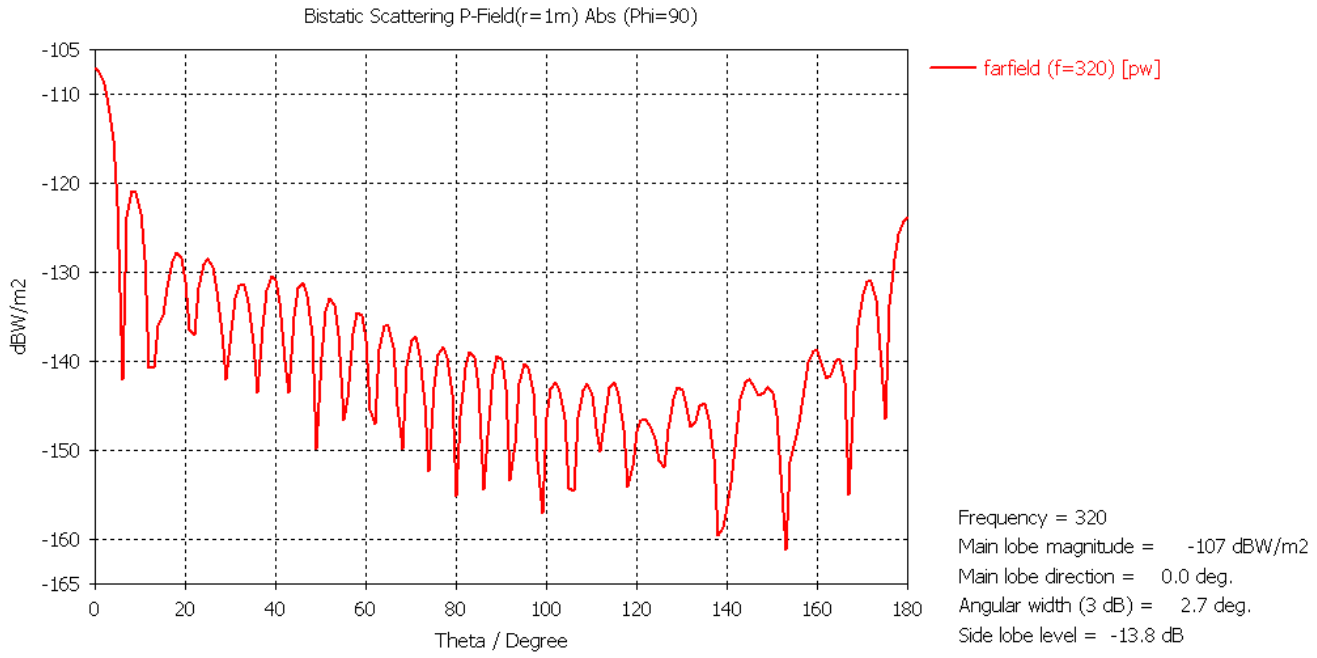

Figure 3.35: Polar scattered power distribution in the far field. Incident plane wave has perpendicular polarisation and the particle size is 5 μm.

Hexagonal Prisms

Hexagonal Prisms as a typical shape for ice crystals are of course central to this thesis and numerically exact FIT calculations have also been performed for such shapes in order to understand the scattered fields for such a particle. Again, just as in the Geometrical Optics case it becomes important to understand the influence of shaped beam incidence. As already explained in section 1, this is largely neglected in most studies on non-spherical particles, but becomes a necessity due to the advent of particle characterization devices applicable to non-spherical particles using highly focused Gaussian beams, such as the PHIPS instrument [ASA+11] and the Time-Shift technique [Sch13].

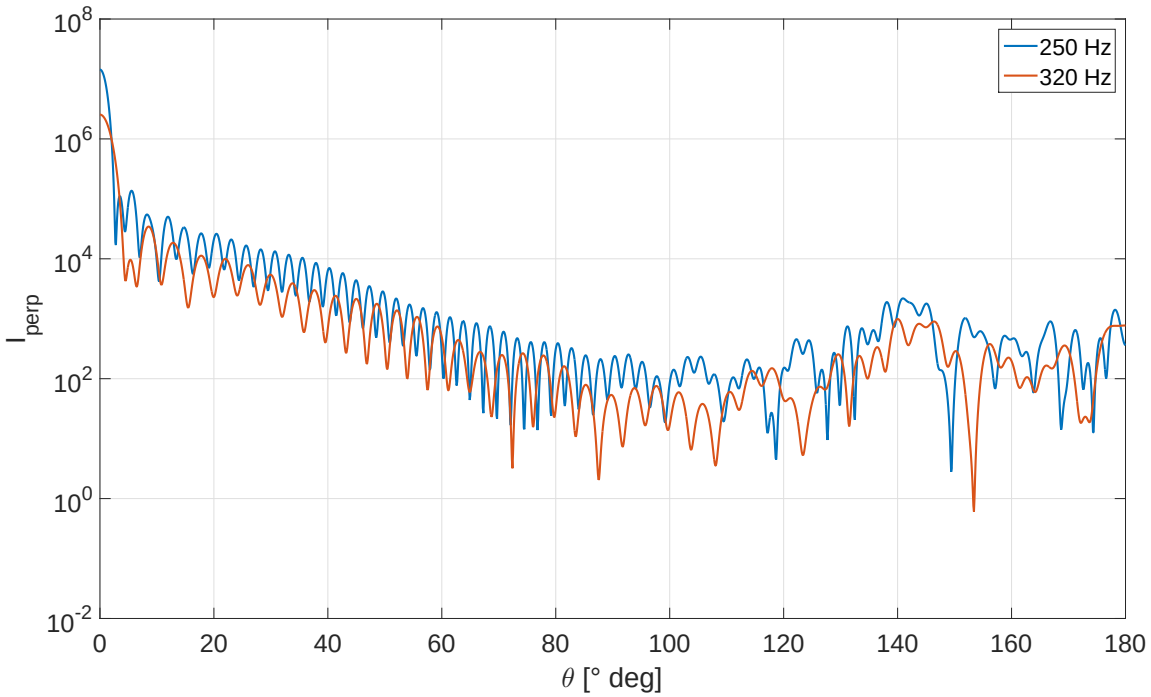

Figure 3.36: Polar scattered power distribution in the far field for perpendicular polarisation. Both cases from figure 3.34 and 3.35 have been recalculated using the Mie code [Lav03].

The geometry of the solution volume is shown in figure 3.37. The discretised volume contains a hexagonal prism of sidelength and height equal to 10 μm. The prism is enclosed in a completely discretised cubic volume terminated by non-reflecting PML layer surfaces.

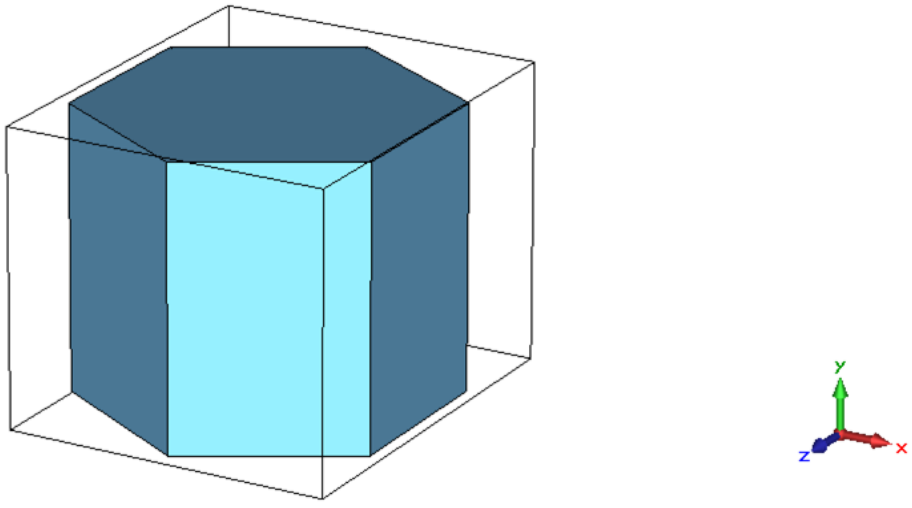

Figure 3.37: Calculation geometry including a hexagonal prism.

The volume of geometry 3.37 is discretised using a 3D staggered grid already presented in figure 3.31 using a resolution of 15 grid points per wavelength, which resulted in a total number of 1,400,000,000 grid points. A sample cutaway of the resulting cubic mesh is shown in figure 3.38.

Applying a Gaussian beam as a time domain exciation is already includes as a Macro in the 2014 version of the CST Studio Suite. The Gaussian beam shown in figure 3.39 was applied at one boundary of the cubic volume with a wavelength of

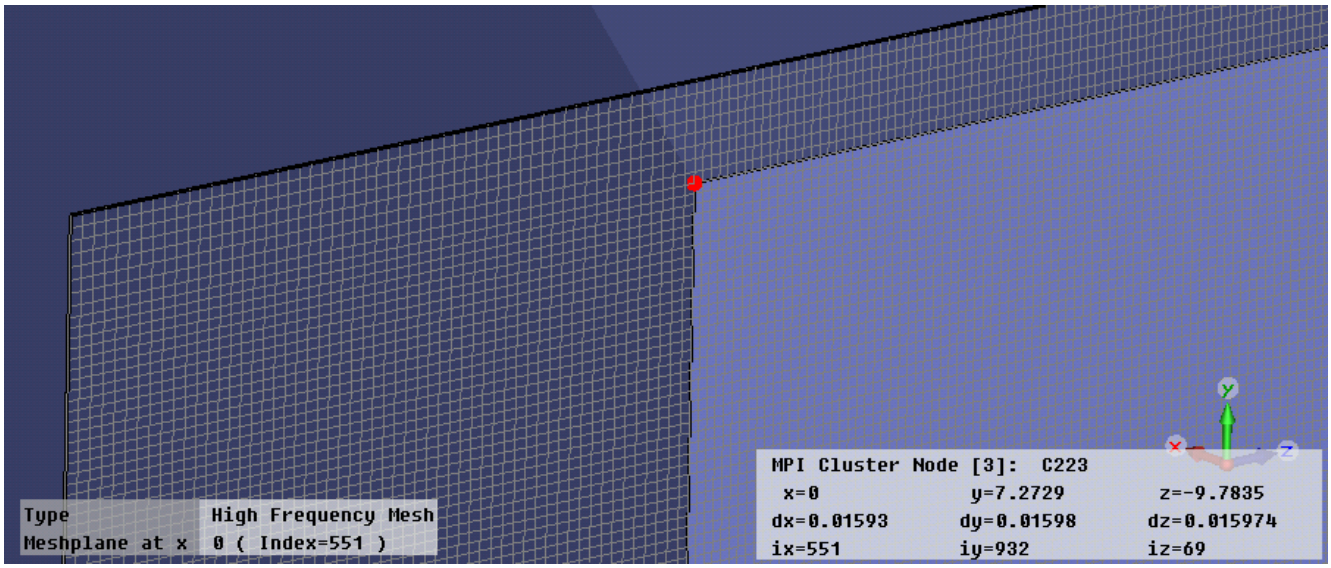

Figure 3.38: Cubic regular high frequency mesh detail.

632.8 nm corresponding to a visible red HeNe laser. The beam was polarised in the $\hat{\mathbf{e}}_x$ direction, i.e. normal to the prism axis.

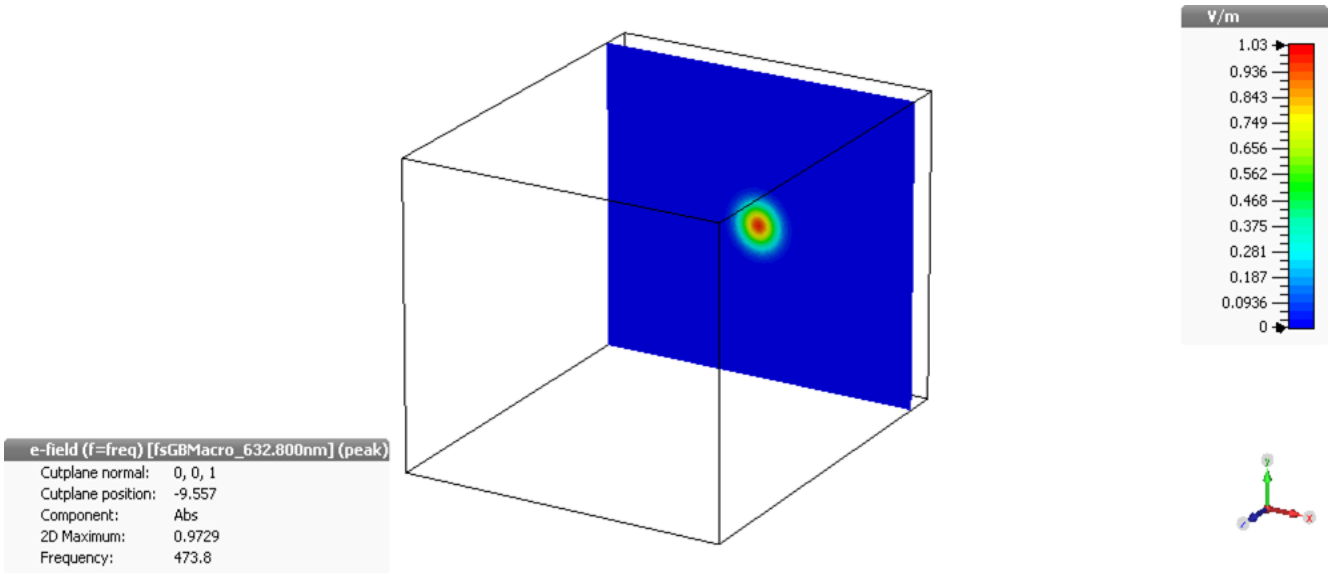

Figure 3.39: Gaussian beam excitation source. The Gaussian profile may be achieved as a Gaussian variation of the amplitude of a standard plane-wave boundary condition as defined in [Ged11] over the boundary of the grid.

The electric field strength of the Gaussian beam in the solution volume without any scatterer present is shown in figure 3.40 and it can be seen that the beam displays a hyperbolic spread parallel and a Gaussian decay perpendicular to the beam axis $\hat{\mathbf{e}}_z$, just as expected. The comparison with the analytic solution in figure 3.15 also shows a strong correspondance.

This behaviour is disrupted by the scattering prism as shown in figure 3.41 and the Gaussian beam is reflected and refracted in several different directions.

The final results are the polar distributions of the power scattered by the hexagonal prismatic particle for Gaussian beam illumination shown in figures 3.42 and 3.43. Again, the incident light wavelength was $\lambda = 632.8nm$ and the dielectric permittivity of the ice was assumed to be 1.75, corresponding to a refractive index of roughly 1.32, which is slightly higher than the usually assumed 1.31. Only single orientation cases have been studied, as orientational averaging is not implemented in CST Studio and largely cost-prohibitive for larger particles. The distributions shown in the figures

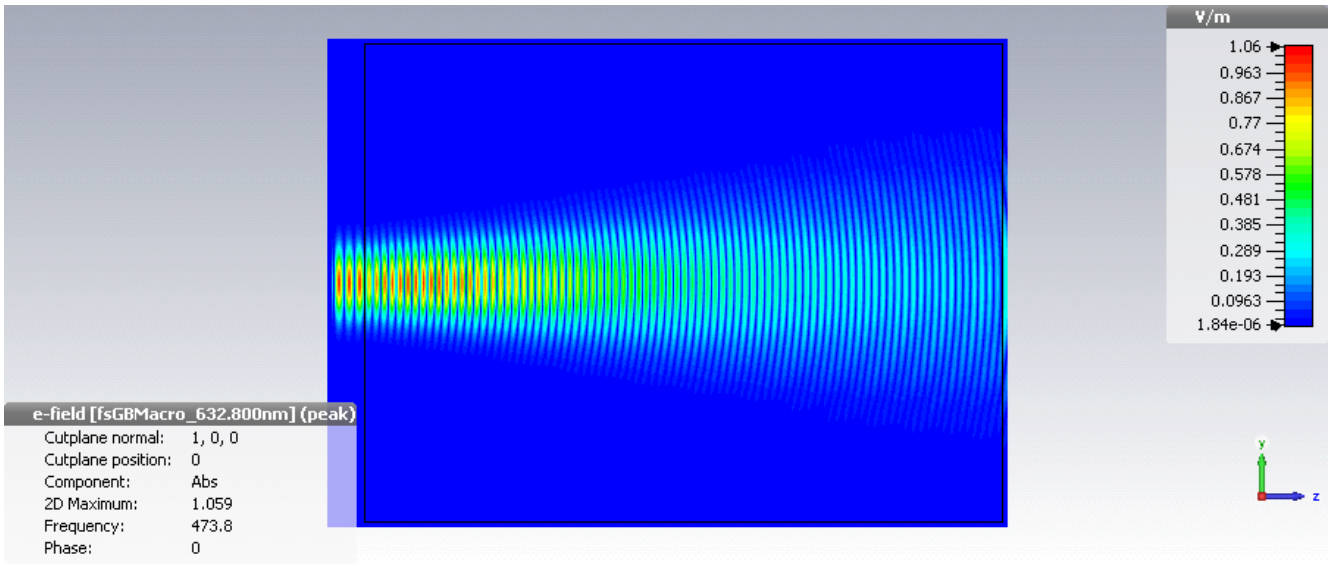

Figure 3.40: Unperturbed propagation of the spatially Gaussian excitation signal on the FIT mesh.

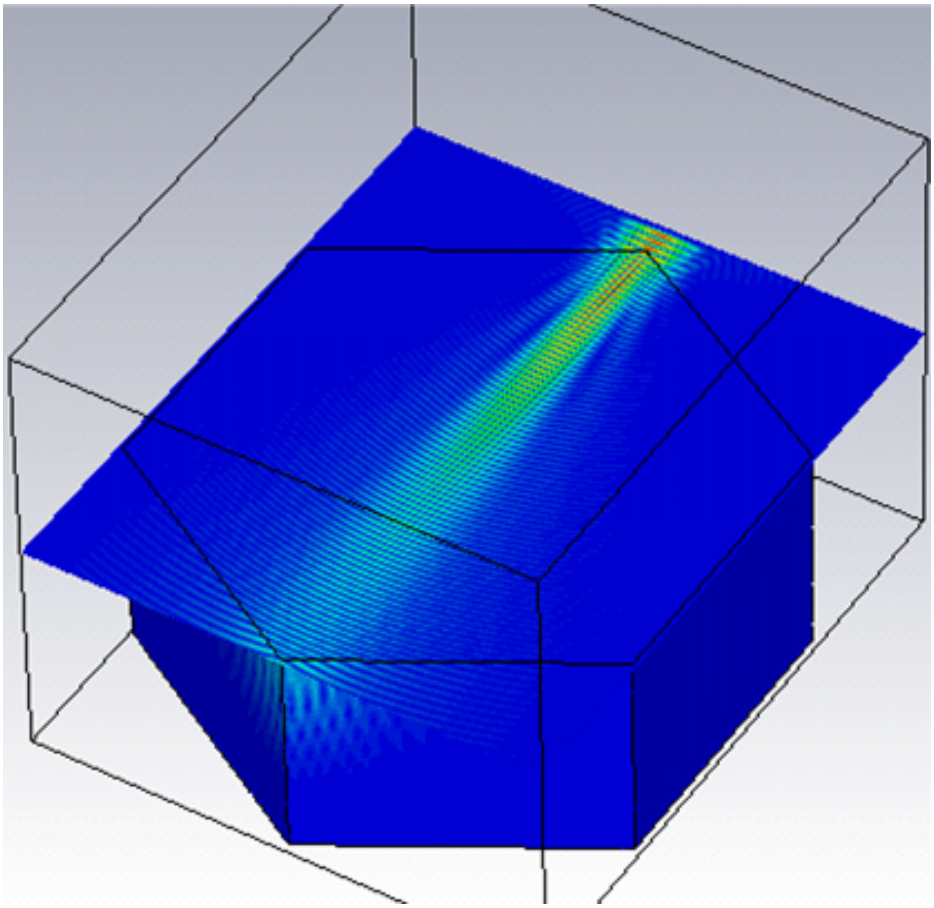

Figure 3.41: Near field of the Gaussian beam scattered by the prism.

form the central conclusion of this subsection and contain a number of important findings. Starting from the plane wave distribution in figure 3.42, it may be seen that **a number of important scattering features** present in the orientationally averaged phase function and also the natural halo display **already show in the single orientation - edge on incidence case**. This includes the 0^o degree peak, the 22^o degree halo and the 46^o halo. All these features are noticably broadened in comparison to the sharp peaks of the Geometrical Optics results. Furthermore one can also observe a peak in the backward direction at roughly 120^o degrees. All these phenomena can already be inferred by applying the Snell-Descartes

law to the facettes of the prism. In a typical experiment such as one conducted with a time-shift apparatus, the expected results may then lie somewhere in between the plane wave and the 5 μm focal radius case, if a hexagonal prismatic particle with the given orientation is encountered. It can be seen that a gradual focusing of the beam leads to a disappearance of the 46^o degree halo and the appearance of a new reflection peak at roughly 150^o degrees. Also, due to the decrease in power incident on the cross-section of the particle by the Gaussian beam, the scattered power also sees a likewise decrease in overall magnitude. Further decreasing the beam waist radius from 4 to 2 μm does not lead to any new scattering features besides a pronounced glory peak at 180^o degrees. Finally, at an almost physically impossible radius of 1 μm, the 22^o degree halo disappears and is replaced by exponentially decreasing side-lobes in a cone of $\pm 40^o$ degrees around the persistant forward peak.

Consequences for single scattering experiments

Summarizing the findings from both the Geometrical Optics calculations and the FIT simulations at this point, it appears prudent to choose a polar angle of either 22^o degrees in the forward direction or 120^o degrees in the backward direction as a detector position for observing natural ice crystal. Figures 3.42 and 3.43 show that the FIT calculations not only complement but also confirm the GO results to a certain degree.

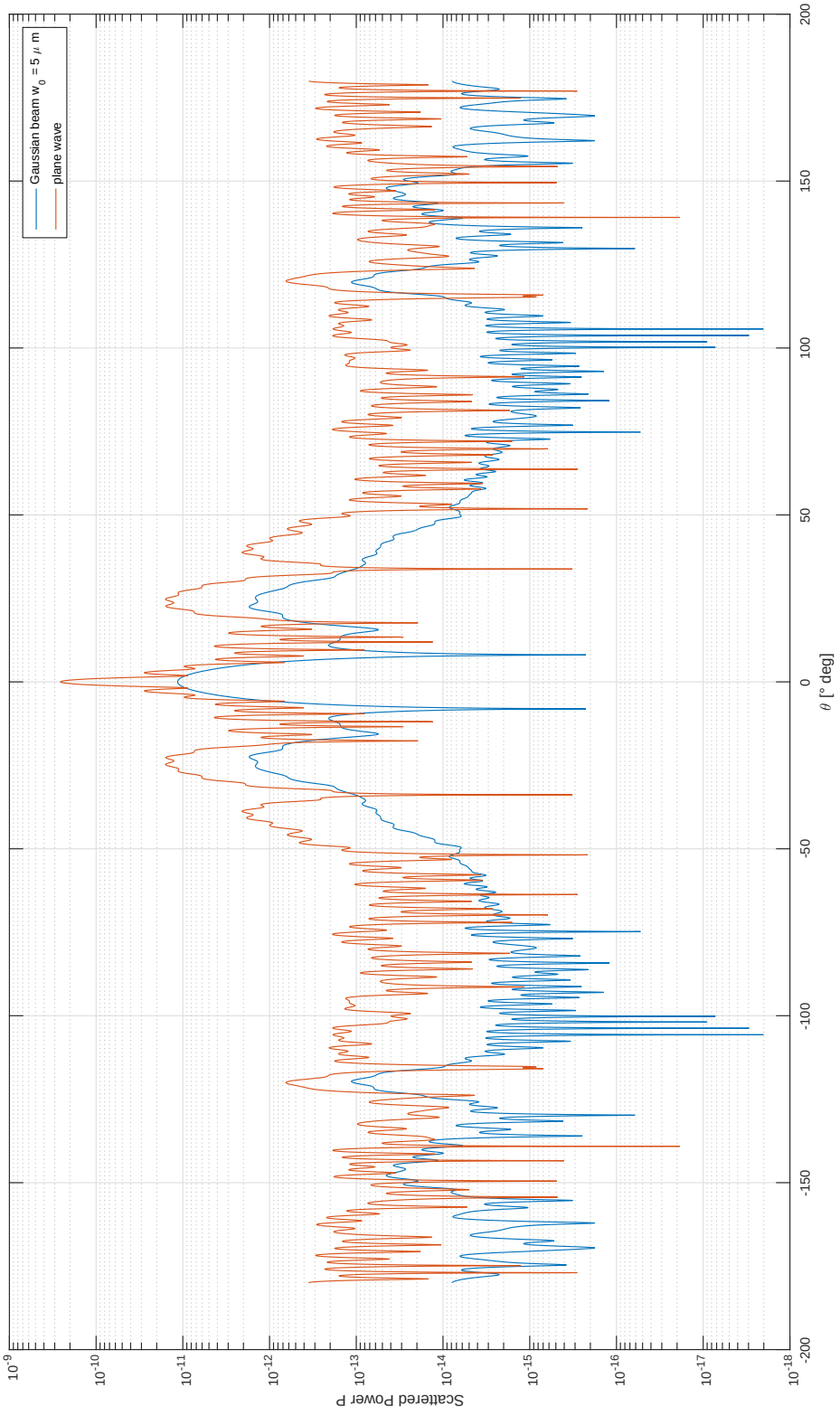

Figure 3.42: Single orientation polar scattered power for configuration identical to figure 3.43 but beam waist radius 5 μm and plane wave incidence.

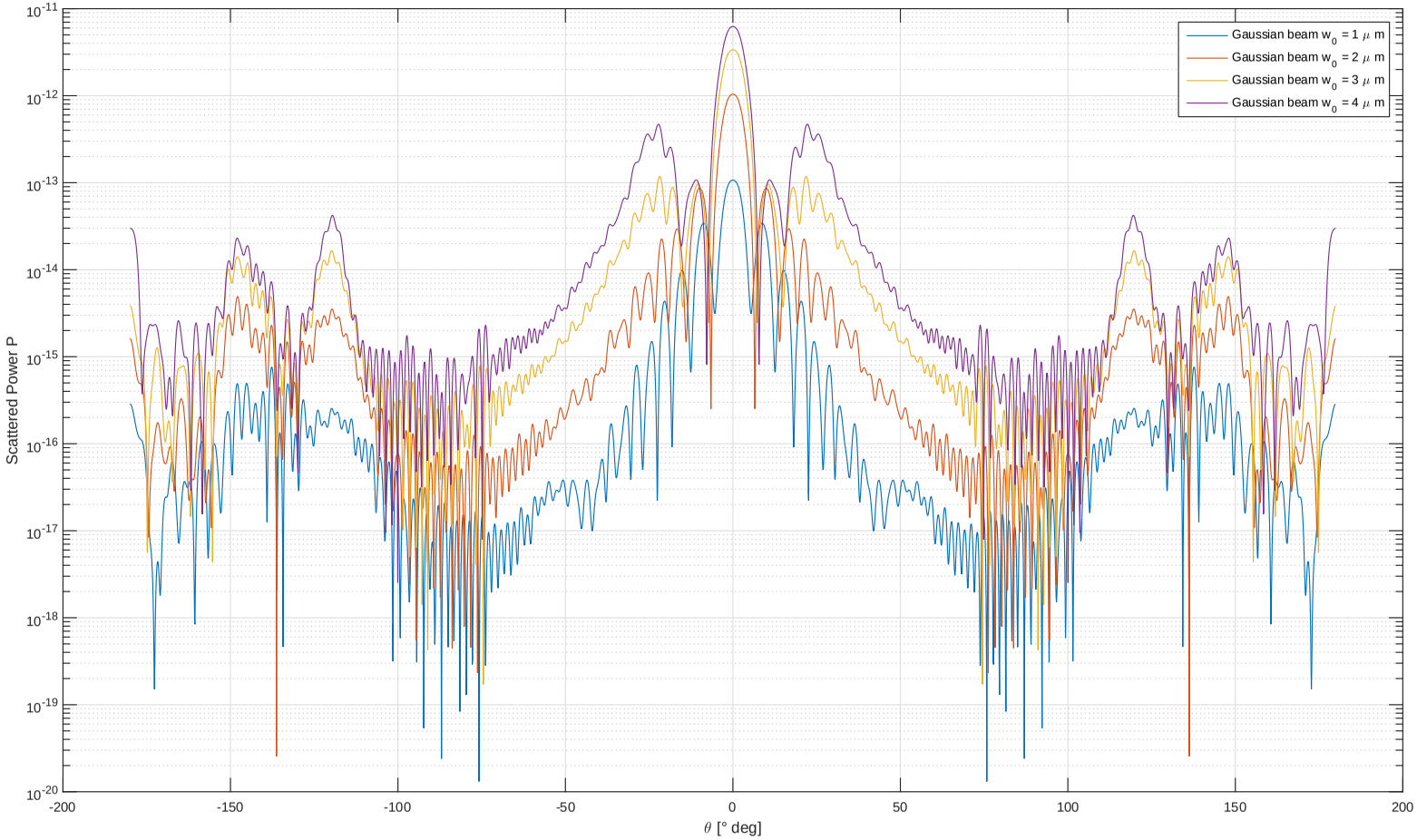

Figure 3.43: Single orientation polar scattered power for a hexagonal prism with a dielectric permittivity of 1.75 and a Gaussian beam with a wavelength of 632.8 nm and varying beam waist radius from 1 to 4 μm.

3.4 Transition Matrix Method

As already mentioned in the introduction 1, the scientist usually credited with concieving the so-called *Transition matrix* method, or T-matrix for short, is Peter C. Waterman. He applied the matrix formalism to electromagnetic and acoustic scattering in a series of publications [Wat71, Wat63, Wat79], with the most widely cited manuscript being [Wat71]. Despite its great importance, the method is another variant of an S-matrix formalism (S for Scattering) [LL80] and there are even other publications of scattering matrix methods for the electromagnetic field considerably earlier then Waterman, such as Saxon [Sax55]. Waterman's approach was later popularized in the scattering community by Mishchenko [Mis91] and the analytical orientation averaging developed by Khlebtsov [Khl92] has made Waterman's T-matrix method a powerful tool for scattering calculations.

3.4.1 Symmetric Particles

The following subsections will discuss a T-matrix variant which is particularly favourable for the application to particles with geometric symmetries.

Classical T-matrix method

For particles having any kind of geometrical symmetry, the classical T-matrix or Null-field method is appropriate. The basic idea here is to expand the incident time-harmonic electromagnetic field on a basis of Hansen vectors $\vec{\Psi}^{(j)}_{n,m,\tau}$ or spherical vector wave functions [Han35] and find a matrix representation of the transition operator $\hat{\mathbf{T}}$ which relates the coefficients of the scattered field expansion to the known coefficients of the incident field. Obviously the linearity of Maxwell's equations (2.33) only permits the expansion of the fields on a linear vector space, while the existance of the T-matrix is a consequence of the linearity of the boundary conditions [Str07, GG11] between the scatterer and its surrounding medium. The incident field may then take the following form:

$$\mathbf{E}_{inc} = \sum_{n=1}^{\infty} \sum_{m=-n}^{n} \sum_{\tau=1}^{2} a_{n,m,\tau} \cdot \vec{\Psi}^{(1)}_{n,m,\tau}(k,\mathbf{r}) \tag{3.82}$$

While the scattered field identically reads:

$$\mathbf{E}_{scatt} = \sum_{n=1}^{\infty} \sum_{m=-n}^{n} \sum_{\tau=1}^{2} p_{n,m,\tau} \cdot \vec{\Psi}^{(3)}_{n,m,\tau}(k,\mathbf{r}) \tag{3.83}$$

Where the superscript $j = 1$ stands for vector spherical wave functions which do not diverge at the origin and $j = 3$ are waves satisfying the Sommerfeld radiation condition [Som64]. The various definitions of the spherical vector wave functions $\vec{\Psi}^{(j)}_{n,m,\tau}$ as listed by Khlebtsov [Khl92] also find their application as the basis of the classical Lorenz Mie theory (LMT) as formulated by Van de Hulst [Hul01] and in the recent formulations of the GLMT [XRG+07]. Specifically, for the GLMT, the expansion coefficients $a_{n,m,\tau}$ would be the beam shape coefficients (BSPs) g^n_m. As it is a discrete basis for a function space over the entire base manifold, it is qualitatively distinct from continuous basis in the FLMT case provided by Damaschke [Dam03] and the discrete basis on a discretized domain used as the root of the Finite Element method (FEM) [LMW12] in numerical mathematics. Following the definition given in the book [RK14] by Kahnert the preceeding expansions permit the definition of the T-matrix:

$$\mathbf{T} = T_{n,m,\tau,n',m',\tau'} = -\sum_{n''=1}^{\infty} \sum_{m=-n''}^{n''} \sum_{\tau''=1}^{2} RgQ_{n,m,\tau,n'',m'',\tau''}\ Q^{-1}_{n'',m'',\tau'',n',m',\tau'} \tag{3.84}$$

with the matrices Q and its regular counterpart RgQ, such that the coefficients of the scattered field may now be expressed as:

$$p_{n,m,\tau} = \sum_{n'=1}^{\infty} \sum_{m=-n'}^{n'} \sum_{\tau'=1}^{2} T_{n,m,\tau,n',m',\tau'}\ a_{n',m',\tau'} \tag{3.85}$$

The surface integral expressions over the particle boundary for calculating the elements of the Q-matrices are given by Waterman [Wat71] and are traditionally evaluated using the Gauss-Legendre quadrature [DR08, PTVF95]. All optical properties of the scattering system such as the orientation-averaged phase function or various cross-sections can now be inferred directly from T-matrix, which only depends on the particle geometry. This property makes the T-matrix approach particularly efficient. Further details on the classical T-matrix method will not be given here, as it is beyond the scope of this thesis.

Continuous symmetries of an electromagnetic system have already been discussed in subsection 2.1.3, but the T-matrix method also allows the consideration of discrete geometrical symmetries of a particle, as elaborated by Kahnert et al. in a series of articles [SS99, KSS01, Kah05, Kah13]. Mathematically, these geometrical symmetries are identified as point groups [McW03]. The simple model of the ice crystal with a hexagonal prismatic shape obviously has a hexagonal symmetry, amongst others, and thus is left invariant under an application of an operator of the $\hat{C}_6$ group to the geometry of the particle, which is a subgroup of the full dihedral group D_6. Elements of $\hat{C}_6$ are rotations about an angle of $\frac{\pi}{3} \cdot m$ radians with $m \in \mathbb{N}_0$. By choosing the same basis as for the T-matrix, i.e. the vector spherical wave functions $\vec{\Psi}^{(j)}_{n,m,\tau}$, one can write down a concrete matrix representation for an operator pertaining to $\hat{C}_6$.

$$\mathbf{U} = U_{n,m,\tau,n',m',\tau'} = \delta_{n,n'}\delta_{m,m'}\delta_{\tau,\tau'}e^{-i\frac{\pi}{3}m} \tag{3.86}$$

with $\delta_{n,n'}$ being the Kronecker delta. The reader may check, that the matrix $\mathbf{U}$ is in fact unitary. As already discussed, the T-matrix in the current context does not depend on the electromagnetic field at all, but solely on the geometry and constitution of the scattering particle. Thus, if the geometry of the particle is left unchanged under a specific symmetry operation, the same must be true for the T-matrix. For two matrices, linear algebra [Brö04] dictates the the following relation:

$$\mathbf{T} = \mathbf{U} \cdot \mathbf{T} \cdot \mathbf{U}^{-1} \tag{3.87}$$

which especially in quantum mechanics [LBCTL13] is often abreviated using the commutator bracket $[\cdot,\cdot]$:

$$[\mathbf{T}, \mathbf{U}] = 0 \tag{3.88}$$

Enforcing this condition on the T-matrix for all symmetry operations of the particle geometry shows the ultimately vanishing elements of the T-matrix before making any calculations. In the case of the perfectly spherical scatterer, it can be shown explicitly that the T-matrix must be diagonal while for the hexagonal prism it is block-diagonal.

TSym Results

The implementation of the methods briefly touched in the preceding subsection is a lengthy and arduous endeavour and requires in-depth knowledge of highly abstract mathematical concepts. As such a process is beyond the scope of this thesis, the existing Fortran 77 research code *TSym* written by Kahnert and based on the T-matrix code of Mishchenko [MM96] was used for sample calculations. TSym implements all methods discussed above and the code is freely available at the scattport website [Wri15], while its user manual is published in form of the article [Kah13]. The parameters of the simulation performed with TSym are summarized in table 3.8 and the resulting phase function is shown in figure 3.44.

particle radius R	particle height h	wavelength λ	index of refraction n	Particle type	Symmetry group
10 μm	20 μm	632.8 nm (red)	1.31	Prism	D_6

Table 3.8: Calculation parameters of the test runs of TSym.

The incident field corresponding to the phase function in figure 3.44 is a plane wave and the truncation parameter for the (theoretically infinite) T-matrix basis size is 150. It is also possible to calculate spheres with TSym, nevertheless it is not yet possible to consider the full symmetry group of spheres. Instead, Kahnert recommends in the manual [Kah13] to use a very large dihedral group $D_{2 \cdot n_{trunc}+1}$, which would be D_{301} in the present case.

The orientation-averaged phase function in figure 3.44 shows some typical features of hexagonal prismatic ice crystals, such as the peak at 0^o degrees, the 20^o degree halo and an indication of a glory peak at 180^o degrees.

3.4.2 Irregular Particles

Another property of ice crystals highlighted in the recent years is their surface roughness. Explanations have been sought as to why for instance the 46^o degree halo was so rarely observed in nature in comparison to the 22^o degree halo and

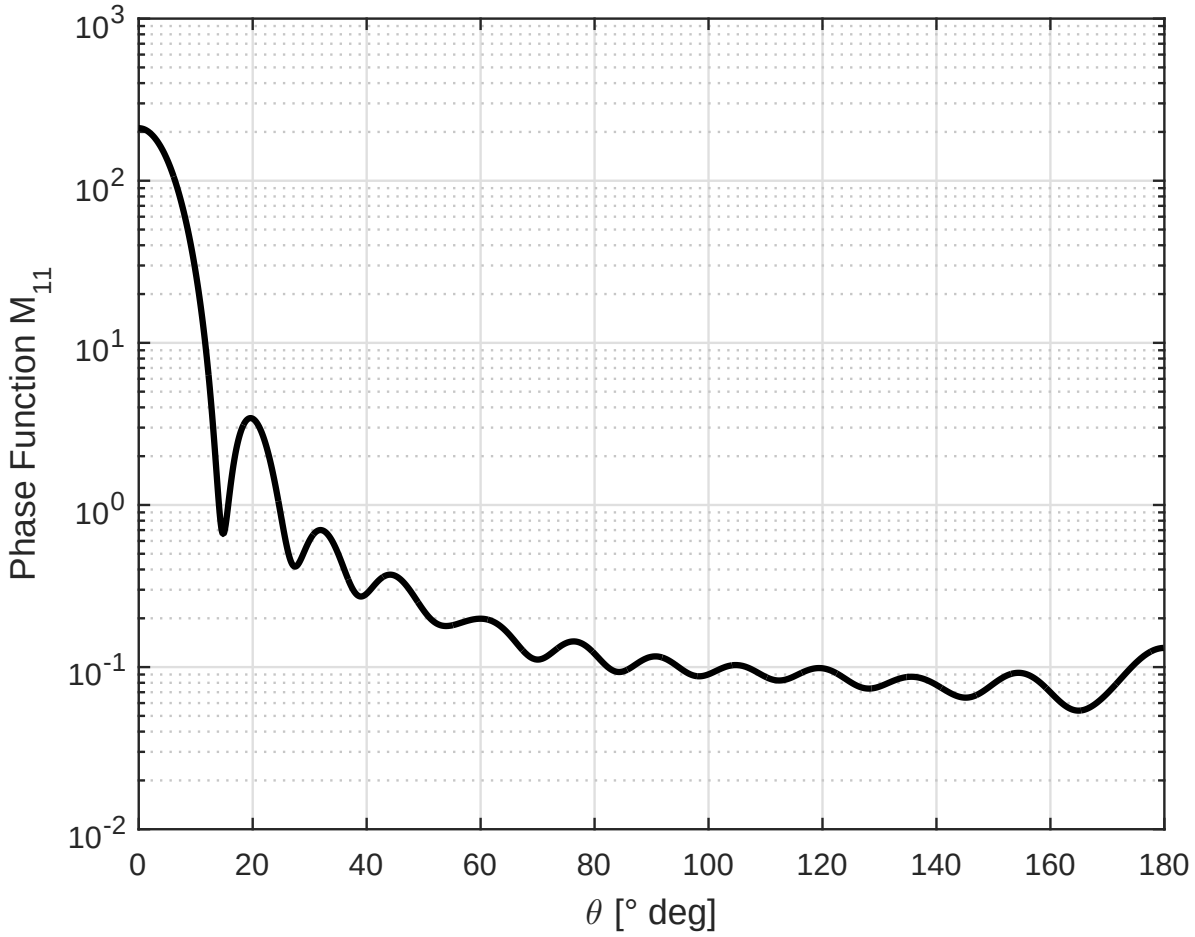

Figure 3.44: Phase function for a hexagonal prismatic ice crystal using TSym.

Yang et al. [WY12] could show that introducing surface roughness in the description of a pristine ice crystal model shape could potentially destroy all characteristic scattering features of an ice crystal completely. This would be the case for strong roughness, while slight and moderate roughness lead to an eventual disappearance of the 46^o degree halo. As natural ice crystals cannot be expected to have a perfect shape, one must be able to take the effects of surface roughness into account. The previously discussed symmetry approach cannot do this, as the random small scale roughness will destroy the ideal symmetry. A recent approach taken by T-matrix codes such as [Kah13] and [TVP15] is to use an iterative Lippmann-Schwinger equation approach, in order to succesively include the effects of ever smaller scales of surface perturbations. A different method taking the roughness into account through its volume discretisation approach is the DDA method [YH07, YH11, PP73] already mentioned in section 1. This approach may also be used to calculate a T-matrix, as the basic formulation of the T-matrix as an operator is sufficiently general.
One particular very recent DDA method is a reformulation of a Green's function method used in Computational Electromagnetics developed from 1994 onward by various researchers and has been applied succesfully to highly irregular particles by Tricoli [TVP15]. An introduction to the method can be found in the article [MDG94]. This particular T-matrix method is chosen here for further development, as its distinguishing feature in comparison to other T-matrix methods is its **extreme simplicity**, making it suitable for implementation even by an undergraduate student. For comparison, the similar FDTD is often quoted as the most simple method in Computational Electromagnetics. Nevertheless, the introduction of absorbing boundary conditions such as PML or other additional features requires considerable thought. A short introduction of the reformulated method by Tricoli [TVP15] will be given in the following. In the case of no sources or currents and harmonic time dependance, Maxwell's equations (2.33) reduce to the vector Helmholtz equation.

$$\Delta \mathbf{E}(\mathbf{r}) + k^2 \varepsilon(\mathbf{r}) \mathbf{E}(\mathbf{r}) = 0 \tag{3.89}$$

Where the inhomogeneous dielectric permittivity $\varepsilon(\mathbf{r})$ depending on the spatial coordinate $\mathbf{r}$ essentially defines the scattering problem geometry for a dielectric particle. As the function $\varepsilon(\mathbf{r})$ may potentially very complex, it is unclear whether

a solution for the PDE (3.89) exists, as the exact form of the PDE is unknown in the first place. Following Martin et al. [MDG94], the scattering particle may be regarded as a perturbation of the background medium ε_0 (vacuum in most cases), such that:

$$\varepsilon(\mathbf{r}) = \varepsilon_0 + \Delta\varepsilon(\mathbf{r}) \tag{3.90}$$

Such that the PDE (3.89) can be reformulated into the inhomogeneous Helmholtz equation with $-k^2\Delta\varepsilon(\mathbf{r})\mathbf{E}(\mathbf{r})$ as a source term.

$$\Delta\mathbf{E}(\mathbf{r}) + k^2\varepsilon_0\mathbf{E}(\mathbf{r}) = -k^2\Delta\varepsilon(\mathbf{r})\mathbf{E}(\mathbf{r}) \tag{3.91}$$

Due to the linearity of the homogeneous Helmholtz equation in the field $\mathbf{E}(\mathbf{r})$, a solution of equation (3.91) may be found as a convolution of its tensor Green's function $\mathbf{G}(\mathbf{r},\mathbf{r}')$ with the inhomogeneity [Jac75].

$$\mathbf{E}(\mathbf{r}) = \mathbf{E}_0(\mathbf{r}) + \iiint_V \mathbf{G}(\mathbf{r},\mathbf{r}') \cdot k^2\Delta\varepsilon(\mathbf{r})\mathbf{E}(\mathbf{r})d\mathbf{r}' \tag{3.92}$$

Where $\mathbf{E}_0(\mathbf{r})$ is the incident field in free space without the scattering object of volume V. The above volume integral equation formally is a Lippmann-Schwinger equation [LS50] for electromagnetic scattering. Unfortunately, different scientific disciplines have different names for the function $\mathbf{G}(\mathbf{r},\mathbf{r}')$. In classical physics it is called a Green's function [Jac75], in QFT it is called a propagator [PS05], in mathematics it is called a fundamental solution and in engineering and systems theory it is called the impulse response [Lun10] of a system. The Green's function used here is the solution of the inhomogeneous Helmholtz equation for an impulse exciation $\delta(\mathbf{r}-\mathbf{r}')$.

$$\Delta\mathbf{G}(\mathbf{r},\mathbf{r}')(\mathbf{r}) + k^2\varepsilon_0\mathbf{G}(\mathbf{r},\mathbf{r}') = \delta(\mathbf{r}-\mathbf{r}')\cdot\mathbb{I} \tag{3.93}$$

The Green's function may be considered known, as they are tabulated in references such as [But82] for specific differential equations. Using the T-matrix and the Born approximation [FH65], the total field in equation (3.92) may then be approximated by the incident field.

$$\mathbf{E}(\mathbf{r}) = \mathbf{E}_0(\mathbf{r}) + \iiint_V \mathbf{G}_0(\mathbf{r},\mathbf{r}') \cdot \left(\iiint_V \mathbf{T}(\mathbf{r'},\mathbf{r''})\mathbf{E}_0(\mathbf{r}'')d\mathbf{r}'' \right) d\mathbf{r}' \tag{3.94}$$

where the T-matrix $\mathbf{T}(\mathbf{r'},\mathbf{r}'')$ also fulfills a Lippmann-Schwinger type equation according to Tricoli [TVP15].

$$\mathbf{T}(\mathbf{r},\mathbf{r}') = \mathbf{T}_0(\mathbf{r},\mathbf{r}') + \iiint_V \mathbf{G}_0(\mathbf{r},\mathbf{r}'') \cdot k^2\Delta\varepsilon(\mathbf{r}'')\mathbf{T}(\mathbf{r}'',\mathbf{r}')d\mathbf{r}'' \tag{3.95}$$

And according to Martin et al. [MDG94] the tensor Green's function obeys the Dyson equation.

$$\mathbf{G}(\mathbf{r},\mathbf{r}') = \mathbf{G}_0(\mathbf{r},') + \iiint_V \mathbf{G}_0(\mathbf{r},\mathbf{r}'') \cdot k^2\Delta\varepsilon(\mathbf{r}'')\mathbf{G}(\mathbf{r}'',\mathbf{r}')d\mathbf{r}'' \tag{3.96}$$

The great simplification in this method now comes from the proposition of Martin et al. to solve equations (3.95) and (3.96) not by numerical integration, but iteratively. This can be achieved by discretising the scatterer in subvolumes V_n and iterating over all of them.

$$\mathbf{T}^n_{i,j} = \mathbf{T}^{n-1}_{i,j} + \mathbf{G}^{n-1}_{i,n}k_0^2\Delta\varepsilon_n V_n \mathbf{T}^n_{n,j} \tag{3.97a}$$

$$\mathbf{G}^n_{i,j} = \mathbf{G}^{n-1}_{i,j} + \mathbf{G}^{n-1}_{i,n}k_0^2\Delta\varepsilon_n V_n \mathbf{G}^n_{n,j} \tag{3.97b}$$

where the indices i, j and n each run over all elements of the discretised scatterer volume separately. An Matlab implementation of the method is given in the appendix for a simple test case and the results are shown in figure 3.45. The test case consists of a plane electromagnetic wave incident from the left upon a slab of dielectric material with various absorption strengths. As can be seen, the code reliably calculates reflection, transmission and absorption due to the dielectric barrier.

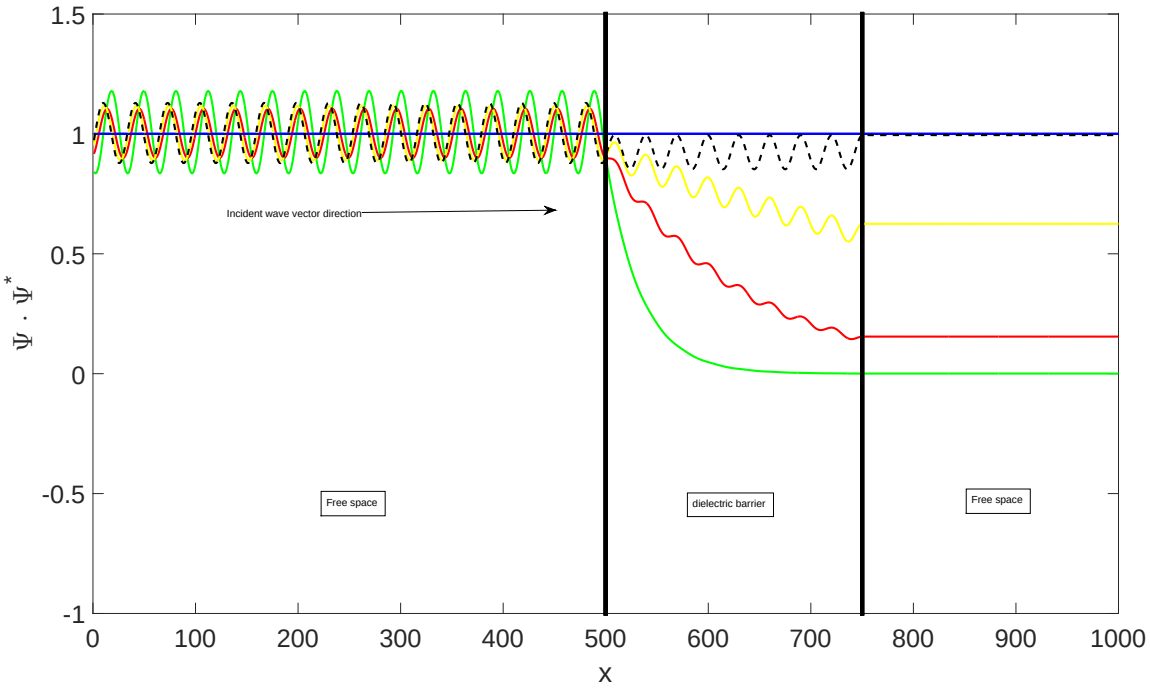

Figure 3.45: Simple onedimensional behaviour of a plane wave incident from the left and scattered by a change in dielectric permittivity between $500 \leq x \leq 750$. The total field intensity is displayed for several values of the imaginary part of the refractive index of the dielectric slab between $500 \leq x \leq 750$. The corresponding absorption in the slab ranges from none (dashed curve) to strictly exponential (green curve). The intensity of the incident plane wave is shown as the blue line and is constant, as expected. The oscillation seen in the intensity is interference between the incident and reflected waves. This includes internal reflection for $500 \leq x \leq 750$ and internal and external reflection for $x \leq 500$. The lack of interference beyond the reflecting permittivity slab is also displayed correctly, as the intensity of the transmitted field stays uniform beyond $x = 750$.

3.5 Brunel's Glare Point Model for the prediction of Speckle patterns

The glare point model developed by Marc Brunel as described in [BRJB15] was a necessity in the development of Interferometric Particle measurement techniques started by Sawitree Saengkaew [Sae14] in order to extend the technique from spherical to morphologically complex and highly irregular particles. Conceptually, the glare point model is simplest model discussed in this thesis. The approach is very similar to the scalar diffraction methods provided by Fourier Optics [Goo05]. The explanation of the method given in this thesis will follow the remarks in Brunel's article [BRJB15] and a concise Matlab implementation is given in the append. The basic geometry of an optical setup considered in the model is shown in figure 3.46 which shows a CCD camera separated from a lens by a distance of z_2, which is in turn separated from the screen carrying a particle sample by a distance of z_1.

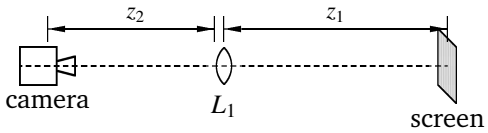

Figure 3.46: Sketch of the optical setup described by the glare point model.

The basic aim of the computational optics method is to determine the intensity pattern recorded on a CCD chip facing a single particle illuminated by coherent laser beam. To this end, two severe simplifications are introduced to cope with highly irregular particles and complex recording lens arrangements. First, the field scattered by a particle is modeled by looking only at its glare points and assuming them to be point sources for scalar spherical waves. Glare points are a reflection phenomenon encountered when looking at spherical droplets first rigorously discussed in an article [Hul91] by Van de Hulst. A microscopic image showing the two reflection and 2^{nd} order refraction glare points of a water droplet is shown in image 4.28. Applying methods similar to the ones used in Fourier optics [Goo05], the scalar wave field may

be propagated through the lens arrangement preceding the CCD chip where the scattered intensity is recorded. A simple illustration of the principle can be seen in Young's famous double slit experiment [You02] as the central element in the glare point model is the coherence of the illumination causing interference. It is well known from Fourier optics, that the Kirchhoff diffraction pattern of a given source field distribution can be equated with the Fourier transform of said distribution. Incidently this is also the case when the source distributions exists at the focal distance of a convex lens, such that the Fourier transform can be observed at the focus on the opposite side of the lens [Goo05]. The scalar theory of Young's double slit experiment may then be applied as a simple model for the double glare points of figure 4.28

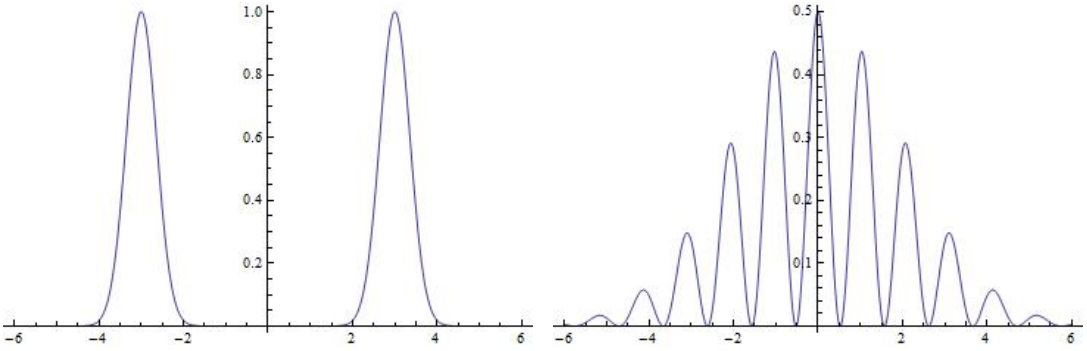

(a) Assumed Gaussian wave field strength distribution directly behind a double slit.

(b) Fourier-transform of distribution 3.47a and incidently Kirchhoff diffraction pattern.

Figure 3.47: Double slit position 3.47a and conjugate momentum representation 3.47b.

The starting distribution of the field is modelled as a sum of two Gaussian functions shown in figure 3.47a. One may realize that this is a quite adequate approximation, as long as one only looks at the fields in the 2D plane formed by the two glare points of figure 4.28 The corresponding Mathematica code is given below for the convenience of the reader intent on replicating the argument.

```
(* slit-screen wave function modeled as a superposition of two \
Gaussian functions *)
Psi[x_] := Exp[-4 (x - 3)^2] + Exp[-4 (x + 3)^2]
Plot[Psi[x], {x, -6, 6}]
```

Following Goodman [Goo05], the Kirchhoff diffraction pattern in the farfield (Fresnel number $F << 1$) from the source 3.47a is calculated via its Fourier transform and the corresponding Mathematica code is again shown below, while its result is displayed in figure 3.47b. The Fourier transform here is calculated numerically and the result is squared in order to obtain the intensity corresponding to the diffraction pattern on a screen in the farfield. The resulting image shows the characteristic interference fringe pattern typical for the double slit experiment. Consequently, a similar pattern may also be expected for the real glare points of a droplet.

```
(* Fourier-transformation of the coordinate wave function Psi into \
momentum space, yielding the far field diffraction pattern *)
Phi[p_] :=
 1/Sqrt[2 \[Pi]] Abs[Integrate[Exp[I p x] Psi[x], {x, -10, 10}]]
Plot[Phi[p]^2, {p, -6, 6}]
```

Before delving deeper into the explanation of the glare point model, the connection to the quantized electromagnetic field shall be made. The distribution of the scalar wave field in the starting plane may be seen as a projection of a wavefunction into position space, while its corresponding Fourier transform is the projection into momentum space. This is a result well known both in Fourier optics [Goo05] as well as quantum mechanics [LBCTL13]. As a distribution both for position and momentum of the wavefunction now is given, it does make sense to calculate a phase-space pseudo-probability distribution, such as the Wigner function (2.48). The resulting phase space surface was in fact already given in section 2.3 and is nothing else but the Wigner function of the Schrödinger's cat state shown in figure 2.6. As a conclusion, it becomes evident that under certain simplifications **the fields associated with the glare points of a simple water droplet form a classical analogon to Schrödingers cat states in quantum mechanics**. Each glare point can be regarded as the coherent state $|\alpha\rangle$ as defined in equation (2.53), with a real displacement $\alpha \in \mathbb{R}$ equal to half the distance between a pair of glare points.

Moving forward in the explanation of Brunel's model, the double slit distribution 3.47a is further simplified to a Dirac point emitter, i.e. an infinitely small point source of a spherical wave. The point emitter configuration corresponding to the double slit 3.47a and ultimately to the real glare points shown in figure 4.28 is shown in the diagram 3.48a as a simple set of two points. A more irregular particle, such as an ice crystal shown in figures 4.29 and 4.30, may now easily be approximated by a larger, equally irregular set of glare points such as the one shown in figure 3.48b. The reasoning in this case is that each point emitter should correspond to a glare point appearing on one of the many facets of such an irregular particle.

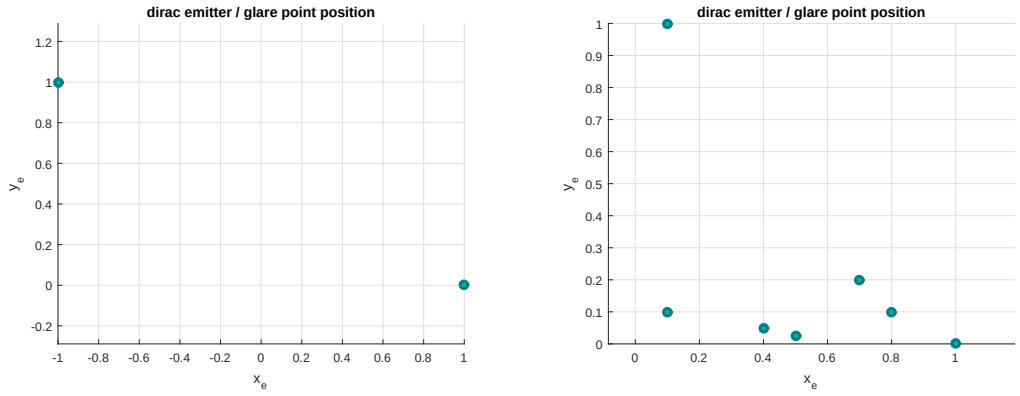

(a) Sphere/Droplet. **(b)** Irregular Particle.

Figure 3.48: Position of spherical wave dirac emitters as a simple model for actual glare points.

The light emanating from the glare points of figures 3.48a or 3.48b then needs to pass an optical setup sketched in figure 3.46, in order to be recorded on the 2D surface of the CCD camera chip. The field distribution due to the glare points in the source plane transverse to the optical axis of the experiment is given by:

$$E_0(x_0,y_0) = \sum_{j=1}^{N_{gp}} A_j \cdot e^{i\cdot\phi_j\cdot\delta(x_0-a_j,y_0-b_j)} \tag{3.98}$$

where (a_j,b_j) is the coordinate of the glare point j in the source plane coordinate system (x_0,y_0), N_{gp} is the total number of glare points (2 in the case of a sphere), A_j is their individual amplitude and ϕ_j the corresponding phase offset. Following the argument of Brunel [BRJB15], the imaging system observing the glare points in figure 3.46 is represented via its optical transfer matrix as defined for instance in the book [Hec02] by Hecht.

$$M_{lens} = \begin{pmatrix} A & B \\ C & D \end{pmatrix} = \begin{pmatrix} 1-\frac{z_2}{f} & z_1+z_2-\frac{z_1 z_2}{f} \\ -\frac{1}{f} & 1-\frac{z_1}{f} \end{pmatrix} \tag{3.99}$$

Using the matrix elements, it becomes possible to give a closed expression for the intensity of the field on the CCD chip as induced by the glare points.

$$I(x,y) \propto \sum_{j=1}^{N_{gp}} \left(\sum_{k=1}^{N_{gp}} \left(\frac{A_j A_k^*}{\lambda^2 B^2} e^{i\frac{\pi A}{\lambda B}\left[\left(a_j^2+b_j^2\right)-\left(a_k^2+b_k^2\right)\right]} \cdot e^{-i\frac{2\pi}{\lambda B}\left[(a_j-a_k)\cdot x+(b_j-b_k)\cdot y\right]} \right) \right) \tag{3.100}$$

where (x,y) are the coordinates in the image plane of the CCD chip. Examples for such a field are given in figure 3.49a for a droplet and 3.49b for a random distribution of glare points. Just as in the double slit case, the intensity in figure 3.49a shows 2D interference fringes perpendicular to the imaginary line connecting the two glare points. This is a first indication for the physical validity of the model. The random distribution of points given in figure 3.48b produces the result shown in figure 3.49b. The irregular distribution of the points produces a likewise irregular interference pattern consisting of distinct speckles. Due to small number of glare points and their small separation the speckles are larger than the naturally occuring speckles shown in figure 4.31. Given the intensity on the CCD chip, it is possible to compute its FFT or autocorrelation function, which has been done in figures 3.50a and 3.50b for the corresponding intensities in figure 3.49a and 3.49b. This enables the numerical simulation of the postprocessing steps of the IPI measurement technique presented in section 4.3. There the glare point separation would be determined via the curvature maximum of autocorrelation functions such as 3.50b.

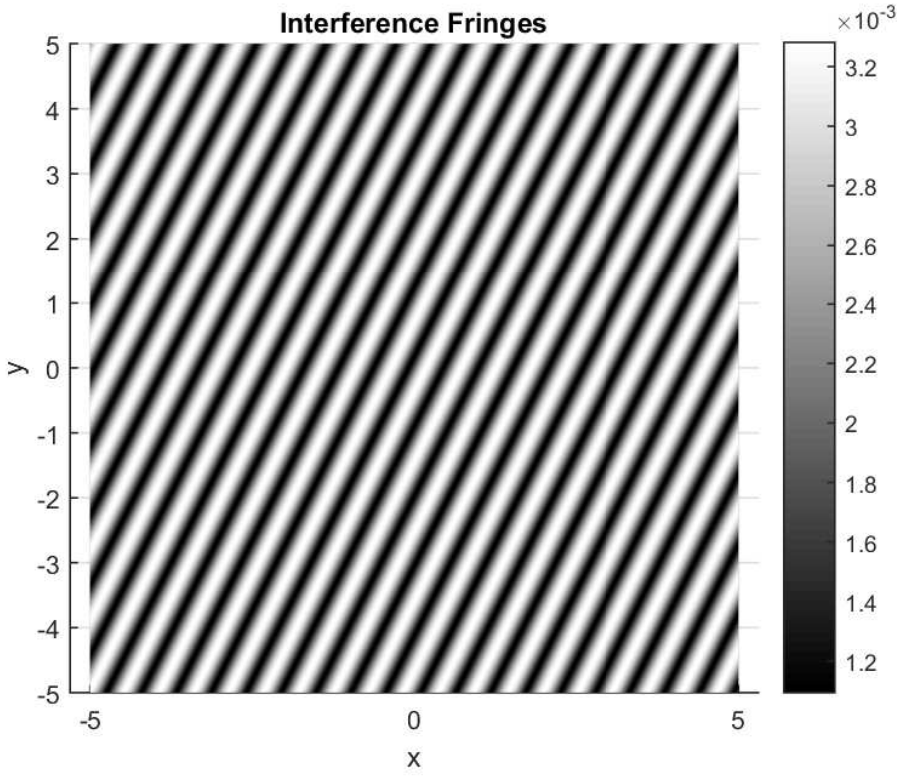

(a) Fringes perpendicular to the axis defined by two glare points as in figure 3.48a, indicating a spherical scattering particle.

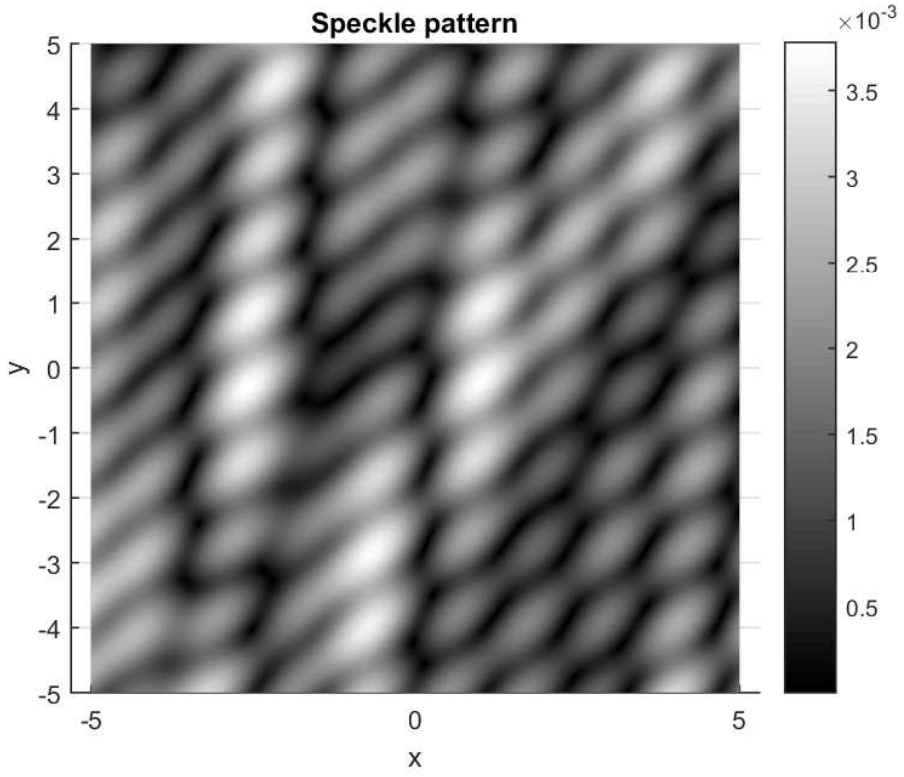

(b) Random speckles created by the emitter distribution shown in figure 3.48b, indicating an irregular particle.

Figure 3.49: Interference arising from the glare point sources.

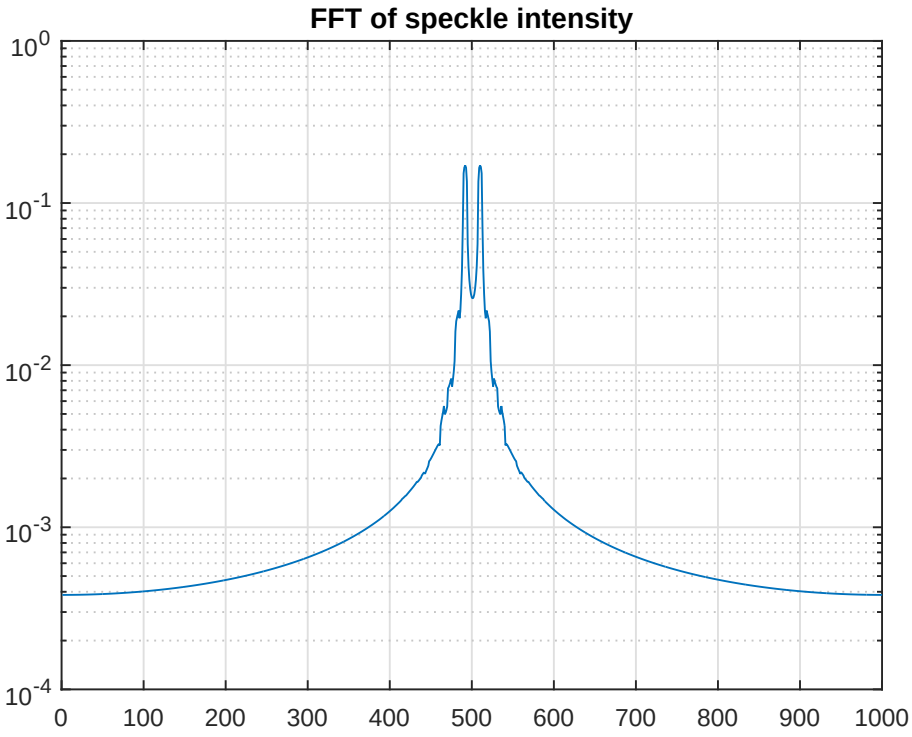

(a) Linear FFT of the interference fringes for a sphere 3.49a.

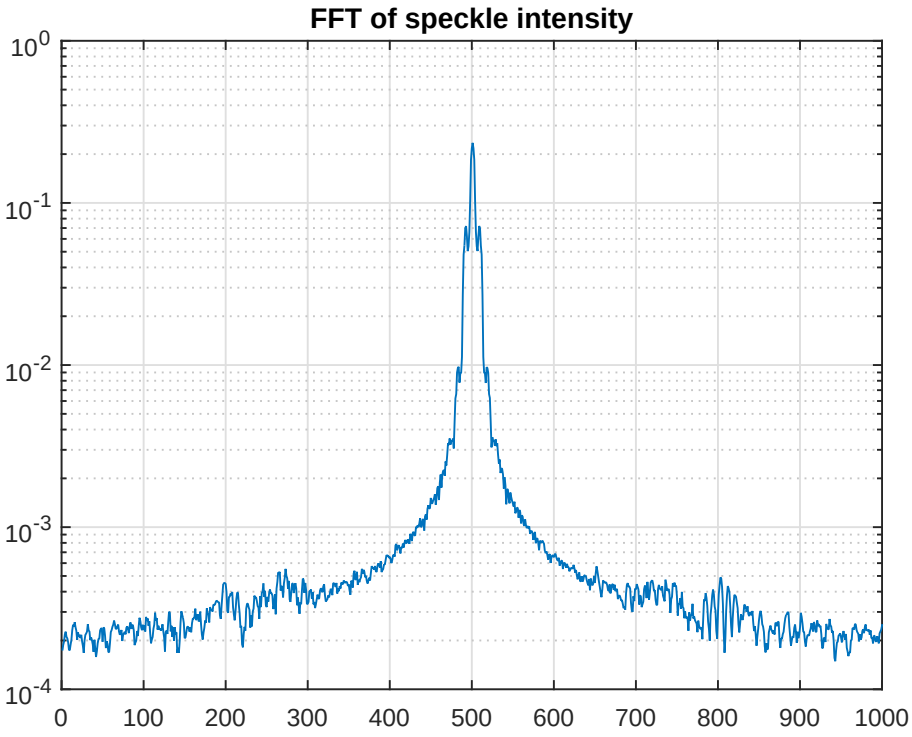

(b) Linear FFT of the speckles in figure 3.49b.

Figure 3.50: Shifted FFT of the centre line of the 2D simulated interference patterns.

4 Experiment

Light, seeking light, doth light of light beguile;

— Berowne in Love's Labour's Lost [Sha12] Act 1. scene 1, l. 77, by Sir William Shakespeare

As argued by Shakespeare in the preceeding quote, it is undesireable to ruin the light of one's eyesight by searching the light of truth solely in books. Thus in order to study the real properties of non-spherical particles, several laser-optical experiments using three distinct measurement principles have been conducted in parallel with the modelisation effort. First of all, the most important quantity extracted from the simulations as well as for the atmospherical physicists and radiative transfer experts, namely the phase function M_{11}, was measured. Second, the applicability of the time-shift method developed by Schäfer [Sch13] to ice crystals was investigated in comparison to direct high-speed imaging. Third, the novel Interferometric Particle Imaging (IPI) technique already sketched in section 3.5 was applied to water droplets and highly irregular ice crystals. All three methods will be explained in detail in the following three sections together with a presentation of the obtained results. Generally, measuring ice crystals is a very difficult endeavour even in comparison with droplet measurements. The extreme irregularity of single crystals lead to likewise irregular results and procurement, storage and handling of real ice crystals necessitated the development of a completely new experimental infrastructure during the course of the Ph.D. thesis.

4.1 Survey of azimuthal distribution of the scattered intensity

As already mentioned, one of the most important quantities to measure for a droplet or an ice crystal in an atmospherical science context is the phase function $M_{11}(\theta)$ as a function of the polar angle θ. Consequently the first experiment conducted during the thesis was aimed at obtaining phase functions of ice crystals. Such measurements of already been performed recently for instance by Smith et al. [SCB+15] in the ice cloud chamber (MICC) of the university of Manchester. Due to the nature of the phase function the principle setup of the experiment carried out at the CSI laboratory needs to be identical with the Manchester experiment. Of course the experiment described here must be considered less sophisticated in the sense that it is not coupled to an ice cloud chamber or a similar expensive device for the delivery of ice crystals as pristine as possible. Before beginning the actual experiments, the first obstacle to overcome was finding a source for ice crystals with the desired properties. To this end, several proposals have been carried out and evaluated. The following subsection will present several of the ice crystal source that have been considered.

4.1.1 Ad-hoc sources of ice crystals

Several simplified sources of ice crystals are described in the following. These ice crystals can only be considered approximations to real atmospheric ice crystals, which can only be provided in a laboratory setting at large facilities such as the MICC in the UK [Eme15] or the AIDA chamber [Han15] at the KIT in Germany.

Rapid Prototyping Crystals

The first approach to provide valuable alternatives to real atmospheric ice crystals were analogues produced using a rapid prototyping (RP) method called stereolithography (STL). The manufactured hexahedral prism shown in figure 4.1a has an edge length of 2.54 mm and a height of 2.4 mm. The index of refraction of the base photopolymer was determined using the method of Duc de Chaulnes [Cha67] and has a value of $n = 1.60 \pm 0.07$, which is a value attained by real ice at a wavelength of roughly $\lambda \approx 10\mu m$ according to Yang [WY12]. The primary advantages of this approach is that the ice analogues are very easy to handle. The polymer does not melt or re-sublimate under laboratory conditions and consequently does not necessitate any atmospheric control. Furthermore the photopolymer is not toxic and has no

adverse effects on the health of the experimenter, if not purposefully ingested. This is in contrast to sodium fluorsilicate compounds [ZFT64] which have a matching geometry and refractive index according to Ulanowski [Ula05], but are highly toxic. Another possible alternative are analogues manufactured microscopically using electron beams, which is again prohibitive due to the high cost associated with the manufacturing process in this case.

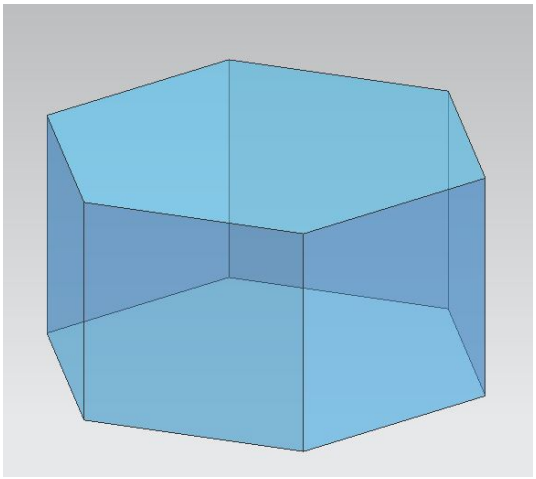

(a) Siemens NX 6.0 CAD model prior to 3D printing.

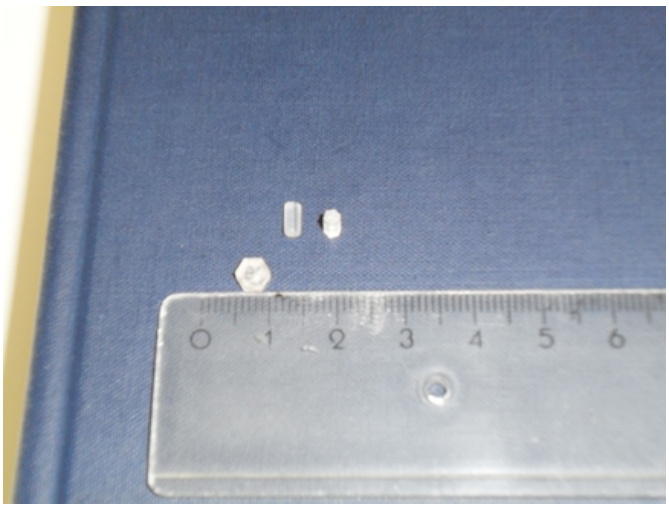

(b) Photograph of a selection of printed crystals. Ruler in cm and mm for scale.

Figure 4.1: Ice crystal analogues manufactured using Rapid Prototyping (RP).

Figure 4.2 demonstrates, that it is also possible to levitate an RP crystal in an acoustic levitator in order to perform optical experiments on it, despite the associated stability issues.

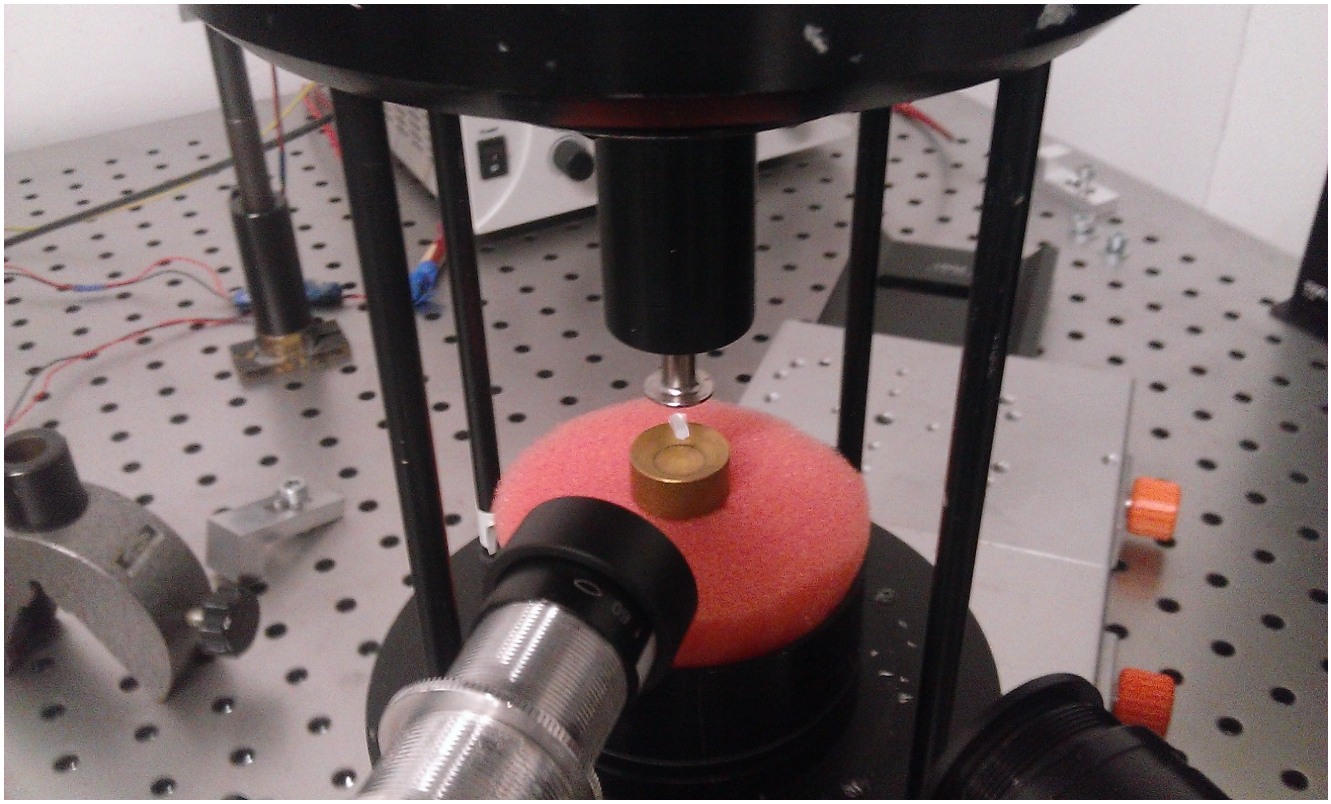

Figure 4.2: RP crystal hovering in an acoustic levitator.

Diffusive growth

Ordinary ice I_h does grow from ambient water vapor as explained by Libbrecht in the review article [Lib05]. This allows one to grow ice dendrites in a very simple elementary school experiment also proposed by Libbrecht [Lib99]. As shown in the sketch of the experiment displayed in figure 4.3a, a central cavity in form of a closed plastic bottle will contain a higher humidity level due to a wet sponge placed at its top. The humid air will then be cooled via chunks of dry ice (solid CO_2) placed outside of the plastic bottle and a diffusive growth of ice needles will take place on any free surface and especially on thin fibres suspended in the centre of the cavity. Despite its simplicity, the method worked flawlessly, as can be seen in figure 4.3b, displaying results obtained in 2013. Nevertheless, it is not entirely devoid of drawbacks. The dry ice used for cooling is difficult to handle itself, poses a risk to the experimenter and needs to be fetched at the chemist's department each time it is depleted. Due to the associated risk of suffocation the dry ice and the experiment itself need to be stored under an extractor hood, where the carbon dioxide quickly sublimates away due to the standard atmospheric conditions and the constant convection of fresh air. Furthermore, the resulting dendrites are very small and very brittle and thus very difficult to handle. This becomes problematic as the volume of ice produced by the experiment is very small and thus the method in its current stage must be deemed insufficient as a source for optical experiments. Early experiments revealed that upscaling the otherwise satisfactory method required a different, more precise approach in temperature and humidity control than a wet sponge and dry ice alone could provide. Much more sophisticated designs based on the same principle will be discussed in section 5.1.

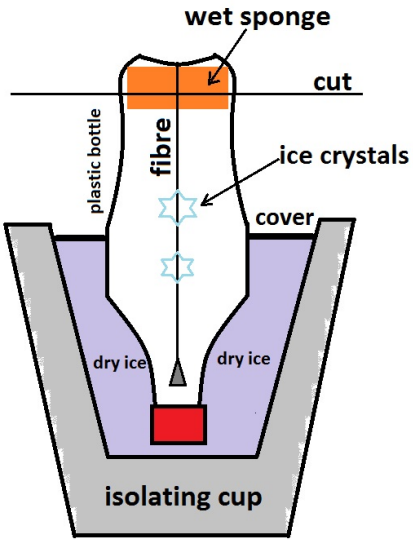

(a) Sketch of the dendrite growth experiment following an idea of Libbrecht [Lib99].

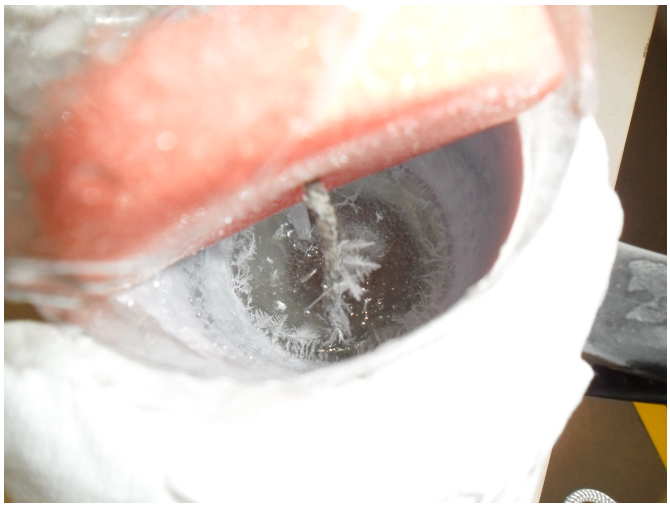

(b) First humble dendrite growth results.

Figure 4.3: Growing dendritic ice crystals in a bottle.

Tropospheric Crystals (Ordinary Snow)

The final approach employed for large scale measurements was the gathering of natural snow. On January the 6^{th} 2015, temperatures at the Darmstadt Lichtwiese campus were between -1.3 and -6.2 degrees Celsius and heavy snowfall as shown in figure 4.4 allowed the collection of tropospheric ice crystals in large quantities. The snow was stored in a closed refrigerated container submerged in a deep freezer for long-term storage. These crystals were available in abundant quantities and easy to handle. Furthermore these were naturally occuring ice crystals. Nevertheless, one can see in figure 4.29 that these crystals are highly irregular and do not retain their hexahedral symmetry. Possible causes for this are partial melting due to short periods in warm rooms, mechanical stresses due to the handling in bulk quantities and resublimation due to extended storage in a very dry climate.

Figure 4.4: Snowfall at Darmstadt's university stadium in January 2015 as a natural source of ice crystals usable in experiments.

4.1.2 Experimental setup for phase function measurements

The setup of the optical components for the phase function measurement is identical to the one used in the experiments carried out at the MICC of the university of Manchester at the exact same time and later published in [SCB+15]. Due to the definition of the phase function this is inevitable. A sketch of the setup employed in the experiments performed at the SLA is shown in figure 4.5a while a photographic illustration is shown in figure 4.6. The first problem to solve when doing optical experiments with water ice crystals is creating an environment that prevents the crystals from melting for the duration of the experiments. The solution employed in this thesis was using the laboratory freezer EL 41 LT from Nordcap GmbH & Co. KG as the environment for the experiment. The inner volume of the freezer was $130 \times 45 \times 68 cm^3$ and the temperature could be pre-set at any value between -25^o and -45^o degrees Celsius. Due to the fact that the laboratory freezer was operated openly during the experiments, a temperature gradient over the experimentation volume was measured. At a laboratory temperature of 20.5^o degrees Celsius and a freezer setting of -30^o C, the following average temperature differences with regard to the pre-set temperature were measured:

- $+2.75^o$ C at the bottom.
- $+3.79^o$ C at half height.
- $+12.81^o$ C at the top.

The detailed distribution of the temperature inside the freezer obtained via thermocouple measurements is listed in the appendix of this thesis and a simulation of the temperature diffusion process is shown in figure 4.7. Diffusion instead of natural convection is assumed to be the dominant heat transfer mechanism in the present case, which is justified by

the layout of the freezer, where the cold air is trapped at the bottom and the warm air at the top creates an atmosphere stratified according to the temperature distribution and with no convective flux. The compressor of the freezer was working in cycles of 7.33 minutes duration for cooling and 6.9 minutes duration of rest. Due to the vibrations associated with the compressor operation, single experiments are always limited to the time window free of vibrations. The decision to conduct the experiments inside a freezer also made special arrangements necessary for the optical components. The basic layout of the phase function measurement is possible in two variants sketched in figures 4.5a and 4.5a. The first variant allows the angular resolution of the polarisation through the application of a polarising beamsplitter in front of the photodiodes, while the second variant dispenses the polarisation measurement in favour of a stronger signal of the scattered intensity. The signal of the photodiodes used to measure the scattered intensity in the unilluminated state is given in the appendix. Common to both variants is the principle that a particle such as an ice crystal or a water droplet is suspended inside an acoustic levitator or atop of a thin needle and illuminated by a continuous coherent light source (i.e. a laser), while the scattered light is recorded over the polar angle θ.

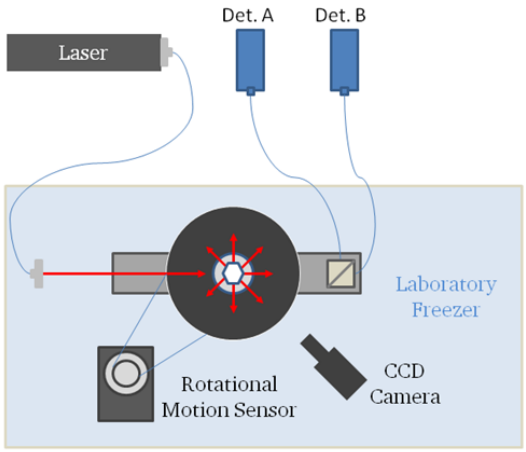

(a) Variant 1 resolving polarisation.

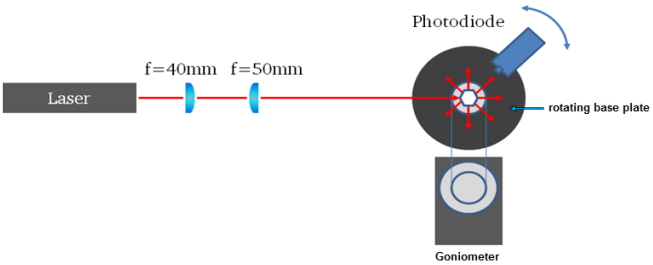

(b) Variant 2 with better Intensity signal.

Figure 4.5: Sketch of the experimental setup used to measure phase functions of ice crystals adapted from [Gan14].

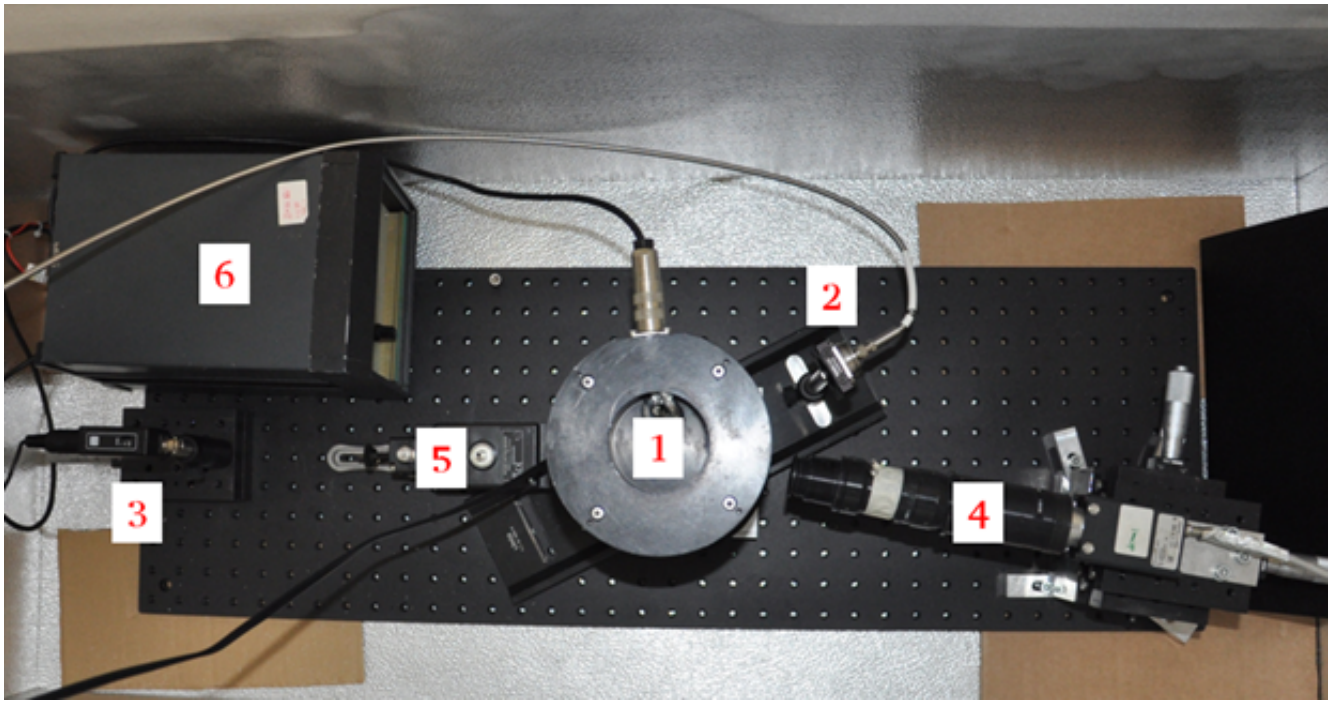

Figure 4.6: Photograph of the actual experimental setup immersed in a laboratory freezer taken by A. Gansmann [Gan14]. The components are (1) acoustic levitator, (2) collimated output of a polarisation conserving optical fibre from the HeNe laser, (3) Single Photodiode as a detector, (4) CCD camera with magnification lens array focused on levitator cavity, (5) Goniometer for the polar angle θ, (6) laboratory voltage supply and frequency control of the acoustic levitator

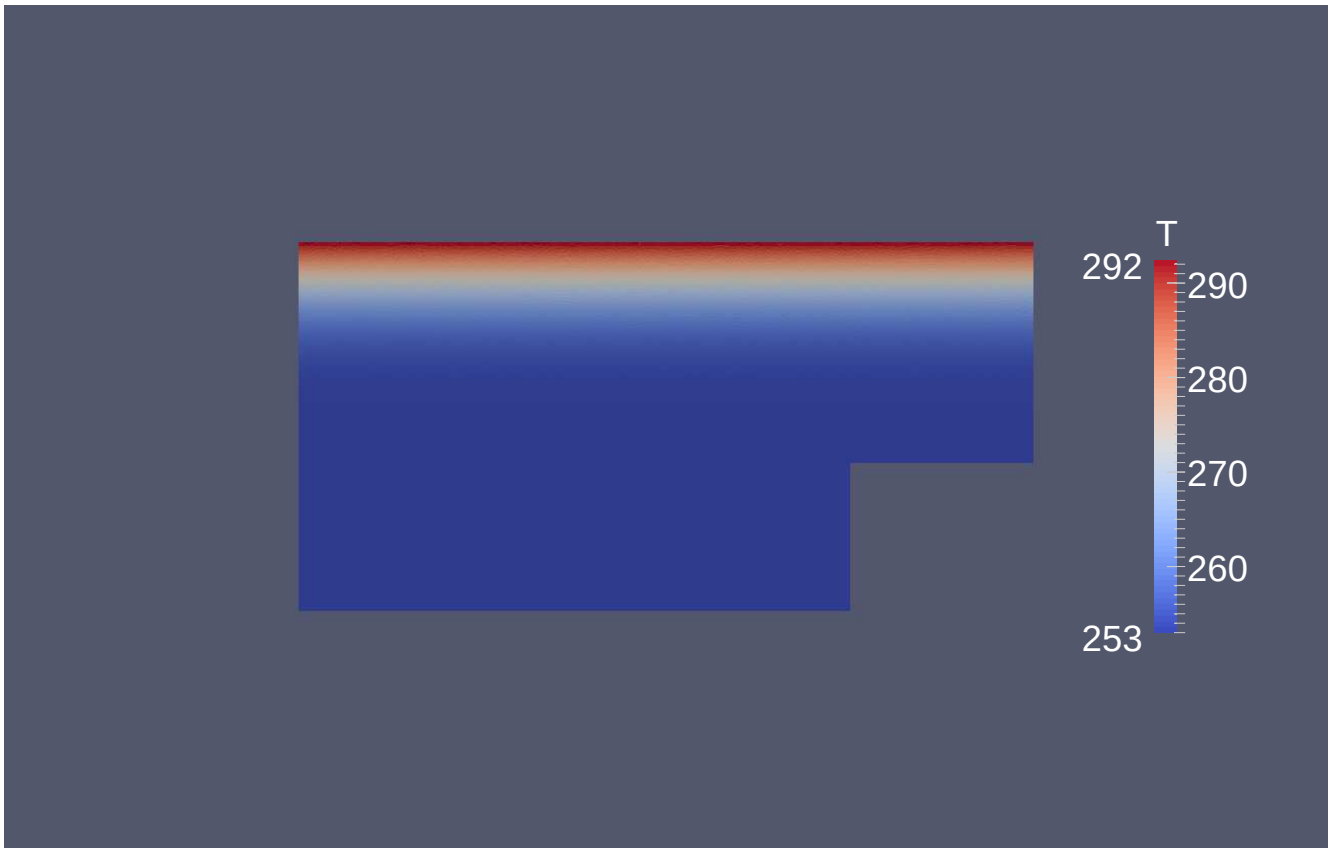

Figure 4.7: Calculated 2D temperature field inside the laboratory freezer after an opening time of 10 minutes. Calculations have been performed on an unstructured quadrilateral mesh using the `laplacianFoam` solver as part of the *OpenFOAM®* bundle, solving the diffusion equation for the temperature. Top and bottom have a Dirichlet boundary condition of 293 and 253 Kelvin respectively and the perfectly insulated side walls have a Neumann boundary condition. The temperature diffusivity of air was assumed to take a value of 19 $\frac{mm^2}{s}$. The corresponding mesh is shown in the appendix.

The acoustic frequency of the acoustic levitator typically resided around 58 kHz. As a source of illumination in the experiments a HeNe laser was used with a wavelength of $\lambda = 632.8nm$, a $\frac{1}{e^2}$ beam diameter of 1mm [Yu13] and a coherence length of 30cm. The laser beam was linearly polarised with a ratio larger than 500 to 1 and had a typical power output of around 18 mW. A detailed description of the operational principle and construction of a Helium-Neon laser can be found in the book [EE03]. A camera focused on the levitated particle is used to obtain a direct image. This camera is a Basler A631f monochrome industry camera equiped with a Sony ICX267/AK progressive-scan CCD chip having a resolution of 1392×1040 pixels at 30 frames per second and a C-type lens mount according to the camera manual [Bas10]. The calibration of the camera and lens system was performed as in reference [Yu13], such that the size of an individual pixel can be determined at $4.65 \times 4.65\mu m$. In order to achieve an appropriate magnification, a Navitar 1-60439 0.5X adapter with the Navitar Zoom 6000 lens array was used, resulting in 12X zoom. The operation principle of the acoustic levitator is already explained in detail for instance in the article [YPT98] and this thesis will only go so far as to say that the contactless levitation of a particle inside a levitator cavity is due to the axial force created in between the pressure nodes of an ultrasonic standing wave inside the levitator cavity, which according to [tec] is given by:

$$F_{ax} = c_{w,ax} \cdot \frac{\rho_0}{2} \cdot v_{max}^2 \cdot d_S^2 \tag{4.1}$$

where $c_{w,ax}$ is the drag coefficient of the sample S in the axial direction, ρ_0 is the density of the surrounding air, v_{max} is the sound particle velocity amplitude and d_S is an equivalent diameter of the particle. An illustration of the principle is given in figures 4.8.

According to the manual, the levitator is not intended for use in environments below 0^o C, nevertheless no problems have been encountered during the experiments. In contrast, an adverse effect of the low temperatures on the HeNe laser is to be expected. The efficiency and stability of the HeNe laser has a strong temperature dependance, as it is in its essence simply a bottle containing a specific gas mixture [EE03]. Thus measures had to be taken in order to keep the laser in the climate controlled laboratory environment at around 20.5^o C and on its optical desk.

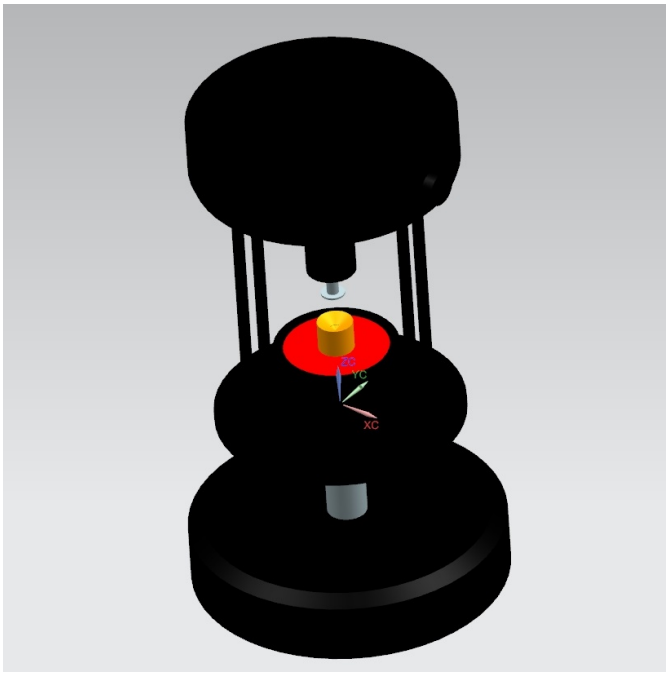

(a) CAD model of the levitator.

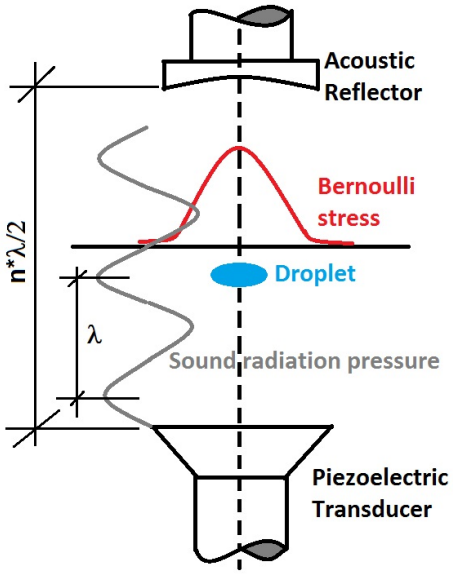

(b) Sketch of the operation of an acoustic levitator based on the description in reference [tec].

Figure 4.8: An Acoustic levitator.

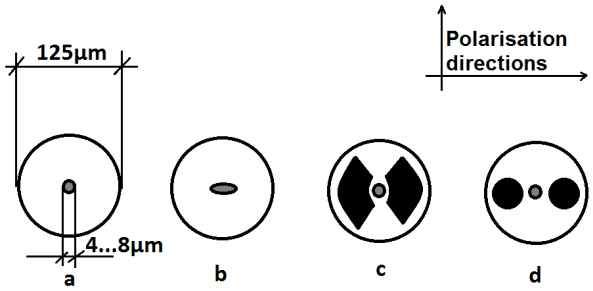

Figure 4.9: Different optical fibre core designs. (a) Monomode fibre with tiny circular core, (b) polarisation-preserving fibre with elliptic core, (c) polarisation-preserving fibre with bow-tie tension elements, (d) polarisation-preserving PANDA fibre with round tension elements. Hollow cores are coloured grey, tension elements black.

Due to this reason and the limited space inside the freezer, the laser and the photodiodes were kept outside of the freezer on a nearby optical desk. An optical coupling of incident and scattered radiation was achieved by connecting the components on the optical desk to the acoustic levitator in the freezer via optical fibres. A series of possible optical fibre core designs is shown in figure 4.9. For the laser beam, a polarisation-preserving monomode fibre was chosen, in order to keep both the linear polarisation and the TEM_{00} profile of the beam after its passage through the fibre. Specifically, this was a PM360-HP fibre with PANDA core from Thorlabs. A simple multimode fibre was chosen for couplaing the photodiodes, in order to maximise the scattered intensity reaching the sensors. This concludes the presentation of the optical setup constructed to measure phase functions.

4.1.3 Phase function results

This subsection presents several measured scattered intensity profiles. As the particles in the acoustic levitator often rotate very fast, it is assumed that the finite time necessary to measure the scattered intensity at one specific angle θ provides a natural orientational averaging.
The first experiments conducted were single orientation measurements with the ice analogues shown in figure 4.1b and using variant 2 of the setup shown in figure 4.5b as a first proof of the soundness of the measurement principle. The

symmetry axis of the analogon under scrutiny was perpendicular to the scattering plane defined by laser and photodiode and the incidence of the laser beam was edge-on to one of the corners of the hexagon, such that the incidence angle of the laser beam with the normals of two faces of the hexahedral prism was $\frac{\pi}{6}$ radians. The saturation of the photodiode over the polar angle θ is shown in percent in figure 4.10. The figure shows small reflection peaks at $\pm 110^o$ degrees, as expected when applying Descartes' law to the prism faces at the given incidence angle. In the forward region between $\pm 25^o$ degrees, the detector quickly gets saturated at 100 %, as it faces the laser beam directly. No halos are observed, due to the high refractive index of the photopolymer constituting the analogon and due to very rough surface of the prism faces.

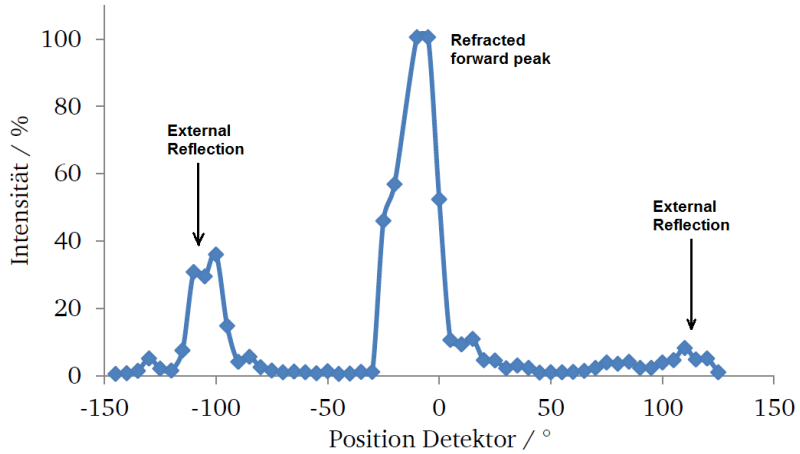

Figure 4.10: Photodiode signal saturation in percent over the polar angle for prismatic analogon at edge-on beam incidence. Constructive restrictions limited the angular domain from -145^o to 125 degrees. The angle was measured in a clockwise direction viewed from above.

The second measurement was conducted using real ice crystals, equivalent in its irregular morphology to the crystal shown in figure 4.29. As it was a polarisation resolving measurement, the variant 1 of the experiment inside the freezer shown in figure 4.5a was used. In this setup, two photodiodes were connected to a polarising beam splitter (PBS) acting as the detector head via two multimode fibres. As the thin-film polariser inside the PBS [Dem09] seperates the two orthogonal scalar waves of the incident wave in an arbitrary state, its polarisation is determined via the quotient of the saturation of the two photodiodes attached to the PBS. Figure 4.11 shows the signal ratio of the photodiodes over the polar rotation angle of an ice crystal fixated on a thin needle tip. The ice crystal is rotated counterclockwise while the PBS records the scattered light at the fixed forward scattering position in order to maximise the signal. Without a particle present, the polarisation ratio of the laser alone as measured by the PBS-photodiode setup is 40:1. A possible reason for not achieving the 500:1 ratio stated by the manufacturer of the laser is the early saturation of the diode. It can be seen clearly that this ratio is reduced drastically by inserting the ice crystal in the beam path, as shown in figure 4.11. The intensity ratio over the particle rotation angle is highly irregular, reflecting the irregular geometry of the ice crystal, but it is speculated [Gan14] that the low frequency variations in the polarisation ratio are directly related to the particle thickness.

The final measurement results obtained using again the experimental setup shown schematically in figure 4.5b can be seen in figure 4.13. In this case the scattered intensity of a levitated ice crystal over the polar angle in the scattering plane was measured directly by positioning the laser fibre output at 180^o degrees and rotating the photodiode fibre input around the acoustic levitator in a counterclockwise fashion. The logarithmic graph shows the expected forward peak and an otherwise highly irregular scattered intensity profile caused by the corresponding highly irregular geometry of the scattering ice crystal. This first of all shows, that it is possible to conduct phase function measurements using the proposed comparatively simple optical setup.

Furthermore, applying a low-pass filter to the data in figure 4.13 or in this case equivalently performing a proper statistical average by measuring the phase function multiple times for one ice crystal will reveal the smooth, featureless exponential function with its highest value at 0^o degrees forward direction, which is the characteristic phase function shape for very rough ice particles as calculated by Yang [WY12] and measured by Smith [SCB+15] for a particle size distribution. It is worthwhile to compare the measured relative scattered intensity to a computed phase function using the present geometrical optics code with a very high surface roughness value of $\sigma = 0.3$, which is beyond the limit of $\sigma = 0.2$ given by Yang and Liou [YN98]. The computed function is shown in figure 4.14. A sample result of the direct imaging sizing is

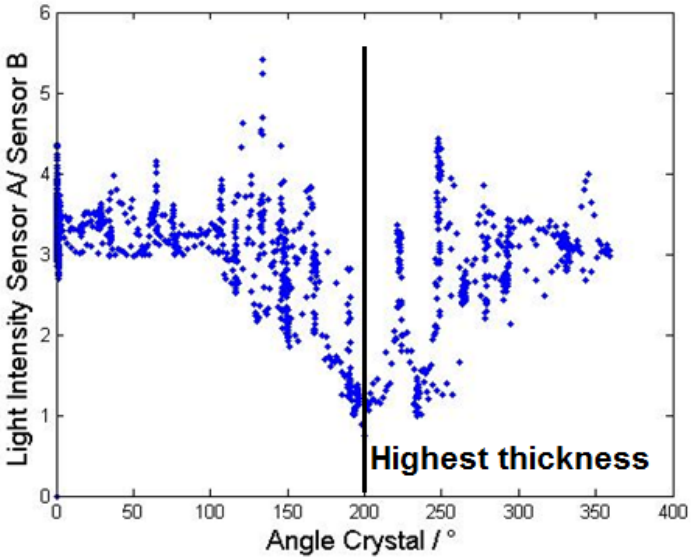

Figure 4.11: PBS-Photodiode signal ratio over the rotation angle of the fixated ice crystal. Detector position at the direct forward scattering angle. The indicated value of highest depolarisation corresponds to the largest thickness of the scattering particle.

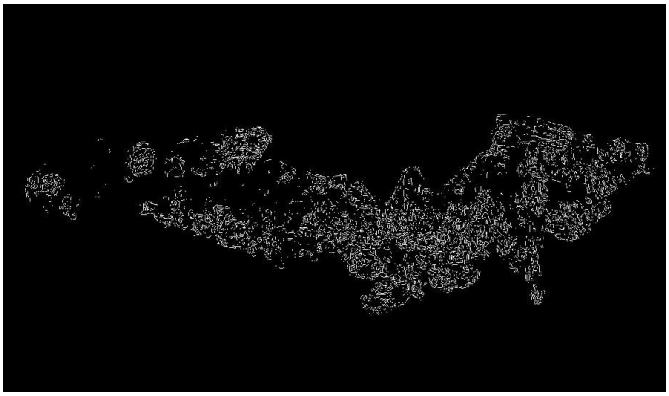

(a) Edge detection for crystal brightfield image.

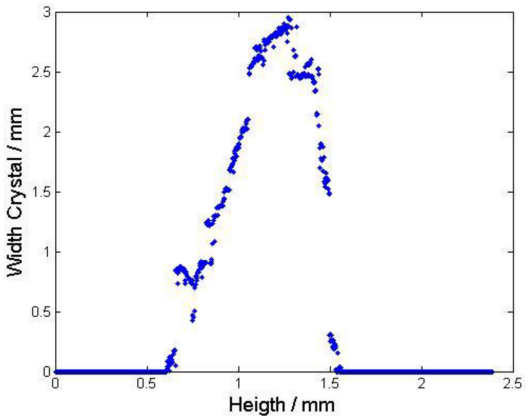

(b) Linear horizontal crystal dimension from top to bottom of image 4.12a.

Figure 4.12: Ice particle sizing from direct imaging.

shown in figure 4.12. Here a simple red LED is used in a brightfield configuration to take a microscopic focused image of the ice crystal and the boundary of the scatterer is extracted in using a Matlab algorithm similar to a high-pass filter [GWE04]. Due to the very rough surface of the ice particle, not only the outer contour but also surface protrusions are detected as edges. This is shown in subfigure 4.12a. From the extracted circumference of the particle, the size in one linear dimension of the image may be obtained as the difference between the first and last white pixel. A size distribution obtained in such a way is shown in subfigure 4.12b. A more sophisticated analysis of the image may rely on its autocorrelation function, applying methods described in section 4.3 which were developed at a later stage of the thesis for the IPI measurement analysis.

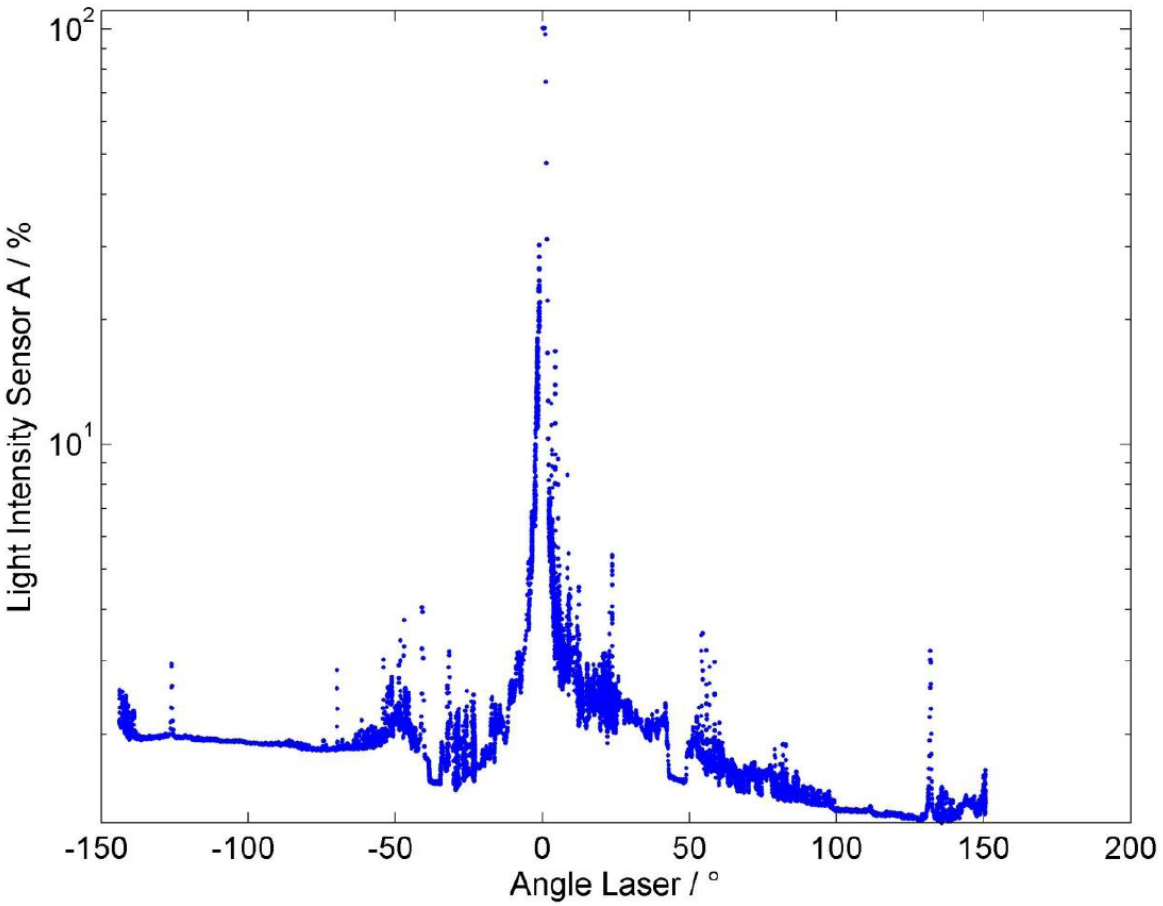

Figure 4.13: Logarithmic photodiode saturation percentage proportional to the scattered intensity over the polar angle θ in the scattering plane.

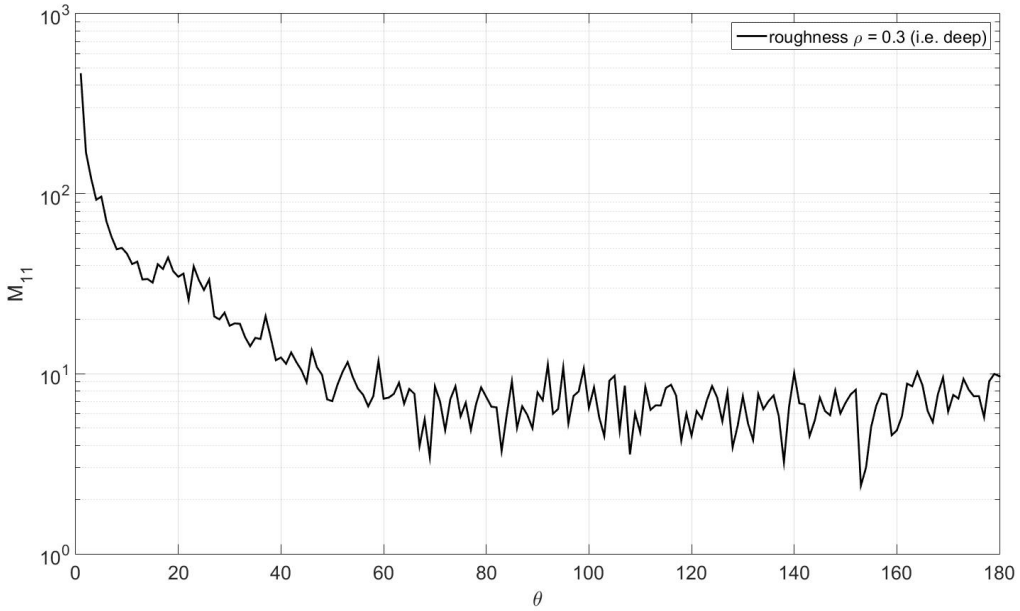

Figure 4.14: Computed phase function of a hexagonal prismatic ice crystal with extremely high surface roughness ($\sigma = 0.3$) for comparison with figure 4.13.

Probably the most simple structured light technique for analysing objects is the so-called time-shift technique, similar in this regard to the earlier but more complex phase Doppler method [ABDT03]. A thorough investigation of this technique for the characerization of transparent and opaque sprays was already performed by Schäfer in his dissertation [Sch13, ST14] and thus a detailed account on the method can be found in the references. The basic approach is to exploit the transverse profile of a beam focused below the size of the particle under investigation in order to extract their size, transverse speed and refractive index. This can be done in a backscattering configuration and a device containing both laser and sensor in a compact module is marketed by the company AOM Systems GmbH founded by Schäfer. A simple sketch of this process is shown in figure 4.15. The *SpraySpy*® probe developed by Schäfer and colleagues combines two conventional Time-Shift devices with a small vertical offset, in order to determine the speed of the particle in the direction of the offset via a time of flight methodology. As such, the Time-Shift signals shown in this section always appear in groups of two and due to the time of flight delay, there is always a short offset between the two pairs of signals. While in principle there is no obstacle towards the application of the method also to ice crystals, the theory for the interpretation of the measurement signals as explained in reference [ST14] relys entirely on the fact that the particles under consideration are perfectly spherical and is inapplicable to non-spherical particles. Irregular particles have nontheless been investigated by Damaschke et al. [KHD11] prior to this thesis using a laser-sheet configuration, and Damaschke clarifies that the loss of shape information in the irregular case reduces the time-shift technique to a simple time-of-flight measurement, or even simple particle number counting in the case of particles smaller than the beam profile.

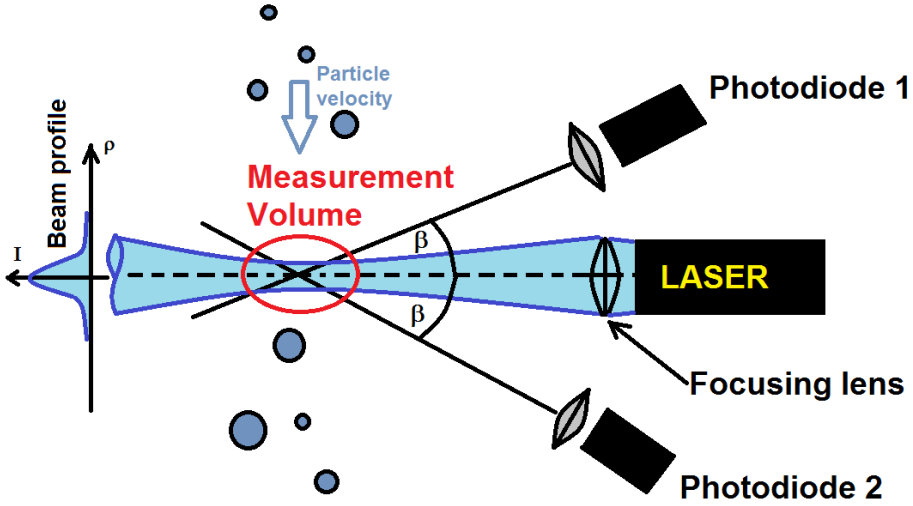

Figure 4.15: Schematic of a time-shift detector.

The time-shift module manufactured by Schäfer and colleagues is an integrated device with a component alignment roughly outlined in figure 4.15. It contains a blue semiconductor laser with a wavelength of $\lambda = 445nm$ and corresponding photo diode sensors positioned roughly at the rainbow angle β in order to capture a sufficient amount of internal and external reflection scattering orders. The coherence of the light source is of no consequence for the time-shift technique, as long as it has a high directionality and a suitable transversal profile (e.g. Gaussian, tophat, etc.). That directionality not necessarily implies coherence and vice-versa has been proven by Wolf [Wol78]. The current measurement data evaluation algorithms are nevertheless written for light sources of low coherence. A detailed account on where to best position the detectors is again given in the article [ST14]. This module has been combined with a Vision Research Inc. Phantom high-speed camera into an experimental setup shown in figure 4.16 at the Griesheim manufacturing site of AOM Systems in order to achieve simultaneous time-shift and imaging measurements.

The Phantom camera has a CMOS chip with a resolution of 1280×800 pixels. The calibration has been performed using the test target shown in figure 4.17 as well as a standard calliper gauge, leading to a pixel to size ratio of:

$$Ratio \quad \frac{Pixel_{CMOS}}{cm} = 100 \, \frac{px}{cm} \pm 4 \, \frac{px}{cm} \tag{4.2}$$

This allows to determine the size of a particle recorded by the camera by counting pixels.

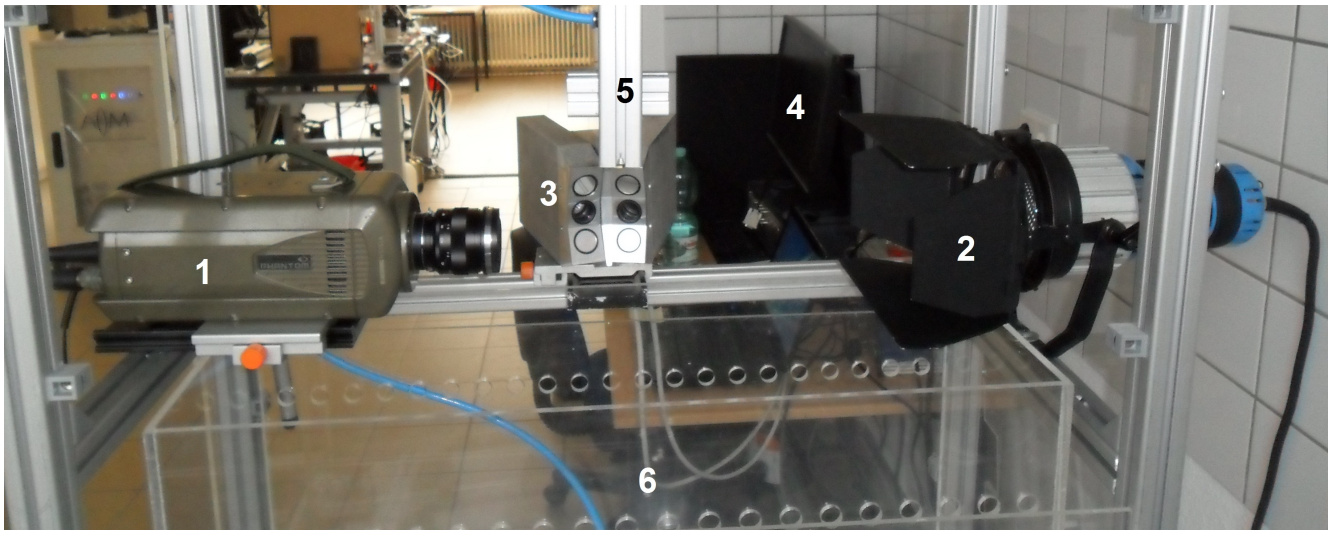

Figure 4.16: Combined Time-shift & Imaging experiment in Griesheim. (1) Phantom high speed camera and lens, (2) incoherent Hg vapor lamp, (3) SpraySpy® dual time-shift sensor prototype, (4) Data processing electronics, (5) spray nozzle or snow funnel, (6) collecting tank. Image kindly supported by AOM Systems GmbH. Not present in the photo is the plastic light diffusor sheet right in front of the mercury-vapor lamp. Also note the correspondance between element (3) and its sketch in figure 4.15.

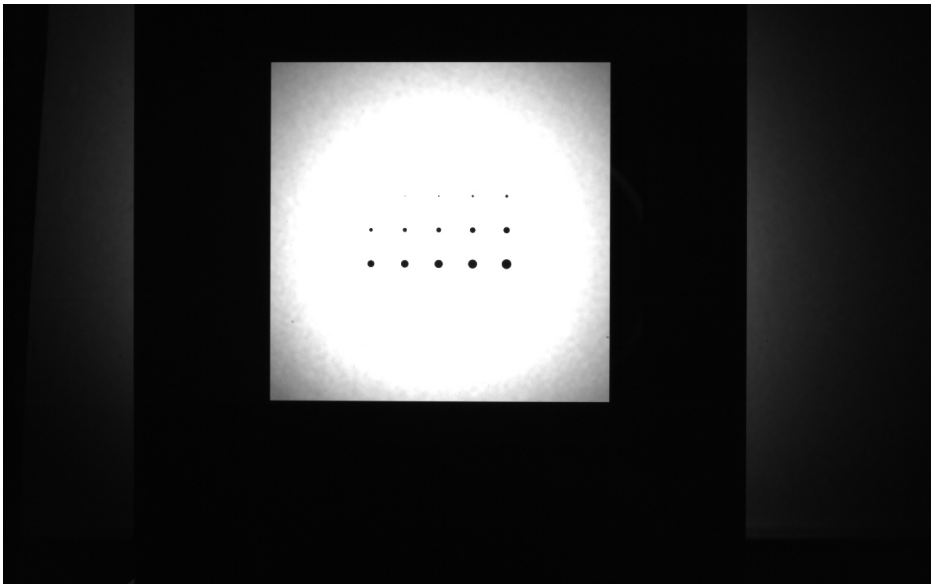

Figure 4.17: Imaging calibration target for the Phantom high speed camera.

An unprocessed image obtained via direct imaging and extracted from the .tiff sequence recorded by the CMOS camera can be seen in figure 4.18 and shows a distribution of natural snow flakes collected on the ground in Darmstadt. They are dropped directly above the field of view of the camera and are accelerating vertically through the image at a rate of 9.81 $\frac{m}{s}$ minus the viscous drag of the room temperature air. A range of time-shift signals obtained during the measurement work package is shown in figures 4.19, 4.20 and 4.21. It can be seen that the description of the signals by Damaschke in [KHD11] could not be reproduced. For comparison, figure 4.19 shows the time-shift signal obtained while measuring a spray with spherical droplets. The signal shows the four channels of the four photodiode detectors in the spray-spy module. The topmost channels in the figure were also corresponding to the topmost detectors in reality. Thus the topmost channel is the first to be influenced by a scattering particle. The 8bit signals have been processed using the software Picoscope and prepared using a low-pass filter at 0.1 MHz. The spray signal shows two signal groups, where the first is interpreted to belong to a single droplet large enough to allow the distinction between internal and external reflection modes. The second peak is interpreted to belong to a droplet smaller than the beam waist diameter, thus only showing one reflection signal.

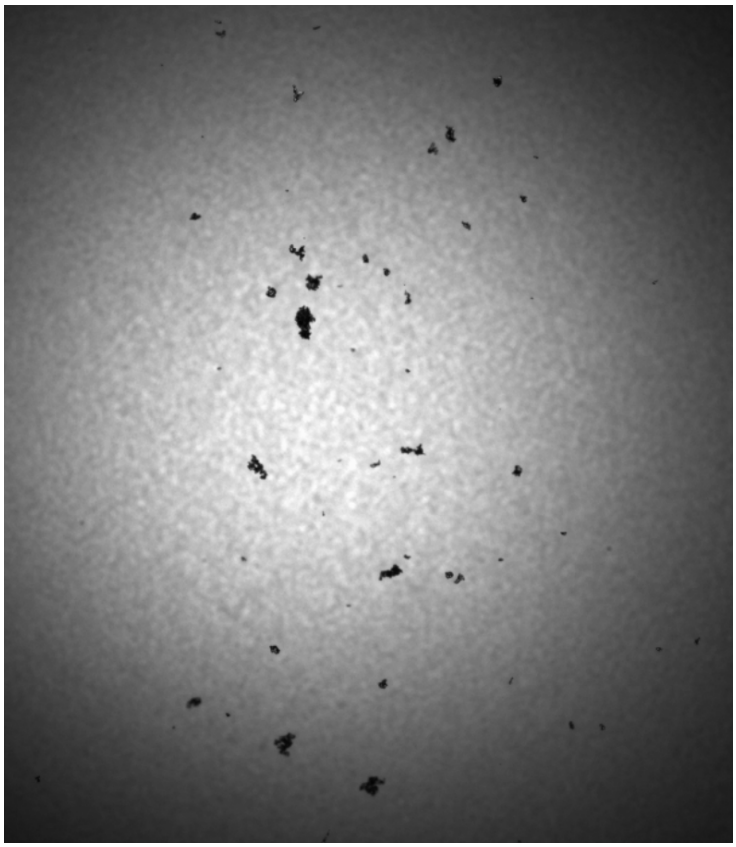

Figure 4.18: Unprocessed image extracted from high speed camera sequence.

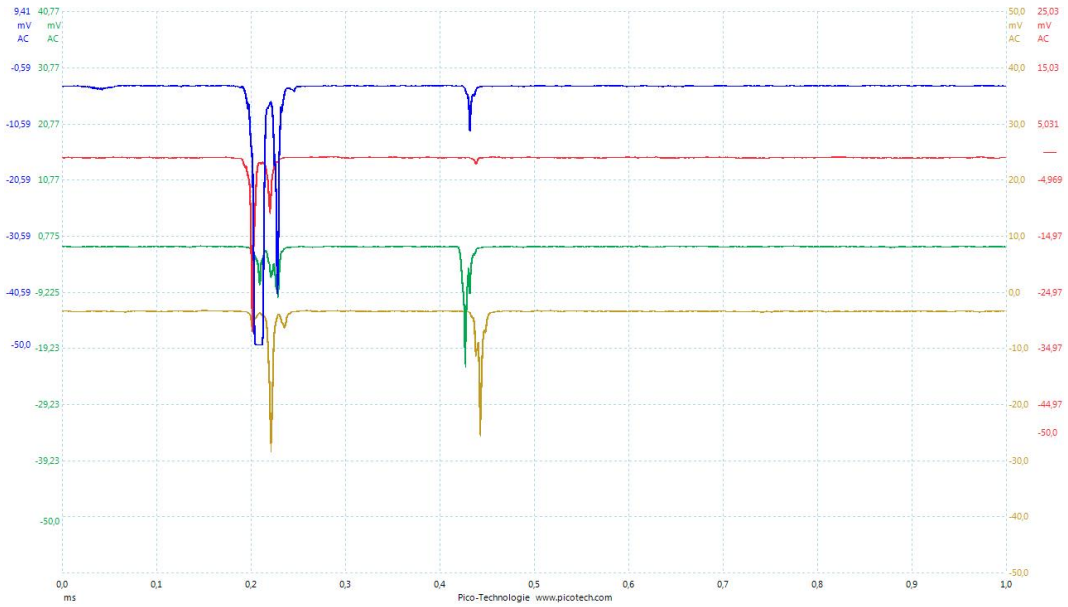

Figure 4.19: Spray oscilloscope signal showing two seperate droplets. The second droplet is smaller than the laser waist diameter and thus cannot be resolved.

The second figure 4.20 shows a signal group for several ice crystals passing the detection volume. The signal is of similar quality as for the droplets and in contrast to the results published by Damaschke [KHD11], the beam profile is also present in the reflected signal detected by the time-shift apparatus. The graph also shows multiple reflections pertaining to a group, indicating internal reflections on smooth facets. This further complicates an evaluation of the signal using the time-of-flight approach.

Figure 4.20: Ice crystal oscilloscope signal showing multiple reflections of the laser beam profile due to internal reflection.

Figure 4.21: Scrambled signal from an ice crystal due to its rough surface.

The situation may also be different if the surface of the ice particle is relatively rough, as in figure 4.21. Here the internal reflections are completely scrambled. All the signals above have been rescaled according to the signal energy, in order to make the signal amplitudes from all four detectors comparable. Figure 4.22 shows the largest problem encountered while postprocessing the data from the ice crystal Time-Shift measurements. The limited dynamic range of the detectors on the one hand necessitates the rescaling of the signals in order to recognise very weak signals, on the other hand the detector quickly gets saturated if it is hit by a bright direct reflection from the scattering particle as shown in figure 4.22.

Figure 4.22: Scrambled signal from an ice crystal with detector saturation and signal cut-off.

Time-Shift results

The current paragraph shows the result of the evaluation of the Time-Shift measurements. Due to the limited dynamic range of the photodetectors, only a very limited amount of data could actually be evaluated in comparison with the actual amount of signal data recorded. For the evaluation of the signals, the same algorithms have been applied that are used for characterizing sprays [ST14]. The measured diameter for the ice crystal ensemble is shown in figure 4.23 with a mean of 6 μm. As the ice crystals were obtained from the laboratory freezer surface, this value is expected to underestimate the size of the ice crystals considerably. The offset of 15 μm between the two Time-Shift devices in the spray spy probe allows the measurement of the falling speed of the ice crystals as shown in figure 4.24.

As the time-of-flight measurement is independent of the morphology of the particle, the speed determination is expected to be less problematic. Here the mean is at 0.035 $\frac{m}{s}$. The measured diameter of the ice crystals plotted against the natural logarithm of the measured speed values is shown in figure 4.25. Therein, a clear direct correlation between an increase in ice crystal diameter and an increase in falling speed becomes evident. Thus while the absolute value of the ice particle diameter might not be measured correctly, a relative size classification might be possible. Finally, it must be emphasized that all measurements have been performed using prototype equipment and the postprocessing of the measured signals was done using algorithms optimised for the application to liquid sprays. Consequently all results contain a considerable margin for error and unknown contributing factors. Certainly, further in-depth study of the response of the Time-Shift technique when facing non-spherical particles is necessary. A recommended course of action in the future would be the systematic creation of scattered intensity databases for specific particle shapes using an appropriate method developed in chapter 3. The inverse scattering problem present in the Time-Shift measurement may then be solved by searching for a best fit for the measured scattered intensity in the database. The number of parameters for which the database has to be calculated can be significantly reduced if the scattering particle shape is known a priori and further if a preferred orientation of the particle is known. This approach seems viable for industrial processes, where often a specific aerosol shape is produced. The immediate characterisation of natural ice crystals on the other hand seems less feasible, given current computational resources.

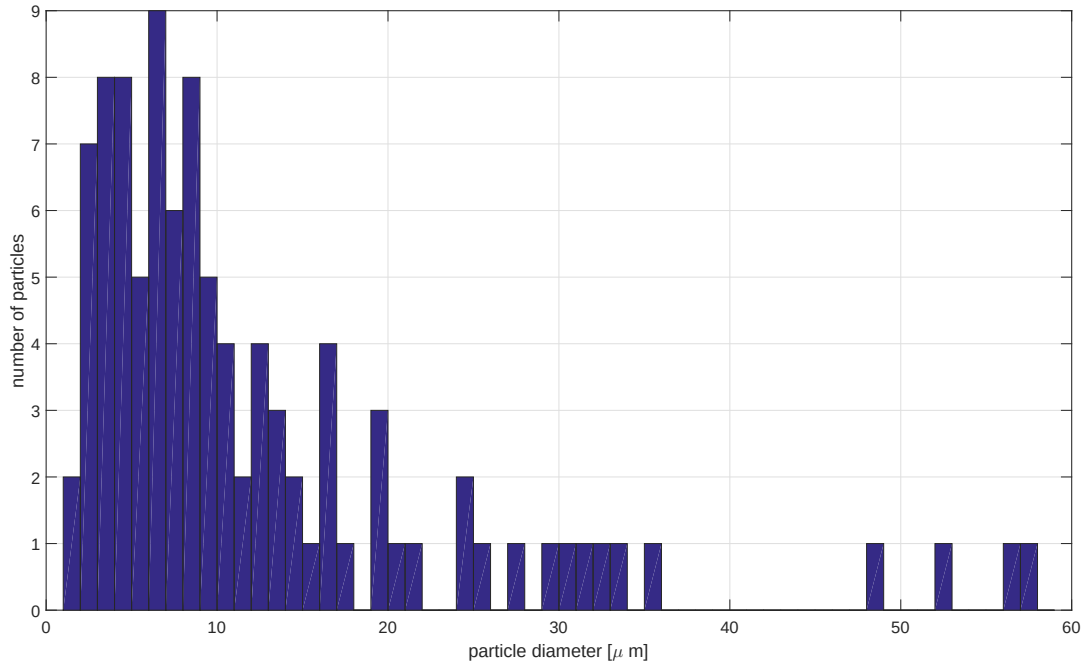

Figure 4.23: Ice crystal diameter histogram.

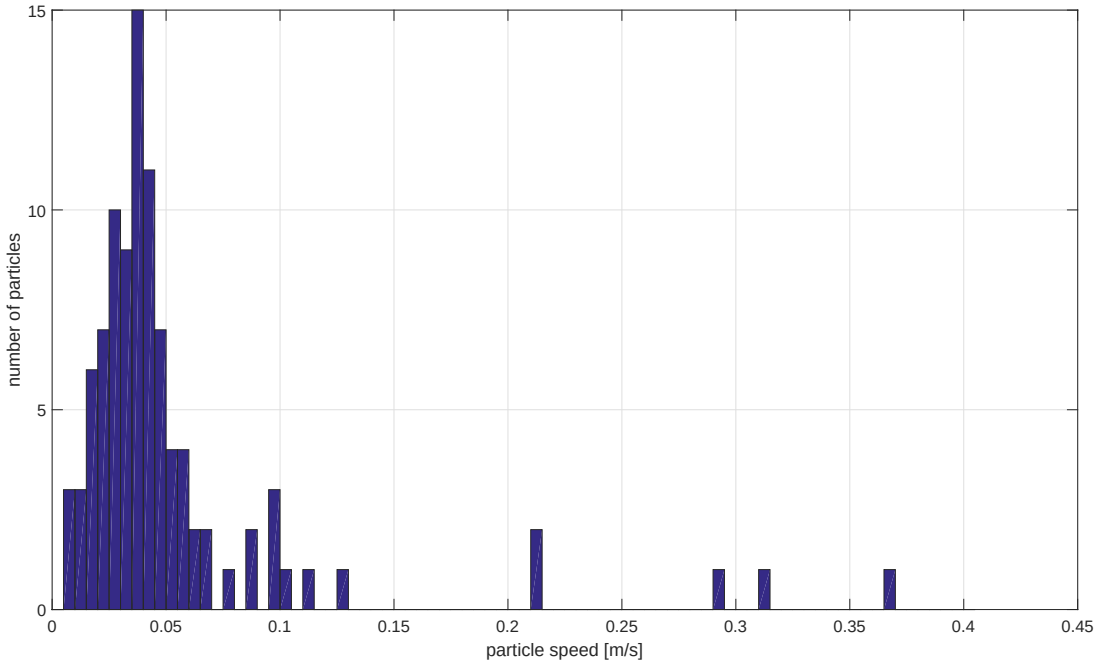

Figure 4.24: Ice crystal falling speed histogram.

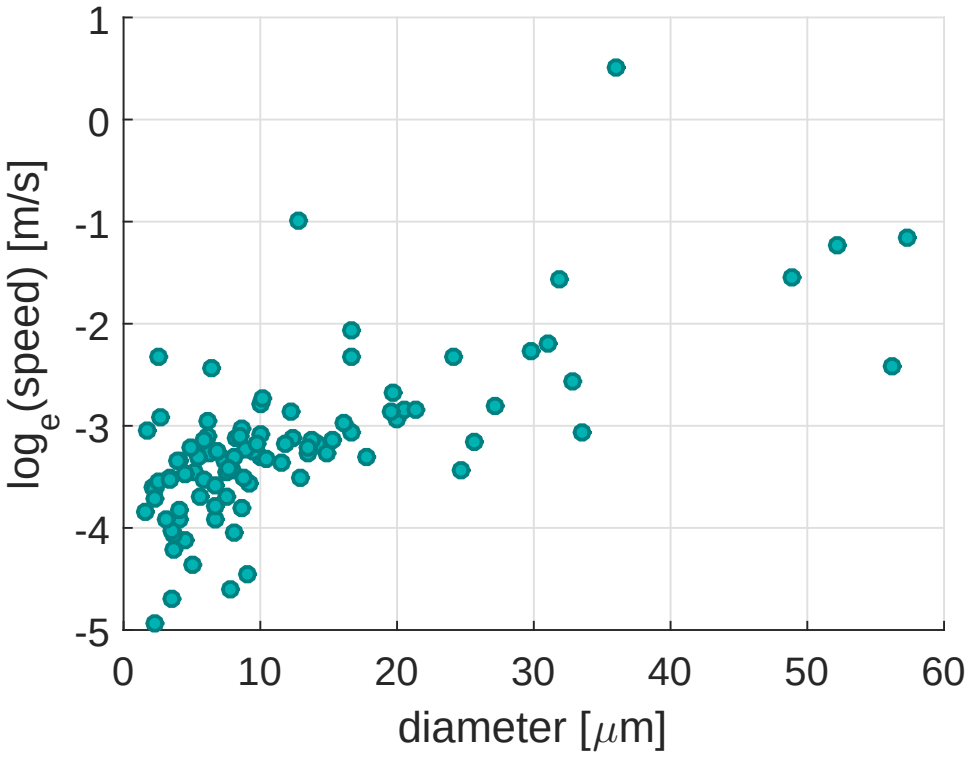

Figure 4.25: Ice crystal diameter versus logarithmic falling speed.

Techniques exploiting the coherence of a single field source for particle characterization have recieved a surge in scientific and engineering interest in the recent years (i.e. 2013-15) and have been applied succesfully to characterize spherical, non-spherical, and nano particles. The theoretical basis of the application of the IPI has already been explained in section 3.5. A broad overview over Fourier-interferometric techniques has been given in the recent habilitation thesis of Saengkaew [Sae14]. The most notable contributors to the field to date are the group of Saengkaew, Brunel and Gréhan [Sae14, SABG14], Van Beeck [GRVB14], and Damaschke [EKAD14]. All groups applied the technique starting from different backgrounds. Notable advantages of the technique are applicability below 30 μm and no microscopic lens array necessary in contrast to conventional imaging [Sae14], and large measurement volume, high data rate and reliable spherical / non-spherical discrimination [EKAD14] in contrast to the phase Doppler technique [ABDT03]. The interpretation of the obtained data in this thesis follows the description given by Van Beeck [GRVB14].
Several cases may occur for a camera-lens arrangement as shown in figure 4.26, where a coherent laser illuminates a scattering particle and the scattered light is collected by a lens and focused on a CCD or CMOS chip.

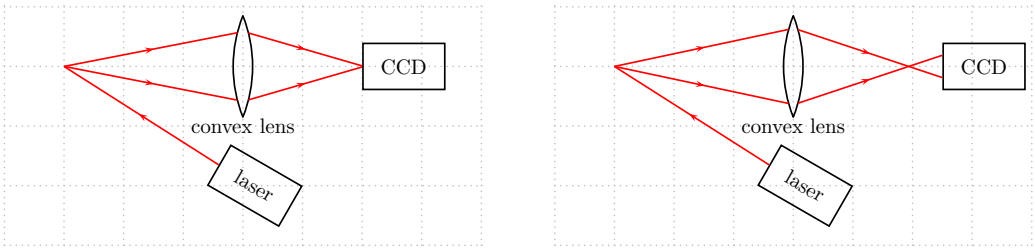

(a) In-focus situation. **(b)** Out-of-focus situation

Figure 4.26: Schematic situation of focused and unfocused imaging.

If the lens law [Hec02] for a lens of focal distance f is satisfied, the chip at z_2 sees a real image of the scatterer at z_1, such as the ones shown in figures 4.28, 4.29, and 4.30.

$$\frac{1}{f} = \frac{1}{z_1} + \frac{1}{z_2} \tag{4.3}$$

Note that in figure 4.30, speckles are already visible, despite the focused image, due to the coherent illumination as explained by Goodman [Goo05]. In the specific case of both $z_1 = z_2 = f$, Fourier optics [Goo05] predicts that in the image plane at $z_2 = f$ the Fourier transform of the scalar wave field distribution of the input at z_1 will be visible, which is identical to the Kirchhoff far-field diffraction pattern. A spatial frequency analysis of the imaging system displayed in figure 3.46 relevant to the current situation following the work of Goodman [Goo05] reveals the following relationship between object and image field:

$$U_f = \frac{A \cdot exp\left[i\frac{k}{2\cdot f}\left(1-\frac{d}{f}\right)(u^2+v^2)\right]}{i\cdot\lambda\cdot f} \cdot \iint_{-\infty}^{\infty} t_A(\xi,\eta)\cdot exp\left[-i\cdot\frac{2\pi}{\lambda f}(\xi\cdot u+\eta\cdot v)\right] d\xi d\eta \tag{4.4}$$

Where A is the amplitude of the illuminating plane wave, k its wavenumber, f the focal length of the lens, d the distance between lens and object, (ξ,η) the coordinates transversal to the optical axis of the lens in the object plane, (u,v) the transversal coordinates in the image plane, which is also the focal plane of the lens, λ the wavelength of the monochromatic light and $t_A(\xi,\eta)$ the change in amplitude of the incident wave due to the object. If the axial object position is at the focal distance $d \equiv f$ away from the lens, the image field becomes an exact Fourier transform of the object field. For all intermediate distances, the light will still interfere and the corresponding theory as applied to the glare point model has been discussed in section 3.5.

The experimental setup is shown in figure 4.27 and is very similar to the phase function measurement setup. A particle is suspended in the levitator cavity. A white LED array provides bright field illumination from the front, while the HeNe laser is posted in a narrow angle below 20^o degrees to the CMOS camera, such that the camera is positioned near the backscattering direction of the laser. A resulting focused image using both dark- and brightfield illumination at the same time is shown in figure 4.28.

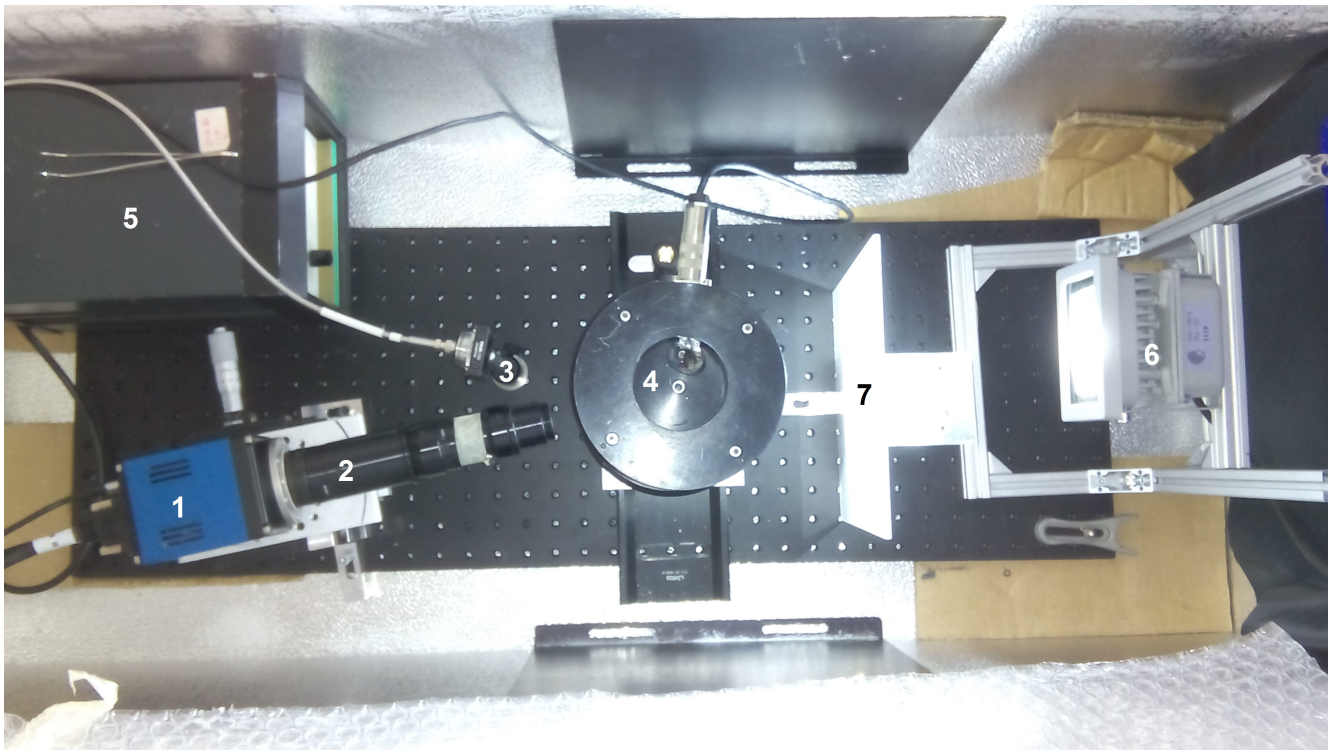

Figure 4.27: Laboratory freezer experiment for coupled direct and interferometric imaging of levitated particles. (1) pco.edge sCMOS camera, (2) Navitar magnification lens array, (3) HeNe fibre output, (4) acoustic levitator (top view), (5) levitator power supply and cold tweezer for ice crystal handling, (6) LED for bright field images, (7) plastic light diffusor sheet.

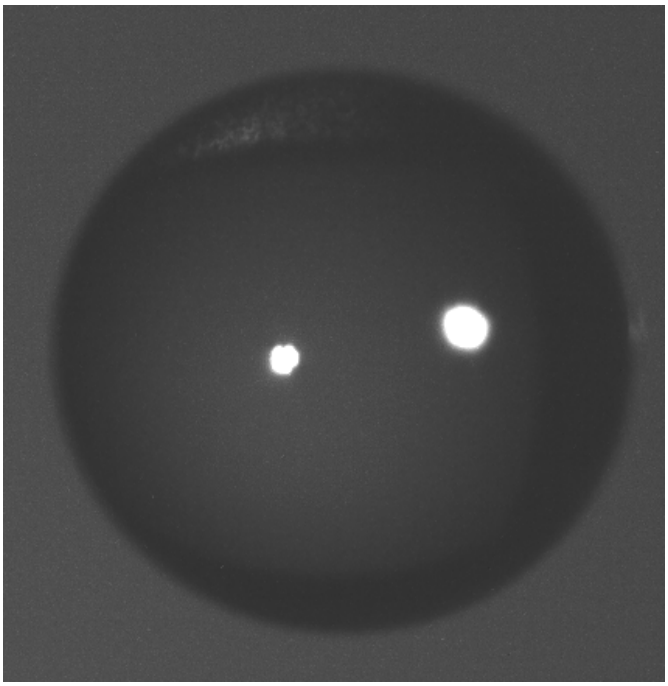

Figure 4.28: Droplet showing glare points. Bright field illumination by incoherent LEDs shows the circumference of the drop. Coherent HeNe Dark field illumination causes reflection (centre) and 2^{nd} order refraction (right) glare points.

In order to evaluate the IPI technique for irregular scatterers, a comparison is made between sizes obtained via direct imaging and via postprocessing of the interference patterns. To this end, focused images were made of a single particle, such as for instance figure 4.29. From such an image, the size of the particle in any linear dimension was obtained by converting the pixel values to black and white and subtracting the first and last white pixel position along the desired

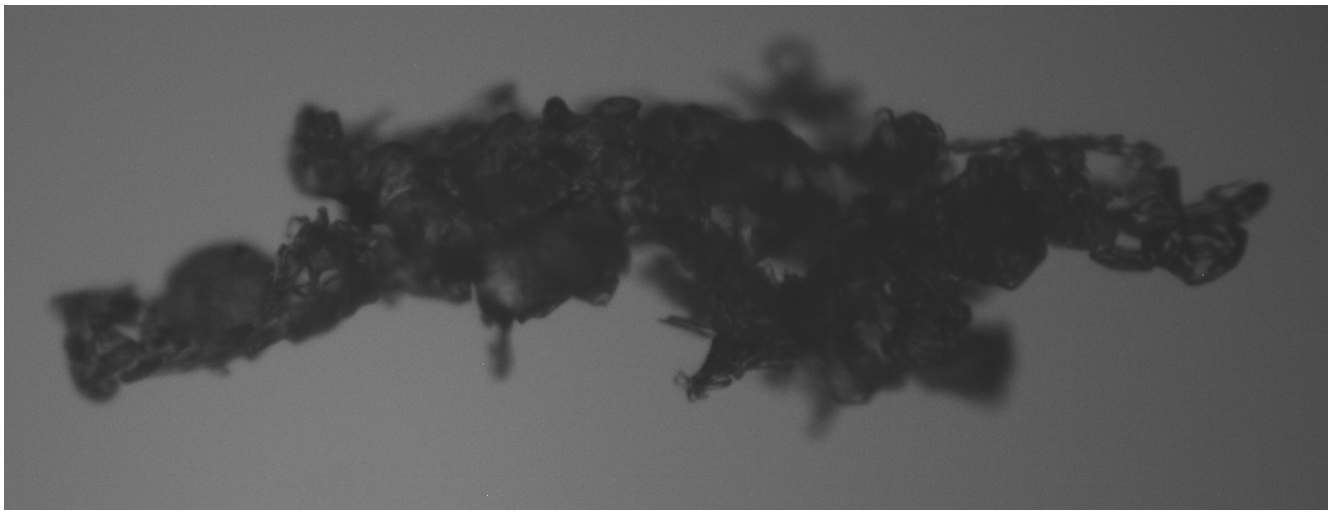

Figure 4.29: Bright field microscopic image of a morphologically highly irregular levitated ice crystal.

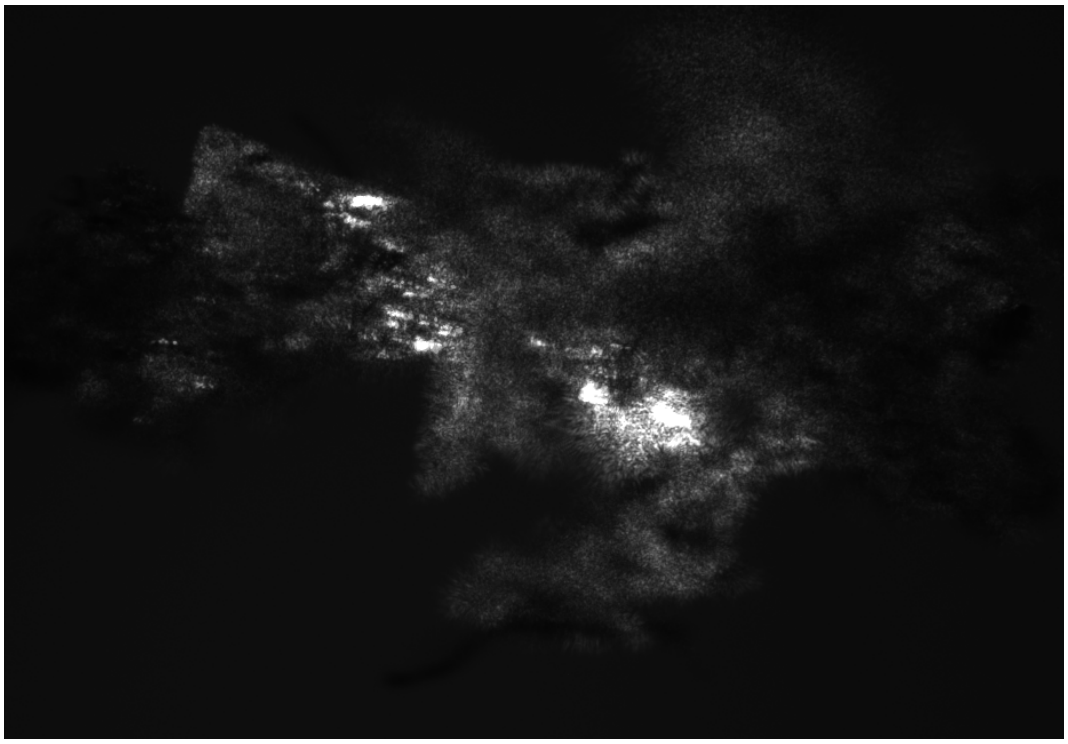

Figure 4.30: Dark field microscopic image of an ice crystal using coherent laser light. The coherence causes granular speckles in the focused image.

linear direction. In the case of rapidly rotating particles inside the levitator cavity, the direct imaging is very sensitive to motion blur and the particle size estimate can have a considerable standard deviation, as shown in figure 4.32. Furthermore, unfocused images were performed, which is either possible by displacing the camera, or by employing a single convex lens at its focal distance. Due to the coherence of the incident laser light, interference patterns become visible, such as interference fringes in the case of two glare points, as was already discussed. For highly irregular particles, speckles appear, which were first described and discussed by Goodman [Goo76, Goo05].

Proceeding to the IPI evaluation, Van Beeck shows by applying the Wiener-Khintchine theorem [Hec02], that the auto-correlation of the initial intensity distribution $g(x)$ (which is supposed to consist of a multitude of glare points in the IPI model) is equal to the Fourier transform of the speckle intensity $\mathscr{F}(i(\xi))$:

$$g(x) \otimes g^*(x) = \mathscr{F}(i(\xi)) \tag{4.5}$$

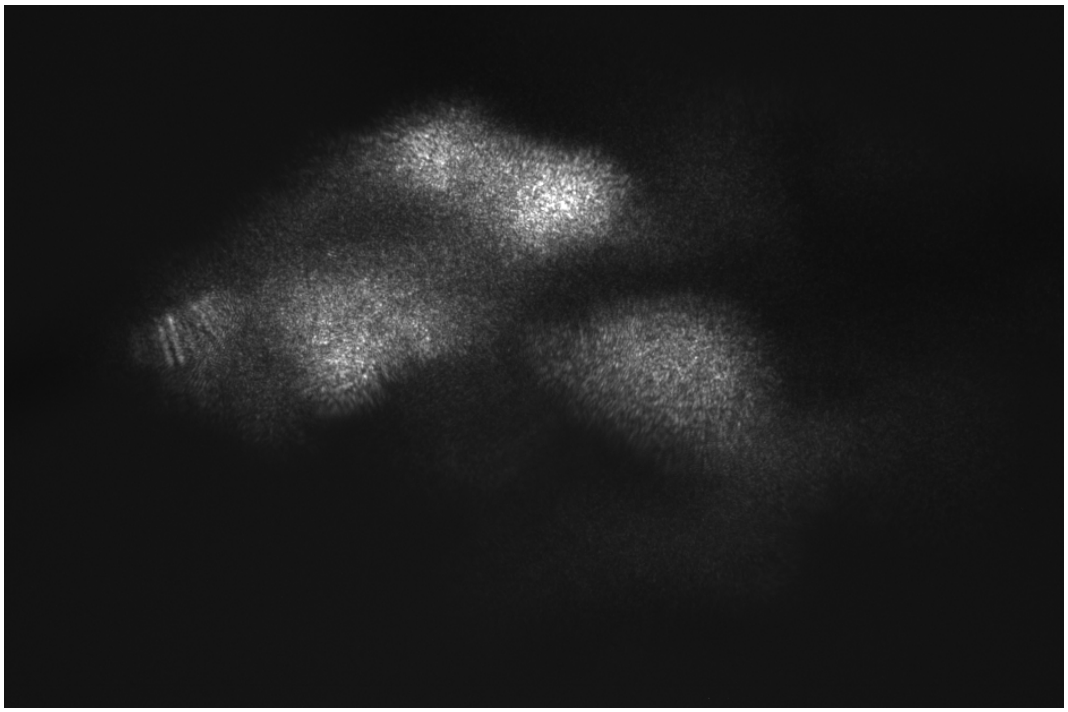

Figure 4.31: Defocused image of the crystal from figure 4.30. Interference of the coherent scattered light causes the speckles to persist, while the detailled features of the crystal become blurred.

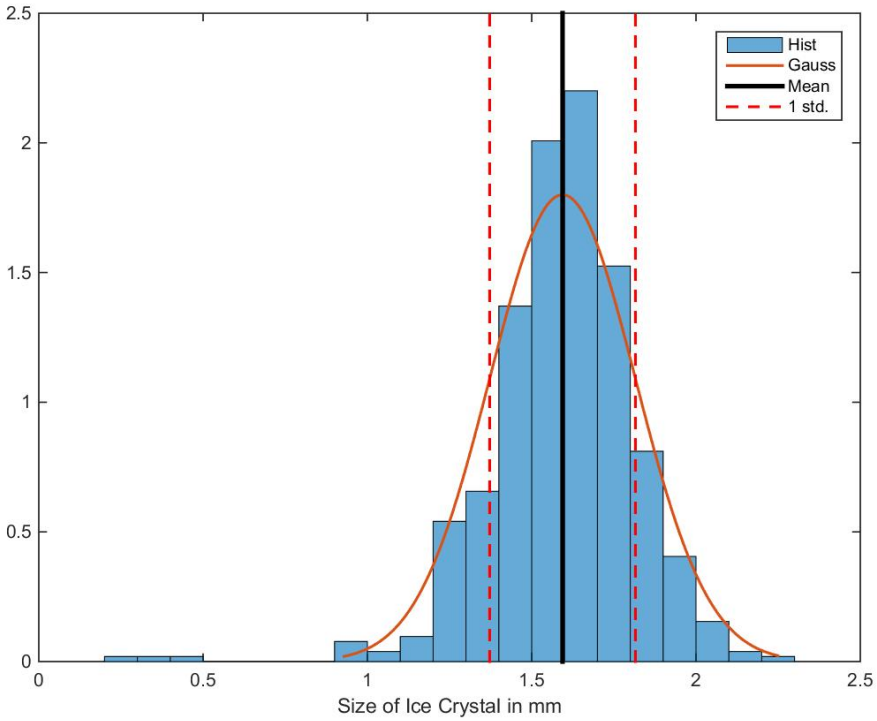

Figure 4.32: Particle size statistics from direct imaging. High standard deviation due to motion blur.

where $\otimes$ denotes the autocorrelation and * the complex conjugate. Assuming for instance a square $g(x)$, leads to a direct interferometric sizing relation.

$$F_D = \frac{D}{\lambda} \tag{4.6}$$

where D is the diameter of the non-zero interval of $g(x)$ and F_D the frequency of the curvature maximum of $\mathscr{F}(i(\xi))$. An experimentally obtained speckle image can be seen for instance in figure 4.31, clearly showing very fine speckles. In order to extract the size from this image, a 2D FFT was performed. One row of such an FFT can be seen in figure 4.33a and from this point on, two different evaluation strategies are possible. The first method, proposed by Van Beeck [GRVB14] uses an exponential fit to the FFT of the form:

$$y(x) = a \cdot e^{-b \cdot x + c} \tag{4.7}$$

where a is the intersection point of the curve with the ordinate $y(0)$, c the flat offset of the FFT from the background noise in the speckle image and b a fit parameter for the slope of the exponential. This fit can be differentiated analytically, in order to obtain the curvature κ of a plane curve [BSM00].

$$\kappa(x) = \frac{|y''(x)|}{(1+y'^2(x))^{\frac{3}{2}}} \approx \left| \frac{d^2y}{dx^2} \right| \tag{4.8}$$

where a prime denotes differentiation with respect to the independant variable x. The second approach was proposed by the author and applies a moving-average filter to the FFT instead of the exponential fit, in order to arrive at a smooth curve. As the measured image data and its FFT is discrete, the curvature 4.8 is then approximated by finite differences:

$$\frac{dy(x)}{dx} \approx \frac{y(x+h) - y(x-h)}{h} \tag{4.9}$$

$$\frac{d^2y(x)}{dx^2} \approx \frac{y(x+h) - 2 \cdot y(x) + y(x-h)}{h^2} \tag{4.10}$$

where h is the distance between neighbouring spatial frequencies corresponding to a value $y(x)$ and $y(x+h)$ in the FFT. Using finite differences in equation 4.8 then leads to the following approximation:

$$\kappa(x) \approx \frac{\left| \frac{y(x+h) - 2 \cdot y(x) + y(x-h)}{h^2} \right|}{\left(\sqrt{1 + \frac{y(x+h) - y(x-h)}{h}} \right)^3} \tag{4.11}$$

Results obtiained by both methods are shown in figure 4.33a. There one can see an overlay of the original FFT of the image (blue), the exponential fit, the filtered FFT and the location of the curvature maximum obtained via finite differences. The comparison between the thus obtained particle sizes is shown in figure 4.33b. The low correlation between the values is accredited to the motion blur present in all CCD images. Nevertheless the newly developed methods may be applied to images obtained with a CMOS system, in order to reduce the spread in the correlation.

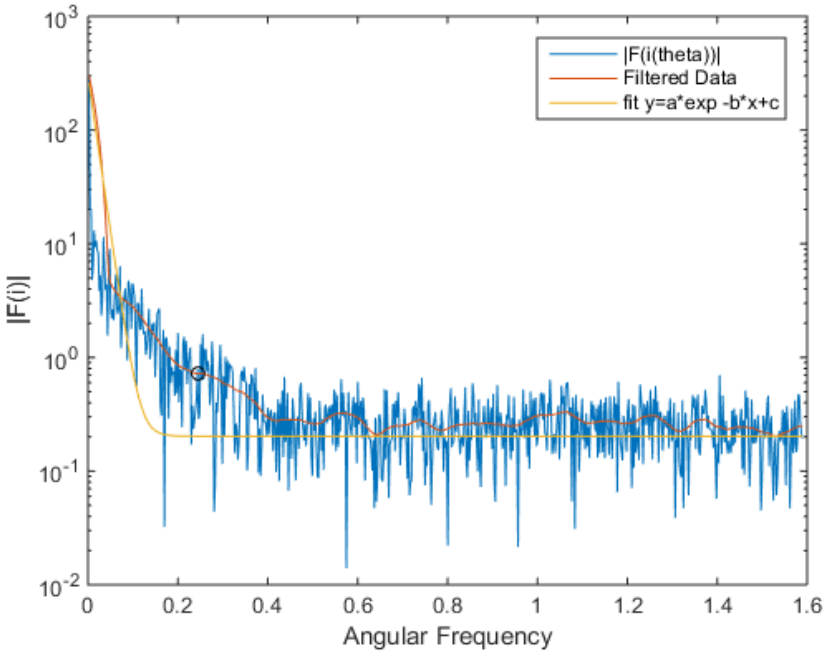

(a) Row-wise section of the 2D FFT of a speckle image. Corresponding exponential fit, low-pass filtered FFT and curvature maximum determined by finite differences as an overlay. Notable is the poor agreement between the FFT and the exponential fit proposed by Van Beeck [BRJB15]. Note the correspondance with figures 3.50a and 3.50b.

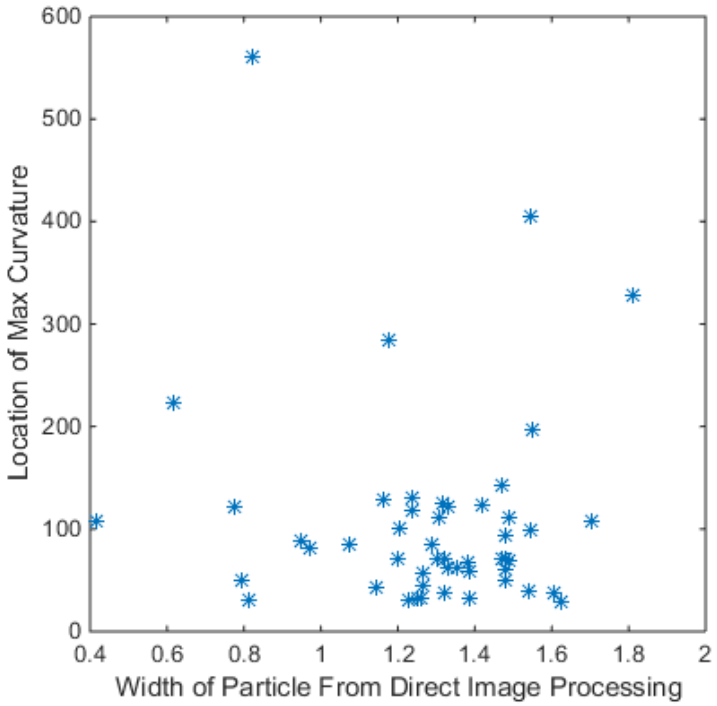

(b) Correlation of particle sizes obtained by imaging and IPI.

Figure 4.33: Postprocessing of interferometric images.

5 Engineering Applications

> Dicendum enim est Socrati de saltu pulicis, hoc est quare nives primo casu, priusquam implicentur in majores floccos, perpetuo cadant sexangulae, villosis, ut pennulae, senis radiis.
>
> —*Ioannes Keplerus*: Strena, seu de nive sexangula (1611) [Kep11].

THIS chapter is divided into two distinct sections. The first section will cover the efforts in designing and manufacturing a prototype device for the production of ice crystals, which are as pristine as possible. As explained in section chapter 4, such a device is a necessary condition for continuing further optical experiments involving ice crystals. Section two of this chapter will demonstrate the application of the light scattering code developed in chapter 3.1 to the calibration of the Particle Habit Imaging and Pllar Scattering (PHIPS) probe developed at the Karlsruhe Institute of Technology (KIT) and the interpretation of the obtained measurement results.

5.1 Nucleation Chamber Design

In this section, the design and construction of facilities and devices for the production of natural water ice crystal shapes in a laboratory environment are discussed. The design was largely carried out by two student design groups [HOSS14, FHH+15] in 2013 and 2015. What may be called the first scientific publication on the peculiar hexahedral shape of snowflake was written by none other than Johannes Kepler as early as 1611, who formulated the treatise [Kep11] as a new year's gift to his aristocratic benefactor. Modern scientific interest on snowflakes essentially was sparked by Ukichiro Nakaya, a Japanese nuclear scientist who carried out the first systematic characterization of natural snowflakes on the island of Hokkaido, compiled in the famous book [Nak54]. Nakaya was also the first to find out that despite the proverbial uniqueness of snowflakes, there is only a finite number of possible shapes occuring in nature. Occurance and growth of ice crystals is a classical process engineering problem, as the two parameters influence ice crystal growth in a given volume of air are relative humidity and temperature. In the context of ice crystal growth, often the supersaturation σ is preferred as a derived quantity over the relative humidity, as ice crystal growth can only occur at a relative humidity above 100 %.

$$\sigma = \frac{p_{vap} - p_{sat}}{p_{sat}} \tag{5.1}$$

where p_{vap} is the water vapour partial pressure in air and p_{sat} the saturation pressure. Relating the different ice crystal shapes, such as columns, plates, needles, and dendritic crystals to different zones in a two dimensional diagram with temperature and supersaturation as the axes leads to the ice crystal morphology diagram published by Libbrecht [Lib05]. This diagram allows to produce ice crystals of a specific shape by creating a state of a specific temperature and supersaturation in an enclosed volume of air. This is the basic operational principle of all ice crystal production facilities existing at present. This is unfortunately notably different from the operational principle of snow cannons used for the quick production of large volumes of frozen water particles. In order to predict the saturation partial pressure of water in air for a given temperature T, empirical regression formulas of high precision exist.

$$p_{sat,water}(T) = \left[2.8262 \cdot 10^9 - 1.0897 \cdot 10^6 \cdot T - 94934 \cdot T^2 + 582.2 \cdot T^3\right] \cdot exp\left(\frac{-5450}{273.15+T}\right) \tag{5.2}$$

$$p_{sat,ice}(T) = \left[3.6646 \cdot 10^10 - 1.3086 \cdot 10^6 \cdot T - 33793 \cdot T^2\right] \cdot exp\left(\frac{-6150}{273.15+T}\right) \tag{5.3}$$

Which according to Libbrecht [Lib05] produces pressure values in units of mbar for temperatures in ° C with an error of 0.1 % between -50^o and 50^o degrees Celsius. Nucleation itself, i.e. the random formation of an ice crystal may then occur in two different ways. Homogeneous nucleation occurs without any exterior influence at temperatures below $-48.3°$ Celsius according to Moore and Molinero [MM11]. In between $0°$ and $-48.3°$ C, the thermodynamic system is in a metastable state [Pfe03] where no immediate crystallisation occurs, until the system is disturbed by an impurity. As soon as the metastable system is disturbed, it will rapidly move into the stable state by freezing. Like any physical system, the vapour-air mixture will minimise its free energy G [Fer56], such that the frozen state is stable due to the fact that the entire system has the lowest possible free energy value. The expression for the chemical potential difference $\Delta\mu$ between a possible state and the equilibrium in a nucleation process is given in reference [Kas00].

$$\Delta\mu = k_B \cdot T \cdot ln\left(\frac{p}{p_{equilibrium}}\right) \tag{5.4}$$

Where T is the absolute temperature in Kelvin, k_B the Boltzmann constant, p the pressure and $p_{equilibrium}$ the pressure of the equilibrium state. Using the chemical potential difference, the nucleation work ΔG^* may be expressed as:

$$\Delta G^* = \frac{16 \cdot \pi \cdot r_{molec}^2 \cdot \sigma^3}{3 \cdot \Delta\mu^2} \tag{5.5}$$

Where r_{molec} is some estimated value for the constituent molecule size, and σ is the surface tension of nucleus. Generally, in all natural and technical situations, impurities acting as nuclei for ice crystallisation are readily available, leading to the ubiquity of snowflakes.

5.1.1 Classic convection cloud chamber design

The first approach towards a snow flake generator was a classical convection chamber, such as the one proposed by Libbrecht [LM08] or realised in the KIT AIDA chamber [MNS+01]. The design of this chamber was carried out during the Advanced Design Project [HOSS14]. A sketch of the proposed operation of the facility is shown in figure 5.1. As shown in the figure, the snow flake generator is a simple double-walled chamber, closed on all sides and isolated towards heat flux. In order to reach and control sufficiantly low temperatures, the double walled mantle is flooded with liquid nitrogen N_2. While this seems quite drastic at first, this cooling principle has already been applied succesfully in droplet cooling experiments performed at SLA [Li13]. The cooling on the sidewalls of the cylindric chamber will then cause a natural convective downdraft of the air inside the chamber. At the bottom center of the chamber are evaporation ponds, which serve to humidify the air inside the chamber and create a convective updraft at the center of the chamber. Thus a vortex ring due to natural convection will be created inside the chamber, as is evident from the CFD simulation result shown in figure 5.2. The figure shows the magnitude of the velocity field obtained via a $k-\varepsilon$ turbulence model. Details on the simulation may be found in [HOSS14]. It could also be shown that the cooling of the sidewalls dominates the temperature field inside the chamber and the evaporation ponds only create a small warm region.
The thus created humid air may now either produce ice crystals in a slow process by being exposed to the cool sidewalls, or by a sudden pressure drop inside the chamber. As such a process can be assumed to be isochoric, a sudden change in chamber pressure creates a linear change in temperature, if the perfect gas law is assumed to hold. A full view of the completed chamber design is shown in figure 5.3.

Chamber humidity

In order to predict the humidity inside the chamber, conservation of mass over the chamber volume is enforced.

$$\frac{dm_{vap}}{dt} = \dot{m}_{evap} - \dot{m}_{cond} \tag{5.6}$$

Where the differential change of m_{vap} over the time t is directly proportional to the evaporation and condensation fluxes $\dot{m}_{evap}$ and $\dot{m}_{cond}$. The mass of water vapor inside the chamber m_{vap} can be expressed through application of the ideal gas law.

$$m_{vap} = V_{Chamber} \cdot \frac{p_{vap}}{R_{vap} \cdot T_{vap}} \tag{5.7}$$

The vapour temperature is assumed to be in equilibrium with the chamber air. According to Libbrecht [LM08], the condensation rate can be expressed as:

$$\dot{m}_{cond} = C_{cond} \cdot (p_{vap} - p_{sat,ice}(T)) \cdot A_{wall,i} \tag{5.8}$$

In turn, the evaporative flux is expressed by the so-called *Penman* equation. This equation is given by Klemm [Kle07] as the potential evaporation ET_{pot}.

$$ET_{pot} = A_W \cdot \frac{\gamma}{\gamma + \Delta} \cdot f(w) \cdot \frac{p_{sat}(T) - p_{vap}}{\Delta h_v} \tag{5.9}$$

Therein $\gamma = 0.667 hPa/K$ is the hygrometer constant, A_W the open surface of the water pond, and h_v the specific evaporation enthalpy of water. The ventilation function $f(w)$ expresses the diffusivity of water vapour in the atmosphere, while $\Delta = \frac{dp_{sat}}{dT}$ is the slope of the water vapour saturation pressure curve. An empirical correlation for the ventilation speed w is:

$$f(w) = 6.43 \cdot (1.0 + 0.53 \cdot w) \tag{5.10}$$

Given the above formulae and a simple energy balance of the heat fluxes over the chamber walls and added by the evaporation pond, a complete numerical model of all thermodynamic properties in the chamber can be created and the results are shown in reference [HOSS14].

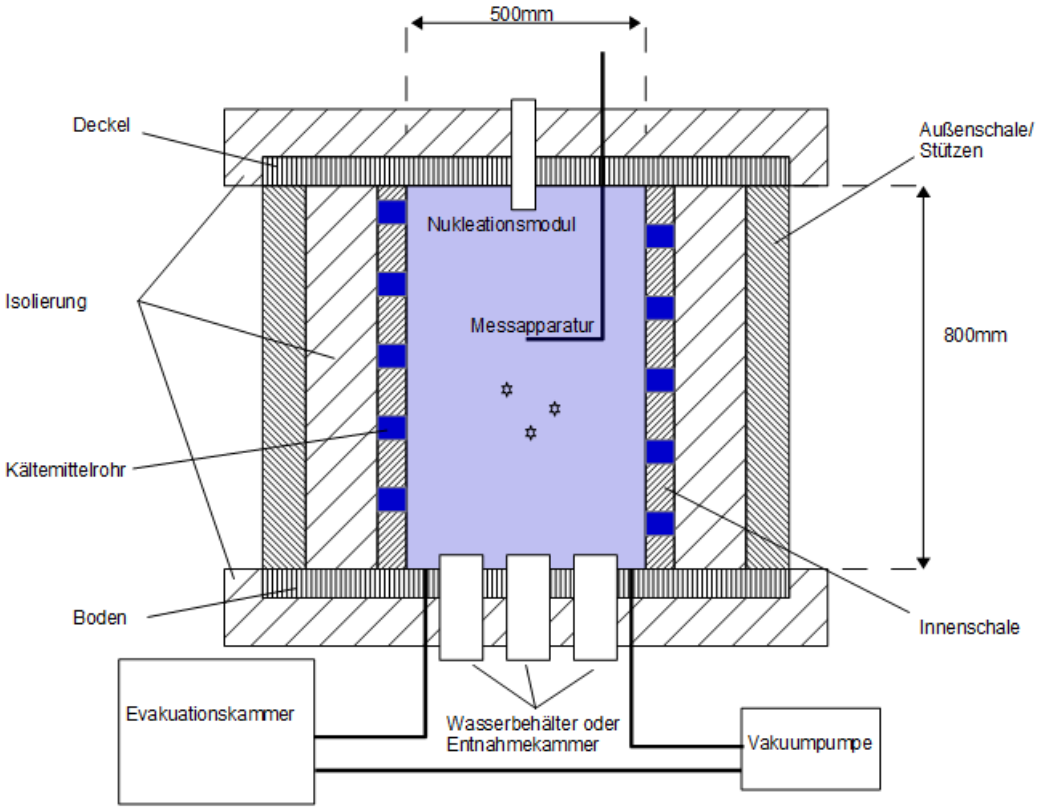

Figure 5.1: Construction sketch of the convective ice crystal growth chamber.

Model for ice crystal dynamics

In order to predict the falling dynamics of a single ice crystal inside the chamber and see if the desired growth is truly to be expected, a simple dynamical model has been created. Exact calculations of ice crystal growth under various conditions are still a topic of ongoing research [BGN12], due to the challenges inherent to multiphase flow simulation [SURS98].

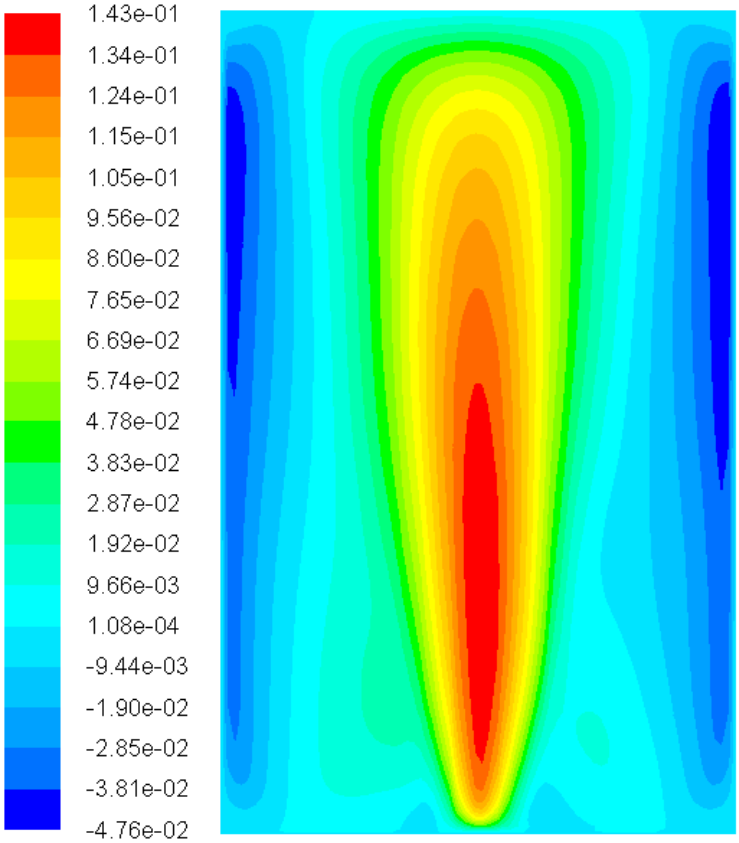

Figure 5.2: ANSYS Fluent 2D CFD steady state solution of the natural convective flow speed inside the chamber in $\frac{m}{s}$.

Thus the model relies on the assumption that the ice crystal is a point particle conducting a one-dimensional motion downward. Thus Newton's first law for a falling ice crystal may be formulated.

$$\frac{d}{dt}\left(m_{crystal}(t)\cdot\frac{dz_{crystal}}{dt}\right) = -F_G + F_W \tag{5.11a}$$

$$F_W = \frac{\pi}{8}\cdot d_{crystal}(t)\cdot\rho_{air}\cdot\left(u(z)-\frac{dz_{crystal}}{dt}\right)^2\cdot c_{w,\ crystal} \tag{5.11b}$$

$$F_G = 9.81\frac{m}{s^2}\cdot m_{crystal}(t) \tag{5.11c}$$

where $u(z)$ is the free stream velocity due to the convection inside the chamber, z the height of the crystal, t the time, and $c_{w,\ crystal}$ the drag coefficient of the crystal given by the following approximation adapted from Takahashi [TF88]:

$$c_{w,\ crystal} = 47\cdot Re_{crystal}^{-0.99} \tag{5.12}$$

The necessary Reynolds number may be defined as:

$$Re_{crystal} = \frac{d_{crystal}}{\nu_{air}}\cdot\left|u(z)-\frac{dz_{crystal}}{dt}\right| \tag{5.13a}$$

$$d_{crystal} = \sqrt[3]{\frac{6}{\pi}\cdot\frac{m_{crystal}}{\rho_{ice}}} \tag{5.13b}$$

as an approximation for the growth of the ice crystal over time, another model developed by Takahahi [TEW91] is used.

$$m_{crystal}(t) = \frac{3.3\cdot10^{-8}}{1000}\cdot\left(\frac{t}{60}\right)^{1.51} \tag{5.14}$$

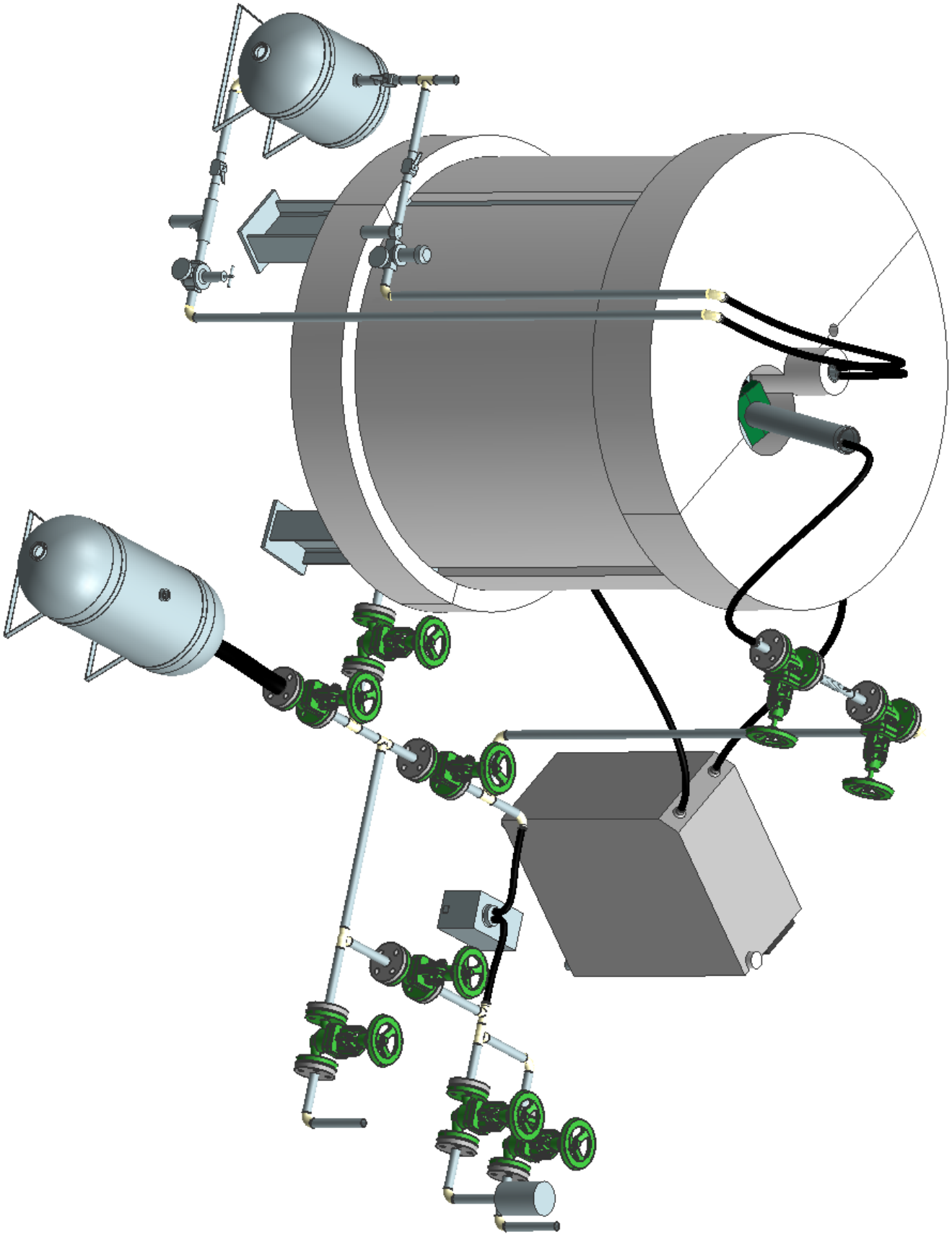

Figure 5.3: CAD model of the full chamber and peripherals.

Closure of the model is achieved by extracting a regression for the convective flow already numerically calculated and shown in figure 5.2. The regression for the flow speed $u(z)$ in the z-direction as a function of the height z then takes the following form:

$$u(z) = (a \cdot zb \cdot z^2 + c) \cdot exp\left(d \cdot z + e \cdot z^2\right) + f \cdot z \cdot exp\left(g \cdot z + h \cdot h^2\right) \tag{5.15}$$

The set of equations 5.11 to 5.15 allows to determine the falling position $z_{crystal}$, the crystal mass $m_{crystal}$, the drag coefficient $c_{w,\ crystal}$ of the crystal and the Reynoldsnumber $Re_{crystal}$ of the flow around the crystal as a function of the time t the snow flake spends in the chamber.

5.1.2 The Braunschweig pattern ice generator as a scaled-down approach

Design overview

Despite the thorough design of the convection chamber sketched in section 5.1.1, a new design approach had to be considered, as the previous design had two serious drawbacks with regard to the global scope of the project. First, estimated costs for parts and raw materials, were already estimated at 9915 €, exluding manufacturing cost. Second, the large number of complex parts makes manufacturing and assembling the chamber both expensive in addition to the acquisition cost, rife with potential error sources and lengthy in terms of time-to-operation. A cheaper and simpler alternative had to be sought and was realised in the Advanced Design Project [FHH+15]. The new design was based on a simplified convective cloud chamber originally assembled by Bansmer [BB15] in order to supply an icing tunnel of the university of Braunschweig with a sufficient amount of largely pristine ice crystals. While the full flexibility of the original design of section 5.1.1 was lost, the extremely simplified design allowed a rapid deployment of the device. An illustration of the design is shown in figure 5.4, where the CAD model of the assembly can be seen on the left side of the figure and a photograph of the finished setup on the right. As one can see, the cylindrical stainless-steel chamber was replaced by a bulb-shaped balloon made out of cheap and robust polyester cloth. The balloon is held upright by a truss of polyamide rods. All other components have been produced exploiting an automatic selective laser-sintering process, indepentent of any human intervention. The material used herefore is the polyamid PA 2200. This peculiar method of manufacturing is identical to the one used to produce the ice crystal analoga and also made it necessary to adapt the construction in specific ways, similar to the way in which a casted part is different from a machined part. Details on which modifications had to be made can be found in [FHH+15, BBWR13]. Any additional parts were cheaply available from industrial suppliers as standardised and mass-produced articles.

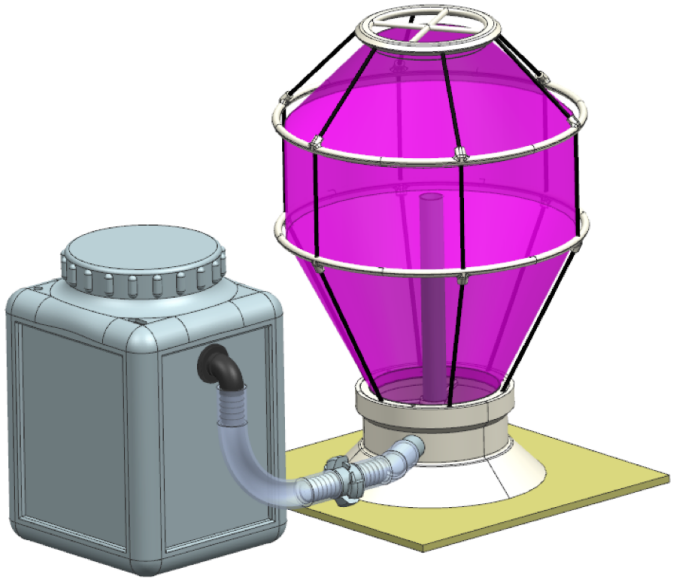

(a) CAD model of the complete assembly of the snow flake generator. Cloud chamber on the right in pink. Water reservoir for evaporation on the left in grey.

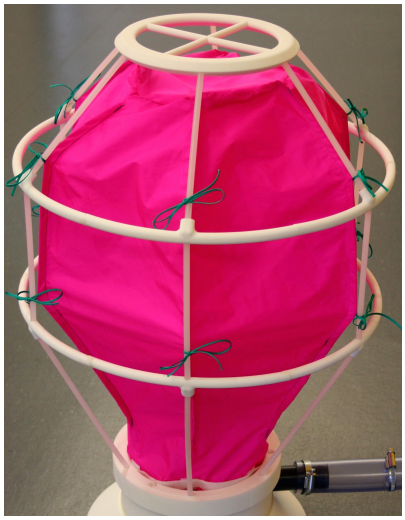

(b) Completely assembled balloon of the snow flake generator.

Figure 5.4: The Braunschweig pattern snow flake generator.

While the humid air is still provided by a now external evaporation pond, when looking at figure 5.4 it becomes clear that the device itself has no measure of controlling the temperature inside the balloon. This was done on purpose, as the temperature control can now be relegated to the already present laboratory freezer, in which the ballon is placed.

Ice particle trajectories and internal flow

The simple Newtonian point mass particle model developed in the preceding section incorporating the system of equations 5.11 to 5.15 is also applicable in the present case. Due to the particularly simple shape of the cloud chamber, the numerical simulation of the system was skipped in favour of a potential flow model. The upper half of the balloon was chosen to be represented as a superposition of a plane flow u_∞ and a source of strength Q. In a two-dimensional polar coordinate system (r, θ), the corresponding potential is given by [SA08]:

$$\Phi = u_\infty \cdot r \cdot cos\theta - \frac{Q}{4\pi r} \tag{5.16}$$

Following the standard procedure, the potential velocity field as displayed in figure 5.5a can be obtained. In order to adapt this model to the cloud chamber, the source strength is identified with the humid air mass flow streaming inside the cloud chamber and the free stream velocity u_∞ is used as a parameter, such that the stagnation line between free stream and source flow as closely resembles the polyester chamber hull as possible. Consequently, the ice crystals are only allowed to move inside the region to the right enclosed by the stagnation line as shown in figure 5.5. The newtonian model can also easily be expanded into two or three dimensions and one can see from figure 5.5 that the snow flake trajectories all drift away form the humid air inlet in the balloon, while simultaneously still drifting downward (i.e. to the right in the figure). Thus the snowflakes in the potential flow model behave exactly as intuitively expected.

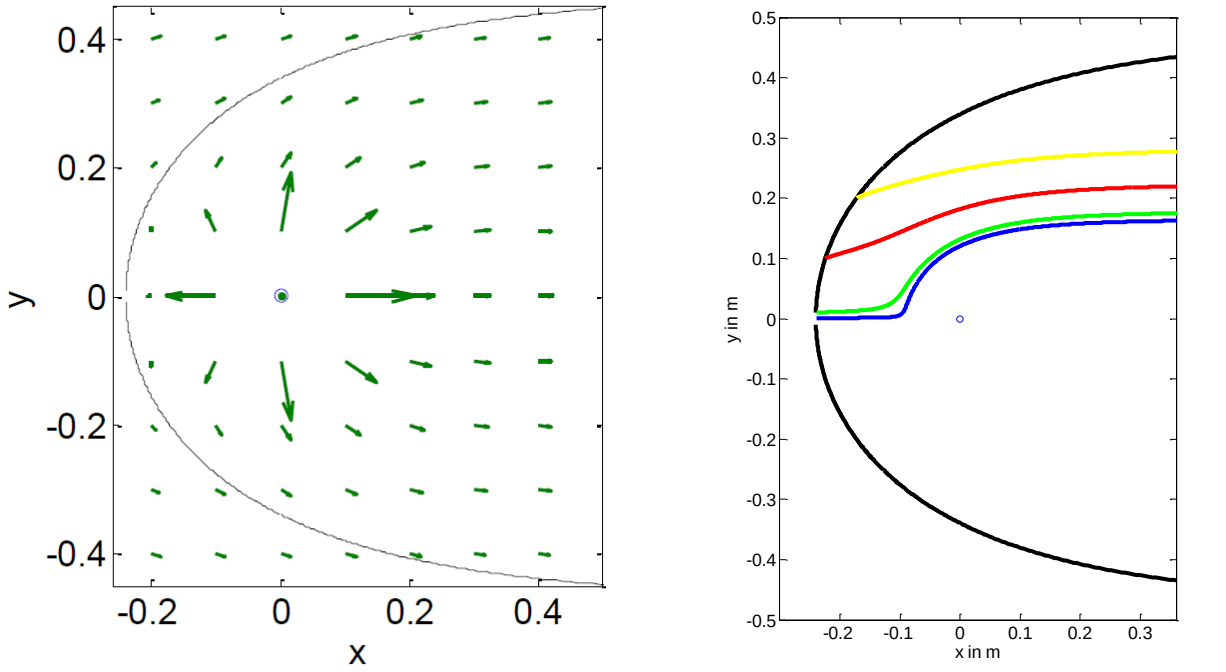

(a) Velocity field vectors for the potential flow model of the balloon convection.

(b) Ice particle trajectories inside the ballon according to the potential flow model.

Figure 5.5: Potential flow model for ice crystal dynamics inside the balloon.

After the completion of the advanced design project and the actual design process, a complete CFD calculation of the flow field inside the balloon of the device has been performed. The mean flow speed and pressure fields are shown in figures 5.6 and 5.7 respectively. Just as in the laboratory freezer heat transfer case shown in figure 4.7, a standard solver of the *OpenFOAM*® package has been used for the calculations. The designation of the solver is `pimpleFOAM` and it provides

an instationary implementation of a combination of the PISO [IGW86] and SIMPLE [FP08] algorithms. As the estimated Reynolds number of the problem is $Re \approx 2550$ [FHH+15] and direct observations of the flow inside the balloon confirm that it is turbulent, a RANS turbulence model has been applied. The default k-ε closure [JL72, Pop00] of the solver has been exchanged for a RNG k-ε model [YOT+92]. Since the flow outlet inside the balloon lies behind the inlet, the streamlines eventually need to turn by 180° degrees. Thus the chosen two-equation model is not expected to perform very well, but is nevertheless accepted for a preliminary assessment of the flow field. The calculation has been performed on a manually refined, and unstructured triangular prismatic grid, limiting the accuracy of the solution. Furthermore, as the simulation is effectively two-dimensional, there is no proper vortex stretching $(\nabla \times \mathbf{u}) \cdot \nabla \mathbf{u}$ in the flow field $\mathbf{u}$ according to Pope [Pop00]. As boundary conditions, the flow velocity was prescribed at the inlet, the pressure at the outlet, symmetry at the central axis, and wall functions on the fabric wall of the balloon and the inlet pipe. Thus the wall boundary layers are not resolved by the mesh in this calculation. A comparison between potential flow results in figure 5.5a and the RANS results in figure 5.6 show a qualitative correspondance in the upper part of the balloon of the ice crystal generator.

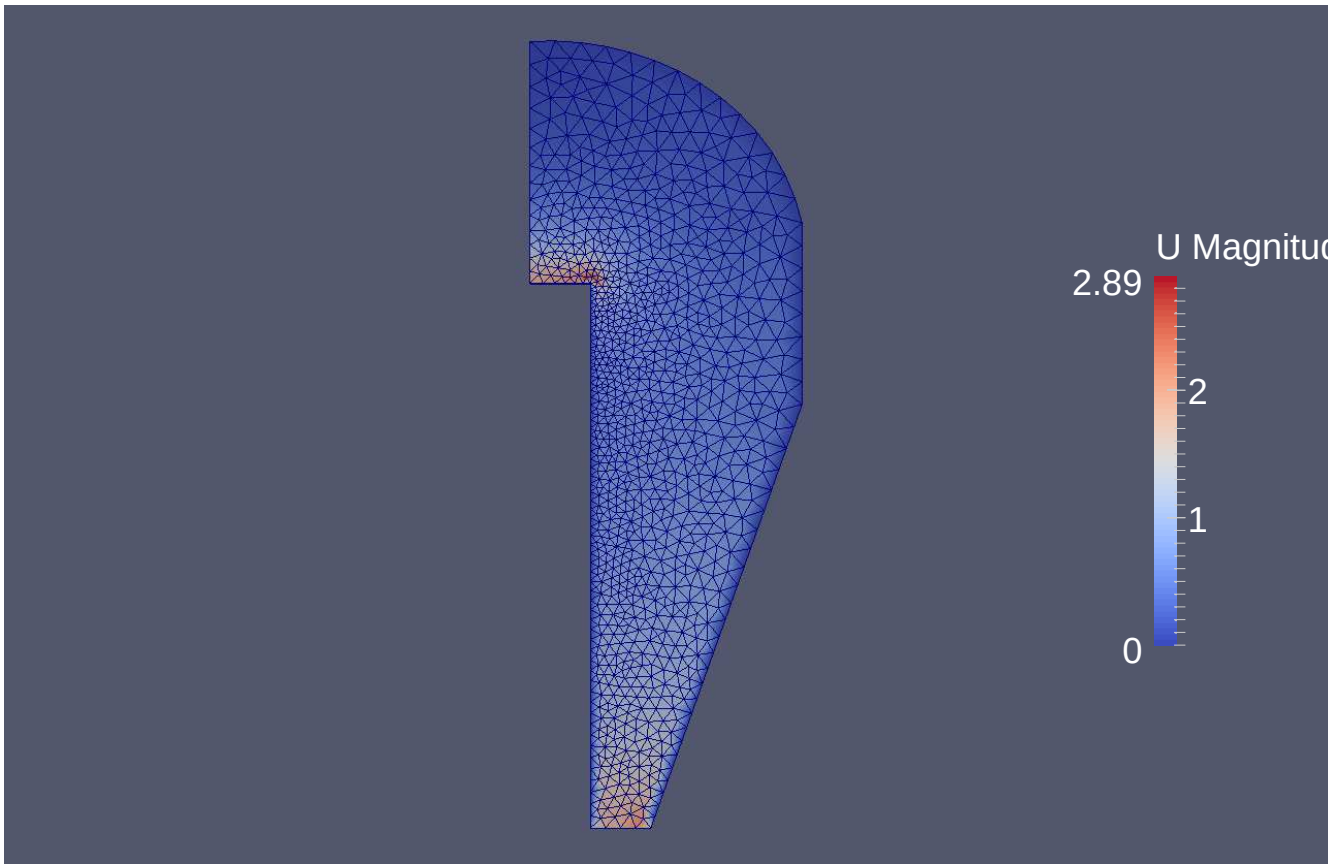

Figure 5.6: Instantaneous 2D mean velocity magnitude field inside the snow flake generator balloon. Incompressible `pimpleFoam` solver (PISO-SIMPLE combination) with RNG k-ε turbulence model on a triangular, unstructured mesh.

Prototype initial operation

In contrast to the first design, the revised design was constructed in a time frame of two months and at a total cost of 278,37 €, excluding manufacturing salaries. Especially the extended use of 3D-printed parts allowed the rapid and flawless progression of the construction despite the limited personnel in the SLA mechanical workshop. A 10 hour test run of the assembled device has been performed in the CSI laser laboratory and the results are shown in figure 5.8. As can be seen, the device entirely fulfills its intended purpose both in terms quantitiy and quality of the produced ice crystals. The preliminary test run has also revealed a number of design flaws, which should be eliminated in future design iterations. The issues are listed below in decreasing order of severity.

- The fan providing the humid air current needs to be heated, as an operation of the device over an extended period of time leads to icing and eventual blockage of the fan opening.

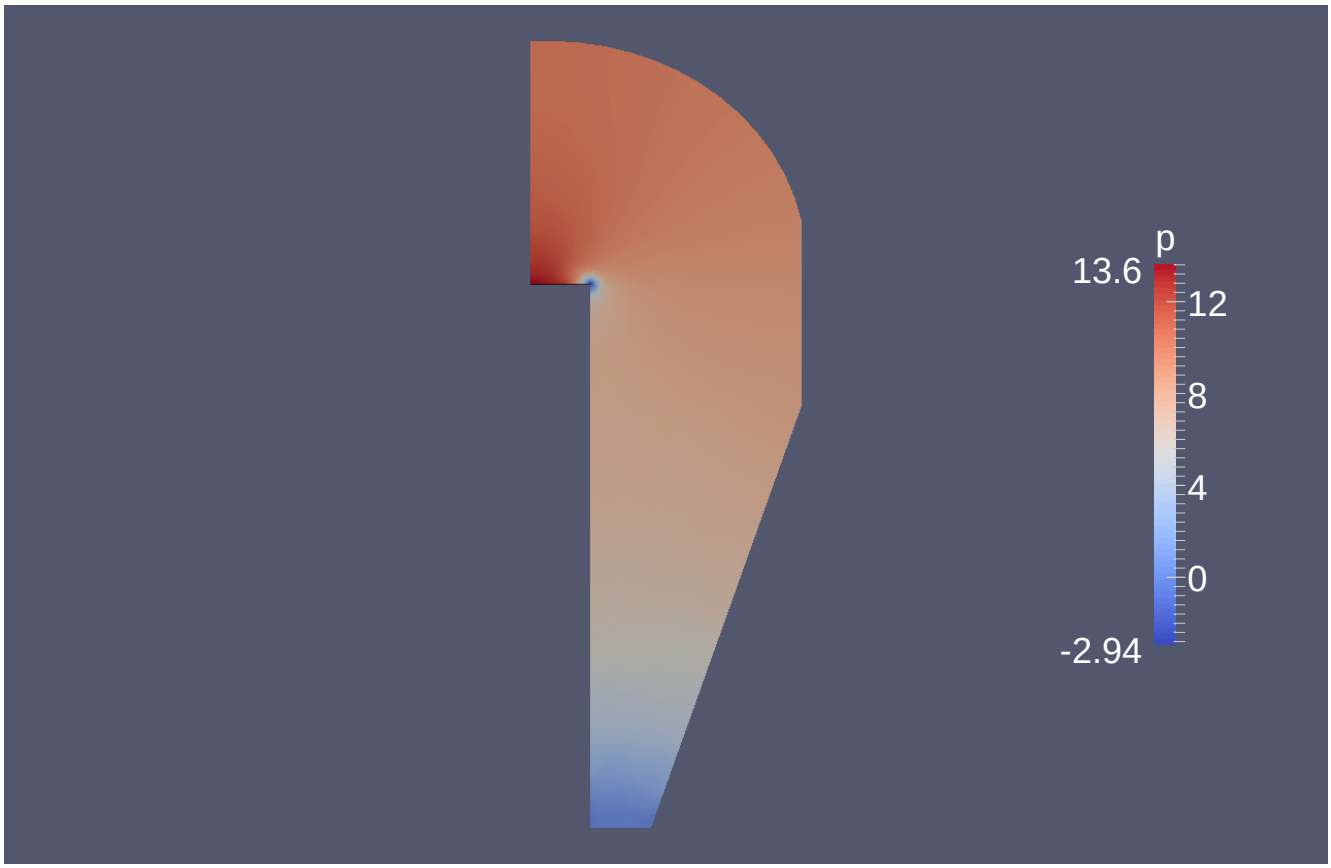

Figure 5.7: Relative pressure field corresponding to the mean velocity shown in figure 5.6.

- Several components of the design, such as the fan speed control electronics and balloon cloth are not waterproof. This becomes problematic as soon as the device is taken out of the freezer and is defrosted.
- Temperature, humidity and air flow speed should ultimately be regulated, in order to achieve a measure of control over the shape of the ice crystals produced by the device.
- Thermal shrinkage of the structural components needs to be taken into account.

After a production run of the ice crystal generator, the produced snow flakes may be stored or transported inside the closed container shown in figure 5.9. This container allows the general handling of the ice crystals outside a freezer for a maximum period of ten minutes. Consequently, the ice crystals may be transported between laboratories, set aside for further optical experiments or prepared for wind tunnel injection. At the end of ten minutes, the thermal insulation provided by the container still preserves a large amount of the frozen water. Nevertheless, the onset of melting occuring after this time span destroys the fine structure of the ice crystals, such as clearly defined edges. This is important for optical experiments but possibly not as much of a concern for aerodynamic experiments.

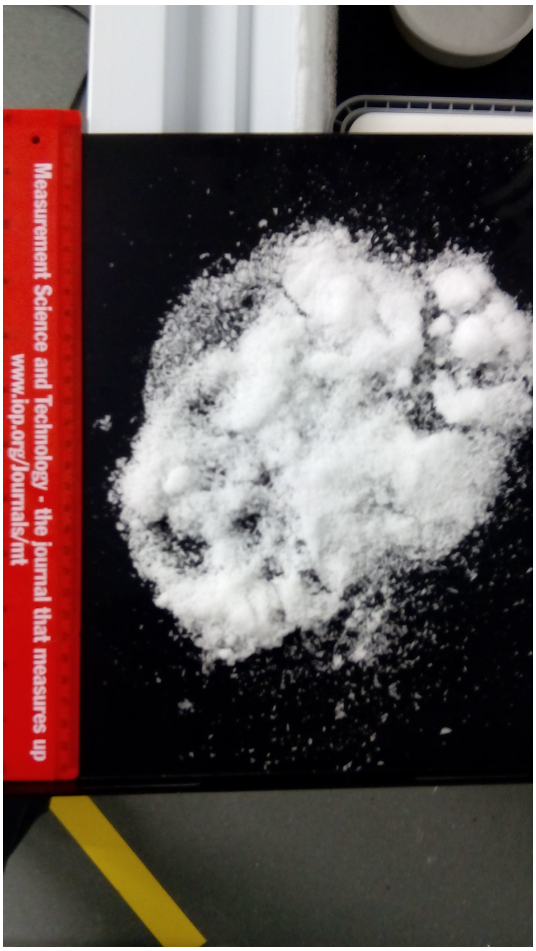

(a) Total amount of ice crystals generated after a twelve hour test run.

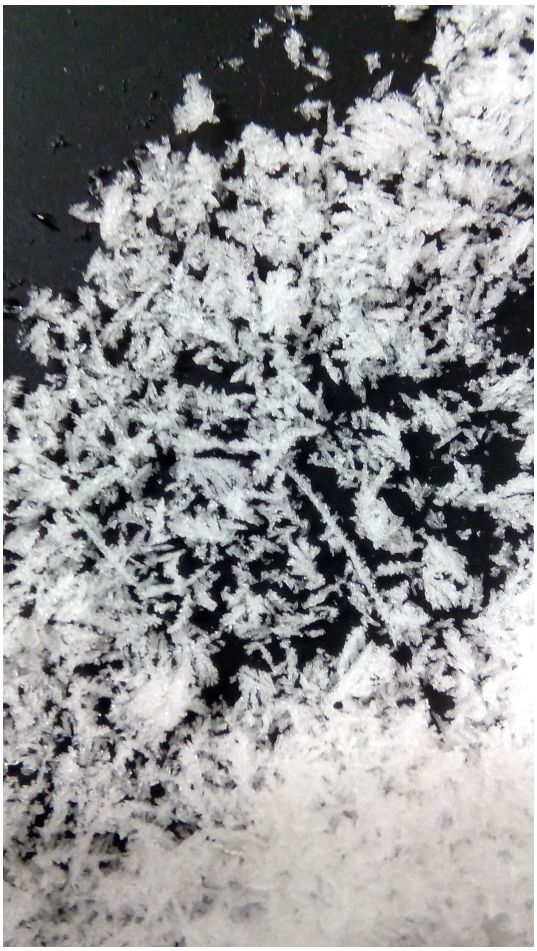

(b) Close-up of figure 5.8a, revealing the needle-like shape of the ice crystals.

Figure 5.8: Artificial ice particle batch from first test run.

Figure 5.9: Handling container for artificial snow flakes.

5.2 Calibration of the PHIPS-HALO device

An example for the application of the light scattering algorithms discussed in chapter 3 is provied by the PHIPS HALO probe, which is an acronym for Particle Habit and Polar Scattering probe aboard the High Altitude Long Range carrier aircraft. A sketch of the operational principle of the device is shown in figure 5.10 and a range of photographs of the interior of the probe and its installation under the wing of the HALO aircraft is shown in figures 5.11 to 5.14. A comprehensive description of the construction and working principle of the probe is given in the article [ASA+11]. The basic operational principle of the probe combines phase function measurement of individual ice crystals with direct imaging, thus correlating a measured phase function with the ice particle creating it. While in flight aboard the HALO aircraft, the free stream carrying ice crystals is ingested into the probe. A single crystal passes a laser beam and the scattered light is recorded by a large number of photomultipliers arranged in a circular arc perpendicular to the direction of the flow carrying the particle. Immediately afterwards, the snow crystal triggers an incoherent flash laser providing brightfield illumination for two cameras which will record a stereoscopic image of the crystal, thus recording shape and orientation of the scatterer. The phase function of a particle is measured between 18° and 170° at intervals of 8°, resulting in twenty parabolic collector angles on the circular arc on each half side, connected to twenty photomultipliers via optical fibres. Needless to say, such a device is of enormous value for investigations in atmospherical and planetary optics, but it may also be applied in other areas where non-spherical particles are present.

5.2.1 Spherical Polystyrene reference particles

In order to compensate for the various sources of error in the measurement by the large number of individual photomultipliers in the PHIPS design shown in figure 5.10, each contribution from a single photomultiplier was weighted by a factor obtained through comparison with exact Mie results. A reference measurement was carried out using standardized polystyrene spheres with known parameters, such as size and refractive index and the measured phase functions were compared to exact Mie and GLMT calculations. The exact material of the spheres was Polystyrene DVB (Divinylbenzene, 4-8 %) and the parameter relevant for the scattering behaviour are listed in table 5.1.

particle radius R	wavelength λ	index of refraction n	Particle type
49.4 ± 1.6 μm and 20.0 ± 0.9 μm	532 nm	1.59	Spherical bead

Table 5.1: Polystyrene bead optical parameters.

The results of the Mie calculations in terms of the scattered Intensity I over the polar angle θ are shown in figure 5.16 for the $50\mu m$ beads and in figure 5.15 for the $20\mu m$ beads, both for plane wave (pw) incidence and the true Gaussian beam incidence with a beam waist radius of $w_0 = 500\mu m$. Again, the code used for the Mie calculations is MiePlot [Lav03].

By inspecting the figures 5.15 and 5.16, one can see that the Gaussian incidence in the $20\mu m$ case leads to differences in the predicted absolute intensity, while there is no apparent difference in the phase. Overall, the observed differences in the scattered intensity are minor. This is different in the $50\mu m$ case, where significant qualitative differences in the scattered intensity over the entire polar angle range can be observed, clearly jusifying the investigation of the influence of the laser beam shape on the measurement results.

5.2.2 Natural Ice crystals

The actual purpose of the PHIPS probe is sampling the phase functions of actual *real* ice crystals, and correlate them to the respective shapes of the individual ice crystals producing the phase functions. This is something that has never been tried before. After the correction of the photomultiplier data by comparing the polystyrene bead measurement results with the GLMT calculations as explained in the previous section, the interpretation of the data was performed using three different light scattering codes presented in chapter 3. From a measurement campaign over Brazil, a tropospheric ice crystal was select, whose stereoscopic images shown in figure 5.17 revealed a particularly simple shape, namely the basic hexahedral prism.

Figure 5.18 shows the comparison of the measured and computed phase function data for the crystal shown in figure 5.17. Three fundamentally different light scattering codes have been used in the comparison. This includes the TSym

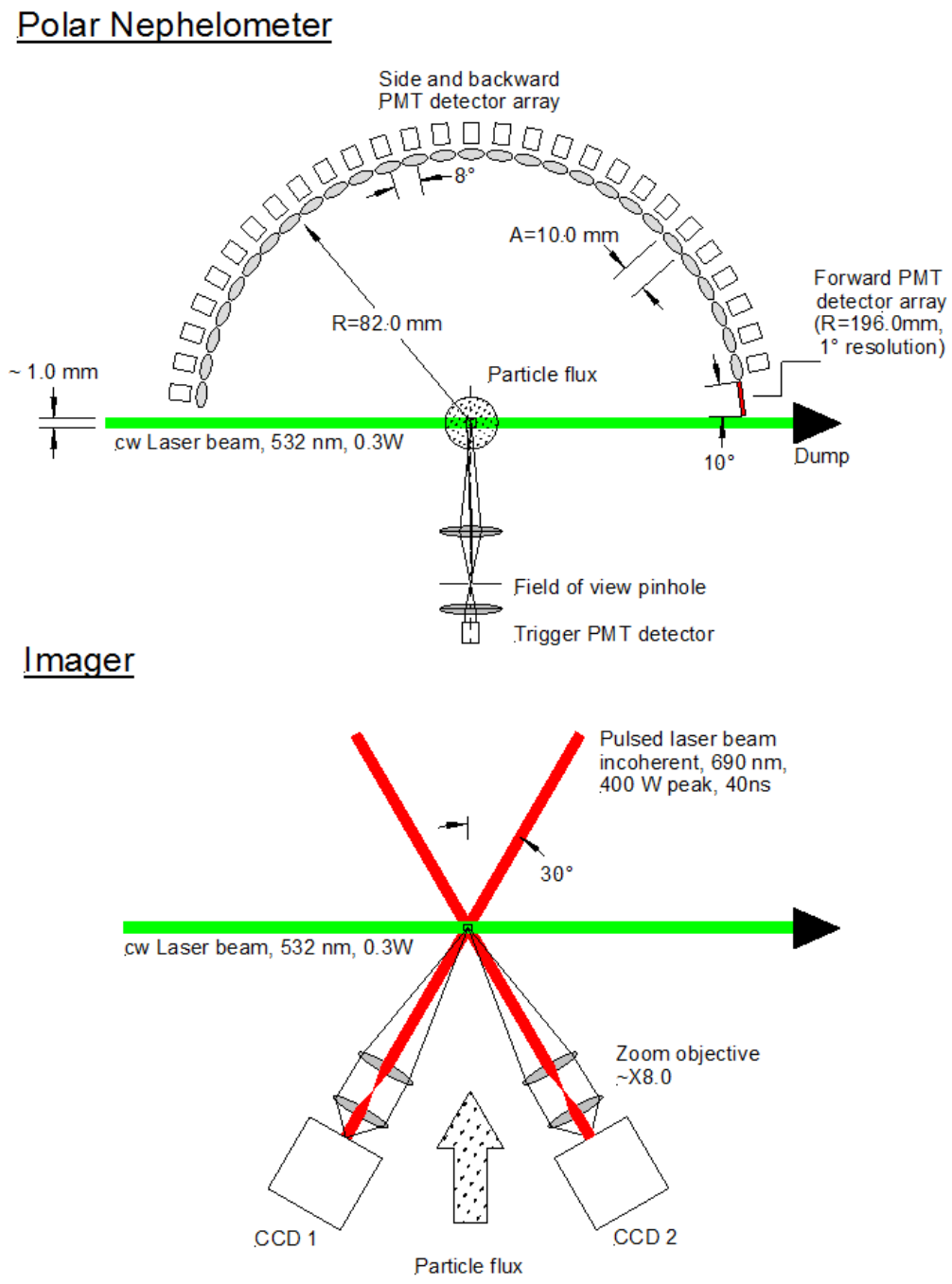

Figure 5.10: Sketch of the operational principle of the PHIPS-Halo measurement device (image courtesy of Martin Schnaiter). The top view shows the circular detector array for measuring the phase function of a single particle, as well as the trigger beam. The bottom view shows the two cameras responsible for the stereoscopic imaging.

code of Kahnert [Kah05], the ray tracing code of Macke [MMR96] as a reference solution and the first order geometrical optics code presented in section 3.1. The particle was illuminated by a Nd-YAG laser with a wavelength of $\lambda = 532nm$, a beam waist radius of $500\mu m$, and a vertical linear polarisation.

The prismatic particle had a height and diameter of roughly $120\mu m$ and its refractive index was set to $n = 1.31$ for the calculations, which is a typical value for water ice at the corresponding wavelength [WY12]. For the T-matrix calculations the symmetry group was again set to the dihedral group Dh_6. In the geometrical optics case, the diffraction peak at the forward scattering angles was excluded, both due to the fact that this region contains the PHIPS beam dump and is thus

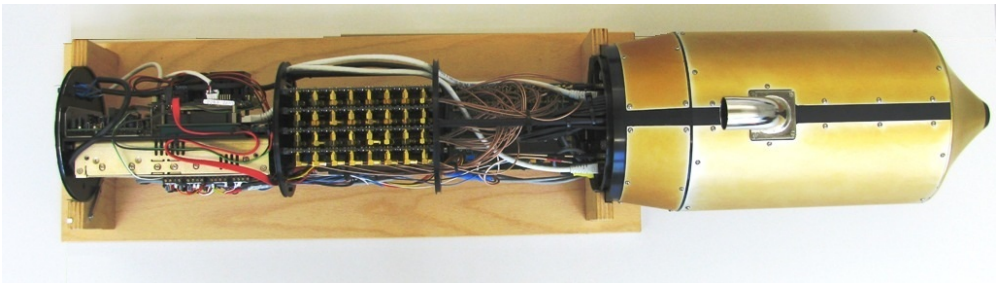

Figure 5.11: Dismantled rear section showing data processing electronics for the stereoscopic CCD cameras and the photomultipliers (image courtesy of Martin Schnaiter).

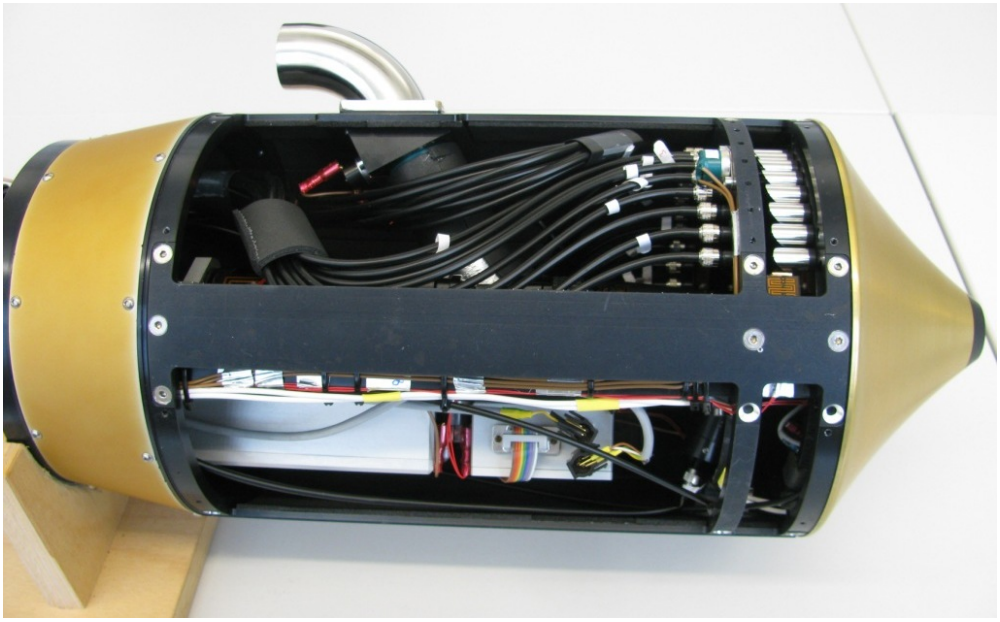

Figure 5.12: Assembled frontal section showing the parabolic mirror array and optical fibres connected to the photomultipliers as well as the primary laser providing illumination for the phase function measurement. Visible echanical components are the inlet of the test section towards the right side of the image as well as the curved outlet at the top. (image courtesy of Martin Schnaiter).

inaccessible to measurements, and due to the fact that the lateral dimensions of the PHIPS probe as shown in figure 5.12 are very limited and a rough estimate for the Fresnel number can thus be given, which is then much larger than one.

$$F = \frac{r^2}{L \cdot \lambda} \approx \frac{(120 \cdot 10^{-6} m)^2}{0.05m \cdot 532.9 \cdot 10^{-9} m} \gg 1 \tag{5.17}$$

Prior to the compilation of the results in figure 5.18 it was found that the T-Matrix results were identical to the ones shown in figure 3.44 and thus displayed a large deviation from both the experimental and the GO results. According to Kahnert [Kah13], the reason for this lies in the evaluation of the surface integrals for the T-matrix elements. The necessary numbers to sum in the numerical quadrature become equally large for large particles and nearly cancel. The ensuing round-off errors will lead to wrong final results if a finite precision data type such as the Fortran 77 real number surrogate `real*8` in the present case is used. Consequently the T-matrix results have been discarded and are not shown in figure 5.18. Agreement between the remaining phase functions is surprisingly good, with the exception of the backscattering polar angles above 120°. In this angular region, all four phase functions diverge completely. A further notable difference between the measured and computed phase functions is the 46° degree halo. While the well known 22° degree halo is predicted by both geometrical optics codes and clearly visible in the experimental data points, there is no trace of the 46° degree halo in the measured data, despite its occurence in both ray tracing simulations. Reasons for this circumstance may be a rough surface of the ice crystal, an oversimplification of its true shape in the necessarily idealised simulations, cross-talk in the photomultipliers, or an incomplete rotation of the ice crystal while passing the instrument. In order to investigate mesoscopic surface roughness as a possible explanation for the differences, another calculation was performed with a surface roughness value of $\sigma = 0.005$, i.e. slight to moderate roughness [YN98]. As can be seen in figure 5.18,

Figure 5.13: DLR HALO mission carrier aircraft(image courtesy of Martin Schnaiter). The High Altitude and Long Range research aircraft is a modified Ultra Long Range Business Jet G 550 from the manufacturer Gulfstream and operated by the German Aerospace Center.

Figure 5.14: In-flight shot of the HALO measurement equipment attached to the wing. The PHIPS device is shown as the outmost instrument towards the wing tip. (image courtesy of Martin Schnaiter).

surface roughness may explain the absence of the 46° degree halo. Nevertheless, the values of the phase function in the backscattering region are slightly too high and the measured results show better agreement with the smooth surface calculations. Thus surface roughness alone cannot deliver a complete explanation for the observed data. As a conclusion, the results clearly show, that present theories on the scattering of light by ice crystals already allow to predict a large number of features present in nature. Nevertheless, further investigations on the precise influence of the morphology and the dynamics of natural ice crystals are necessary in order to arrive at a complete picture.

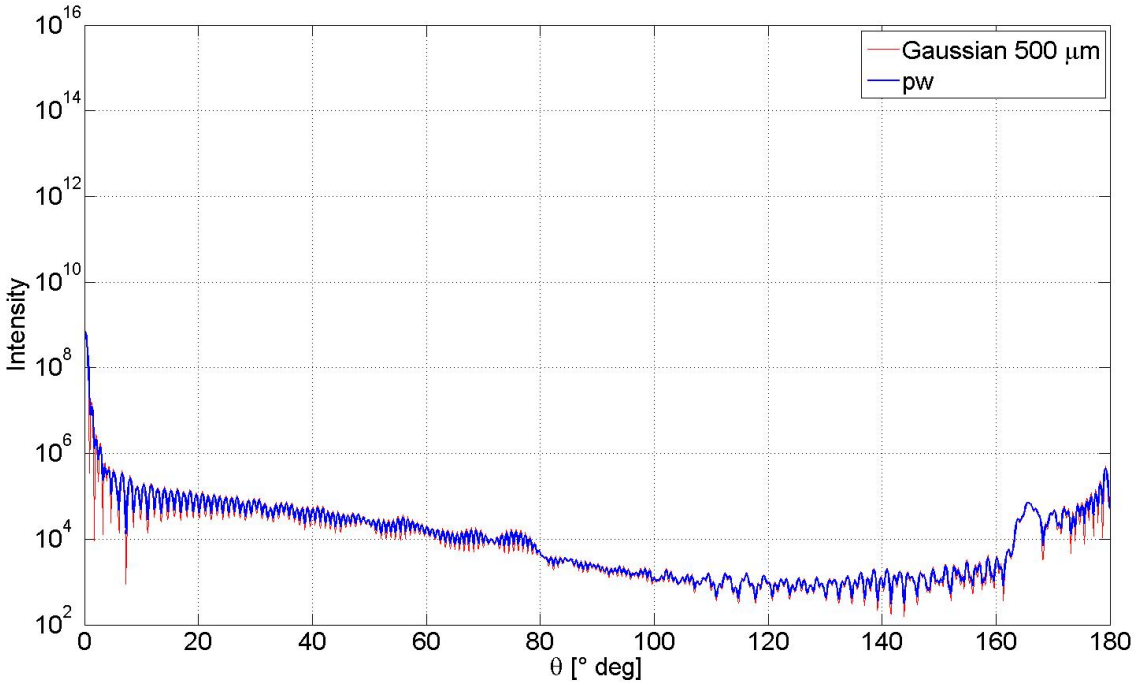

Figure 5.15: Polar scattered intensity for the $20\mu m$ polistyrene beads. Comparison of pw and Gaussian incidence.

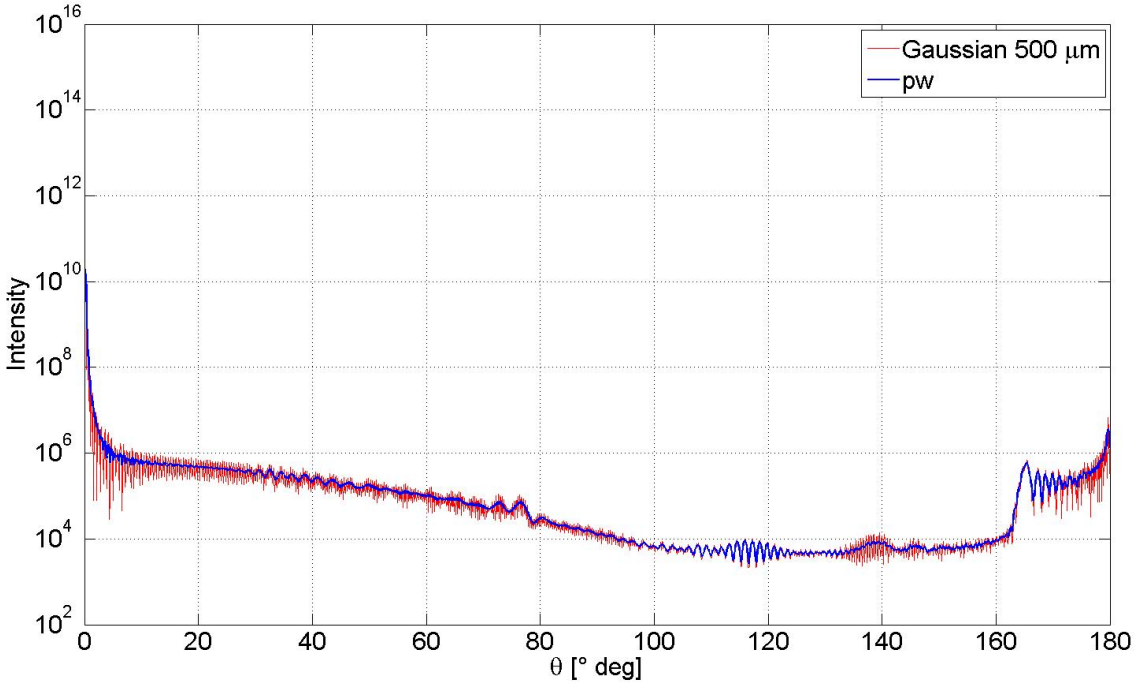

Figure 5.16: Polar scattered intensity for the $50\mu m$ polistyrene beads.Comparison of pw and Gaussian incidence.

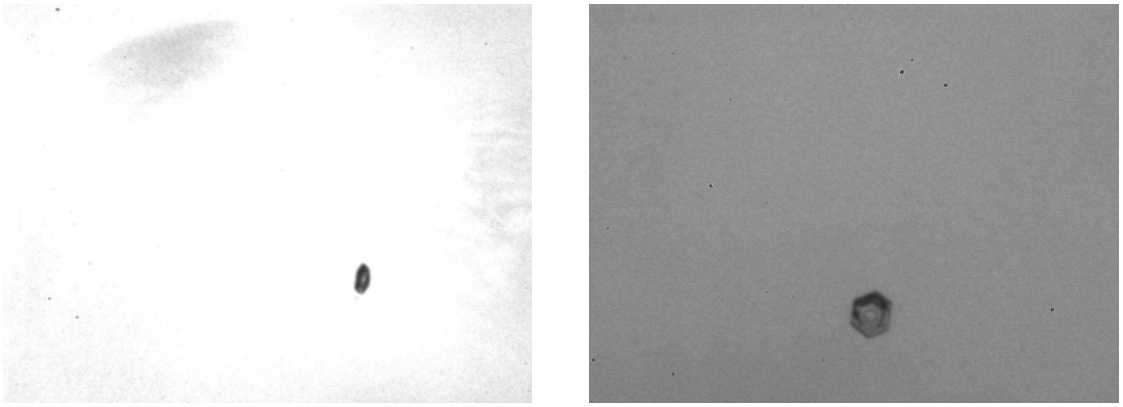

(a) Left stereoscopic view.

(b) Right stereoscopic view.

Figure 5.17: Stereoscopic images of the hexahedral ice crystal pertaining to the phase function in figure 5.18.

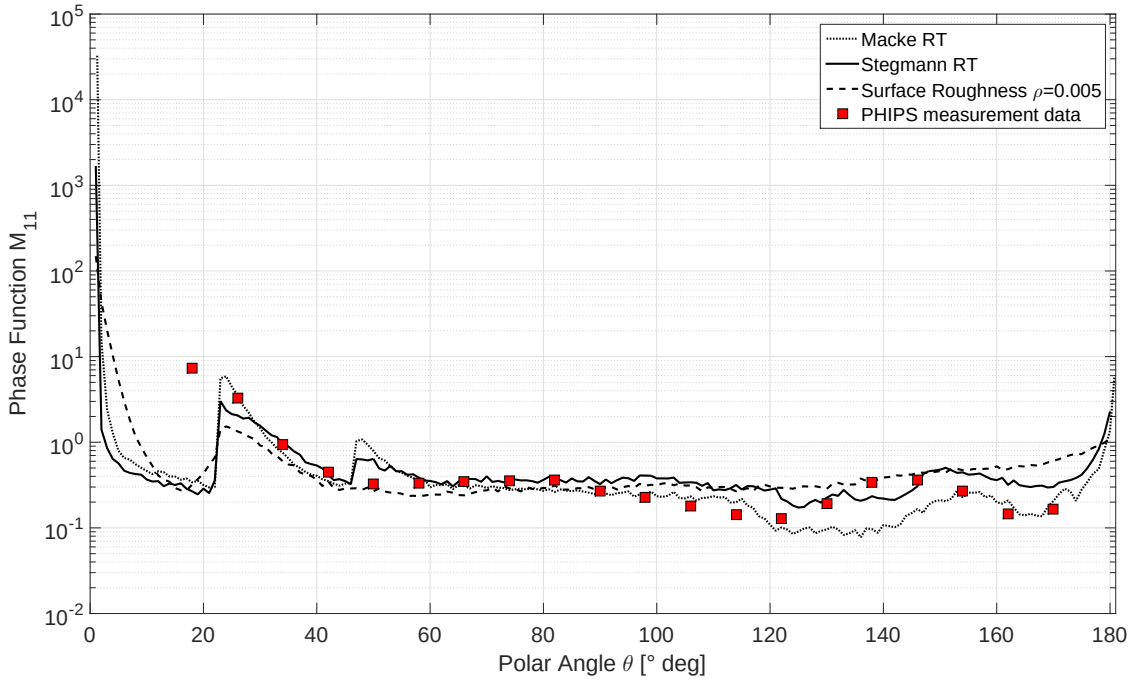

Figure 5.18: Comparison between experimental results after calibration and Ray tracing solutions. Experimental data courtesy of Martin Schnaiter and Emma Jaervinnen.

6 Further Perspectives

Let the winter sun shine on
Let me feel the frost of dawn
Fill my dreams with flakes of snow
Soon I'll feel the chilling glow

—*John Michael Osbourne* [OBIW72].

As shown in this thesis, the current experimental and numerical development in the effort to characterize non-spherical particles is promising, despite the apparent difficulties due to the randomness of essentially all characteristic features of the particles. While the mathematical and theoretical effort is ongoing and by no means complete, novel measurement techniques and the current rapid increase in computational power [Moo98] show great promise to «impose order on the chaos» that are non-spherical particles. While the simulation of complex particle shapes is now possible, future remaining problems are especially the detailed characterisation of the aerosols with respect to their surface roughness and inclusions, such as air bubbles or ice nucleation cores for instance. This problem was identified by Prof. Andreas Macke from the TROPOS institute in Leipzig at the 2015 conference on Electromagnetic and Light Scattering as a common impetus for future investigations.

6.1 Null Geodesics and Metamaterials

The domain of optics concerned with the scattering of light by metamaterials was established in the last decade and is called **Transformation Optics** [LP09] and draws largely on the analogy between the dielectric permittivity tensor ε_{ij} and the spatial metric $g_{\mu\nu}$. The first extended publication on the similarities between ray tracing inhomogeneous media and the optics of gravitational fields was written by Plebanski [Ple60]. Furthermore it is a well known fact [HKW+94] that the null geodesic equation on a manifold with an affine connection $\Gamma^{\mu}_{\alpha\beta}$ and an affine parameter τ:

$$\frac{d^2x^{\mu}}{d\tau^2} + \Gamma^{\mu}_{\alpha\beta}\frac{dx^{\alpha}}{d\tau}\frac{dx^{\beta}}{d\tau} = 0 \tag{6.1}$$

may be reformulated in terms of canonical variables for an appropriate metric, such that the second order ODE becomes first order. Consequently, the ray tracing code for inhomogeneous media from section 3.2 may be modified with little effort, in order to allow its application in an astronomical context or in the design of optical metamaterials.

6.2 Discontinuous Galerkin Methods in Computational Electromagnetics and Radiative Transfer

While Discontinuous Galerkin (DG) methods have already been introduced in the 1970s [RH73], their widespread use is fairly recent. According to Hesthaven and Warburton [HW08], this class of methods all constitute a hybrid form between Finite Volume methods (FVM) and Finite Elements (FEM), combining the respective advantages of stability, conservativity and accuracy of the different methods. While DG methods have recieved interest mainly in the field of fluid dynamics [Kum12], they are also particularly apt for solving wave problems and were first applied to radiation transport problems in reference [RH73] for good reason, as these methods excel if there is a flux of a conserved quantity in the physical problem to solve, which is by definition true for all radiation problems. Generally, DG methods are used to find the solution $u(x)$ of a conservative PDE on the domain Ω:

$$\frac{\partial u}{\partial t} + \frac{\partial f}{\partial x} = g, \qquad x \in \Omega \tag{6.2}$$

where $f(u,x,t)$ is a flux and $g(x,t)$ is a forcing function. The reader may check that the FIT equation (3.76) is of this form, as well as the radiation transport equation (RTE) [Cha03]. As the Finite Integration Technique is a second-order FVM, exploiting a DG approach for Maxwell's equations in the future in order to easily achieve higher accuracy seems natural. Implementations of the DG methods applied to Maxwell's equations in fact already exist and are applicable to large problems with comparatively minor effort, if existing high performance FEM and ODE integrator libraries are used [BHK07, LMW12, boo14].

The timeshift technique as developed for instance by Schäfer in [Sch13] is but the simplest case of a structured light technique in the 1D case. One can imagine to increase the amount of information gained from a time-shift experiment by employing a two-dimensional grid-like structure such as a higher Hermite-Gauss mode [KL] of a laser beam as depicted in figure 6.1. This approach has already been applied succesfully in the fields of super-resolution microscopy [Gus05] and consumer electronics [ZXYW14] in order to detect and identify geometrically complex objects.

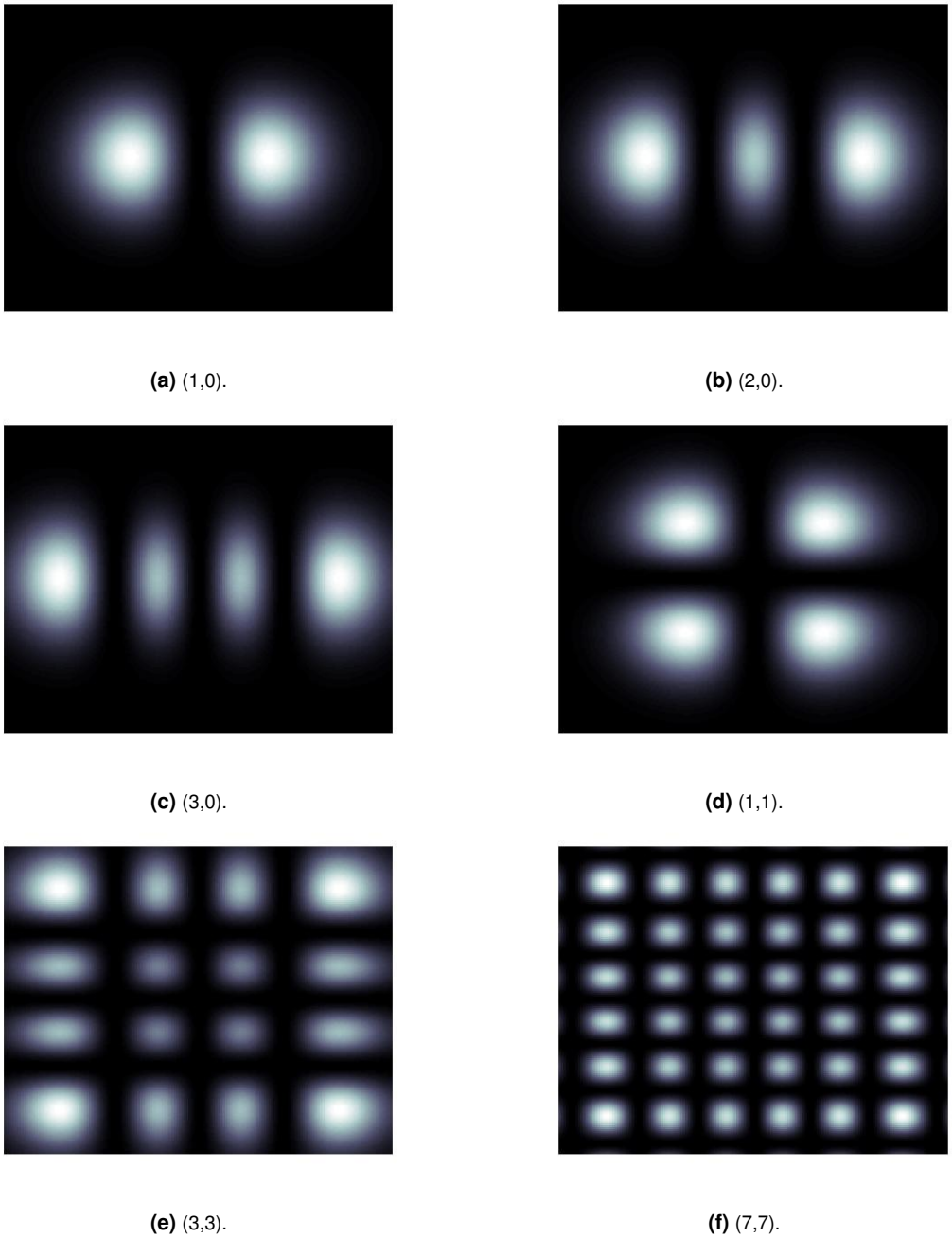

(a) (1,0). **(b)** (2,0). **(c)** (3,0). **(d)** (1,1). **(e)** (3,3). **(f)** (7,7).

Figure 6.1: Surface plots of various (n,m) Hermite-Gauss modes of a laserbeam.

Acknowledgement

THIS research is financially supported by the German Research Foundation under Grant TR 194/49-1 and through the collaborative research centre SFB/TRR 75. The author would also like to express his gratitude to the Graduate School of Excellence Computational Engineering at TU Darmstadt for the provision of various occasions to exchange knowledge with other Ph.D. students and several opportunities for professional development and to the Research Training Group GRK1114 of the Deutsche Forschungsgemeinschaft for their respective support of his Ph.D. project.

Nowadays, a doctoral thesis can hardly be thought of as the solitary work of an isolated, singular individual. To the contrary, many people take part in the gestation of such a project and the exchange of knowledge and mutual support of experts in very diverse fields are central to finding new ideas. Thus this last unofficial chapter is dedicated to the expression of my sincere gratitude towards all the people who, directly or indirectly, have contributed to the ultimate success of this project.

First of all I would like to thank Prof. Dr.-Ing. **Cameron Tropea** for providing me with the opportunity to pursue a doctorate at the respected Institute of Fluid Mechanics and Aerodynamics in Darmstadt and under his personal supervision. His physical intuition, purposeful questions and the possibility to follow independent ideas during the thesis were a major contributing factor to the success of this work. Furthermore his efforts in providing opportunities for scientific exchange and professional development were of utmost importance in gaining new insights.

Second, I would like to thank Prof. **Gérard Gréhan**, who also took part in enabling me to persue this doctorate and whose unique expertise in the field of laser light scattering as a whole has proven to be invaluable. Lastly, I am indebted for his hospitality in welcoming me at the university of Rouen, France in 2012.

Connected to Prof. Gréhan, I would of course also like to thank Prof. em. **Gérard Gouesbet** for providing me with my first scientific problem in the field of scattering theory, which was completely unknown to me before this instance in time and also for sharing some of his wide experience on various occasions.

Third, my gratitude goes to several colleagues here at TU Darmstadt and elsewhere, including **Jan-Niklas Hau** for the discussions on symmetry, **Andreas Fenner** for his expertise on high-speed imaging, **Ilona Kaufhold** for manufacturing even the oddest prototypes, **Hubert Marschall** for the discussions on tensors, as well as Rüdiger Röhrig, Daniel Kintea, Markus Schremb and Hannah Kittel for the occasional discussions on OpenFOAM® and camera lenses. Furthermore I would like to thank my former colleague Dr. **Walter Schäfer**, without whom the Time-Shift measurements would have been impossible, as well as Dr. **Erion Gjonaj** for the discussions on FIT and symplectic geometry, as well as for providing me with a workstation at the TEMF institute.

Lastly, from the university of Stuttgart I would like to thank **Dr. Norbert Roth**, **Stefano Ruberto** and **Matthias Giegerich**. At the Karlsruhe Institute of Technology I would like to thank Dr. **Martin Schnaiter** and Ms **Emma Järvinen** for including me in the PHIPS analysis process, at the university of Hertfordshire I would like to thank Dr. **Helen Smith** and at the NASA Jet Propulsion Laboratory I would like to thank Dr. **Xu Feng**.

From the multitude of supervised undergraduate students I would especially like to mention **Markus Degenhardt** and the ADP group of 2015 for their outstanding work.

Bibliography

[AB59] AHARONOV, Y. ; BOHM, David: Significance of Electromagnetic Potentials in the Quantum Theory. In: *Physical Review* 115 (1959), S. 485–491

[ABDT03] ALBRECHT, H. E. ; BORYS, M. ; DAMASCHKE, N. ; TROPEA, C.: *Laser Doppler and Phase Doppler Measurement Techniques*. Springer-Verlag Berlin Heidelberg, 2003

[Ahn12a] AHNERT, K.: *Boost odeint solar system tutorial*. website. `http://www.boost.org/doc/libs/master/libs/numeric/odeint/doc/html/boost_numeric_odeint/tutorial/solar_system.html`. Version: 2012

[Ahn12b] AHNERT, Karsten: *Boost odeint Web presence*. website. `http://headmyshoulder.github.io/odeint-v2/`. Version: 2012

[AKH10] ARGYROPOULOS, Christos ; KALLOS, Efthymios ; HAO, Yang: FDTD analysis of the optical black hole. In: *Journal of the Optical Society of America B* 27 (2010), S. 2020–2025

[AMHH08] AKENINE-MOELLER, T. ; HAINES, E. ; HOFFMAN, N.: *Real-Time Rendering*. CRC Press, 2008

[Arn84] ARNOL'D, Vladimir I. ; HALMOS, P.R. (Hrsg.) ; GEHRING, F. W. (Hrsg.) ; MOORE, C. C. (Hrsg.): *Mathematical Methods of Classical Mechanics*. Springer-Verlag New York Heidelberg Berlin, 1984

[AS64] ARBRAMOWITZ, Milton ; STEGUN, Irene: *Handbook of Mathematical Functions with Formulas, Graphs and Mathematical Tables*. Dover Publications, Inc., 1964

[ASA+11] ABDELMONEM, A. ; SCHNAITER, Martin ; AMSLER, P. ; HESSE, Evelyn ; MEYER, J. ; LEISNER, T.: First correlated measurements of the shape and light scattering properties of cloud particles using the new Particle Habit Imaging and Polar Scattering (PHIPS) probe. In: *Atmospheric Measurement Techniques* 4 (2011), S. 2125–2142

[AY75] ASANO, Shoji ; YAMAMOTO, Giichi: Light Scattering by a Spheroidal Particle. In: *Applied Optics* 14 (1975), S. 29–49

[Bar07] BARCHANSKI, Andreas: *Simulations of Low-Frequency Electromagnetic Fields in the Human Body*, TEMF TU Darmstadt, Diss., 2007

[Bas10] BASLER VISION TECHNOLOGIES AG (Hrsg.): *Basler A630f User's Manual*. 1. An der Strusbek 60 - 62 22926 Ahrensburg Germany: Basler Vision Technologies AG, December 2010

[BB15] BAUMERT, Arne ; BANSMER, Stephan: Implementation of an innovative ice crystal generation system to the Icing Wind Tunnel Braunschweig. In: *53rd AIAA Aerospace Sciences Meeting*, 2015

[BBWR13] BREUNINGER, Jannis ; BECKER, Ralf ; WOLF, Andreas ; ROMMEL, Steve: *Generative Fertigung mit Kunststoffen: Konzeption und Konstruktion für Selektives Lasersintern*. Springer Verlag Berlin-Heidelberg, 2013

[Ber94] BERENGER, Jean-Pierre: A Perfectly Matched Layer for the Absorption of Electromagnetic Waves. In: *Journal of Computational Physics* 114 (1994), S. 185–200

[Ber09] BERRY, Michael V.: Optical Currents. In: *Journal of Optics A: Pure and Applied Optics* 11 (2009), S. 12

[BGN12] BARRET, John W. ; GARCKE, Harald ; NÜRNBERG, Robert: Numerical computations of faceted pattern formation in snow crystal growth. In: *Physical Review E: Statistical, Nonlinear, and Soft Matter Physics* 86 (2012), S. 011604

[BHK07] BANGERTH, W. ; HARTMANN, R. ; KANSCHAT, G.: deal.ii – a General-Purpose Object Oriented Finite Element Library. In: *ACM Transactions on Mathematical Software* 33 (2007), S. 24/1–24/27

[Blo46] BLOCH, Felix: Nuclear induction. In: *Physical Review* 70 (1946), S. 460–474

[BM08] BERRY, Michael V. ; MCDONALD, K. T.: Exact and geometrical optics energy trajectories in twisted beams. In: *Journal of Optics A: Pure and Applied Optics* 10 (2008)

[BN94] BARTON, John J. ; NACKMAN, Lee R.: *Scientific and Engineering C++: An Introduction with Advanced Techniques and Examples*. Addison Wesley Publishing Co., 1994

[boo14] *Boost homepage*. website. `http://www.boost.org`. Version: November 2014

[boo15] *Boost Quaternion Library*. `http://www.boost.org/doc/libs/1_46_1/libs/math/doc/quaternion/html/`. Version: August 2015

[Bor67] BORK, Alfred M.: Maxwell and the Electromagnetic Wave Equation. In: *American Journal of Physics* 35 (1967), S. 844

[Brö04] BRÖCKER, Theodor: *Lineare Algebra und Analytische Geometrie: Ein Lehrbuch für Physiker und Mathematiker*. Birkhäuser, 2004

[Brä15] BRÄUNLING, Willy J. G.: *Flugzeugtriebwerke, 4. Auflage*. Springer Vieweg, 2015

[Bre07] BREYMANN, Ulrich: *C++: Einführung und professionelle Programmierung*. Carl Hanser Verlag GmbH & Co. KG, 2007

[BRJB15] BRUNEL, Marc ; RUIZ, Sara G. ; JACQUOT, Justin ; BEECK, Jeroen van: On the morphology of irregular rough particles from the analysis of speckle-like interferometric out-of-focus images. In: *Optics Communications* 338 (2015), S. 193–198

[BSC+14] BRUNEL, Marc ; SHEN, Huanhuan ; COETMELLEC, Sébastien ; GRÉHAN, Gérard ; DELOBEL, Tony: Determination of the Size of Irregular Particles Using Interferometric Out-of-focus Imaging. In: *International Journal of Optics* 1 (2014), S. 1–8

[BSM00] BRONSTEIN, Ilja N. ; SEMENDJAJEW, Konstantin A. ; MUSIOL, Gerhard: *Taschenbuch der Mathematik*. Harri Deutsch, 2000

[BU80] BERRY, M. V. ; UPSTILL, C.: Catastrophe Optics: Morphologies of Caustics and their Diffraction Patterns. In: *Progress in Optics* (1980), S. 259–343

[But82] BUTKOVSKY, Anatoliy G.: *Green's Functions and Transfer Functions Handbook*. Ellis Horwood Limited, 1982

[BW99] BORN, Max ; WOLF, Emil: *Principles of optics: Electromagnetic theory of propagation, interference and diffraction of light (7th expanded edition)*. Cambridge University Press, 1999

[BY14] BI, Lei ; YANG, Ping: Accurate simulation of the optical properties of atmospheric ice crystals with the invariant imbedding T-matrix method. In: *Journal of Quantitative Spectroscopy & Radiative Transfer* 138 (2014), S. 17–35

[Car06] CARTAN, Henri: *Differential Forms*. Dover publications, Inc., 2006

[CBDMDB96] CHOUQUET-BRUHAT, Yvonne ; DEWITT-MORETTE, Cécile ; DILLARD-BLEICK, Margaret: *Analysis, Manifolds and Physics Part 1: Basics (Revised Edition)*. Elsevier Science, 1996

[Cha67] CHAULNES, M. Duc d.: Mémoire sur quelques Expériences relatives à la Dioptrique. In: *Histoire de l'Academie Royale des Sciences* 1 (1767), S. 423–471

[Cha03] CHANDRASEKHAR, Subrahmanyan: *Radiative Transfer*. Dover Publications, Inc., 2003

[Cor83] CORNBLEET, Sidney: Geometrical Optics Reviewed: A New Light on an Old Subject. In: *Proceedings of the IEEE* 4 (1983), S. 471–502

[Cri14] CRISCIONE, Antonio: *Influence of Ice Formation on Drop Dynamics*, Fachgebiet Strömungslehre und Aerodynamik, TU Darmstadt, Diss., 2014

[CST06] CST, of A.: A software suite with total synergy. In: *Microwave Journal* 49 (2006), S. 150ff.

[CST15] CST: *CST Studio applications*. website. `https://www.cst.com/Applications`. Version: August 2015

[CTDRG96] COHEN-TANNOUDJI, Claude ; DUPONT-ROC, Jacques ; GRYNBERG, Gilbert ; LEDUC, Michèle (Hrsg.): *Processus d'interaction entre photons et atomes*. EDP Sciences/CNRS Éditions, 1996

[CW01] CLEMENS, M. ; WEILAND, T.: Discrete Electromagnetism with the Finite Integration Technique. In: *Progress in Electromagnetics Research* 32 (2001), S. 65–87

[Dam03] DAMASCHKE, Nils: *Light Scattering Theories and Their Use for Single Particle Characterization*, Fachgebiet Strömungslehre und Aerodynamik Technische Universität Darmstadt, Diss., 2003

[Dav79] DAVIS, L. W.: Theory of electromagnetic beams. In: *Physical Review A: Atomic, Molecular, and Optical Physics* 19 (1979)

[Deg14] DEGENHARDT, Markus J.: *Entwicklung einer ODE-Solver-Bibliothek zur Berechnung von inhomogenen elektrodynamischen Wellenfeldern*. September 2014. – Bachelor Thesis

[Dem09] DEMTRÖDER, W.: *Experimentalphysik 2: Elektrizität und Optik, Elektromagnetische Wellen im Vakuum*. Springer Verlag Berlin-Heidelberg, 2009

[Des72] DESCHAMPS, G. A.: Ray Techniques in Electromagnetics. In: *Proceedings of the IEEE* 60 (1972), S. 1022–1035

[Des81] DESCHAMPS, George A.: Electromagnetics and Differential Forms. In: *Proceedings of the IEEE, Vol. 69, No. 6*, 1981

[DEW00] DOICU, Adrian ; EREMIN, Yuri ; WRIEDT, Thomas: *Acoustic & Electromagnetic Scattering Analysis using discrete sources*. Academic Press, 2000

[Dir64] DIRAC, Paul Adrien M.: *Lectures on Quantum Mechanics*. Belfer Graduate School of Science Monographs, 1964

[Dir88] DIRAC, Paul Adrien M.: *The Principles of Quantum Mechanics*. Oxford University Press USA, 1988

[DP80] DORMAND, J. R. ; PRINCE, P. J.: A family of embedded Runge-Kutta formulae. In: *Journal of Computational and Applied Mathematics* 6 (1980), S. 19–26

[DR08] DAHMEN, Wolfgang ; REUSKEN, Arnold: *Numerik für Ingenieure und Naturwissenschaftler*. Springer Verlag Berlin-Heidelberg, 2008

[EE03] EICHLER, Jürgen ; EICHLER, Hans-Joachim: *Laser: Bauformen, Strahlführung, Anwendungen*. Springer Verlag Berlin-Heidelberg, 2003

[Ein16] EINSTEIN, Albert: Die Grundlagen der allgemeinen Relativitätstheorie. In: *Annalen der Physik* 354 (1916), S. 769–822

[Ein36] EINSTEIN, A.: Lens-like action of a star by the deviation of light in the gravitational field. In: *Science* 84 (1936), S. 506f.

[EKAD14] EBERT, E. ; KLEINWÄCHTER, A. ; A., Kostbade ; DAMASCHKE, N.: Interferometric Particle Imaging for cavitation nuclei characerization in cavitation tunnels and in the wake flow. In: *17th International Symposium on Applications of Laser Techniques to Fluid Mechanics Lisbon, Portugal*, 2014

[Eme15] EMERSIC, Christopher: *MICC website*. website. `http://data.cas.manchester.ac.uk/micc/micc.htm`. Version: August 2015

[FB09] FANG, Qianqian ; BOAS, David A.: Monte Carlo simulation of photon migration in 3D turbid media accelerated by graphics processing units. In: *Optics Express* 22 (2009), S. 20178–20190

[Feh68] FEHLBERG, Erwin: Classical Fifth-, Sixth-, Seventh-, and Eighth-order Runge-Kutta formulas with stepsize control / George C. Marshall Space Flight Center, Huntsville, Alabama (NASA). 1968. – Forschungsbericht

[Fer56] FERMI, Enrico: *Thermodynamics*. Dover Publications, Inc., 1956

[Fey42] FEYNMAN, Richard P.: *The principle of least action in quantum mechanics*, Department of Physics, Princeton University, Diss., 1942

[Fey82] FEYNMAN, Richard P.: Simulating Physics with Computers. In: *International Journal of Theoretical Physics* 21 (1982), S. 467–488

[FH65] FEYNMAN, R. P. ; HIBBS, Albert R.: *Quantum Mechanics and Path Integrals*. McGraw-Hill Companies, Inc., New York, 1965

[FHH+15] FISCHER, Killian ; HOFMANN, Timo ; HORN, André ; MÜLLER, Lilian ; WEHNER, Tina: *ADP: Aufbau einer Nukleationskammer für Wassereis-Kristalle*, Fachgebiet Strömungslehre und Aerodynamik, TU Darmstadt, Diplomarbeit, 2015

[Fla89] FLANDERS, Harley: *Differential Forms with Applications to the Physical Sciences*. Dover publications, Inc., 1989

[Fli12a] FLIESSBACH, T.: *Allgemeine Relativitätstheorie*. Springer Spektrum Akademischer Verlag, 2012

[Fli12b] FLIESSBACH, Thorsten: *Elektrodynamik: Lehrbuch zur Theoretischen Physik II*. Springer Spektrum Akademischer Verlag, 2012

[FLS65] FEYNMAN, Richard P. ; LEIGHTON, Robert B. ; SANDS, Matthew: *The Feynman Lectures on Physics, Volume III: Quantum Mechanics*. Addison Wesley Publishing Co., 1965

[Foc26a] FOCK, Valdimir: Über die invariante Form der Wellen- und der Bewegungsgleichungen für einen geladenen Massenpunkt. In: *Zeitschrift für Physik* 39 (1926), S. 226–232

[Foc26b] FOCK, Valdimir: Zur Schrödingerschen Wellenmechanik. In: *Zeitschrift für Physik* 38 (1926), S. 242–250

[For06] FOREST, É.: Geometric integration for particle accelerators. In: *Journal of Physics A: Mathematical and General* 39 (2006), S. 5321–5377

[FP08] FERZIGER, Joel H. ; PERIC, Milovan: *Numerische Strömungsmechanik*. Springer Verlag Berlin-Heidelberg, 2008

[FR90] FOREST, É. ; RUTH, Donald D.: Fourth-Order Symplectic Integration. In: *Physica D* 43 (1990), S. 105–117

[Gal] GALASSI, M. et a.: *GNU Scientific Library Reference Manual (2nd edition)*, 2014

[Gan14] GANSMANN, Ann-Kathrin: *Charakterisierung und Nutzung der Laserlichtstreuung an Eiskristallen*, Fachgebiet Strömungslehre und Aerodynamik, TU Darmstadt, Diplomarbeit, 2014

[Gao12] GAO, Jing: *Generation of postured voxel-based human body models used for electromagnetic applications*, TEMF TU Darmstadt, Diss., 2012

[GBC+02] GJONAJ, Erion ; BARTSCH, Michael ; CLEMENS, Markus ; SCHUPP, Sören ; WEILAND, Thomas: High-resolution human anatomy models for advanced electromagnetic field computations. In: *IEEE transactions on magnetics* 3 (2002), S. 357–360

[GDC91] GLADMAN, Brett ; DUNCAN, Martin ; CANDY, Jeff: Symplectic integrators for long-term integrations in celestial mechanics. In: *Celestial Mechanics and Dynamical Astronomy* 52 (1991), S. 221–240

[Ged11] GEDNEY, Stephen D. ; BALANIS, Constantine A. (Hrsg.): *Introduction to the Finite-Difference-Time-Domain (FDTD) Method for Electromagnetics*. Morgan & Claypool Publishers, 2011

[GG11] GOUESBET, Gérard ; GRÉHAN, Gérard: *Generalized Lorenz Mie Theories*. Springer-Verlag, 2011

[GKZC04] GRIEBEL, Michael ; KNAPEK, Stefan ; ZUMBUSCH, Gerhard ; CAGLAR, Attila: *Numerische Simulation in der Moleküldynamik*. Springer Verlag Berlin-Heidelberg, 2004

[Gla63] GLAUBER, Roy J.: Coherent and incoherent states of the radiation field. In: *Physical Review* 131 (1963), S. 2766–2788

[GLS+06] GJONAJ, E. ; LAU, T. ; SCHNEPP, S. ; WOLFHEIMER, F. ; WEILAND, T.: Accurate modelling of charged particle beams in linear accelerators. In: *New Journal of Physics* 8 (2006), S. 285ff.

[GM69] GLOGE, D. ; MARCUSE, D.: Formal Quantum Theory of Light Rays. In: *Journal of the Optical Society of America* 59 (1969), S. 1629–1631

[Goo76] GOODMAN, J. W.: Some fundamental properties of speckle. In: *Journal of the Optical Society of America* 66 (1976), S. 1145–1150

[Goo05] GOODMAN, Joseph W.: *Introduction to Fourier Optics*. Roberts & Company, 2005

[GRVB14] GONZÁLEZ-RUIZ, Sara ; VETRANO, Maria R. ; BEECK, J. van: Feasibility of using glory and speckle patterns for sizing spherical and irregular particles. In: *Applied Optics* 53 (2014), S. 4722–4728

[GSS67] GOLDBERG, Abraham ; SCHEY, Harry M. ; SCHWARTZ, Judah L.: Computer-Generated Motion Pictures of One-Dimensional Quantum-Mechanical Transmission and Reflection Phenomena. In: *American Journal of Physics* 35 (1967), S. 177–186

[Gus05] GUSTAFSSON, Mats G. L.: Nonlinear structured-illumination microscopy: Wide-field fluorescence imaging with theoretically unlimited resolution. In: *PNAS* 102 (2005), S. 13081–13086

[GW29] GIBBS, J. W. ; WILSON, Edwin B. ; WILSON, Edwin B. (Hrsg.): *Vector analysis, a text-book for the use of students of mathematics and physics, founded upon the lectures of J. Willard Gibbs*. New Haven: Yale University Press, 1929

[GWE04] GONZALEZ, Rafael C. ; WOODS, Richard E. ; EDDINS, Steven L.: *Digital Image Processing Using MATLAB*. Pearson Education, Inc., 2004

[Hag78] HAGEDORN, Peter: *Nichtlineare Schwingungen*. Akademische Verlagsgesellschaft Wiesbaden, 1978

[Han35] HANSEN, W. W.: A New Type of Expansion in Radiation Problems. In: *Physical Review* 47 (1935), S. 139–143

[Han15] HANSELKA, Holger: *AIDA website*. website. `https://www.imk-aaf.kit.edu/73.php`. Version: August 2015

[Hec02] HECHT, Eugene: *Optik*. Oldenbourg Wissenschaftsverlag, 2002

[Hei27] HEISENBERG, Werner: Über den anschaulichen Inhalt der quantentheoretischen Kinematik und Mechanik. In: *Zeitschrift für Physik* 43 (1927), S. 172–198

[Her80] HERTZ, Heinrich: *Ueber die Induction in rotierenden Kugeln*, Philosophische Facultät der Friedrich-Wilhelms-Universität zu Berlin, Diss., 1880

[HH84] HECKBERT, P. S. ; HANRAHAN, P.: Beam Tracing Polygonal Objects. In: *Computer Graphics* 18 (1984)

[HKW+94] HUGHES, Scott A. ; KEETON, Charles R. I. ; WALKER, Paul ; WALSH, Kevin T. ; SHAPIRO, Stuart L. ; TEUKOLSKY, Saul A.: Finding black holes in numerical spacetimes. In: *Physical Review D* 49 (1994), S. 4004–4015

[HNU03] HU, Junhui ; NAKAMURA, Kentaro ; UEHA, Sadayuki: Stability Analysis of an Acoustically Levitated Disk. In: *IEEE Transactions on Ultrasonics, Ferroelectrics and Frequency Control* 50 (2003), S. 117–127

[Hoe94] HOEKSTRA, Antoon G.: *Computer Simulations of Elastic Light Scattering*, Universiteit van Amsterdam, Fakulteit Wiskunde en Informatica, Diss., 1994

[HOSS14] HEUSSER, Jens ; OSTOLSKI, Alexander ; SCHIEMANN, Robert ; SEMBACH, Philipp: *Auslegung einer Nukleationskammer für Wassereis-Kristalle*, Fachgebiet Strömungslehre und Aerodynamik, TU Darmstadt, Diplomarbeit, 2013/14

[HU03] HECHT, Evelyn ; ULANOWSKI, Zbigniew: Scattering from long prisms computed using the ray tracing combined with diffraction on facets. In: *Journal of Quantitative Spectroscopy & Radiative Transfer* 79-80 (2003), S. 712–732

[Hul91] HULST, H. C. d.: Glare points. In: *Applied Optics* 30 (1991), S. 4755–4763

[Hul01] HULST, Hendrik C. d.: *Light Scattering by Small Particles*. Dover Publications, Inc., 2001

[HW08] HESTHAVEN, Jan S. ; WARBURTON, Tim: *Nodal Discontinuous Galerkin Methods*. Springer Science+Businnes Media LLC, 2008

[IGW86] ISSA, R. I. ; GOSMAN, A. D. ; WATKINS, A. P.: The Computation of Compressible and Incompressible Recirculating Flows by a Non-iterative Implicit Scheme. In: *Journal of Computational Physics* 62 (1986), S. 66–82

[IZ06] ITZYKSON, Claude ; ZUBER, Jean-Bernard: *Quantum Field Theory*. Dover Publications, Inc., 2006

[Jac75] JACKSON, John D.: *Classical Electrodynamics (2nd edition)*. John Wiley & Sons, 1975

[JHR13] JIANG, Keli ; HAN, Xiang'e ; REN, Kuan F.: Scattering of a Gaussian beam by an elliptical cylinder using the vectorial complex ray model. In: *Journal of the Optical Society of America* 30 (2013)

[JL72] JONES, W. P. ; LAUNDER, B. E.: The prediction of laminarization with a two-equation model of turbulence. In: *International Journal of Heat and Mass Transfer* 15 (1972), S. 301–314

[JNN13] JOHANSSON, J. R. ; NATION, P. D. ; NORI, F.: QuTiP 2: A Python framework for the dynamics of open quantum systems. In: *Computational Physics Communcations* 184 (2013), S. 1234 ff.

[Joh93] JOHNSON, B. R.: Theory of morphology-dependant resonances: shape resonances and width formulas. In: *Journal of the Optical Society of America* 10 (1993), S. 343–352

[Kah05] KAHNERT, Michael: Irreducible representations of finite groups in the T-matrix formulation of the electromagnetic scattering problem. In: *Journal of the Optical Society of America* 22 (2005), S. 1187–1199

[Kah13] KAHNERT, Michael: The T-matrix code Tsym for homogeneous dielectric particles with finite symmetries. In: *Journal of Quantitative Spectroscopy & Radiative Transfer* 123 (2013), S. 62–78

[Kas00] KASHCHIEV, Dimo: *Nucleation: Basic Theory with Applications*. Butterworth-Heinemann, 2000

[Kep11] KEPLERUS, Joannes: *STRENA SEU DE NIVE SEXANGULA*. January 1611

[KHD11] KRETSCHMER, A. ; HÖHNE, S. ; DAMASCHKE, N.: Particle characerization with the Time-Shift-Technique. In: *Sensors, IEEE,* 2011

[KHG+08] KAYE, P. ; HIRST, E. ; GREENWAY, R. ; ULANOWSKI, Z. ; HESSE, E. ; DEMOTT, P.: Classifying atmospheric ice crystals by spatial light scattering. In: *Optics Letters* 33 (2008), S. 1545–7

[Khl92] KHLEBTSOV, Nikolai G.: Orientational averaging of light-scattering observables in the T-matrix approach. In: *Applied Optics* 31 (1992), S. 5359–5365

[KL] KOGELNIK, H. ; LI, T.: Laser Beams and Resonators. In: *Applied Optics* 5, S. 1550–1567

[Kle07] KLEMM, Otto: Wasserdampffluss (Umweltmeteorologie) / Universität Münster. 2007. – Forschungsbericht

[KNL14] KAHNERT, M. ; NOUSIAINEN, Timo ; LINDQVIST, Hannakaisa: Review: Model particles in atmospheric optics. In: *Journal of Quantitative Spectroscopy & Radiative Transfer* 146 (2014), S. 41–58

[KO90] KRAVTSOV, Yury A. ; ORLOV, Yury I.: *Geometrical Optics of Inhomogeneous Media*. Springer-Verlag, 1990

[KSS01] KAHNERT, Michael F. ; STAMNES, Jakob J. ; STAMNES, Knut: Application of the extended boundary condition method to homogeneous partices with point-group symmetries. In: *Applied Optics* 40 (2001), S. 3110–3123

[Kum12] KUMMER, Florian: *The BoSSS Discontinuous Galerkin solver for incompressible fluid dynamics and an extension to singular equations*, Fachgebiet für Strömungsdynamik, TU Darmstadt, Diss., 2012

[LAH98] LAWSON, Paul ; ANGUS, Leigh ; HEYMSFIELD, Andrew: Cloud Particle Measurements in Thunderstorm Anvils and Possible Weather Threat to Aviation. In: *Journal of Aircraft* 35 (1998)

[Lav03] LAVEN, Philip: Simulation of Rainbows, Coronas, and Glories by use of Mie Theory. In: *Applied Optics* 42 (2003), S. 436–444

[Lav15] LAVEN, P.: *MiePlot website*. website. `http://www.philiplaven.com/mieplot.htm`. Version: July 2015

[LBCTL13] LE BELLAC, Michel ; COHEN-TANNOUDJI, Claude ; LALOE, Franck: *Physique Quantique: Tome 1, Fondements*. EDP Sciences, 2013

[Leo06] LEONHARDT, Ulf: Optical Conformal Mapping. In: *Science* 312 (2006), S. 1777–1780

[LGW05] LAU, Thomas ; GJONAJ, Erion ; WEILAND, Thomas: Time Integration Methods for Particle Beam Simulations with the Finite Integration Theory. In: *Frequenz: Journal of RF-Engineering and Telecommunications* 59 (2005), S. 210–219

[Li13] LI, Hai: *Drop Impact on Dry Surfaces*, Fachgebiet Strömungslehre und Aerodynamik, TU Darmstadt, Diss., 2013

[Lib99] LIBBRECHT, K. G.: *Growing Your Own Snow Crystals ... Snowflakes in a bottle...* website. `http://www.its.caltech.edu/~atomic/snowcrystals/project/project.htm`. Version: February 1999

[Lib05] LIBBRECHT, Kenneth G.: The physics of snow crystals. In: *Reports on Progress in Physics* 68 (2005), S. 855–895

[Lit05] LITFIN, G.: *Technische Optik in der Praxis, Fasern und Sensorik*. Springer Verlag Berlin-Heidelberg, 2005

[LL75] LANDAU, Lew ; LIFSCHITZ, Jewgeni: *Lehrbuch der theoretischen Physik, Band II: Klassische Feldtheorie*. Akademie-Verlag Berlin, 1975

[LL80] LANDAU, L. D. ; LIFSCHITZ, E. M. ; ZIESCHE, Paul (Hrsg.): *Lehrbuch der theoretischen Physik, Band IV: Relativistische Quantentheorie*. Akademie-Verlag Berlin, 1980

[LL90] LANDAU, Lew D. ; LIFSCHITZ, Jewgeni M.: *Lehrbuch der Theoretischen Physik, Band III: Quantenmechanik*. Akademie-Verlag Berlin, 1990

[LLA14a] LAVEN, Philip ; LOCK, J. A. ; ADAM, J. A.: Scattering of a plane electromagnetic wave by a generalized Luneburg sphere-Part 2: Wave scattering and time-domain scattering. In: *Journal of Quantitative Spectroscopy & Radiative Transfer* 162 (2014), S. 164–174

[LLA14b] LOCK, James A. ; LAVEN, Philip ; ADAM, John A.: Scattering of a plane electromagnetic wave by a generalized Luneburg sphere-Part 1: Ray Scattering. In: *Journal of Quantitative Spectroscopy & Radiative Transfer* 162 (2014), S. 154–163

[LM08] LIBBRECHT, K. G. ; MORRISON, Helen C.: A Convection Chamber for Measuring Ice Crystal Growth Dynamics. In: *arxiv.org* (2008)

[LMW12] LOGG, Anders ; MARDAL, Kent-Andre ; WELLS, Garth: *Automated Solution of Differential Equations by the Finite Element Method: The FEniCS book*. Springer Verlag Berlin-Heidelberg, 2012

[Lün64] LÜNEBURG, Rudolf K.: *Mathematical Theory of Optics*. University of California Press, Berkley/Los Angeles, 1964

[LP09] LEONHARDT, Ulf ; PHILBIN, Thomas G.: Transformation Optics and the Geometry of Light. In: *Progress in Optics* 53 (2009), S. 1–72

[LRP+10] LADAK, S. ; READ, D.E ; PERKINS, G. K. ; COHEN, L. F. ; BRANFORD, W. R.: Direct observation of magnetic monopole defects in an artificial spin-ice system. In: *Nature Physics* 6 (2010), S. 359–363

[LS50] LIPPMANN, Bernard A. ; SCHWINGER, Julian: Variational Principles for Scattering Processes I. In: *Physical Review Letters* 79 (1950), S. 469

[Lun10] LUNZE, Jan: *Regelungstechnik 1: Systemtheoretische Grundlagen, Analyse und Entwurf einschleifiger Regelungen*. Springer Verlag Berlin-Heidelberg, 2010

[Mac94] MACKE, Andreas: *Modellierung der optischen Eigenschaften von Cirruswolken*, Fachbereich Geowissenschaften der Universität Hamburg, Diss., 1994

[Mac15] MACKE, Andreas: *Source Codes for single scattering and radiative transfer simulations in UNIX environments. Codes are written in Fortran77 and Fortran90*. website. `http://tools.tropos.de/`. Version: June 2015

[Man67] MANDELBROT, Benoît: How Long is the Coast of Britain? Statistical Self-Similarity and Fractal Dimension. In: *Science, New Series* 156 (1967), S. 636–638

[Man82] MANDELBROT, Benoît: *The Fractal Geometry of Nature*. W. H. Freeman and Company, New York, 1982

[Max54] MAXWELL, J. C.: In: *Cambridge Dublin Mathematical Journal* 8 (1854), 188 S.

[Max65] MAXWELL, James C.: A Dynamical Theory of the Electromagnetic Field. In: *Philosophical Transactions of the Royal Society of London* 155 (1865), S. 459–512

[McM54] MCMASTER, William H.: Polarization and the Stokes Parameters. In: *American Journal of Physics* 22 (1954), S. 351–362

[McM61] McMaster, William H.: Matrix Representation of Polarization. In: *Reviews of Modern Physics* 33 (1961), S. 8–28

[McW03] McWeeny, Roy: *Symmetry: An Introduction to Group Theory and its Applications*. Dover Publications, Inc., 2003

[MDG94] Martin, Olivier J. F. ; Dereux, Alain ; Girard, Christian: Iterative scheme for computing exactly the total field propagating in dielectric structures of arbitrary shape. In: *Journal of the Optical Society of America* 11 (1994), S. 1073–1080

[Mie08] Mie, Gustav: Beiträge zur Optik trüber Medien, speziell kolloidaler Goldlösungen (contributions to the optics of diffuse media, especially colloid metal solutions). In: *Annalen der Physik* 25 (1908), S. 377–445

[Mis91] Mishchenko, M. I.: Light scattering by randomly oriented axially symmetric particles. In: *Journal of the Optical Society of America* 8 (1991), S. 871–882

[Mis10] Mishchenko, M. I.: Poynting-Stokes tensor and radiative transfer in discrete random media: The microphysical paradigm. In: *Optics Express* 18 (2010), S. 19770–19791

[MM96] Mackowski, Daniel W. ; Mishchenko, Michael I.: Calculation of the T matrix and the scattering matrix for ensembles of spheres. In: *Journal of the Optical Society of America* 13 (1996), S. 2266–2278

[MM11] Moore, Emily B. ; Molinero, Valeria: Structural transformation in supercooled water controls the crystallization rate of ice. In: *Nature* 479 (2011), S. 506–508

[MMAC14] Magee, N. B. ; Miller, A. ; Amaral, M. ; Cumiskey, A.: Mesoscopic surface roughness of ice crystals pervasive across a wide range of ice crystal conditions. In: *Atmos. Chem. Phys.* 14 (2014), S. 12357–12371

[MMR96] Macke, Andreas ; Müller, J. ; Raschke, E.: Single scattering properties of atmospheric ice crystals. In: *Journal of Atmospheric Sciences* 53 (1996), S. 2813–2825

[MN98] Matsumoto, M. ; Nishimura, T.: Mersenne Twister. A 623-dimensionally equidistributed uniform pseudorandom number generator. In: *ACM Transactions on Modeling and Computer Simulation* 8 (1998)

[MNS+01] Möhler, O. ; Nink, A. ; Saathoff, H. ; Schaefers, S. ; Schnaiter, M. ; Schöck, W. ; Schurath, U.: The Karlsruhe aerosol chamber facility AIDA: technical description and first results of homogeneous and heterogeneous ice nucleation experiments. In: *Proceedings of Workshop on Ion-Aerosol-Cloud-Interactions (IACI)*, 2001

[Moo98] Moore, Gordon E.: Cramming More Components onto Integrated Circuits. In: *Proceedings of the IEEE* 86 (1998), S. 82–85

[MSC06] Mason, Jeanne G. ; Strapp, Walter J. ; Chow, Philip: The Ice Particle Threat to Engines in Flight. In: *44th AIAA Aerospace Sciences Meeting and Exhibit, Reno, Nevada*, 2006

[MT92] Macke, Andreas ; Tzschichholz, Frank: Scattering of light by two-dimensional deterministic Koch islands. In: *Physica A* 191 (1992), S. 545–548

[MTM10] Mishchenko, Michael I. ; Travis, Larry D. ; Mackowski, Daniel W.: T-matrix method and its applications to electromagnetic scattering by particles: A current perspective. In: *Journal of Quantitative Spectroscopy & Radiative Transfer* 111 (2010), S. 1700–1703

[MTN08] Mohr, J. P. ; Taylor, Barry N. ; Newell, David B.: CODATA recommended values of the fundamental physical constants: 2006. In: *Reviews of Modern Physics* 80 (2008), S. 633–730

[Nak54] Nakaya, Ukichiro: *Snow Crystals: Natural and Artificial*. Harvard University Press, 1954

[Neu32] NEUMANN, John von: Über einen Satz von Herrn M. H. Stone. In: *Annals of Mathematics* 33 (1932), S. 567–573

[Nic51] NICHOLSON, G. F.: An introduction to the rationalized M.K.S. system of units. In: *British Journal of Applied Physics* 2 (1951), S. 177–182

[Noe18] NOETHER, Emmy: Invariante Variationsprobleme. In: *Göttinger Nachrichten* (1918), S. 235–257

[OBIW72] OSBOURNE, John M. ; BUTLER, Terence M. J. ; IOMMI, Tony ; WARD, Bill: *Black Sabbath Vol. 4*. CD, LP (Vertigo Records, Los Angeles), September 1972

[Pau35] PAULING, Linus: The Structure and Entropy of Ice and of Other Crystals with Some Randomness of Atomic Arrangement. In: *Journal of the American Chemical Society* 57 (1935), S. 2680–2684

[PF96] PARSA, Zohreh ; FOREST, Étienne: Symplectic Integration. In: *Proceedings of the 12th Advanced ICFA Beam Dynamics Workshop on Nonlinear and Collective Phenomena in Beam Physics: Theory and Experiments*, 1996

[Pfe03] PFENNIG, Andreas: *Thermodynamik der Gemische*. Springer Verlag Berlin-Heidelberg, 2003

[PFW12] PITT-FRANCIS, Joe ; WHITELEY, Jonathan: *Guide to Scientific Computing in C++*. Springer Verlag London, 2012

[Ple60] PLEBANSKI, Jerzy: Electromagnetic Waves in Gravitational Fields. In: *Physical Review* 118 (1960), S. 1396–1408

[PLMS00] PLAUGER, P. J. ; LEE, Meng ; MUSSER, David ; STEPANOV, Alexander A.: *C++ Standard Template Library*. Prentice Hall, 2000

[Pop00] POPE, Stephen B.: *Turbulent Flows*. Cambridge University Press, 2000

[PP73] PURCELL, Edward M. ; PENNYPACKER, Carlton R.: Scattering and Absorption of Light by nonspherical dielectric grains. In: *The Astrophysical Journal* 186 (1973), S. 705–714

[PS05] PESKIN, Michael E. ; SCHROEDER, Daniel V.: *An Introduction to Quantum Field Theory*. Levant Books, 2005

[PSS06] PENDRY, J.B. ; SCHURIG, D. ; SMITH, D. R.: Controlling Electromagnetic Fields. In: *Science* 312 (2006), S. 1780–1782

[PTVF95] PRESS, William H. ; TEUKOLSKY, Saul A. ; VETTERLING, William T. ; FLANNERY, Brian P.: *Numerical Recipes in C: The Art of Scientific Computing*. Cambridge University Press, 1995

[pyt] *Python Language Reference, Version 2.7*. `http://www.python.org`

[RH73] REED, W. H. ; HILL, T. R.: Triangular mesh methods for the neutron transport equation / University of California, Los Alamos Scientific Laboratory. 1973. – Forschungsbericht

[RK14] ROTHER, Tom ; KAHNERT, Michael: *Electromagnetic Wave Scattering on Nonspherical Particles: Methodology and Simulations*. Springer Verlag Berlin-Heidelberg, 2014

[RORG11] REN, K. F. ; ONOFRI, F. ; ROZE, C. ; GIRASOLE, T.: Vectorial complex ray model and application to two-dimensional scattering of a plane wave by a spheroidal particle. In: *Optics Letters* 36 (2011), S. 370–372

[Ros95] ROSSUM, Guido van: Technical Report CS-R9526 / Centrum voor Wiskunde en Informatica (CWI), Amsterdam. 1995. – Forschungsbericht

[SA08] SPURK, Joseph H. ; AKSEL, Nuri: *Fluid Mechanics*. Springer-Verlag, 2008

[SABG14] SAENGKAEW, S. ; ALLANO, Daniel ; BRUNEL, M. ; GRÉHAN, G.: FII technique: Introduction of a simple model and experimental validation on a line of monodispersed droplets. In: *Optics Communications* 332 (2014), S. 269–278

[Sae14] SAENGKAEW, Sawitree: *Optical characerization of discrete media: From Rainbow to Fourier Interferometric Imaging*, Université de Rouen, Diss., 2014

[Sax55] SAXON, David S.: Tensor Scattering Matrix for the Electromagnetic Field. In: *Physical Review* 100 (1955), S. 1771–1775

[SB05] STOER, J. ; BULIRSCH, Roland: *Numerische Mathematik 2*. Springer Verlag Berlin-Heidelberg, 2005

[SCB+15] SMITH, Helen R. ; CONNOLLY, Paul J. ; BARAN, Anthony J. ; HESSE, Evelyn ; SMEDLEY, Andrew R. D. ; WEBB, Ann R.: Cloud chamber laboratory investigations into scattering properties of hollow ice particles. In: *Journal of Quantitative Spectroscopy & Radiative Transfer* 157 (2015), S. 106–118

[Sch26] SCHRÖDINGER, Erwin: Der stetige Übergang von der Mikro- zur Makromechanik. In: *Naturwissenschaften* 14 (1926), S. 664–666

[Sch35] SCHRÖDINGER, Erwin: Die gegenwärtige Situation in der Quantenmechanik. In: *Die Naturwissenschaften* 48 (1935), S. 807–812

[Sch12] SCHECK, Florian: *Classical Field Theory*. Springer-Verlag Berlin Heidelberg, 2012

[Sch13] SCHÄFER, Walter: *Time-Shift Technique for Particle Characterization in Sprays*, Fachgebiet Strömungslehre und Aerodynamik, TU Darmstadt, Diss., 2013

[SH94] SCHNEIDER, M. ; HIRLEMAN, E. D.: Influence of internal refractive index gradients on size measurements of spherically symmetric particles by phase Doppler anemometry. In: *Applied Optics* 33 (1994), S. 2379–2388

[Sha07] SHALAEV, Vladimir M.: Optical negative-index metamaterials. In: *Nature Photonics* 1 (2007), S. 41–48

[Sha12] SHAKESPEARE, William: *Love's Labour's Lost*. Dover Publications, Inc., 2012

[Shc13] SHCHERBAKOV, V.: Why the 46° halo is seen far less often than the 22° halo. In: *Journal of Quantitative Spectroscopy & Radiative Transfer* 124 (2013), S. 37–44

[SK11] SANDERS, Jason ; KANDROT, Edward: *CUDA by Example: An Introduction to General-Purpose GPU Programming*. Pearson Education, Inc., 2011

[SM05] STOLL, Axel ; MANNICH, Arno: *Das Wissen um die wahre Physik: Bis heute unterdrückt*. Extrem Verlag, 2005

[Som64] SOMMERFELD, Arnold: *Vorlesungen über Theoretische Physik, Band IV: Optik*. Akademische Verlagsgesellschaft Geest und Portig Leipzig, 1964

[Som67] SOMMERFELD, Arnold ; BOPP, Fritz (Hrsg.) ; MEIXNER, Josef (Hrsg.): *Vorlesungen über Theoretische Physik, Band III: Elektrodynamik*. Akademische Verlagsgesellschaft Geest und Portig Leipzig, 1967

[SS99] SCHULZ, Michael F. ; STAMNES, Knut: Point-group symmetries in electromagnetic scattering. In: *Journal of the Optical Society of America* 16 (1999), S. 853–865

[ST14] SCHÄFER, Walter ; TROPEA, Cameron: Time-shift technique for simultaneous measurement of size, velocity, and relative refractive index of transparent droplets or particles in a flow. In: *Applied Optics* 53 (2014), S. 588–597

[Sto05] STOER, Josef: *Numerische Mathematik 1*. Springer Verlag Berlin-Heidelberg, 2005

[Str] STROUSTRUP, Bjarne: *ISO/IEC 14882:2014 Information technology - Programming languages - C++*

[Str07] STRATTON, Julius A.: *Electromagnetic Theory*. Wiley-IEEE Press, 2007

[SURS98] SHYY, Wei ; UDAYKUMAR, H. S. ; RAO, Madhukar M. ; SMITH, Richard W.: *Computational Fluid Dynamics with Moving Boundaries*. Dover Publications, Inc., 1998

[SW01] SCHUHMANN, R. ; WEILAND, T.: Conservation of discrete energy and related laws in the finite integration technique. In: *Progress in Electromagnetics Research* 32 (2001), S. 301–316

[Syn58] SYNGE, J. L.: *Relativity: The Special Theory*. North-Holland Publishing Company, 1958

[tec] TEC5 GMBH (Hrsg.): *Ultrasonic Levitator Manual*. In der Au 27, 61440 Oberursel / Taunus: tec5 GmbH

[TEW91] TAKAHASHI, T. ; ENDOH, Tatsuo ; WAKAHAMA, Gorow: Vapor Diffusional Growth of Free-Falling Snow Crystals between -3° and -23° C. In: *Journal of the Meteorological Society of Japan* 69 (1991), S. 150–30

[TF88] TAKAHASHI, Tsuneya ; FUKUTA, Norihoko: Supercooled Cloud Tunnel Studies on the Growth of Snow Crystals between -4° C and -20° C. In: *Journal of Meteorological Research, Japan* 66 (1988), S. 841–855

[TVP15] TRICOLI, Ugo ; VOCHEZER, P. ; PFEILSTICKER, Klaus: Transition operator calculation with Green's dyadic technique for electromagnetic scattering: A numerical approach using the Dyson equation. In: *Journal of Quantitative Spectroscopy & Radiative Transfer* 162 (2015), S. 77–88

[UKH+14] ULANOWSKI, Z. ; KAYE, P. ; HIRST, E. ; GREENWAY, R. ; COTTON, R. ; HESSE, E.: Incidence of rough and irregular atmospheric ice particles from small ice detector 3 measurements. In: *Atmospheric Chemistry and Physics* 14 (2014), S. 1649–62

[Ula05] ULANOWSKI, Z.: Ice analog halos. In: *Applied Optics* 44 (2005), S. 5754–5758

[Unk65] UNKNOWN ; PP., Ionnes Paulus I. (Hrsg.): *Nova Vulgata*. sacrosanctum oecumenicum concilium Vaticani secundum, 1965

[Wat63] WATERMAN, P. C.: Matrix Formulation of Electromagnetic Scattering. In: *Proceedings of the IEEE* (1963), S. 805–812

[Wat71] WATERMAN, Peter C.: Symmetry, unitarity, and geometry in electromagnetic scattering. In: *Physical Review D* 4 (1971), S. 825–839

[Wat79] WATERMAN, P. C.: Matrix methods in potential theory and electromagnetic scattering. In: *Journal of Applied Physics* 50 (1979), S. 4550–4566

[Wei77] WEILAND, Thomas: Eine Methode zur Lösung der Maxwellschen Gleichungen für sechskomponentige Felder auf diskreter Basis. In: *Archiv für Elektronik und Übertragungstechnik / International Journal of Electronics and Communications* 31 (1977), S. 116–120

[Wei84a] WEILAND, T.: On the unique numerical solution of Maxwellian eigenvalue problems in three dimensions / Deutsches Elektronen-Synchrotron (DESY). 1984. – Forschungsbericht

[Wei84b] WEILAND, Thomas: On the Numerical Solution of Maxwell's Equations and Applications in the Field of Accelerator Physics. In: *Particle Accelerators* 15 (1984), S. 245–292

[Wei96] WEILAND, Thomas: Time Domain Electromagnetic Field Computation with Finite Difference Methods. In: *International Journal of Numerical Modelling: Electronic Networks, Devices and Fields* 9 (1996), S. 295–319

[Wey50] WEYL, Hermann: A Remark on the Coupling of Gravitation and Electron. In: *Physical Review* 77 (1950), S. 699–701

[WFM08] WALLS F.R.S, D. F. ; MILBURN, Gerard J. ; WALLS F.R.S, D. F. (Hrsg.) ; MILBURN, Gerard J. (Hrsg.): *Quantum Optics*. Springer-Verlag Berlin Heidelberg, 2008

[Wig32] WIGNER, Eugene: On the quantum correction for thermodynamic equilibrium. In: *Physical Review* 40 (1932), S. 749–759

[Wol78] WOLF, Emil: Coherence and radiometry. In: *Journal of the Optical Society of America* 68 (1978), S. 6–17

[Wor04] WORRINGEN, Annette geb. R.: *Untersuchungen zu optischen Eigenschaften atmosphärischer Aerosolpartikel*, Technische Universität Darmstadt, Fachbereich Material- und Geowissenschaften, Diss., 2004

[WR10] WOLFRAM RESEARCH, Inc.: *Mathematica*. Software. `http://www.wolfram.com/mathematica/`. Version: 2010

[Wri02] WRIEDT, T.: Using the T-Matrix Method for Light Scattering Computations by Non-axisymmetric Particles: Superellipsoids and Realistically Shaped Particles. In: *Part. Part. Syst. Charact.* 19 (2002), S. 256–268

[Wri08] WRIEDT, Thomas: Mie theory 1908, on the mobile phone 2008. In: *Journal of Quantitative Spectroscopy & Radiative Transfer* 109 (2008), S. 1543–1548

[Wri15] WRIEDT, T.: *Scattport homepage*. website. `http://www.scattport.org/`. Version: August 2015

[WSA97] WARNICK, Karl F. ; SELFRIDGE, Richard F. ; ARNOLD, David V.: Teaching Electromagnetic Field Theory Using Differential Forms. In: *IEEE Transactions on education, Vol. 40, Nr. 1*, 1997

[WY12] WENDISCH, Manfred ; YANG, Ping: *Theory of Atmospheric Radiative Transfer*. Wiley VCH GmbH & Co. KG, 2012

[XRG+07] XU, Feng ; REN, K. F. ; GOUESBET, G. ; GRÉHAN, G. ; CAI, Xiaoshu: Generalized Lorenz-Mie theory for an arbitrarily oriented located and shaped beam scattered by a homogeneous spheroid. In: *Journal of the Optical Society of America* 24 (2007), S. 119–131

[Yee66] YEE, Kane S.: Numerical Solution of Initial Boundary Value Problems Involving Maxwell's Equations in Isotropic Media. In: *IEEE Transactions on Antennas and Propagation* 14 (1966), S. 302–307

[YH07] YURKIN, Maxim A. ; HOEKSTRA, A. G.: The discrete dipole approximation: An overview and recent developments. In: *Journal of Quantitative Spectroscopy & Radiative Transfer* 106 (2007), S. 558–589

[YH11] YURKIN, M. A. ; HOEKSTRA, A. G.: The discrete-dipole-approximation code ADDA: capabilities and known limitations. In: *Journal of Quantitative Spectroscopy & Radiative Transfer* 112 (2011), S. 2234–2247

[YL96] YANG, Ping ; LIOU, K. N.: Geometric-optics-integral-equation method for light scattering by nonspherical ice crystals. In: *Applied Optics* 35 (1996), S. 6568

[YL97] YANG, Ping ; LIOU, K. N.: Light scattering by hexagonal ice crystals: solutions by a ray-by-ray integration algorithm. In: *Journal of the Optical Society of America* 14 (1997), S. 2278–2289

[YN95] YANG, Ping ; N., Liou K.: Light scattering by hexagonal ice crystals: comparison of finite-difference time domain and geometric optics models. In: *Journal of the Optical Society of America* 12 (1995), S. 162–176

[YN98] YANG, P. ; N., Liou K.: Single-scattering properties of complex ice crystals in the terrestrial atmosphere. In: *Contributions to Atmospheric Physics* 48 (1998), S. 71:223

[YOT+92] YAKHOT, V. ; ORSZAG, S. A. ; THANGAM, S. ; GATSKI, T. B. ; SPEZIALE, C. G.: Development of turbulence models for shear flows by a double expansion. In: *Physics of Fluids A* 4 (1992), S. 1510–1520

[You02] YOUNG, Thomas: The Bakerian Lecture: On the Theory of Light and Colours. In: *Philosophical Transactions of the Royal Society of London* 92 (1802), S. 12–48

[YPT98] YARIN, A. L. ; PFAFFENLEHNER, M. ; TROPEA, C.: On the acoustic levitation of droplets. In: *Journal of Fluid Mechanics* 356 (1998), S. 65–91

[Yu13] YU, Haitao: *Laser Beam Interaction with Spheroidal Droplets: Computation and Measurement*, Fachgebiet Strömungslehre und Aerodynamik, TU Darmstadt, Diss., 2013

[Yur14] YURKIN, M. A.: *a-dda web presence*. google web page. `https://code.google.com/p/a-dda/`. Version: February 2014

[ZFT64] ZALKIN, Allan ; FORRESTER, J. D. ; TEMPLETON, David H.: The Crystal Structure Sodium Fluorosilicate. In: *Acta Crystallographica* 17 (1964), S. 1408–1412

[ZXYW14] ZHANG, Yueyi ; XIONG, Zhiwei ; YANG, Zhe ; WU, Feng: Real-Time Scalable Depth Sensing With Hybrid Structured Light Illumination. In: *IEEE Transactions on Image Processing* 23 (2014), S. 97–109

This bibliography conforms with the standardized layout defined in DIN 1505-02.

Appendix

The source code listed in the appendix has been written by or under the supervision of the author himself during the course of his Ph.D. thesis.

Matlab script KochSnowflake.m for generating 3D Koch fractals

Execute script directly in Matlab.

```
1
2  %% initialization
3  %figure();
4  clear all;
5  clc;
6  %% initial tetrahedron
7  radius = 1.;
8  theta = pi/6.;
9  %% initial tetrahedron triangles:
10 triangle_1.vertices = [radius.*cos(theta) radius.*sin(theta) 5. % Vertex 1 (x-y-z)
11      -radius.*cos(theta) radius.*sin(theta) 5
12     0. -radius 5.]; % Vertex 3 (x-y-z)
13 triangle_1.faces = [1 2 3];
14 triangle_1.facecolor= 'b';
15 %patch(triangle_1);
16
17 triangle_2.vertices = [radius.*cos(theta) radius.*sin(theta) 5. % Vertex 1 (x-y-z)
18     0. -radius 5. % Vertex 2 (x-y-z)
19     0 0 5.-radius]; % Vertex 3 (x-y-z)
20 triangle_2.faces = [1 2 3];
21 triangle_2.facecolor='b';
22 % patch(triangle_2);
23 triangle_3.vertices = [0 0 5.-radius % Vertex 1 (x-y-z)
24     0. -radius 5. % Vertex 2 (x-y-z)
25     -radius.*cos(theta) radius.*sin(theta) 5.]; % Vertex 3 (x-y-z)
26 triangle_3.faces = [1 2 3];
27 triangle_3.facecolor='b';
28 %patch(triangle_3);
29 triangle_4.vertices = [radius.*cos(theta) radius.*sin(theta) 5. % Vertex 1 (x-y-z)
30     0 0 5.-radius% Vertex 2 (x-y-z)
31     -radius.*cos(theta) radius.*sin(theta) 5.]; % Vertex 3 (x-y-z)
32 triangle_4.faces = [1 2 3];
33 triangle_4.facecolor='b';
34 %patch(triangle_4);
35 list_of_triangles = [triangle_1
36     triangle_2
37     triangle_3
38     triangle_4];
39 %list_of_triangles = [triangle_1];
40
41 %% main iteration loop for creating the sub-tetrahedra
42 max_iter = 2;
43 for index1 = 1:max_iter
44     % figure
45     % loop over the list of existing former triangles
46     swap_list = [];
47     for index2 = 1:length(list_of_triangles)
48         % list_of_triangles(index2).vertices(1,:)
49         % 1. calculate three new points on top of the original triangular surface
50         sh1 = 0.5*list_of_triangles(index2).vertices(1,:)+0.5*list_of_triangles(index2).vertices
               (2,:);
51         sh2 = 0.5*list_of_triangles(index2).vertices(1,:)+0.5*list_of_triangles(index2).vertices
               (3,:);
```

```
        sh3 = 0.5*list_of_triangles(index2).vertices(2,:)+0.5*list_of_triangles(index2).vertices
            (3,:);
        % 2. calculate triangular surface normal and corresponding fourth point
        normal_factor = cross(list_of_triangles(index2).vertices(1,:)-list_of_triangles(index2).
            vertices(2,:),list_of_triangles(index2).vertices(3,:)-list_of_triangles(index2).
            vertices(1,:));
        normal = -1.*normal_factor./norm(normal_factor);
        sp = (list_of_triangles(index2).vertices(1,:)+list_of_triangles(index2).vertices(2,:)+
            list_of_triangles(index2).vertices(3,:))./3.;
        sh4 = sp+normal.*norm(sh2-sh1).*0.7;
        % 3. patch additional tetrahedron
        triangle_a.vertices = [list_of_triangles(index2).vertices(1,:)
            sh1
            sh2];
        triangle_a.faces = [1 2 3];
        triangle_a.facecolor = [0.4 0.4 0.4];
        triangle_b.vertices = [list_of_triangles(index2).vertices(2,:)
            sh3
            sh1];
        triangle_b.faces = [1 2 3];
        triangle_b.facecolor = [0.4 0.4 0.4];
        triangle_c.vertices = [list_of_triangles(index2).vertices(3,:)
            sh2
            sh3];
        triangle_c.faces = [1 2 3];
        triangle_c.facecolor = [0.4 0.4 0.4];
        triangle_d.vertices = [sh1
            sh4
            sh2];
        triangle_d.faces = [1 2 3];
        triangle_d.facecolor = [0.4 0.4 0.4];
        triangle_e.vertices = [sh1
            sh3
            sh4];
        triangle_e.faces = [1 2 3];
        triangle_e.facecolor = [0.4 0.4 0.4];
        triangle_f.vertices = [sh3
            sh2
            sh4];
        triangle_f.faces = [1 2 3];
        triangle_f.facecolor = [0.4 0.4 0.4];
        if(index1 == max_iter)
            patch(triangle_a);
            patch(triangle_b);
            patch(triangle_c);
            patch(triangle_d);
            patch(triangle_e);
            patch(triangle_f);
        end
        swap_list = [swap_list
            triangle_a
            triangle_b
            triangle_c
            triangle_d
            triangle_e
            triangle_d
            triangle_f];
    end
    clear list_of_triangles;
    list_of_triangles = swap_list;
    clear swap_list;
    % replace former triangles with new triangles from the current
    % iteration:

    %% eye candy
    axis equal
%axis off
view(3)
set(gca,'FontSize',24)
title 'Koch snowflake'
```

```
xlabel x
ylabel y
zlabel z
grid on
% alpha(.5)
lighting phong
end
```

Matlab script GreensFunctionTechnique1D.m

Execute script directly in Matlab.

```
function main
    %% incident field
    z = 0:.002:2.;
    k = 50;
    incident = exp(1i.*k.*z);
    %figure
    %plot(1:1001,real(incident));
    plot(1:1001,incident.*conj(incident),'b','LineWidth',2);
    hold on
    linefig1 = [500 500];
    linefig2 = [-1,1.5];
    plot(linefig1,linefig2,'k','LineWidth',4);
    linefig1 = [750 750];
    plot(linefig1,linefig2,'k','LineWidth',4);

    %% initialization
    startg = 0.;
    endg = 2.;
    elements = 1000;
    grid = linspace(startg,endg,elements);
    gridsize = (endg-startg)/elements;
    permeability = ones(elements,1);
    permeability(500:750) = 400.+1i.*0;
    psi1 = zeros(elements,1);
    ps1k1 = psi0(startg)/(1.-greensfunction(startg,startg)...
        *gridsize...
        *permeability(1));
    G1k1j = zeros(elements,1);
    for ii = 1:elements
        G1k1j(ii) = greensfunction(startg,grid(ii))...
            /(1-greensfunction(startg,startg)...
            *gridsize*permeability(1));
%         G1k1i(ii) = (G1k1j(1) - greensfunction(grid(ii),startg))...
%             /(permeability(ii)*gridsize*greensfunction(startg,startg));
        psi1(ii) = psi0(grid(ii)) + greensfunction(grid(ii),startg)...
            *permeability(1)*gridsize*ps1k1;
    end


    itwavefunc = zeros(elements);
    itwavefunc(1,:) = psi1;

    BigG = zeros(elements);
    for ii = 1:elements
        for jj = 1:elements
            BigG(ii,jj) = greensfunction(grid(ii),grid(jj)) ...
                + greensfunction(grid(ii),grid(1))*permeability(1)...
                *gridsize*G1k1j(jj);
        end
    end

    for iteration = 2:elements
        psi2k2 = itwavefunc(iteration-1,iteration)...
            /(1-BigG(iteration,iteration)*permeability(iteration)*gridsize);
        itwavefunc(iteration,:) = itwavefunc(iteration-1,:)...
```

```
            + BigG(iteration,:).*permeability(iteration).*gridsize.*psi2k2;
        BigGj = BigG(iteration,:)./(1-BigG(iteration,iteration)...
            *permeability(iteration)*gridsize);
        BigG(iteration:elements,iteration:elements) =...
            BigG(iteration:elements,iteration:elements)...
            +BigG(iteration:elements,iteration)*permeability(iteration)...
            *gridsize*BigGj(iteration:elements);
    end
    %figure
    %plot(1:1000,real(itwavefunc(elements,:)),'r');
    %for kk = 1:elements
        plot(1:1000,(itwavefunc(elements,:).*conj(itwavefunc(elements,:))),'k--','LineWidth',2);
        %plot(1:1000,real(itwavefunc(elements,:)),1:1000,imag(itwavefunc(elements,:)));
    %end
    set(gca, 'FontSize', 24)
    xlabel x;
    ylabel '\Psi \cdot \Psi^*';
    %title('Field Intensity')
    xlim([0 1000]);
end

function result = psi0(z)
    k = 50;
    result = exp(1i*k*z);
end

% function result = greensfunction(x,x_prime)
%     k = 25;
%     result = exp(k*abs(x_prime-x))/(4.*pi*abs(x_prime-x));
% end

function result = greensfunction(x,x_prime)
    k = 50;
    result = (1i*exp(1i*k*abs(x_prime-x)))/(2*k);
end
```

Python 1D FDTD script OneDExample.py

Execute the Python script directly by using the following shell command:

```
# python OneDExample.py
```

Or translate the Python source code to the C language via the cython utility for increased runtime speed and efficiency:

```
# cython -embed -o OneDExample.c OneDExample.py
```

Compile the C source using the gcc or LLVM clang compiler under a UNIX certified environment:

```
# clang++ -O2 -I/System/Library/Frameworks/Python.framework/Versions/2.7/include/python2.7 -o OneDExampleExec OneDExample.c
```

Please note that the given compilation command needs to be modified according to the exact specification of your system and *will* fail to compile for operating systems other than Mac OS.
Execute the compiled binary as usual:

```
# ./OneDExampleExec
```

```

# !/usr/bin/env python
import cmath
import numpy as np
import matplotlib.pyplot as plt
import matplotlib.animation as animation

################################################
# Courant number
sigma = 0.95
```

```
11
12  ##################################################
13  # interval boundaries
14  xmin = -1
15  xmax = 1
16
17  ##################################################
18  # grid nodes
19  Nnodes = 200
20  x = np.linspace(xmin, xmax, num = Nnodes)
21  dx = x[2] - x[1]
22
23  ##################################################
24  # number of time steps
25  Nperio = 10.
26  Time = Nperio*(xmax-xmin)
27
28  dt = sigma * dx
29  Nsteps = Time / dt
30
31  ##################################################
32  # INITIAL SOLUTION
33  # You need in this case [Ez(0), Hy(-1/2)] as initial condition
34
35  Ez = np.zeros(Nnodes) + 1j*np.zeros(Nnodes)
36  Hy = np.zeros(Nnodes) + 1j*np.zeros(Nnodes)
37
38  # truncated sine wave
39  for i in range(0,Nnodes):
40      if ((x[i] < 0.25) & (x[i] > -0.25)):
41          Ez[i] = np.cos(2.*np.pi*x[i])*cmath.exp(1j*2.*np.pi*x[i])
42          Hy[i] = -np.cos(2.*np.pi*(x[i]+dx/2.-dt/2.))*cmath.exp(1j*2.*np.pi*(x[i]+dx/2.-dt/2.))
43
44  ##################################################
45  # TIME STEPPING
46
47  # Animated Plot:
48  fig1 = plt.figure()
49  ax1 = fig1.add_axes()
50
51  # periodic boundary condition
52  Ez[Nnodes-1] = Ez[0]
53  Hy[Nnodes-1] = Hy[0]
54
55  # Time stepping loop
56  imsE = []
57  #imsH = []
58
59  for j in range(0,(int(Nsteps)-1)):
60      #Ez[0] = Ez[0] + sigma*(Hy[0] - Hy[Nnodes-2]) # periodic boundary for Ez
61      Ez[0] = 0.
62      Ez[Nnodes-1] = Ez[0]
63
64      for i in range(1, Nnodes-1):
65          Ez[i] = Ez[i] + sigma * (Hy[i] - Hy[i-1])
66
67      #Hy[0] = Hy[0] + sigma * (Ez[1] - Ez[0]) # periodic boundary for Hy
68      Hy[0] = 0.
69      Hy[Nnodes-1] = Hy[0]
70
71      for i in range(1, Nnodes-1):
72          Hy[i] = Hy[i] + sigma * (Ez[i+1] - Ez[i])
73
74      #plt.plot(x,Ez,'b')
75      #plt.plot(x,Hy,'r')
76      imsE.append(plt.plot(x,abs(Ez*Ez.conjugate()),'b'))
77      #imsH.append(plt.plot(x,Hy,'r'))
78
79  im_aniE = animation.ArtistAnimation(fig1, imsE, interval=20, repeat_delay=3000, blit=False)
80  #im_aniH = animation.ArtistAnimation(fig1, imsH, interval=50, repeat_delay=3000, blit=True)
```

```
im_aniE.save('ElectricField.mp4')
plt.xlabel('x [length]')
plt.ylabel('Intensity')
plt.show()
```

Matlab script Brunelgpmodel.m, implementing Brunel's Glare Point model

Execute script directly in Matlab.

```
%%%%%%%%%%%%%%%%%%%%%%%%%%%%%%%%%%%%%%%%%%%%%%%%%%%%
%
%   Implementation of Marc Brunel's Speckle
%   Simulation method. Simplified DDA-approach
%   for a very low number of dipoles. Convolution
%   of the Green's function over the particle
%   volume is replaced by a summation over
%   a discrete number of 'glare points' (see
%   code lines 50f.).
%
%   Author: P. Stegmann
%   Date:   2015-07-17
%
%%%%%%%%%%%%%%%%%%%%%%%%%%%%%%%%%%%%%%%%%%%%%%%%%%%%

% Clearing workspace
clear all
clc

% Dirac emitter description

% Large number of glare points for irregular particles
posx = [1. 10. 4 7. 8. 5. 1.].*1.e-1;        % emitter plane x coord
posy = [1. 0. 0.5 2 1 0.25 10.].*1.e-1;       % emitter plane y coord
alpha = [1. 2. 1. 1. 1. 1. 1.];      % Amplitude
phi = [0. pi/3. 0. 0. 0. 0.25 0.];     % Phase

% Exactly two glare points for a (roughly) spherical droplet
% posx = [-1. 1.];
% posy = [1. 0.];
% alpha = [1. 2.];
% phi = [0. pi/3.];
x = -5.:.01:5.;          % CMOS plane x coord
y = -5.:.01:5.;          % CMOS plane y coord
m = numel(x);
n = numel(y);
Intens = zeros(m,n);     % CMOS Intensity array
z1 = 100.;               % distance lens to particle
z2 = 200.;               % distance lens to CCD
f = 10.;                 % focal distance of lens
A = 1.-z2/f;             % 11 entry of optical lens matrix
B = z1+z2-z1*z2/f;       % 12 entry of optical lens matrix
lambda = 632.8e-6;       % laser wave length
Ngp = numel(posx);       % number of dirac emitters
%Intens = cell()

% Intensity calculation
% Iteration over all detector (i.e. CMOS camera) pixels
for mm = 1:m
    for nn = 1:n
        swap1 = 0;
        % Summation over all emitter (i.e. glare point) contributions
        for jj = 1:Ngp
            for kk = 1:Ngp
                swap2 = alpha(jj).*conj(alpha(kk)).*exp(1i.*(phi(jj)-phi(kk)))...
                    ./(lambda.*B.^2).*exp(1i.*pi.*A./(lambda*B)...
                    .*((posx(jj).^2+posy(jj).^2.)-(posx(kk).^2+posy(kk)^2)))...
                    .*exp(-1i.*2.*pi./(lambda*B)...
```

```
                    .*((posx(jj)-posx(kk)).*x(mm)-(posy(jj)-posy(kk)).*y(nn)));
            end
            swap1 = swap1 + swap2;
        end
        Intens(mm,nn) = swap1;
    end
end

% plotting commands for the intensity
[x,y] = meshgrid(x,y);
figure()
surf(-x,y,abs(Intens'),'LineStyle','None')
set(gca,'ZScale','log')
colormap gray
xlabel x
ylabel y
title 'Speckle pattern'
colorbar
view(2)
axis equal

% plot Fourier transform of the Intensity (1D)
figure()
transformedint = abs(fftshift(fft2(abs(Intens))));
%surf(x,y,transformedint,'LineStyle','None')
semilogy(smooth(transformedint(1,:)))
%set(gca,'YScale','log')
xlim([0 1000])
colormap gray
title 'FFT of speckle intensity'
view(2)
grid on

% plot emitters
figure()
scatter(posx,posy,'MarkerEdgeColor',[0 .5 .5],...
              'MarkerFaceColor',[0 .7 .7],...
              'LineWidth',2.5);
          axis equal
          xlabel x_e
          ylabel y_e
          title 'dirac emitter / glare point position'
          grid on
```

Measured temperature distribution inside the laboratory freezer

The following section displays the thermocouple measurements of the temperature distribution inside the laboratory freezer used for optical experiments on ice crystals. The orientation of the temperature values is roughly equivalent to the true spatial position at which they were measured. Blue values were measured at the end of a cooling cycle, while red values were measured right before its beginning. The first box displays the temperature at the bottom of the freezer. The second box shows the values in the middle between top and bottom The last box shows the measured values right at the top of the freezer.

The figure 5 shows the computational mesh used for the *OpenFOAM*® calculations consisting of quadrilateral elements and created using the *gmsh* software.

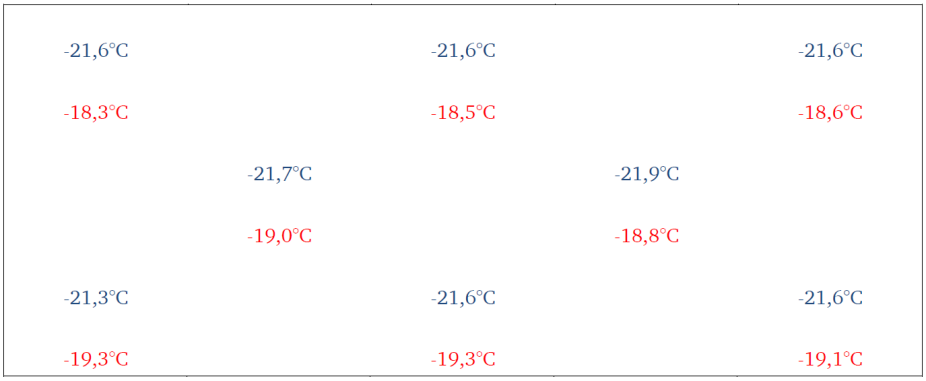

Figure 2: Laboratory freezer bottom temperature distribution .

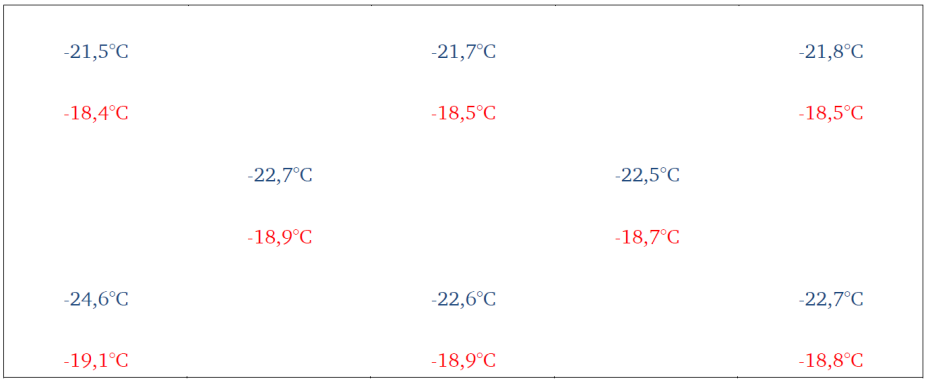

Figure 3: Laboratory freezer temperature distribution at half height.

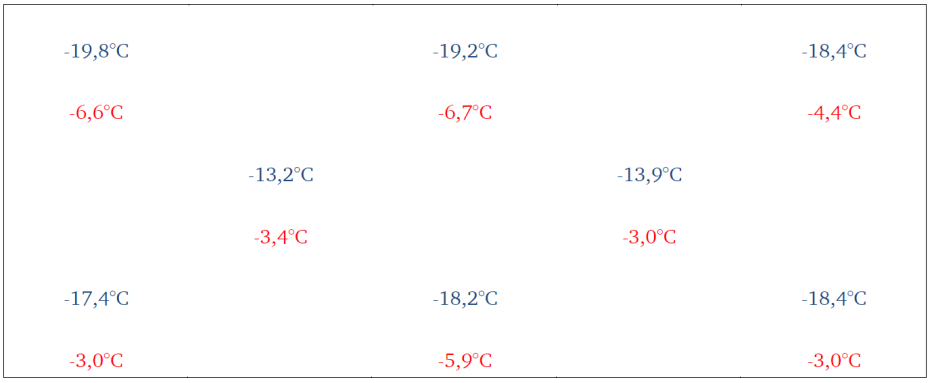

Figure 4: Laboratory freezer temperature distribution at the top lid.

Background signal of the Photodiodes

The signal of the Photodiode A measured in the laboratory freezer without coherent laser illumination is shown in figure 6 as measured.

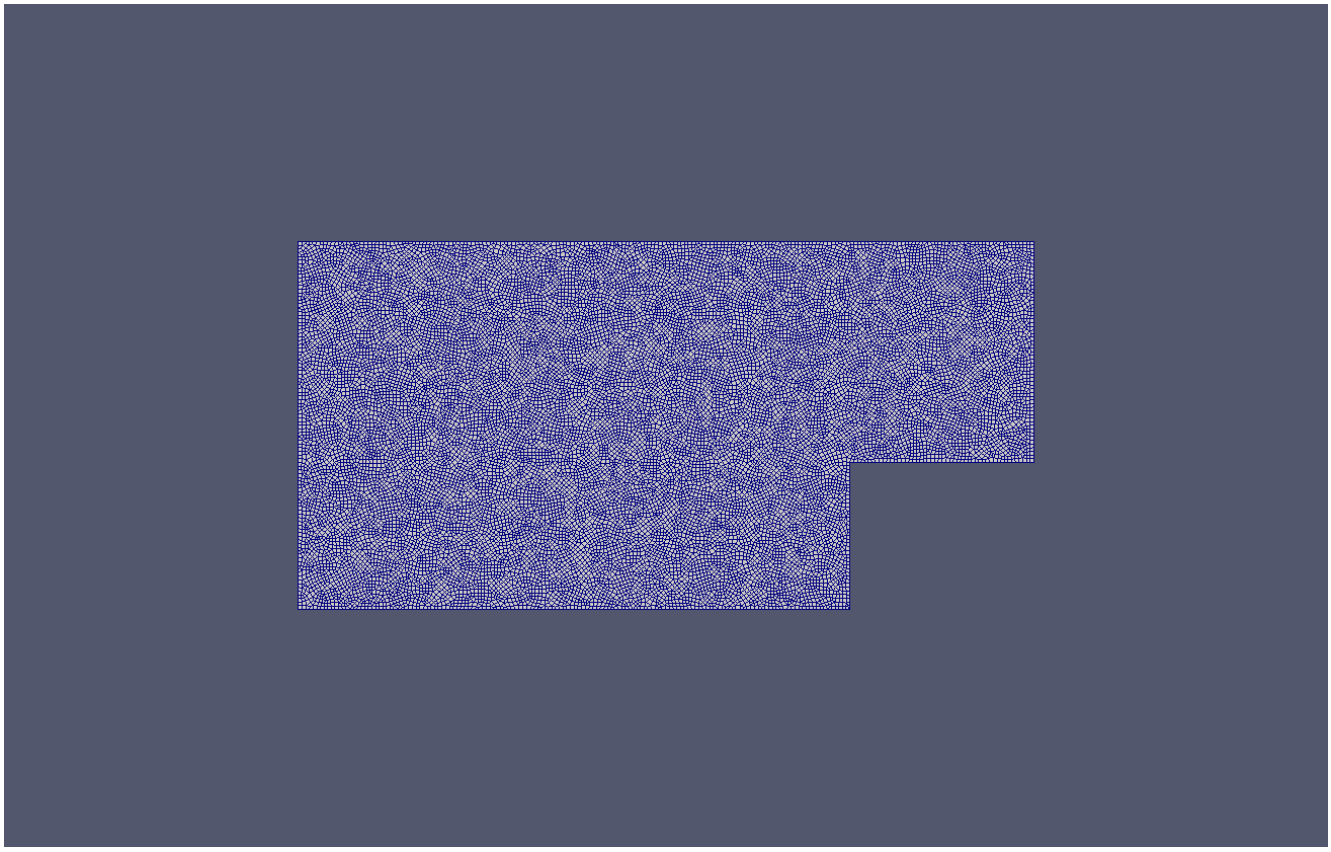

Figure 5: 2D mesh created using gmsh as a cross-section of the laboratory freezer.

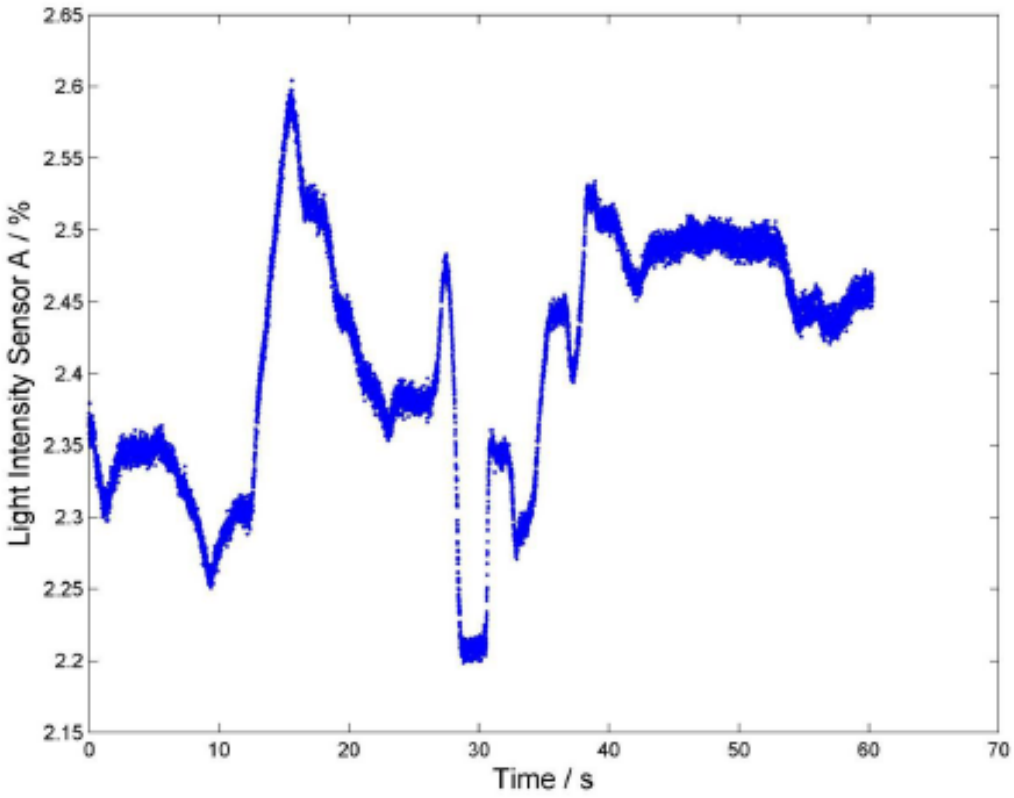

Figure 6: Background signal for photodiode A in the unillumated state recorded over a time of 60 seconds. A variation of the detector signal between 2.2 and 2.6 % is measured with laboratory lights on.